Novel test protocols and characterization techniques for OER based reversal tolerant PEFC anodes for automotive applications

Von der Fakultät Energie-, Verfahrens- und Biotechnik der Universität Stuttgart
zur Erlangung der Würde eines Doktors der
Ingenieurwissenschaften (Dr.-Ing.) genehmigte Abhandlung

Vorgelegt von

Dominik Claudius Bentele

aus Memmingen

Hauptberichter: Prof. Dr.-Ing. Elias Klemm
Mitberichter: Prof. Dr. rer. nat. K. Andreas Friedrich

Tag der mündlichen Prüfung: 11.07.2023

Institut für Technische Chemie der Universität Stuttgart

2023

"The future is not determined, the future is in our hands; what happens over the next centuries will be determined by how we play our cards this decade."

Prof. Dr. Johan Rockström,
Director of the Potsdam Institute for Climate Impact Research,
on the planetary boundaries and climate change.

Contents

List of Acronyms

ACL	Anode catalyst layer
AST	Accelerated stress test
BOL	Beginning-of-life
BOT	Beginning-of-test
CCL	Cathode catalyst layer
CCM	Catalyst coated membrane
COR	Carbon oxidation reaction
CR (AST)	Cyclic reversal (AST)
CV	Cyclic voltammetry
ECSA	Electrochemical surface area
EDX	Energy dispersive X-ray spectroscopy
EIS	Electrochemical impedance spectroscopy
EOL	End-of-life
EOT	End-of-test
EW	Equivalent weight
GDE	Gas diffusion electrode
GDL	Gas diffusion layer
HER	Hydrogen evolution reaction
HFR	High frequency resistance
HHV	Higher heating value
HOR	Hydrogen oxidation reaction
H_{upd}	Hydrogen under potential deposition
IPCC	Intergovernmental panel on climate change
MEA	Membrane electrode assembly
MPL	Microporous layer
NCR (AST)	Non-cyclic reversal (AST)
OCV	Open circuit voltage
OER	Oxygen evolution reaction
ORR	Oxygen reduction reaction
PEFC	Polymer electrolyte fuel cell
PEM(FC)	Proton exchange membrane (fuel cell)
PEN	Polyethylene naphthalene
PFSA	Perfluorosulfonic acid
PITM	Platinum in the membrane
PTFE	Polytetrafluorethylene
RH	Relative humidity
RHE	Reversible hydrogen electrode
RTA	Reversal tolerant anode
SEM	Scanning electron microscope
SHE	Standard hydrogen electrode
SUSD	Start-up and shut-down
TEM	Scanning transmission electron microscope
XPS	X-ray photoelectron spectroscopy

List of Symbols and Greek letters

Symbol	Description	Unit
A	Surface area	m^2
E	Potential	V
E^0	Reversible equilibrium potential	V
E_{cell}	Cell voltage	V
E_{rev}	Equilibrium potential	V
$ECSA$	Electrochemical surface area	$m_{catalyst}^2\,g_{catalyst}^{-1}$
F	Faraday constant	$C\,mol^{-1}$
G	Gibb's free energy	$J\,mol^{-1}$
H	Reaction enthalpy	$J\,mol^{-1}$
I	Current	A
i	Current density	$A\,cm^{-2}$
i_{H_2}	Crossover current density	$A\,cm^{-2}$
i_0	Exchange current density	$A\,cm_{catalyst}^{-2}$
i_{Cdl}	Double layer capacitance current density	$A\,cm^{-2}$
L	Catalyst loading	$g_{catalyst}\,cm_{electrode}^{-2}$
m	Mass	kg
$\dot{n}$	Molar flow	$mol\,s^{-1}$
Q	Electrical charge	C
R	Elctrical resistance	Ω
R	Universal gas constant	$J\,K^{-1}\,mol^{-1}$
rf	Roughness factor	$m_{catalyst}^2\,cm_{electrode}^{-2}$
RH	Relative humidity	-
p	Gauge or absolute pressure	bar_g or bar_a
S	Reaction entropy	$J\,K^{-1}\,mol^{-1}$
Q	Electrical charge	C
W_{el}	Electrical energy	J
W_{H_2}	Energy of hydrogen consumed	J
z	Number of transferred electrons	-

Greek letter	Description	Unit
$\alpha_{a/c}$	Anodic and cathodic transfer coefficient	-
β	Symmetry factor	-
η_{eff}	Efficiency	-
η_i	Overpotential of reaction or component i	V

Subscript	Description
a	Absolute
act	Activation or kinetic
ads	Adsorption
ce	Current efficiency
des	Desorption
el	Electrical
fu	Fuel utilization
g	Gauge
geo	Geometrical
H^+	Proton
mtx	Mass transport
Ω	Ohmic resistance

Superscript	Description
0	Normal conditions
eff	Effective
theo	Theoretical

Abstract

In a world facing climate change, the application of low temperature polymer electrolyte fuel cells (PEFCs) for automotive and stationary applications gained major attention recently. In particular, commercialization advances are being made for their usage in medium and heavy-duty vehicles. Durability is a key aspect for commercial success of PEFCs. To resist reversal events originating from gross fuel (i.e. H_2) starvation in affected cells, the introduction of oxygen evolution reaction (OER) co-catalysts to the PEFC anode has been established as material-based mitigation strategy. This work focuses on the development of test protocols and characterization techniques on single cell level to investigate iridium-based reversal tolerant PEFCs regarding performance and degradation.

The first part of this thesis aims at techniques which are providing insights into reversal tolerance of OER based PEFCs. An accelerated stress test (AST) was developed investigating short-term recurring reversal operation to meet the expectations of automotive field application. An OER recovery effect, indicated by unaffected OER activity, was observed for short-term reversal events while normal operation caused PEFC failure. In addition, a significant dependence between hydrogen oxidation reaction (HOR) catalyst and reversal tolerance was found. Using further characterization methods such as hydrogen pump polarization curves, PEFC failure for short-term reversal events could be ascribed to hydrogen oxidation mass transfer increase originating from severe carbon corrosion and structural collapse within the anode catalyst layer. The electrochemical results were validated analyzing scanning electron microscope images (SEM).

The second part of the thesis focuses on PEFC degradation by transient anode conditions originating from start-up/shut-down (SUSD) events. SUSD ASTs were developed to provoke substantial anode degradation while minimizing cathode degradation due to the so-called reverse-current effect. Advanced characterization methods to investigate the significant degradation of the HOR and OER catalyst were developed, uncovering a structural change of the anode catalyst layer and a substantial decline in reversal tolerance when PEFCs were exposed to SUSD events. In addition, characterization methods are presented to investigate the crossover of IrO_2 based OER catalyst to the cathode catalyst layer, promoted by transient anode conditions. Iridium crossover was found to significantly impact the determination of electrochemical surface area (*ECSA*) for platinum-based catalysts by state-of-the-art characterization methods. The introduction of a voltage clipping step during SUSD events was showing to have a minor impact on anode degradation and iridium crossover. Using energy dispersive X-ray spectroscopy (EDX) and SEM imaging, the electrochemical degradation characteristics were substantiated.

Zusammenfassung

In einer mit dem Klimawandel konfrontierten Welt hat die Anwendung von Niedertemperatur-Polymerelektrolyt-Brennstoffzellen (PEFCs) für Kraftfahrzeuge und stationäre Anwendungen in jüngster Zeit große Beachtung gefunden. Insbesondere wurden kommerzielle Fortschritte beim Einsatz in mittelschweren und schweren Nutzfahrzeugen erzielt. Die Langlebigkeit ist ein zentraler Aspekt für den kommerziellen Erfolg von PEFCs. Um sogenannten Reversal-Ereignissen zu widerstehen, welche durch Wasserstoffunterversorgung der betroffenen Zellen entstehen können, hat sich die Einführung von Co-Katalysatoren für die Sauerstoffentwicklungsreaktion (OER) innerhalb der PEFC Anode als materialbasierte Mitigation etabliert. Diese Arbeit konzentriert sich auf die Entwicklung neuartiger Testprotokolle und Charakterisierungsmethoden auf Einzelzellebene, um Degradationseffekte von Iridium-basierten, reversal-toleranten PEFCs hinsichtlich Leistung und Degradation zu untersuchen.

Der erste Teil dieser Arbeit zielt auf Testmethoden ab, die Einblicke in die Widerstandsfähigkeit von OER-basierten PEFCs bei Reversal-Ereignissen ermöglichen. Es wurde ein Alterungstest (AST) entwickelt, bei dem ein wiederkehrender, kurzzeitiger Reversalbetrieb appliziert wird, um Reversal-Ereignisse im Feldbetrieb erwartungsgerecht zu simulieren. Für kurzfristige Reversal-Ereignisse trat ein Erholungseffekt des OER Katalysators auf, der zu gleichbleibender OER Aktivität führte. Es zeigte sich, dass die Brennstoffzelle hingegen während des Normalbetriebs versagte. Darüber hinaus wurde ein signifikanter Einfluss des Katalysators der Wasserstoffoxidationsreaktion (HOR) auf die Reversal-Toleranz festgestellt. Unter Verwendung weiterer Charakterisierungsmethoden, beispielsweise der elektrochemischen Wasserstoffpumpe, konnte das Versagen der PEFC bei kurzzeitigen Reversal-Ereignissen auf eine Zunahme der Massentransportwiderstände für die Wasserstoffoxidationsreaktion (HOR) zurückgeführt werden. Diese Zunahme wurde wiederum verursacht durch starke Kohlenstoffkorrosion und einen strukturellen Zusammenbruch der Anodenkatalysatorschicht. Die elektrochemischen Ergebnisse wurden durch Aufnahmen mittels Rasterelektronenmikroskop (SEM) validiert.

Der zweite Teil der Arbeit befasst sich mit der Degradation aufgrund transienter Anodenbedingungen durch Start/Stopp (SUSD) Ereignisse. SUSD Alterungstests wurden entwickelt, um entsprechende Anodendegradation hervorzurufen und simultan Kathodendegradation durch den sogenannten Stromumkehreffekt zu minimieren. Es wurden Charakterisierungsmethoden entwickelt, um die signifikante Degradation des HOR- und OER-Katalysators zu untersuchen. Dabei kam es zu einer strukturellen Veränderung der Anodenkatalysatorschicht und eines substanziellen Rückgangs der Reversal-Toleranz, sobald Brennstoffzellen Start/Stopp Ereignissen ausgesetzt waren. Darüber hinaus

werden Charakterisierungsmethoden vorgestellt, um den Iridiumübertritt des OER-Katalysators auf die Kathode zu untersuchen, welcher durch transiente Anodenbedingungen begünstigt wird. Es wurde festgestellt, dass Iridium die Bestimmung der elektrochemischen Oberfläche (*ECSA*) von Katalysatoren auf Platinbasis erheblich beeinträchtigen kann. Die Einführung einer Spannungsbegrenzung während Start/Stopp Ereignissen wies lediglich geringfügige Auswirkungen auf Anodendegradation und Iridiumübertritt auf. Die elektrochemischen Degradationsergebnisse wurden mittels energiedispersiver Röntgenspektroskopie (EDX) und REM Aufnahmen untermauert.

Acknowledgements

1   Motivation

"We are the first generation to feel the effect of climate change and the last generation who can do something about it" [1]. This quote from the former US president Barack Obama illustrates the urgency of political, social, economic, and technological transitions to tackle one of humanity's most challenging issues: anthropogenic climate change. The crucial need for decarbonization of vast sectors of our economies has become a intended goal throughout society, politics and economy within the past decade [2]. The economic decarbonization is mandatory to combat and decelerate the rapidly progressing climate change.

From the first considerations in the 19th century, when Svante Arrhenius stated that coal mines are literally evaporated into the air and he drew the connection between emitted CO_2 and an anthropogenic global warming effect [3], the research and knowledge of anthropogenic climate change has been significantly improved until today. Within the 20th century further scientific insights have been obtained, corroborated and spread beyond the scientific community. For example, when James Hansen, a National Aeronautics and Space Administration (NASA) climate scientist, stated and explained the direct interconnection between substantial anthropogenic greenhouse gas accumulation in the earth's atmosphere and its impact on climate change 1988 in the United States (US) congress [4]. In the same year the Intergovernmental Panel on Climate Change (IPCC) was formed, whose main purpose is to review the latest findings of climate science and to disseminate knowledge to policy makers and governments around the globe [5]. These efforts succeeded in international climate change conferences and international treaties, as e.g. the Kyoto Protocol from 1992 [6] or the Paris Agreement from 2015 [7], where a vast majority of the world's countries agreed on climate change mitigation, adaption and finance.

Unfortunately, on the way from a scientific consensus to political, social and economic actions, valuable time has elapsed to mitigate climate change and effectively cut the CO_2 emissions from fossil fuels. However, science was not just able to reveal that the influence of humans has warmed the global climate at a rate unprecedented within the last 2000 years, but also managed to provide guiderails in future predictions on climate change dependent on the mitigating efforts [5]. The 2021 Nobel Prize in Physics most recently honored the outstanding research of Syukuro Manabe and Klaus Hasselmann which set the foundation for the scientific tools to predict climate change accurately [8]. Based on Manabe's and Hasselmann's work, scientists found that there is most likely still time left to mitigate climate change and prevent climate tipping points [9] – if we start acting now to achieve net-zero CO_2 emissions as soon as possible.

The recent disruptive changes during the COVID-19 pandemic illustrated, that society and politics can mitigate a global crisis governed by policies working with an individuals' biases and perceptions of risk [10]. Applying these experiences and knowledge on climate change could help to achieve the ambitious goal to reach net-zero carbon emissions by 2050, a goal set by the United States and many European countries as part of the Paris Agreement [7].

Upon the journey to net-zero carbon emissions, hydrogen will play a major role to meet the decarbonization targets of various sectors: from heating over food production, metallurgy and refining to transportation [11]. Renewable energy production by solar and wind has become cost effective recently [12, 13], generating the demand for energy conversion and energy storage. Hydrogen is able to store this renewable energy at a gigawatt-hour scale to overcome both daily and seasonal renewable energy fluctuation on a commercial level today [11]. Besides, hydrogen storage and transport can be realized at low cost, e.g. within the existing natural gas system infrastructure enabling massive storage capacity [14]. With the help of hydrogen, sustainable primary energy can be provided for all economic sectors, enabling a 100% zero emission energy grid in combination with renewable energy production [14].

Most recently, the European Union as well as the United States enhanced their efforts for hydrogen deployment at scale. The US Department of Energy is targeting to reduce the costs of clean hydrogen by 80% to 1 $/kg within a single decade [15]. Simultaneously, the European Union committed on three major legislative packages aiming for the transition to a green hydrogen economy upon 2050 [16]. The focus on hydrogen is regarded as critical for the European energy security and independence, in the fields of electric power, transportation, manufacturing, food production and supply [14, 17]. In addition, the establishment of a hydrogen economy is also expedited in other countries, e.g. China, Japan and Australia [18]. These billion-dollar investments [15, 16, 18, 19], massive activities and enormous efforts are a clear sign for the key role attributed to hydrogen mitigating climate change. Furthermore, establishing a strong hydrogen sector is crucial to accomplish a sustainable and fossil free economy in the abovementioned regions and worldwide.

Besides its capability in energy storage, hydrogen can act as base material for synthetic fuels in transportation, for stationary power applications and in various industrial sectors (e.g., ammonia production) [11]. However, as hydrogen provides a gravimetric energy density already sufficient for heavy duty transportation, aviation or other transportation applications, it can also be used directly as a fuel. Commonly, the transportation sector includes little renewable energy (estimated 3% in the US [20]) while simultaneously being responsible for 20 to 30% of the global greenhouse gas emissions [5, 21–23]. Consequently, hydrogen can directly be used to support the decarbonization of transport in a global and interconnected world.

One of the most promising technical solutions using hydrogen as fuel for transportation are polymer electrolyte fuel cells (PEFCs). PEFCs have many benefits over internal combustion engines, especially higher efficiencies ($> 60\%$) [11]. For light-duty vehicles, such as passenger cars, they can provide similar driving ranges ($> 500\,\mathrm{km}$) and refueling times ($< 5\mathrm{min}$) [24]. Therefore, almost all major automotive manufacturers are developing fuel cell electric vehicles [24]. However, the substantial decrease in lithium-ion battery costs most recently lead to a significant shift in production and development towards battery electric vehicles for light-duty usage [25].

Nevertheless, the usage of PEFC within medium to heavy-duty vehicles has recently attracted significant attention [11, 26, 27]. Within the transportation sector, medium- and heavy-duty trucks play a major role regarding CO_2 emissions. For the US these trucks cause 24% of the greenhouse gas emissions from the US transportation sector (2019) [22]. Besides, truck manufactures are recently facing challenging regulations regarding CO_2 fleet emission within the upcoming years, both in the EU and the US [11, 28]. In addition, major truck and car manufactures agreed on more ambitious targets and decided to stop selling combustion engine based vehicles within their main markets by 2040 [29, 30].

Consequently, fuel cells offer a great opportunity for the transportation sector, as similar to battery power they allow for local CO_2 emission-free transportation with an electric powertrain. But in addition to battery vehicles, fuel cells can offer an extended range, shorter refueling times and most important enable heavier payload capabilities [11]. The increased payload capability is caused by the higher mass specific energy of hydrogen compared to batteries and the possible decoupling of energy (hydrogen tank capacity) and power (fuel cell stack size) for fuel cell systems [24]. This effect can lead to a decreased total-cost of ownership for fuel cell trucks with respect to battery technology and state-of-the-art diesel trucks [31, 32]. This advantage gains particular importance for heavy duty and long-haul trucks. At the same time, the usage within the medium- and heavy-duty truck segment mitigates one of the major disadvantages of fuel cells in transportation: the current lack of hydrogen refueling stations (≈ 300 total in Germany, US and Japan [11]). The deployment of heavy-duty vehicles enables more predictable and dedicated routes, requiring fewer refueling stations and therefore less infrastructure investments [11, 24]. In addition, if using green hydrogen (e.g. from electrolysis of renewable energy), fuel cell vehicles not just offer zero tailpipe CO_2 emissions, but can offer fully decarbonized transportation from well-to-wheel [33].

Within the last two decades the major commercial research and development focus for PEFC technology was the passenger car sector [24]. The shift in intended transport application towards medium- and heavy-duty trucks comes along with a significant requirement increase regarding PEFC efficiency and durability [24, 34]. While the required efficiency increase is in the range of $< 5\%$, the durability requirements for

trucks increase by a factor of 5 to 6 with respect to passenger cars. Instead of aiming for 5 000 operating hours or ≈ 250 000 km lifetime range, truck applications are targeting for >25 000 operating hours or 1.6 million km vehicle durability [24].

Beside costs, PEFC durability has been identified as major barrier for commercial application [34]. The substantially increased requirements for truck applications shown above are further amplifying and illustrating the crucial need for PEFC durability. Commonly, the durability of the membrane and cathode catalyst layer are in focus regarding PEFC durability [34]. Despite that common focus, anode degradation has gained increased attention recently [35–37]. In particular, anode degradation caused by hydrogen fuel starvation is recognized as a key lever for durability [38]. The introduction of oxygen evolution reaction (OER) co-catalyst to the anode has been established as material-based mitigation strategies for these fuel starvation events [39]. Commercially available materials and manufacturing technologies can be employed to achieve reversal tolerant anodes (RTAs) with this approach.

To attain highly durable commercial PEFC systems, advanced in-situ characterization methods are mandatory for research and development. The mitigating capability of the reversal tolerant anodes needs to be realistically characterized with respect to field application [40]. Furthermore, in-situ methods to investigate the stability of the OER co-catalyst and the reversal tolerant anodes during transient anode conditions are crucial for further understanding in PEFC degradation. Both of these aspects are considered within this thesis, to subsequently allow academia and industry for effective in-situ characterization of RTA degradation and simultaneously provide further insights in the degradation mechanisms.

2 PEFC fundamentals

In this section the fundamentals of low temperature polymer electrolyte fuel cells (PEFC) are briefly introduced. The fundamentals within the following sections can be found in comprehensive scientific literature [21, 38, 41–48].

2.1 Working principle and applications

Fuel cells convert chemical energy from fuels into electrical energy and heat by a pair of redox reactions. For low temperature PEFCs, hydrogen is used as fuel in combination with oxygen as oxidant, while water is produced (cf. Equation 2.1).

Total reaction:
$$H_2 + \frac{1}{2}O_2 \rightarrow H_2O \tag{2.1}$$

Hydrogen oxidation reaction (HOR):
$$H_2 \rightarrow 2H^+ + 2e^- \tag{2.2}$$

Oxygen reduction reaction (ORR):
$$\frac{1}{2}O_2 + 2H^+ + 2e^- \rightarrow H_2O \tag{2.3}$$
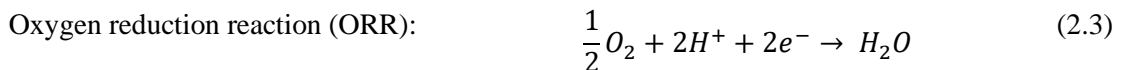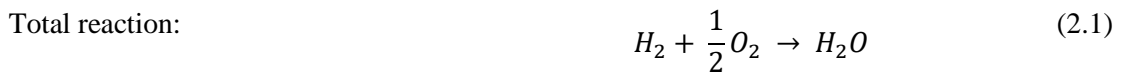
On the anode, the hydrogen oxidation reaction (HOR; cf. Equation 2.2) takes place. The formed protons migrate through the polymer electrolyte to the cathode. The electrons are passing through an external electrical circuit, which provides the ability to perform electrical work. The protons react at the cathode with oxygen and electrons provided by the external electrical circuit, forming water molecules within the so-called oxygen reduction reaction (ORR; cf. Equation 2.3).

Besides the low temperature polymer electrolyte fuel cell, a wide range of fuel cells have been established using besides hydrogen also other fuels such as methane, methanol or formic acid as a reductant and air as oxidant. Classification by the type of electrolyte incorporated in the cell is common. Major fuel cell types aside PEFCs are solid oxide (SOFC), molten carbonate (MCFC), phosphoric acid (PAFC) and alkaline (AFC) fuel cells. The varying electrolyte mainly dictates the fuel cell characteristics, as e.g. cell components, fuel purity, operating temperature, efficiency and durability. Induced by the varying characteristics, applications also differ significantly for each fuel cell type. Amongst others, the range of applications spreads from stationary power generation (SOFC, MCFC, PAFC) to marine applications (MCFC) up to early space programs (Apollo mission) for AFCs.

PEFCs are also pursued for a wide variety of applications. Whereas high temperature (HT-) PEFCs are promising for stationary power applications (e.g. as combined heat and power generator), low temperature (LT-) PEFCs gained major attention within the

automotive sector due to their capability for dynamic operation, high power densities and promising potential regarding costs and durability. Low temperature PEFCs are typically operated at temperatures between 60 to 80° C imposed by the incorporated polymer electrolyte.

Within the last decade, several automotive manufacturers as e.g. Toyota (model Mirai), Hyundai (model Nexo), Honda (model Clarity) and Daimler (model GLC F-Cell) released PEFC based cars, highlighting the early commercialization of PEFC technology. To realize mass production, many manufacturers recently extended their efforts in addition, aiming for heavy duty applications as e.g. long haul trucks [24, 26].

2.2   Thermodynamics

The Gibbs free energy of a reaction $\Delta_R G$ is defining the maximum electrical energy which can be provided by a PEFC:

$$\Delta_R G = \Delta_R H - T\Delta_R S \tag{2.4}$$

where $\Delta_R H$ describes the reaction enthalpy, T the occurring temperature and $\Delta_R S$ the reaction entropy (irreversible heat loss). Combustion engines or comparable classic thermo-mechanical machines are strictly limited to the Carnot cycle and use only a fraction of the Gibbs free energy. Their efficiency typically does not exceed 50%. In contrast, fuel cells directly convert $\Delta_R G$ into electrical energy. Therefore, fuel cells can reach efficiencies higher than 50% [21, 45, 47] (see section 2.4).

The difference between the Gibbs free energy of the products and the reactants describes the change in Gibb's free energy of a reaction $\Delta_R G$.

$$\Delta_R G = \sum G_{\text{products}} - \sum G_{\text{educts}} = G_{\text{H}_2\text{O}} - G_{\text{H}_2} - G_{\text{O}_2} \tag{2.5}$$

The change in Gibbs free energy of a reaction is dependent on pressure and temperature. Considering the ideal gas law and isothermal conditions, it can be expressed as

$$\Delta_R G = \Delta_R G^0 - RT \, ln\left(\frac{\Pi p_{\text{educts}}^v}{\Pi p_{\text{products}}^v}\right) \tag{2.6}$$

with the Gibbs free energy $\Delta_R G^0$ at standard pressure (101.3 kPa) and temperature T, the universal gas constant R, the partial pressures p and the respective stoichiometric factor v.

For the reaction in a PEFC (cf. Equation 2.1) Equation 2.6 results in

$$\Delta_R G = \Delta_R G^0 - RT \, ln \left(\frac{p_{H_2} \cdot p_{O_2}^{\frac{1}{2}}}{p_{H_2O}} \right). \tag{2.7}$$

The equilibrium potential E_{rev} corresponding to the Gibbs free energy is defined as

$$E_{rev} = -\frac{\Delta_R G}{zF} \tag{2.8}$$

where F is Faraday's constant and z the number of transferred electrons by the reaction. For PEFCs under standard conditions with $z = 2$ (cf. Equations 2.1 to 2.3), E_{rev} corresponds to a voltage of 1.23V.

Combining Equations 2.7 and 2.8 is resulting in the so-called Nernst equation

$$E_{rev} = E^0 + \frac{RT}{zF} * \ln \left(\frac{p_{H_2} \cdot p_{O_2}^{\frac{1}{2}}}{p_{H_2O}} \right) \tag{2.9}$$

with the reaction's reversible equilibrium potential E^0 at standard pressure and the temperature T. E^0 can be calculated using Equation 2.8 and values for $\Delta_R G^0$ available from standard reference tables [45].

2.3 Voltage losses / Kinetics

In contrast to the theoretical cell potential, E_{rev} at the prevailing operating conditions, given by the Nernst equation, the thermodynamic potential is lowered by the, so called, overpotentials when current is drawn from the cell. Commonly, three main voltage loss contributions were considered: activation (or kinetic) overpotentials η_{act}, ohmic overpotentials η_Ω and the mass transport overpotentials η_{mtx}. These overpotentials, their composing subcategories and the corresponding equation to derive the actual cell potential E_{cell} are illustrated in Figure 2.1.

Mixed potential region

The practical observed open circuit voltage (OCV) is typically lower than the theoretical cell voltage calculated by the Nernst equation, despite no current being drawn. As root causes mixed potentials by gas crossover and side reactions are considered. The former is mainly caused by permeation of hydrogen through the membrane and the subsequent direct reaction on the cathode with oxygen. This gas crossover effect also can occur for oxygen permeation from the cathode to the anode, but due to the fast kinetics on the anode and the decreased permeability of the larger oxygen molecule through the membrane, this effect is typically regarded as minor. Other side reactions considered to result

in mixed potentials lowering the cathode potential are the reduction of oxygen to hydrogen peroxide as well as the oxidation of carbon and platinum.
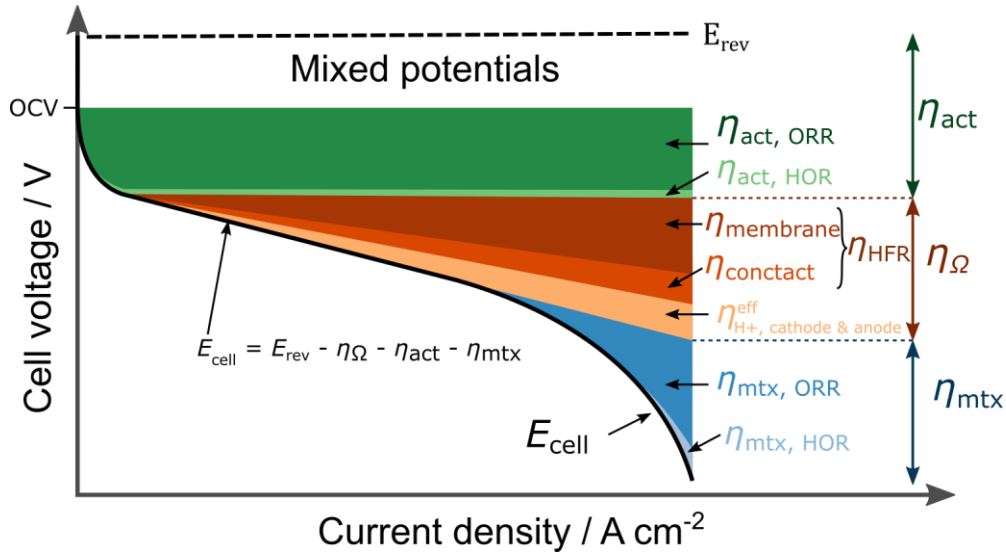
Figure 2.1: The overpotential contributions occurring in a PEFC dependent on the applied current density. The illustration is intended to provide a qualitative overview rather than a correct qualitative distribution.

Activation overpotential

The activation overpotential η_{act} is caused by the electrochemical reaction kinetics due to charge transfer. It occures as soon as current is drawn from the cell. The Butler-Volmer equation (cf. Equation 2.10) is describing activation overpotentials for each electrode mathematically:

$$i = i_0 \cdot L \cdot ECSA \left(e^{\frac{\alpha_a \cdot F}{R \cdot T} \eta_{\mathrm{act}}} - e^{-\frac{\alpha_c \cdot F}{R \cdot T} \eta_{\mathrm{act}}} \right). \tag{2.10}$$

Within the Butler-Volmer equation i represents the current density, i_0 is the exchange current density, L is the catalyst loading (usually given in $\mathrm{g_{catalyst}\, cm_{electrode}^{-2}}$), *ECSA* describes the electrochemical surface area (usually given in $\mathrm{m_{catalyst}^2\, g_{catalyst}^{-1}}$), α_a and α_c are the anodic and cathodic transfer coefficients, F is the Faraday constant ($96485\ \mathrm{C\ mol^{-1}}$), R is the universal gas constant ($8.3145\ \mathrm{J\ K^{-1}\ mol^{-1}}$), T is the cell temperature ($203.15\ \mathrm{K}$) and η_{act} is the kinetic overpotential. The Butler-Volmer equation consideres the redox reactions occuring at one electrode, e.g. the ORR and the associated oxygen evolution reaction (OER) on the cathode, and is weighting the contribution of the reduction (i.e. ORR) and the oxidation (i.e. OER) to the overall current by the transfer coefficient. The exchange current density represents a current flowing at zero net reactant conversion and equilibrium potential for the redox reaction. Therefore, a high exchange current density, which is associated to a fast reaction kinetics, is resulting in a small activation overpotential. However, a lower exchange

current density can be compensated by a large catalytic surface area (product of $L \cdot ECSA$).

For large overpotentials, e.g. far away from the equilibrium potential where one reaction dominates, the Butler-Volmer equation can be simplified to the so-called Tafel equation:

$$\eta_{\text{act}} = \frac{R \cdot T}{\alpha_{a/c} \cdot F} \ln \left(\frac{i}{i_0 \cdot L \cdot ECSA} \right) \tag{2.11}$$

which also can be written as:

$$\eta_{\text{act}} = \left(\frac{2.303 \cdot R \cdot T}{\alpha_{a/c} \cdot F} \right) \log(i_0) - \left(\frac{2.303 \cdot R \cdot T}{\alpha_{a/c} \cdot F} \right) \log|i| = a + b \cdot \log|i| \tag{2.12}$$

where b is the so-called Tafel slope.

The total activation overpotential is composed by the activation overpotential for the PEFC reactions taking place at the anode $\eta_{\text{act, HOR}}$ and the cathode $\eta_{\text{act, ORR}}$, as illustrated in Figure 2.1 (green areas). For both reactions, Pt is the best monometallic catalyst known to date. However, the HOR (i_0 in the range of 10^{-3} A $\text{cm}_{\text{Pt}}^{-2}$) exhibits a 6 orders of magnitude higher exchange current density compared to the ORR (i_0 in the range of 10^{-8} A $\text{cm}_{\text{Pt}}^{-2}$). Therefore, the activation overpotential η_{act} for PEFC is widely attributed solely to the activation overpotential of the ORR on the cathode, whereas the HOR activation overpotential, due to its fast kinetics, is neglected. Simultaneously, this explains the commonly higher platinum loadings on the cathode in contrast to the anode for PEFC applications.

Ohmic overpotential

As illustrated in Figure 2.1 (brown to orange areas), the ohmic overpotential η_{Ω} is composed by ohmic losses of the membrane η_{membrane}, contact resistances η_{contact} and losses due to proton conduction within the catalyst layers $\eta_{\text{H}^+, \text{cathode \& anode}}^{\text{eff}}$. The ohmic overpotential linearly increases with current density according to Ohm's law and dominates at moderate to high current densisites. The membrane overpotential caused by ionic resistance of the membrane is significantly dependent on the membrane's thickness and water content. Simultaneously, the membrane overpotential is dominating the ohmic overpotential. The contact resistance η_{contact} is summing up the resistances occuring by conductions of electrons trough the catalyst layers, gas diffusion layers (GDLs), flowfields and bipolar plates. In addition to the dependency on the incorporated materials, the contact resistance also is a function of the cell compression. η_{membrane} and η_{contact} are commonly summarized in the high frequency resistance (HFR) overpotential η_{HFR}. Furthermore, the transport of protons through the catalyst

layers results in the effective proton overpotential $\eta_{\mathrm{H^+,cathode\,\&\,anode}}^{\mathrm{eff}}$, also referred to as sheet resistance. As for the activation overpotential, the contribution of the anode sheet resistance is commonly neglected due to a minor impact. Commonly, a lower anode thickness (resulting in increased gas diffusion) and the fast HOR kinetics lead to the fact that the HOR reaction takes place close to the membrane interface, resulting in short protonic pathways and thus in negligible protonic resistance. Therefore, solely the proton resistance of the cathode $\eta_{\mathrm{H^+,cathode}}^{\mathrm{eff}}$ is taken into consideration for PEFC cell voltage loss.

Mass transport overpotential

At high current densities, the mass transport overpotential η_{mtx} is dominating (cf. Figure 2.1, blue areas). Mass transport overpotentials are originating from convective and/or diffusive gas transport limitations. Convective gas transport predominatly occurs within the flow field domain and the GDL. Convective mass transport limitation is commonly attributed to blockages of reactant gas flow, e.g. by liquid water. Diffusive gas transport limitations of reactant gases occur between flow channel and to the so-called triple or three-phase boundaries, predominantly in the porous pathways of the GDL and the catalyst layer. Three-phase boundaries refer to active catalyst sites within the catalyst layer, where gaseous rectant is present and simultaneously protonic and electrical conduction is ensured (for further details see section 2.5.2). Within the GDL domain, predominantly diffsuive transport phenomena are considered following a Stefan-Maxwell or Fickian-type diffusion approche [21, 49]. Within the catalyst layers, Knudsen diffusion is commonly assumed [21, 49]. As diffusive mass transport is considered as major contributor, mass transport overpotential becomes apparent for diluted reactants, e.g. oxygen in air or for the enrichment of N_2 in the anode loop (further discussed in section 2.5.5). In addition, the (temporary) loss of available porous volume in the GDL, microporous layer and catalyst layer can lead to an increase in mass transport overpotential. Loss in pore volume can occur for example due to pore blockage by accumulated water [50] (humidifying water in gas supply or product water), increased compression (predominantly decreasing the GDL void volume) or due to degradation and collapse of the catalyst layer and/or GDL.

As the above described effects are more likely relevant on the cathode (product water formation, dilluted oxygen, electroosmotic drag), the overpotential on the anode is commonly disregarded due to it's minor contribution to mass transport. However, for degraded anode catalyst layers significant mass transport increase has been reported [35].

2.4 Fuel cell efficiency

For PEFCs, commonly the electrical efficiency $\eta_{\text{eff, el}}$ is considered as major efficiency parameter. The maximum theoretical electrical efficiency $\eta_{\text{eff, el}}^{\text{theo}}$ can be described as:

$$\eta_{\text{eff, el}}^{\text{theo}} = \frac{\Delta_R G^0}{\Delta H^0} \tag{2.13}$$

Using the higher heating value of hydrogen $(\Delta H_{\text{HHV}}^0 = 286 \text{ kJ mol}^{-1})$, for PEFCs a theoretical electrical efficiency of 83% can be achieved [47]. The theoretical efficiency is also known as the thermodynamic efficiency or the maximum efficiency limit.

The actual electrical efficiency $\eta_{\text{eff, el}}$ of a fuel cell is defined by the actual electrical energy W_{el} divided by the energy of hydrogen consumed W_{H_2} [51]:

$$\eta_{\text{eff, el}} = \frac{W_{\text{el}}}{W_{\text{H}_2}} = \frac{I \cdot E_{\text{cell}}}{\Delta H^0 \cdot \dot{n}_{\text{H}_2}}, \tag{2.14}$$

with the current I, actual cell voltage E_{cell} and molar flow of hydrogen consumed $\dot{n}_{\text{H}_2}$.

Considering Faraday's Law and the higher heating value of hydrogen in equation 2.14, the electrical efficiency of a fuel cell can be written as [51]:

$$\eta_{\text{eff, el}} = \frac{E_{\text{cell}}}{1.482 \, V} \tag{2.15}$$

Instead of the higher heating value, also the lower heating value can be considered. The lower heating value is considering the heat of product water condensation. For PEFCs, both approaches can be reasonable as the product water may leave in liquid or gaseous form. The actual fuel cell efficiency is dependent on the occurring overpotentials (see section 2.3). If the overpotential increases (e.g. due to aging), the electrical efficiency decreases. Simultaneously, the waste heat increases.

The current efficiency $\eta_{\text{eff, ce}}$ (considering internal currents) and the fuel utilization $\eta_{\text{eff, fu}}$ (considering commonly applied overstoichiometric operation) can be considered in addition to calculate the electrical efficiency more accurately [47, 51]:

$$\eta_{\text{eff, el}} = \frac{E_{\text{cell}}}{1.482 \, V} \, \eta_{\text{eff, ce}} \, \eta_{\text{eff, fu}} \tag{2.16}$$

For fuel cell systems, the electrical efficiency is decreased by electrical consumers. Balance of plant components (e.g. compressors) decrease the electrical net power output and thus the system efficiency. At the same time, the thermal energy by waste heat can complement the electrical energy for fuel cell systems. For example, the thermal energy can be used within the fuel cell system (e.g. for gas conditioning) or adjacent systems (e.g. truck cabin). Consequently, the overall system efficiency can be increased. How-

ever, if the thermal heat exceeds the usable portion of the system, additional cooling power has to be provided. This, in turn, can decrease the net power output of the fuel cell system [42, 45].

2.5 PEFC components

In the following section an overview of the main PEFC components and materials from membrane electrode assembly (MEA) to stack level shall be provided as well as their main characteristics and requirements. The membrane electrode assembly is the core element within PEFCs. As depicted in Figure 2.2 the MEA is surrounded by bipolar plates (stack configuration) or flow fields (single cell) including flow channels on the anode and cathode. The flow channels are commonly aiming for a homogenous gas distribution. Within the MEA, the membrane is sandwiched between the catalyst layers and the gas diffusion layers (GDLs). The GDL commonly consists of a microporous and a microporous layer (MPL) on the interface next to the catalyst layer. The electro-chemical reaction takes place within the catalyst layers at the so-called three-phase boundary (see section 2.5.2).
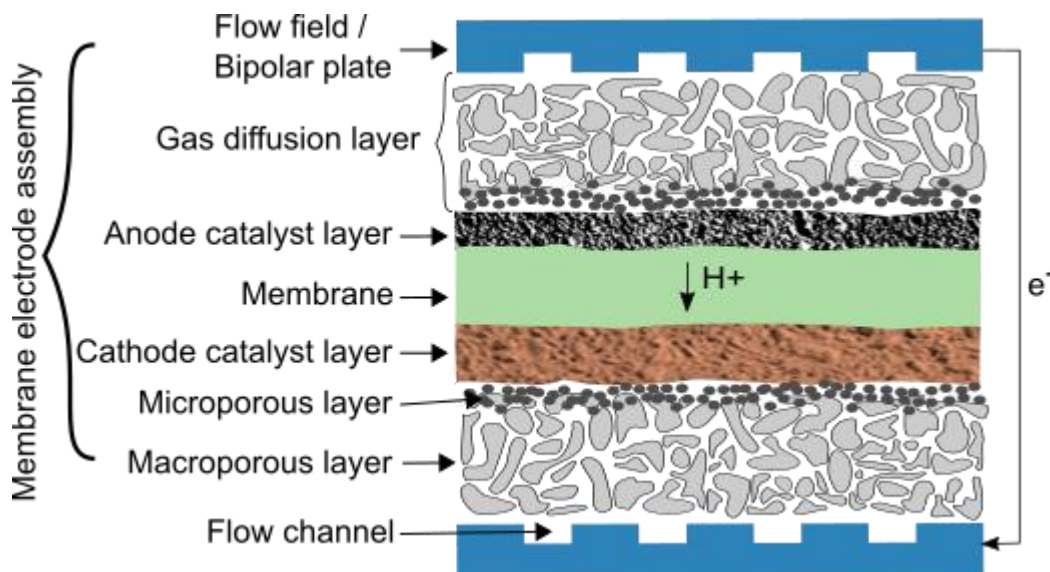
Figure 2.2: Schematic sketch of a PEFC, including membrane electrode assembly, flow field/bipolar plate and external electrical circuit.

2.5.1   Membrane

Low temperature PEFCs are often referred to as polymer exchange membrane fuel cells (PEMFCs), due to the common introduction of the polymeric electrolyte in form of a membrane. The membrane is the geometrically centered component in the MEA. To locally separate the overall reaction within a fuel cell (see Equation 2.1) into anodic HOR and cathodic ORR reaction, the polymeric membrane ideally can conduct protons

while being impermeable to (educt) gases as well as being completely electrically insulating. Membranes with perfluorosulfonic acid (PFSA) groups carried on a (fluoro-)polymeric backbone have been established as state-of-the-art. A general chemical structure of theses polymers is shown in Figure 2.3.

$$\left[(CF-CF_2)_x \!\!-\!\! (CF_2-CF_2)_y \right]_z$$
$$(OCF_2CF)_m \!\!-\!\! O-(CF_2)_n-SO_3H$$
$$| $$
$$CF_3$$
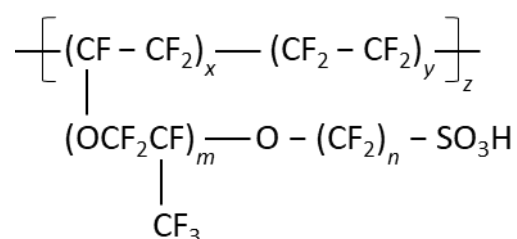
Figure 2.3: Chemical structure of perfluorosulfonic acid (PFSA) ionomers.

The sulfonic acid groups form hydrophilic clusters, whereas the main chains are showing hydrophobic characteristics. Consequently, a phase separation in PFSA based membranes is observed. Water, introduced to the MEA with the supply of reactant gases and from the chemical reaction at the cathode, is forming a network within the hydrophilic phase. The water molecules are forcing the dissociation of sulfonic acid groups, enabling proton conduction, and resulting in a highly acidic medium. The proton transport takes place either via structural diffusion (Grotthuss shuttling) or vehicular diffusion and is strongly dependent on the humidification level of the membrane. The proton transport is accompanied by the so-called electroosmotic drag, which describes the co-transport of water molecules within the membrane for each proton transported. This effect is further complicating the management of byproducts as water and heat.

To meet the requirements for high-performance commercial applications, especially the following requirements are mandatory for PEFC membranes:

  i.   high proton conductivity
  ii. impermeability for fuels and oxidants
  iii. high durability (chemical and physical stability)

To achieve a high proton conductivity and low ohmic losses, membranes are designed as thin as possible to provide a low ionic resistance while maintaining acceptable gas permeation. State-of-the art thicknesses are in the range of 40 to 10 µm. In addition to membrane thickness, the ionic conductivity is highly dependent on temperature and the membrane's water content. To achieve high ionic conductivity, a key strategy is to humidify the gas supply of the reactant gases, especially on the anode. However, humification requires space and resource intensive power of plant components.

The gas permeability is inversely proportional to the membrane thickness. The thicker the membrane, the higher the resistance for hydrogen or oxygen molecules to crossover from anode to cathode or vice versa. Permeating reactants crossing the membrane are

leading to an electrical efficiency loss either via hydrogen consumption at the anode by reaction with crossed-over O_2 or by consumption of crossed-over hydrogen and subsequent reaction with oxygen on the cathode. Therefore, commonly a trade off in membrane thickness between optimized proton conductivity and acceptable gas impermeability has to be found.

The thickness of the membrane is significantly decreased by chemical and physical membrane degradation over lifetime. Thus, gas impermeability and membrane durability are closely related. Membrane degradation is discussed in detail in section 2.6.3. However, a short overview in membrane durability is given in the following to account for the mitigating materials incorporated. Chemical membrane degradation is mainly driven by the formation of peroxide, hydroxyl and related radicals due to permeated oxygen and hydrogen molecules or as intermediate species in the ORR [21, 52, 53]. As a consequence of chemical degradation, severe membrane thinning can occur, leading to increased gas crossover rates as well as even leading to complete electrical shorting of the cell. To improve the chemical stability of PFSA based membranes, either the ionomer can be improved (e.g. by decreasing oxygen crossover) or radical scavengers (e.g. Ce or Mn) can be integrated within the membrane [21, 52]. The physical or mechanical durability is mainly influenced by mechanical stress. Mechanical stress can be caused by compression, punctures or membrane swelling and shrinkage due to changing water content within the membrane. To improve mechanical durability, the employment of a mechanical reinforcement layer within the membrane has been established [21].

Beside the above discussed membrane properties, membranes for commercial applications have to meet low-cost targets, processability, compatibility with the electrodes and environmental compatibility. Hydrocarbon based ionomers have been identified as promising alternatives to PFSA based membranes, especially regarding costs and enhanced environmental impact due to the absence of perfluorination. But they still have to overcome disadvantages as decreased proton conductivity and durability compared to PFSA membranes.

2.5.2   Catalyst layer

The catalyst is a key component in all fuel cell types. Catalysts are lowering the activation energy and are thereby significantly increasing the reaction rates. In PEFCs the hydrogen oxidation and the oxygen reduction reaction are catalyzed on the anode and cathode electrode, respectively.

To enable the electrochemical reaction in a fuel cell, electrons, protons and the reactant gas (H_2 or O_2, cf. Equations 2.2 & 2.3) have to be present at the respective catalyst simultaneously. This is also referred to as the three-phase interface or boundary (see Figure 2.4).
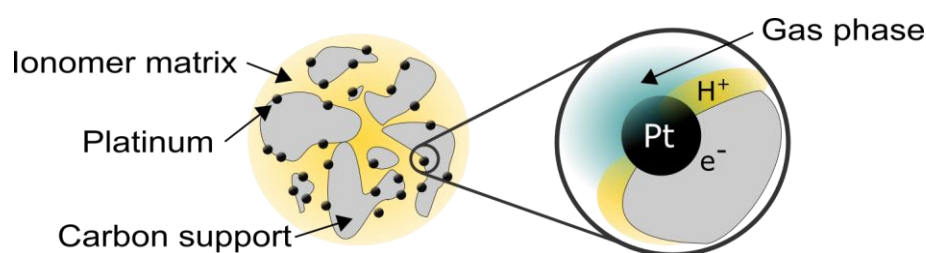
Figure 2.4: Three-phase boundary within the catalyst layer.

Therefore, the catalyst layer should provide the following characteristics:

  i.   provide a high catalyst surface area
  ii. high electrical conductivity (between flow field and three-phase boundaries)
  iii. high proton conductivity (between membrane and catalyst sites)
  iv. distribute reactant gases homogeneously
  v.   remove product water efficiently

State-of-the-art catalyst layers employ platinum or platinum-alloy nanoparticles (commonly with particle sizes of 2-5 nm) supported on carbon for the HOR as well as for the ORR. For automotive applications, loadings of 0.2 to 0.35 $mg_{Pt}\,cm^{-2}$ and 0.05 $mg_{Pt}\,cm^{-2}$ are commonly realized on the cathode and anode, respectively. Typically Pt/C catalysts with 20 to 50 wt.% of Pt [21] are used. The commonly used carbon support (e.g. carbon black such as Vulcan™, high surface area carbon, graphitized carbon) ensures a fine catalyst distribution and thereby a high electrochemical surface area (*ECSA*, typically in the order of 100 cm^2 catalyst surface area per g platinum) as well as a high electrical conductivity. In addition, the carbon support leads to a high porosity within the catalyst layer, enabling gas transport of reactant gases as well as removal of product water on the cathode through the void volume of the catalyst layer.

In order to provide protons on the active sites of the catalyst, a proton transport medium, the so-called ionomer, has to be incorporated in the catalyst layer. Typically, the same material as for the membrane is used and deposited as a thin ionomer layer on the carbon surface, ensuring the proton transport within the catalyst layer to the membrane. As the incorporated Pt particles are commonly covered by ionomer, the ionomer needs to be permeable for O_2 or H_2 on the cathode and anode, respectively. As permeability is inversely proportional to ionomer film thickness, the ionomer thin film on Pt has to be in the nm scale. In contrast, the ionomer thickness of the membrane, hindering gas permeation to a high extent, is in the scale of >10 µm. An optimum between accessing all Pt sites by the ionomer matrix and an excess of ionomer, resulting in gas transport limitations and pore blocking, has to be found to achieve a high fuel cell performance. The total amount of ionomer can be controlled via the ionomer to carbon (I/C) weight ratio during MEA fabrication. However, to overcome the complex dependencies of

ionomer distribution within the catalyst layer, the catalyst layer and it's production has to be optimized to achieve high performance MEAs [54, 55].

Besides, a PEFC catalyst layer should ensure a high durability. A key lever for catalyst layer durability is the use of corrosion resistant support material (see chapter 2.6). Therefore, efforts are made to replace carbon-based supports, which are prone to corrosion, by alternative support materials. Promising candidates are for example antimony doped tin oxides [56], nano-structured thin films (NTFS, developed by 3M) [21] or Pt-Ni aerogels [57]. However, there are still various challenging issues for these approaches as e.g., low electrical conductivity, low stability in reductive atmosphere or issues with amplified water flooding due to the reduced thickness of NTFS electrodes [21].

In addition to the above-described characteristics, the catalyst layer should feature reasonable cost and processability. As catalyst layer costs are mainly driven by the precious metal loadings, there are a lot of efforts to lower the catalyst loading while maintaining comparable performance and durability [58]. From a processing perspective, the catalyst layer can be attached to the membrane to form a catalyst coated membrane (CCM), either by direct coating or the so-called decal transfer coating process [21, 44]. Another option is to coat the catalyst layer to the diffusion medium resulting in a so-called gas diffusion electrode (GDE). Commonly, GDE based fabrication is reported to result in lower PEFC performance with commercially available materials [59]. It was recently indicated, the lower performance is caused by increased water retention and mass transport resistances for GDEs [59]. However, the GDE approach is often employed for research activities investigating alternative catalysts with different structures and morphologies, which requires different ink formulations.

2.5.3 Gas diffusion layer

The gas diffusion layer (GDL) is placed between catalyst layer and the flow field/bipolar plates. Its main requirements are:

  i.   distribute gases homogeneously to the catalyst layer
  ii. high electrical conductivity
  iii. efficient heat and water removal

If these requirements are met, a homogeneous current density distribution and thus high performances can be achieved. To attain homogeneous gas distribution to the catalyst layer, the GDL has to ensure efficient in-plane transport of gases, especially to the contact areas between GDL and flow field, the so-called landing area.

To meet the requirements, carbon fibers or carbon paper GDLs are commonly employed, offering a high porosity and thus enabling efficient convective and diffusive gas phase transport. Concurrently, carbon provides a high electrical conductivity, minimiz-

ing ohmic losses occurring due to electrical conduction between the flow field and the catalyst layer.
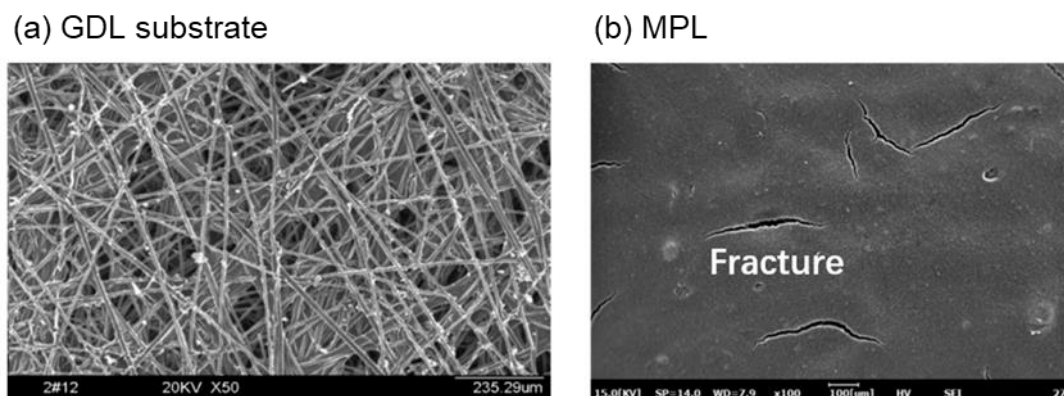
Figure 2.5: Scanning electron microscope (SEM) images of a gas diffusion layer (GDL) containing (a) a macroporous GDL substrate and (b) a microporous layer (MPL). Reprinted from Zhou et al. [60] under the terms of Creative Comments Attribution 4.0.

The GDL's ability for effective reactant supply is accompanied by the need for removal of water from the MEA to avoid GDL and catalyst layer flooding, which can lead to gas transport limitations. Therefore, the carbon fibers are commonly treated with hydrophobic polymer, typically polytetrafluoroethylene (PTFE). Simultaneously, the polymer is acting as a binder between the fibers and is increasing mechanical stability.

To further improve water removal from the interface to the catalyst layer and prevent mechanical damage of the electrodes by carbon fibers, a microporous layer (MPL) can be coated on the macroporous GDL substrate. State-of-the-art MPLs incorporate carbon black in combination with a hydrophobic PTFE binder, establishing pore sizes three orders of magnitudes smaller than the typical pore sizes of the macroporous layer (MPL: 10 nm, GDL substrate: $\gg 10\,\mu$m). The small pores of the MPL are causing a high capillary pressure preventing the accumulation of water in the catalyst layer. At the same time, the higher surface area of the MPL is improving the electric contact between the catalyst layer and the GDL as well as preventing carbon fiber based mechanical damage within the catalyst layer or the membrane by ensuring a homogeneous pressure distribution. An example for a GDL is illustrated in Figure 2.5.

Finally, GDLs are able to provide mechanical stability and even balances external and internal mechanical stress, (e.g., different gas pressures on the anode and cathode or varying compression caused by membrane swelling).

Within GDL manufacturing, either carbon paper or woven structures are used as production substrate. During manufacturing the substrate is further processed, e.g. by hy-

drophobic impregnation with PTFE. To achieve low cost and high performance, the manufacturing has to be optimized regarding these parameters.

2.5.4 Flow field / bipolar plate

The bipolar plate (stack) or flow field (single cell) is commonly made of corrosion resistant metal or graphite. The MEA in a single cell is sandwiched between two flow fields on the anode and cathode, respectively. In stack configuration, the bipolar plates are connecting the cathode of one unit cell to the anode of the adjacent cell. The bipolar plate's main purpose is to supply reactant gas to the MEA and to remove water by convection from the gas channels. Concurrently, the bipolar plates provide electrical connection of the MEA, support the MEA mechanically and separate the unit cells in stack configuration physically. In addition, the bipolar plates commonly remove the waste heat by additional internal channels for cooling fluids.

A wide range of flow channel designs is available, e.g. parallel-, serpentine-, or interdigitated channels. Each of them has advantages and disadvantages [21, 61]. Especially for automotive applications, the flow field needs to enable gas transport at varying current densities and therefore gas flow rates and pressure drops. Furthermore, the water removal should be ensured at varying operating conditions and humidification levels, as channel blockage of single channels or the whole flow field can lead to severe degradation of the fuel cell (H_2 starvation, see section 2.7.1) or performance decay.

Commonly, metallic bipolar plates use stainless steel or titania as base material. Stainless steel is less costly but comes with disadvantages regarding corrosion resistance in the acidic PEFC environment. However, corrosion resistance can be enhanced by coating layers of more corrosive resistant materials. When using metallic bipolar plates, the risk of promoting membrane degradation (see section 2.6) should be considered by the introduction of iron or titanium to PEFC cells [62]. Consequently, the usage of carbon based graphite bipolar plates is a promising and well established alternative, also showing an increased plate lifetime compared to metal plates [3]. But the commonly increased plate thickness of graphite plates, compared to metal ones, can lower the volumetric power density of the fuel cell stack. For production of graphite plates either compression molding or injection molding (higher production rate) can be applied [21].

2.5.5 PEFC stack and system

For automotive and stationary applications several cells are stacked in series to achieve a sufficient power output. A schematic stack assembly is shown in Figure 2.6. The current flows through each cell and subsequently the voltage adds up along the stack according to Kirchhoff's circuit laws. As mentioned above, the electrical connection between two adjacent unit cells is achieved by the bipolar plate.
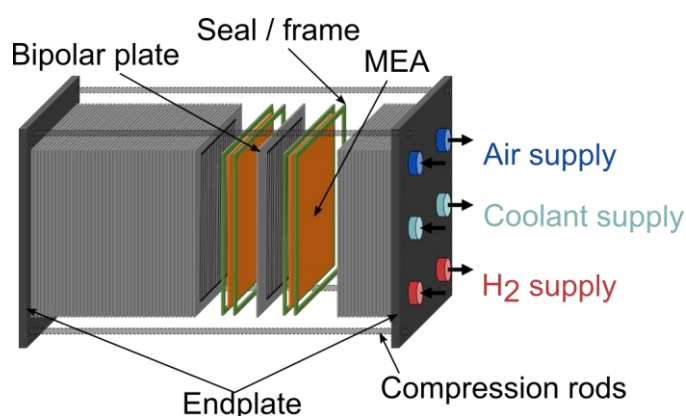
Figure 2.6: Schematic setup of a stack assembly including an explosion drawing of a single bipolar plate sandwiched between two MEAs.

To prevent leakage from or to the ambient, the MEA's sealing commonly is realized by incorporating a frame/seal combination. Frames are typically based on polyethylene naphthalate (PEN) and sealings are frequently made of silicone. The applied sealing technology has to prevent the mixture of supplied media within the stack (e.g. between the reactants or between one reactant and cooling) to enable a safe operation. The first and the last plate in stack configuration, the so-called endplates, only have a single flow field facing to the stack-inside, respectively. They are typically used to mechanically compress and fix the stack assembly with the help of metal straps, rods or other compression techniques. In addition, the endplates typically contain the media supply ports for air, hydrogen and coolant.

To meet the requirements of the PEFC components and to ensure controlled operating conditions, the stack is embedded into a fuel cell system. A simplified fuel cell system for automotive applications is illustrated in Figure 2.7.
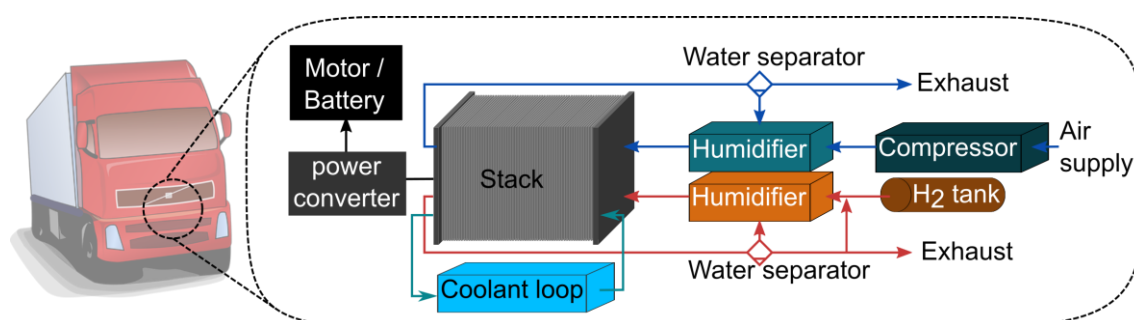
Figure 2.7: Schematic setup of a fuel cell system. The setup is simplified displaying only the main components while many elements (pumps, valves, sensors, etc.) are not shown. Scheme should be considered exemplary, as real systems can vary significantly dependent on manufacturer and application.

A compressor supplies the oxygen from the surrounding environment at the desired operating pressure and stoichiometry (characteristically value between 1 and 2). High gas pressures commonly improve fuel cell performance while simultaneously increasing

power consumption, compressor module costs and requirements for sealing technology. This results in typical operating gas gauge pressures of 1 to 2 bar_g for automotive applications. To ensure a well-humidified membrane, the compressed air is often humidified prior entering the stack. Humidification is typically realized by recovering water from the exhaust gas. As the employment of a humidifier adds complexity and costs to the system, also humidification strategies without humidifiers are used (e.g. reported for the Toyota Mirai 1 [63]). For automotive applications H_2 supplied from an onboard pressure tank, based on composite pressure vessels, has been established (350 or 700 bar). Therefore, for these systems no compressor is required on the anode side. However, also tank technologies using liquid hydrogen at cryogenic temperatures ($< -252.8\,°C$) are under research and development to achieve a higher gravimetric and volumetric energy density and a subsequently higher range. This is of special interest for long haul truck applications [26]. Consequently, the realization of the desired operating conditions has to be adapted to the tank technology (e.g. using heaters, pressure reducers or compressors). Commonly, desired gas pressures on the anode are in the same order of magnitude as for the cathode compartment (1 to 2 bar_g). Likewise, hydrogen is typically humidified before entering the stack. Due to the above-mentioned electroosmotic drag of water from the anode to the cathode, this is mandatory to ensure a stable membrane humidification. Gas humidification is commonly realized by either a humidifier, hydrogen recirculation, or a combination of these. Since the fuel efficiency can be improved by recovering residual, overstoichiometric H_2 (typically stoichiometry in applications ≈ 1.2 to 1.7) from the exhaust gas, recirculation within the fuel supply is commonly established regardless of the humidification. Nevertheless, the enrichment of N_2 or O_2 in the anode loop by crossover from the air side may make it necessary to purge the gas mixture (N_2/H_2) from the anode loop to the exhaust at certain time intervals. Otherwise, the hydrogen partial pressure can decrease the fuel cell performance or even (local) fuel starvation can occur due to (locally) understoichiometric (< 1) operation (see mechanism in section 2.7.1).

Fuel cell systems commonly contain a coolant loop to control the operating temperature and prevent degradation by unintended high temperatures, low humidity or large local gradients within the stack or the cells. To ensure a homogeneous temperature distribution in the stack, commonly coolant is flowing through each bipolar plate. Thus, to avoid high voltage safety concerns as well as parasitic currents, the coolant must have a low conductivity. To further utilize waste heat and increase system efficiency, the coolant loop can provide thermal energy to other system components (e.g. heaters) or to external systems (e.g. to a vehicle interior). Finally, a power converter is used (e.g. a DC/DC converter for a DC motor) to supply the electrical power at the desired properties to the vehicle's powertrain. The hybridization of the latter can vary dependent on the application as well as the operating strategies. Therefore, the fuel cell can either be

connected directly to an electrical motor or to an interconnected battery via the power converter.

2.6 Material degradation mechanisms

Durability is the major lever to achieve the ambitious lifetime targets for commercial stationary and automotive targets, e.g. for long haul truck applications where lifetimes of $> 20,000$ h are aspired [21, 38, 64]. With a performance decay of $\geq 10\%$ commonly the end-of-life criterium is reached for automotive or stationary applications (e.g. emergency power generators). Consequently, high durability is a mandatory requirement to establish PEFCs on a commercial level as carbon neutral alternative to prevailing combustion engines for sectors such as transportation.

Fuel cells cannot always be operated in their ideal operating window, which is a steady state operation at constant voltage in the range of 0.5 to 0.7 V under mild temperatures ($\approx 70°$ C), fully humidified conditions and using hydrogen and air free of pollutants. Each stack component is subject to specific degradation processes, commonly amplified outside the ideal operating window.

To provide a comprehensive understanding of MEA and in particular anode catalyst layer degradation, the major degradation mechanisms for all MEA components are outlined in this chapter.

2.6.1 Bipolar plate and seal degradation

As discussed above, bipolar plates are commonly based on graphite or metal. Degradation of bipolar plates can result in a loss of mechanical integrity or electrical conductivity. The former will lead to mixture of air or fuel with coolant and subsequently to severe degradation or performance decay. The latter increases ohmic losses and heat generation, e.g. by decreased electrical conductivity or increased contact resistance.

During operation, the bipolar plates are in contact with an acidic water phase (commonly pH values in the range of 3 to 5 [65] are reported). For graphite-based plates, this environment can lead to chemical degradation due to carbon oxidation in the presence of H_2O_2 or increased potentials, e.g. during fuel starvation or start-up/shut-down conditions (discussed in section 2.7). Besides, elevated temperatures can lead to mechanical degradation of graphite based bipolar plates resulting in deformation and brittleness. Metal bipolar plates experience serious durability issues as well. At the cathode side, most metals form a passivating oxide layer on the surface. However, low cathode potentials can result in reducing this passivating layer and subsequently releasing metal ions. These ions can contaminate membrane and catalysts. Under normal operating conditions such passivating oxide layers are not formed on the anode side. However, during

specific operating conditions, such as fuel starvation, catalyst poisoning or so-called start-up/shut-down events, resulting transients in the anode potential can promote the release of metal ions on the anode side as well.

Beside bipolar plate degradation, seal degradation also can occur. So far degradation phenomena for seals are rarely investigated in general. However, they can either lead to functionality loss of the seal (e.g. external or internal leakages) or lead to poisoning of the MEA due to contaminant leaching from seal components [66]. Seal degradation is mainly caused due to exposure to coolant or the acidic environment.

2.6.2 GDL degradation

The GDL experience comparable conditions as the bipolar plates. They are exposed to acidic environment (pH $\approx$ 3 to 5). As mentioned above, in combination with water peroxide or increased potentials, this can lead to carbon oxidation of the commonly carbon based GDL. The incorporated hydrophobic fluorinated binders can protect the carbon surface to a certain extend from oxidation. Nevertheless, carbon (surface) oxidation and decomposition of the additives can occur, leading to increased electrical resistance (in- and through-plane or contact resistances), loss in hydrophobic character and pore structure change. Subsequently, a significant increase in ohmic loss can occur as well as an increase in mass transport overpotential by (temporary) porosity loss, e.g. caused by water flooding or structural collapse. This can severely decrease the fuel cell performance. Mass transport increase due to enhanced water accumulation or pore collapse is regarded as most critical for GDL durability.

Moreover, mechanical stress (e.g. change in compression) can lead to GDL degradation, which can affect other MEA components. Broken GDL fibers for example can lead to membrane puncture and consequently to complete failure of the fuel cell.

2.6.3 Membrane degradation

Membrane degradation can be separated into two major classes: chemical and mechanical membrane degradation. Whereas chemical degradation is resulting in changes within the chemical structure of the polymer (e.g. by polymer chain decomposition), mechanical degradation is caused by physical stress. However, both degradation processes result in increased membrane permeability for fuel and/or air up to complete short circuit between the electrodes. Besides, contamination by ionic species (e.g. metal cations or NH_4^+) can lead to proton exchange at the sulfonate sites and consequently reduced proton conductivity and/or reduced hydrophilicity, influencing the membrane water content.

Chemical degradation

Chemical degradation of membranes is mainly associated with the formation of hydroxyl radicals leading to chain scission. The radicals are formed in the concurrent environment of O_2, H_2 (consider above discussed crossover between anode and cathode) and Pt. Adsorbed hydrogen on Pt sites can react with oxygen molecules forming hydroperoxide radicals. These radicals can react in turn with other adsorbed hydrogen atoms, resulting in hydrogen peroxide (H_2O_2) permeating through the MEA. Besides, H_2O_2 can be formed as intermediate species during ORR [53]. Catalyzed by transition metal ions, such as Fe^{2+}, hydroxyl radicals ($\cdot OH$) are formed from the decomposition of the hydrogen peroxide. The hydroxyl radicals can attack hydrogen covalent bonds within the ionomer, leading to either unzipping of end groups from the perfluorinated backbone or unzipping of sulfonic acid groups present at the polymer side chains. The release rate of HF from this chemical decomposition is typically taken as indicator for membrane stability. This degradation mechanism is also valid for ionomer incorporated within the catalyst layers.

As material-based mitigation strategies either gas crossover rates can be decreased (e.g. by Pt additives within the membrane), radical scavengers (e.g. Ce^{3+}) can be introduced or non-perfluorinated end groups can be removed from the polymer chain. These mitigation strategies aim to decrease the rate of polymer decomposition by unzipping. In addition, the adaption of operating strategies can also reduce chemical membrane degradation. Low relative humidity (*RH*), open circuit voltage (OCV) conditions and elevated temperature accelerate the chemical degradation and should be limited [21].

Mechanical degradation

Mechanical stress can lead to a failure in mechanical integrity of the membrane. External materials (for example carbon fibers from the GDL or production residues) can puncture the membrane or external forces (e.g. nonuniform compression, or high differential gas pressure between anode and cathode) can lead to mechanical failure. Besides, the high affinity of membrane swelling upon water uptake can result in membrane failure under cycling conditions, especially when temperature or relative humidity is cycled. Consequently, fatigue stress or membrane thinning can occur. Cracks within catalyst layers can accelerate the mechanical degradation during cyclic membrane swelling [67].

The introduction of a reinforcement layer (e.g. based on PTFE) has been established to reduce mechanical degradation and to enhance the dimensional stability. Thereby, the MEA lifetime can be increased while maintaining membrane thickness, or the membrane thickness can be reduced (simultaneously increasing proton conductance) while maintaining the required lifetime. In addition, also the operating strategies can be optimized aiming for decreased *RH* and temperature cycling.

2.6.4 Catalyst layer degradation

Catalyst layer degradation is a major concern for PEFC durability, as the electrodes have a significant impact on the occurring overpotentials in a PEFC (see section 2.3). This chapter describes the appearing material degradation processes and their impact on the cathode and in particular the anode catalyst layer. As platinum is the best monometallic catalyst know to date for HOR and ORR, the incorporation of Pt supported on carbon for commercial PEFC applications is state-of-the-art.

Pt deactivation

During PEFC operation several degradation processes for the catalyst (commonly Pt supported on carbon) can occur. The main degradation processes are depicted schematically in Figure 2.8. All shown mechanisms are leading to an *ECSA* decrease and therefore to an increased activation overpotential.
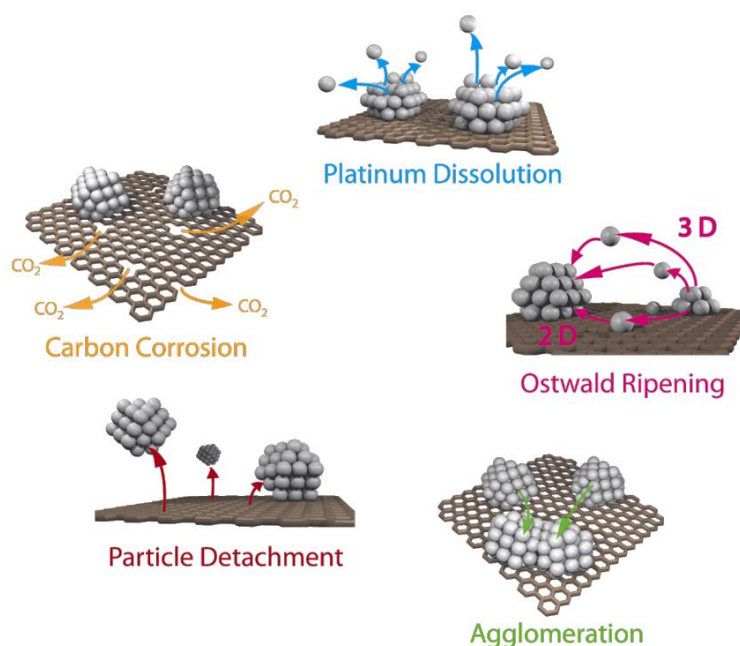
Figure 2.8: Schematic overview of carbon supported Pt nanoparticle degradation in PEFCs. Reprinted with permission from Meier et al. [68] under the terms of the Creative Comments Attribution 2.0.

Platinum dissolution (e.g. to the ionomer phase) and carbon corrosion are considered primary degradation mechanisms, while Pt detachment and agglomeration as well as Ostwald ripening are considered secondary mechanisms which can be induced by a primary mechanism.

From a mechanistic point of view, Ostwald ripening and electrochemical Pt dissolution are strongly related. Despite being one of the most stable elements, Pt can be dissolved in acidic media at potentials present in a fuel cell. The Pt dissolution can either take

place by direct oxidation of platinum nanoparticles to Pt^{2+} or via the reduction of platinum oxides, which are commonly formed on the surface during operation within the commonly observed potentials of 0.95 to 0.65 V_{RHE} (voltage against reversible hydrogen electrode, RHE) on the cathode. Subsequently, the formed Pt^{2+} ions are soluble in the ionomer phase (ionomer and membrane) and can dissolve. Dissolved Pt can either been washed out (Pt dissolution) or redeposited again within the catalyst layer on other Pt particles, resulting in particle growth or the so-called Ostwald ripening. Furthermore, Ostwald ripening can also occur via Pt atoms diffusing along carbon support [69], depicted as 2D Ostwald ripening in Figure 2.8. The resulting larger nanoparticles are more stable than smaller particles, but consequently the average Pt diameter increases while the *ECSA* decreases. Besides, the Pt^{2+} ions also can be reduced within the ionomer phase, e.g. by H_2 crossing over from the anode side, commonly building out a band-like precipitation near the cathode/membrane interface [69]. As these Pt nanoparticles are electrically not connected, they cannot participate in the electrochemical reaction in the absence of a three-phase boundary. The same mechanism is hypothesized for other metallic catalysts, as exemplary discussed by Tovini et al. for re-precipitation of Ir^+ cations, originating from an anode co-catalyst, in the membrane or cathode [70]. Pt dissolution and Ostwald ripening are further enhanced by small initial Pt particle sizes [71] as well as repetitive voltage cycles, e.g. due to load cycles during dynamic automotive applications.

Coalescence of whole platinum nanoparticles can cause catalyst degradation. The agglomeration can be driven either by nanoparticle migration on the support and subsequent collision of nanoparticles or due to carbon corrosion resulting in contact and agglomeration of initially separated particles [68].

In addition to dissolution of Pt atoms in ionic form, whole platinum particles can detach from the surface of the support material. This particle detachment is caused by a weakening of the particle/support interaction, which can for example originate from carbon corrosion [72, 73].

Carbon corrosion

Apart from platinum dissolution, carbon corrosion is another primary degradation mechanism for the catalyst layer (see Figure 2.8). Carbon is thermodynamically not stable for potentials $> 0.2\,V_{RHE}$ [74] and can be electrochemically oxidized to carbon dioxide or carbon monoxide:

$$C + 2\,H_2O \rightleftharpoons CO_2 + 4H^+ + 4e^-\,, E^0 = 0.207\,V_{RHE} \tag{2.17}$$

$$C + H_2O \rightleftharpoons CO + 2H^+ + 2e^-\,, E^0 = 0.518\,V_{RHE} \tag{2.18}$$
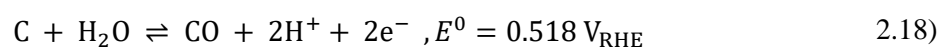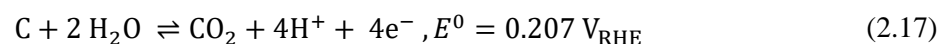
Due to the sluggish reaction kinetics of the carbon oxidation reaction (COR), carbon can be exposed to potentials $\leq 0.9\,V_{RHE}$ without significant corrosion [21, 75–77].

However, high potentials (> 1 V_{RHE}) can occur during fuel cell operation, e.g. during start-up / shut-down (SUSD) events with air/hydrogen fronts occurring or during fuel starvation events (see section 2.7). Beside high potentials, the presence of water is mandatory (see Equation 2.17) and can further accelerate carbon corrosion [78, 79]. Additionally, the presence of platinum was shown to catalyze carbon corrosion via oxidation pathways including intermediate carbon surface species (e.g. formation of the quinone group) [21]. In contrast to electrochemical oxidation, thermal carbon corrosion is not expected in the common operating window of automotive and stationary applications for PEFCs below 100 °C [80].

As outlined above, carbon corrosion can enable secondary catalyst degradation, as particle coalescence and particle detachment, resulting in decreased *ECSA* values and commonly coming along with an increase in activation overpotential predominantly for the ORR. However, as the carbon support material contributes mainly to the electrode's structural properties and porosity, carbon corrosion adds a structural electrode degradation to the above discussed degradation of the catalyst layer. The oxidation of small amounts of carbon (5-10 wt.%) is already sufficient to cause a carbon structure collapse [81–83]. Consequently, the gas transport and the (liquid) water removal from the catalyst layer can suffer, leading to an increased mass transport overpotential and severe performance decay at high current densities. In addition, increased local heat generation has been reported, caused by carbon corrosion and structural collapse, leading to a change in water distribution within the catalyst layer or even local catalyst layer dehydration [84]. Also, complete failure of the cell can occur, e.g. due to flooding of residual pores in the electrode. Furthermore, carbon corrosion can also degrade the electron-conducting network, resulting in increased ohmic losses or culminating in catalyst particles becoming inactive by electric decoupling.

Commonly, the impact of carbon corrosion on the cathode is regarded as more severe, due to the more demanding gas transport of oxygen diluted in air in addition with the demand for reactant water removal. However, significant carbon corrosion at the anode can also be observed during fuel starvation events and subsequently the mass transport and activation overpotential can increase significantly and severe performance decay, up to complete PEFC failure, can occur.

Mitigation strategies for carbon corrosion and Pt dissolution

Mitigation strategies for catalyst layer degradation mainly focus on the primary degradation mechanisms. Operational mitigation strategies can decrease degradation due to avoiding accelerating factors (e.g. voltage cycles, low relative humidity, fuel starvation, high voltages) [85]. On the other hand, material-based mitigation strategies can decrease the rate of degradation. The incorporation of Pt alloys (e.g. Co, Ni, Fe, Mn, Ir) was shown to diminish platinum dissolution [86–88]. To mitigate carbon corrosion, several approaches have shown promising results. The incorporation of carbon support materi-

als which are less prone to oxidation (e.g. graphitized carbon) [89–91], or the complete substitution of carbon as support material [57] have been investigated. Especially for carbon corrosion events occurring on the anode, the additional incorporation of a water splitting catalyst (commonly based on Ru or Ir in the form of co-catalyst or alloys) has been established to promote the oxygen evolution reaction (OER) over the competing carbon oxidation reaction [39, 92]. These mitigation concepts will be discussed in detail in section 2.7.

Contaminants

Beside Pt dissolution and oxidation of the support, catalyst deactivation via surface poisoning or (electro)chemical reactions can degrade the catalyst layer severely. The contaminants originate from outside (e.g. supplied fuel and air) or inside the system (e.g. coolant, leaching species). The most common gas contaminants from outside are CO, CO_2, CH_4, H_2S, NH_3, NO, NO_2, SO_2, SO_3 and O_3. For example the adsorption of CO on Pt sites blocks the access of hydrogen or oxygen and consequently decreases the *ECSA* for HOR and ORR, at least temporary [21, 38]. A major mitigation strategy to mitigate CO contamination on the anode is the incorporation of Ru within the anode catalyst layer. However, Ru introduction to the MEA can be used at the same time as an example for internal contaminants. It was shown, that Ru can dissolve from the anode catalyst layer and migrate to the cathode, resulting in Pt catalyst activity decrease for the ORR and consequently a significant performance decay [92–94].

2.7 Anode degradation and mitigation strategies

For pristine platinum based anode catalyst layers their contribution to the entire overpotential is often regarded as negligible, due to the high HOR exchange current density and thus minor activation overpotentials and mass transport overpotentials [36, 95]. However, over the lifetime of a fuel cell, anode degradation can lead to a significant HOR overpotential increase. Consequently, the lifetime of the fuel cell system can either be drastically reduced, or mitigation strategies have to be applied to minimize the impact on anode degradation.

Of special interest for anode degradation are so-called cell reversal events, as during the temporary undersupply of fuel (also referred to as gross fuel starvation) substantial, irreversible damage to the anode catalyst layer (ACL) and other cell components occurs in association with severe performance decay. Therefore, cell reversal events are a major lever for anode and PEFC degradation and a common material-based mitigation concept is incorporating an OER co-catalyst to the ACL [39].

In contrast, other anode degradation effects are not as harsh as cell reversal events. Anode degradation due to contaminants for example is often reversible (e.g. by CO) or

can be mitigated by monitoring fuel impurities [21]. Therefore, the aspect of poisoning by external contaminants is not part of this thesis. However, despite a less severe impact, anode degradation due to start-up/shut-down (SUSD) processes or local fuel starvation is investigated, particularly focusing on the degradation impact on reversal tolerant anodes incorporating OER catalysts. The impact of these SUSD events on anode degradation has recently gained attention [35, 96], but the impact and the attention for SUSD events on cathode degradation is commonly higher [35, 78, 97].

Therefore, the cell reversal mechanism, common mitigation strategies for the latter and the comprehensive impact of anode degradation during transient conditions, with focus on OER based anode concepts, are discussed in the following.

2.7.1 Cell reversal events

Introduction

During normal operation, hydrogen and oxygen (commonly in air) are supplied to the fuel cell system at sufficient stoichiometry with regard to the actual load demand. As outlined in section 2.1, HOR and ORR proceed on the anode and cathode, respectively. If the required fuel stoichiometry for one or several cell(s) is not achieved, a gross fuel starvation can occur in the affected cell(s). The former can result in the so-called reverse-current effect (discussed in detail in section 2.7.2), commonly associated with severe cathode degradation due to SUSD events. The latter, in complete absence of hydrogen in the affected cell, is associated with severe anode degradation and can be indicated by the observation of negative cell voltages [39].

The starvation events are a result of mass transport limitations of fuel either due to system malfunction (e.g. anode recirculation blower malfunction) or due to impurities, foreign substances (e.g. carbon fibers), water flooding or ice formation (at freezing temperatures) which can occur at the cell inlet/supply lines, the flow field's gas channels or the GDL/catalyst layer pores [39, 98, 99]. Transient conditions such as rapid load changes at dynamic operation or start-up can exacerbate the hydrogen starvation. These hydrogen mass transport limitations are predominantly temporary events, commonly being resolved within time scales of seconds or minutes, e.g. by convective water removal or ice melting due to heating (e.g. by waste heat or cooling circuit). However, uninterrupted and unmitigated cell reversal events can lead to catastrophic cell failure within the timescale of seconds or minutes [37, 100].

Mechanism

When the anode of a particular cell in stack configuration (see Figure 2.9a) is starved of hydrogen, electrons and protons cannot be provided via HOR. Due to the series connection of cells in stack configuration, the same current is imposed on each single cell in the stack (Kirchhoff's circuit laws). Subsequently, in the absence of the HOR in the

starved cell, a capacitive charging effect of the adjacent cells leads to an increased anode potential, promoting alternative reactions to provide electrons and protons to close the load circuit again.
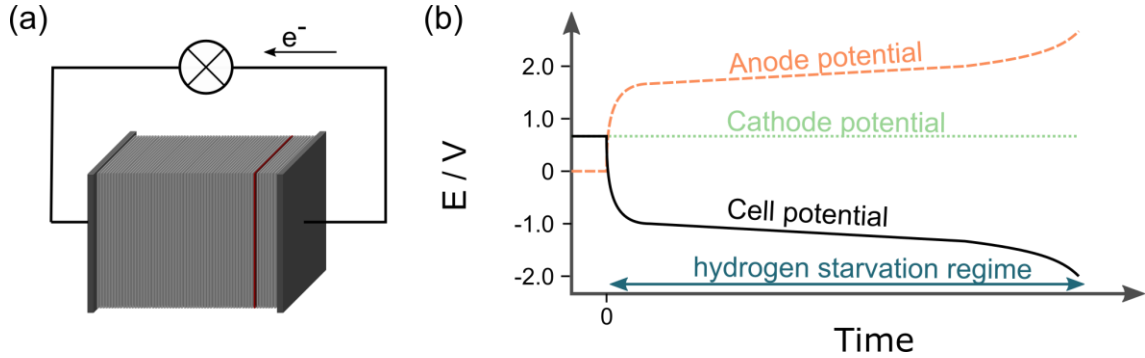
Figure 2.9: (a) Stack under load with one cell facing a gross fuel starvation (highlighted in red). (b) Anode, cathode and cell potential during a switch from normal operation (t < 0; H₂/air on the anode/cathode respectively) to a fuel starvation event (t ≥ 0; N₂/air on the anode/cathode respectively) in the affected cell schematically depicted according to [98, 100].

The time dependent cell voltages as well as the anode and cathode half-cell potentials for a cell exposed to a gross fuel starvation is schematically depicted in Figure 2.9b. For t < 0, HOR and ORR are performed on the anode and cathode in the affected cell, respectively. Thus, anode half-cell potential E_{anode} is approximately ≈ 0 V$_{RHE}$, whereas the resulting cathode potential commonly ranges between 0.6 and 0.9 V$_{RHE}$ (dependent on the applied electric load). With the onset of fuel starvation (for t ≥ 0 in Figure 2.9b) and the absence of the HOR, the anode potential increases significantly due to the capacitive charging effect in the stack. The anode potential commonly exceeds the cathode potential instantly, resulting in negative cell potentials ($E_{cell} = E_{cathode} - E_{anode}$), designating the so-called (cell) reversal event. At the cathode, the ORR reaction proceeds continuously, resulting in an almost time independent cathode potential [98]. Consequently, the affected cell is acting as a power consumer during the reversal event instead of a power source, supplied by the other cells in the stack. Therefore it acts as an electrolytic cell.

The increased anode potential was found to result in carbon oxidation reaction (COR, see Equations 2.17 and 2.18) as well as oxygen evolution reaction (OER, see Equation 2.19) to provide the necessary electrons and protons and to close the electrical circuit of the stack [37, 39, 77, 100, 101].

$$H_2O \rightleftharpoons \frac{1}{2}O_2 + 2H^+ + 2e^- , E^0 = 1.23 \text{ V}_{RHE} \tag{2.19}$$
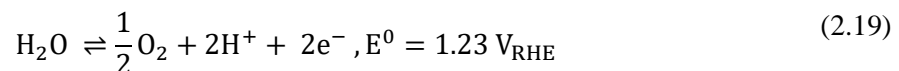
The carbon oxidation reaction is thermodynamically favored. But as discussed before, the COR almost exclusively takes place at high potentials (> 1 V$_{RHE}$) due to sluggish reaction kinetics. This is why OER (also referred to as water splitting reaction) is com-

monly taking place at lower anode potentials (see plateau in anode and cell voltage in Figure 2.9b prior to the harsh incline of these potentials), whereas significant COR contribution to the faradic current is predominantly detected at subsequent higher anode potentials [37, 39, 100]. Pt requires high overpotentials for the OER to proceed [102]. Therefore, anode catalyst layers solely containing carbon supported platinum (Pt/C) are exposed to increasing anode potentials (> 1.5 V_{RHE}), resulting in concurrent severe carbon corrosion. This, in turn, is accelerating Pt dissolution and anode degradation. Consequently, with unmitigated Pt/C based anodes the observed water splitting plateau is very short (range of seconds) and subsequently electrons during the reversal event are predominantly provided by COR [103]. Assuming all electrons are provided by the electrochemical oxidation of carbon to carbon dioxide (cf. Equation 2.17) at a current density of 0.2 A cm^{-2}, a state-of-the-art anode catalyst layer (values according to Lipman et al. [21]: Pt supported on carbon, 2 µm layer thickness, porosity of 60%, ionomer to carbon volume ratio of 1/1 and a carbon bulk density of 96 kg/m³ for Vulcan XC72R [104]) would have lost all its carbon within 0.62 s according to Faraday's law. As a collapse of the catalyst layer is typically reported after 5-10 wt.% carbon loss [81–83], this highlights the catastrophic impact of a cell reversal event regarding irreversible degradation. For example, at a current density of 2 A cm^{-2} a threshold of 5 wt.% carbon would be lost after 3.05 ms (similar assumptions as above). Consequently, severe carbon corrosion in the anode catalyst layer is observed during cell reversal events [37, 100, 105]. A significant loss of void volume and secondary anode degradation, such as platinum particle agglomeration and detachment, can occur. In addition, a carbon based MPL of a GDL, was shown to be also exposed to severe carbon corrosion during reversal events, concomitant with a significant change in the MPLs hydrophobic character [106]. Besides, the reversal events can cause severe degradation within other cell components as bipolar plates, GDL and ionomer (in the catalyst layer and the membrane), due to the occurring high potentials (> 1.5 V_{RHE}) and thermal impact induced by high overpotentials for COR and OER.

This illustrates the importance of cell reversal mitigation strategies for PEFCs, as fuel starvation events cannot be completely avoided during stack operation, even with very sophisticated operating strategies, harmonized components and design guidelines.

Reversal tolerant anodes

To mitigate cell reversal events, either system mitigation strategies or material-based mitigation strategies can be applied.

For system-based mitigation, regulating the operating conditions as pressure, cell temperature, humidity and load demand is not sufficient to completely avoid cell reversal events by fuel starvation. In addition, a cell voltage monitoring has to be applied to recognize cell reversals at an early stage and subsequently disconnect the electric load at the onset of a reversal event [107, 108]. Therefore, as outlined above, the control system

must be able to detect cell reversals on timescales $\ll 1$ ms to prevent the anode from substantial degradation. Thus, requirements for control units are quite challenging with sampling rates in the order of kHz to GHz.

In contrast to system-based mitigation strategies, material-based mitigation does not require active stack control or additional electrical hardware components for surveillance. Therefore, system control complexity and space requirements are significantly decreased. Two main concepts have been established to achieve reversal tolerant anodes via material-based mitigation:

i. Incorporating corrosion resistant support material
ii. Incorporating an OER catalyst to promote water splitting over corrosion of the carbon support

Carbon supports which are less prone to corrosion can decrease the COR rate for carbon based support materials exposed to reversal events [89, 109, 110]. However, their mitigation capability is still insufficient to overcome multiple reversal events as e.g. expected in automotive applications. Therefore, alternative support materials for platinum are under research to achieve reversal tolerant anodes (RTAs). For example Ni-aerogels [57] or nanostructured thin-films [111, 112] are investigated as support material for platinum catalysts. But the risk of corroding other MEA components (e.g. GDL or bipolar plates) is still present and anode degradation due to the high OER onset potential of platinum accompanying with (local) thermal impact by waste heat is still conceivable.

Thus, the introduction of oxygen evolution reaction catalyst to the ACL has been established as material-based mitigation strategy [113]. The introduction of OER catalyst was shown to reliable decrease the onset potential of the water splitting reaction, coming along with decreased anode potentials during reversal events and thus a lower degree of carbon corrosion [39, 98, 100]. Consequently, this concept is very promising to achieve reversal tolerant anodes for PEFC applications on commercial level.

The OER catalyst can either be added as co-catalyst to common platinum based HOR catalysts [37, 39, 70, 109, 114] or can be introduced in the form of metal alloys with activity for both, HOR and OER [115, 116]. The concept of adding a supported OER catalyst to a common Pt/C based HOR catalyst in order to achieve RTAs is depicted in Figure 2.10.
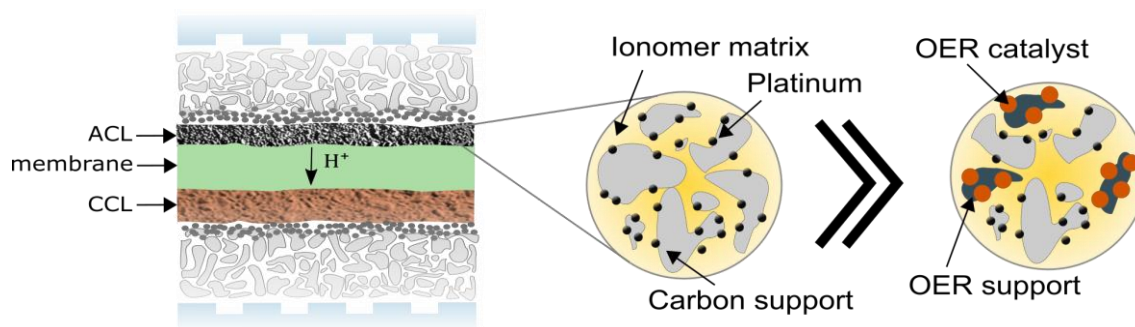
Figure 2.10: Concept of reversal tolerant anodes (RTAs) based on adding an OER co-catalyst to the ACL, while maintaining the other MEA components as membrane and cathode catalyst layer (CCL).

This concept allows the utilization of commercially available catalysts, both for OER and HOR, which is beneficial when aiming for commercial applications. In contrast, the applicability of researched materials (e.g. metal alloys) or concepts is commonly aggravated either by the commercial availability of the catalysts or limitations within commercial MEA manufacturing processing. Therefore, RTA concepts including supported IrO$_x$, the most promising OER catalyst for commercial PEM based water electrolyzers to date, are under amplified research recently [70, 100, 114, 117, 118].

Characterization methods for reversal tolerant anodes

Various research groups investigated reversal events and the accompanying degradation effects for OER based RTAs using accelerated stress tests (ASTs) on differential cells as well as (segmented) cells with large active areas [37, 39, 70, 98, 100, 105, 109, 114, 116, 117, 119–125]. The topic gained much attention recently, and the commonly researched aspects can be grouped to either aim for material improvement [125–128], reveal the underlying degradation effects [100, 103, 117, 120] or investigate the impact of varying operating conditions [37, 105, 118] on the mitigation capability.

Typically, the tolerance for reversal events is evaluated by simulating a fuel starvation in a single cell experiment by flowing humidified air/N$_2$ through the cathode and anode, respectively. Simultaneously, a constant current (commonly 0.2 A cm^{-2}) is applied. As depicted in Figure 2.9b, during this AST the cell voltage initially drops in the absence of hydrogen. Subsequently, an almost stable negative cell voltage is observed with gradual voltage decay, referred to as water electrolysis plateau. This plateau is followed by a drastic drop in cell potential (typically to potentials < -1.5 V), which is commonly considered to complete anode (and accompanied MEA) failure, caused by carbon corrosion going along with severely increased ohmic resistance [39, 98, 100, 103, 122]. The time for this single, continuous prolonged reversal event (in Figure 2.9b referred to as 'hydrogen starvation regime') is commonly taken as figure-of-merit to compare the reversal tolerance, e.g. for varying operating conditions, materials or OER loadings.

Recently, the impact of varying relative humidity [37, 105], either due to different feed gas humidification or due to resulting *RH* gradients in large cells, as well as the impact of a wide range of operating temperatures (-15° C to 90° C) [37, 118, 119, 121] has been investigated during prolonged reversal events for IrO_x based RTAs. With additional characterization methods, as in-situ online mass spectroscopy [100, 114] and X-ray computed tomography [103], the carbon corrosion rate could be quantified and a prolonged water splitting plateau was observed with increased IrO_x loadings [100, 103, 124]. The higher OER catalyst loading is decreasing the rate of carbon corrosion. However, the discrepancy between the lifetime of IrO_x based polymer electrolyte membrane water electrolyzers (PEMWE; in the order of >10,000 hours [129]) and PEFCs incorporating IrO_x based RTAs is still challenging, with the latter showing commonly a drastic drop in cell potential after a comparable short time in OER operation during water electrolysis plateau (timescale of minutes or hours). Hong et al. showed using X-ray computed tomography, that OER catalyst is still present in the anode after MEA failure, but is probably deactivated [37]. Recently the same research group further investigated this topic and proposed an OER catalyst deactivation mechanism by carbon oxidation products for prolonged fuel starvation, explaining this discrepancy [117].

This OER degradation effect highlights the need for more realistic ASTs on single cell level, mimicking short reversal events (timescale of seconds/minutes). Reversal events with a duration < 5 min are more likely expected during field operation, as the fuel starvation root causes are often due to temporary transient conditions or events (e.g. start-up at freezing conditions, rapid load changes etc.). The root causes for fuel starvation most likely will disappear when stable operating conditions are achieved. Especially for improved reversal tolerant anode designs, where several hours of reversal operation can be performed before anode failure during prolonged reversal events is observed. The above-mentioned prolonged reversal test procedures are far from realistically mimicking reversal events occurring during field operation.

However, investigations on short-term reversal events are rarely seen for OER based RTAs [114, 120]. Therefore, in this thesis the degradation impact of an AST simulating more realistic short-term reversal events in contrast to prolonged reversal events is investigated. In addition to reveal differences in degradation dependent on the duration of reversal events, further insights can be achieved by monitoring the anode's HOR capability on a regular basis instead of focusing exclusively on the anode's OER capability during a prolonged reversal event. This test approach was coupled with the application of field-relevant operating conditions, representative for reversal events occurring during start-ups at freezing conditions, and the investigation of different HOR catalysts. Furthermore, a voltage loss analysis for the HOR was performed to analyze the occurring anode degradation, incorporating additional characterization methods (e.g. hydrogen pump experiments and cyclic voltammetry).

2.7.2 Transient anode potentials

Introduction

Besides the above discussed reversal events caused by fuel starvations, also significant anode degradation can occur during transient anode conditions, resulting in the so-called reverse-current effect. The reverse-current effect was first reported by Reiser et al. [130]. The transient anode conditions can be either caused by start-up/shut-down (SUSD) events [130] or during local fuel starvation events [101]. The occurring mechanism in the affected cell is comparable for both events. The reverse-current mechanism is predominantly regarded as mechanism causing severe cathode degradation by increased cathode potentials, resulting in significant carbon corrosion at the cathode. However, also significant anode degradation has been reported recently caused during reverse-current events. SUSD events applied on single cell level were shown to significantly degrade Pt/C based anode catalyst layers going along with an increase of the HOR overpotential (activation and mass transport) [35]. In addition, the transient anode potentials during SUSD were shown to have a degrading impact on anode co-catalysts as Ru [92, 94] (commonly incorporated for anode CO tolerance) and most recently IrO_2 [70]. Consequently, it was shown to not only degrade the anode, but also the ORR on cathode can suffer from anode degradation by co-catalyst species crossing over to the cathode. Therefore, these transient anode conditions are important to comprehensively evaluate the application-relevant degradation of OER based reversal tolerant anodes and the subsequent impact on MEA performance as well as on reversal tolerance.

In this chapter transient anode potentials and the resulting reverse-current effect are explained by the SUSD mechanism, followed by common mitigation strategies for SUSD events. Finally, local fuel starvation issues and their impacts are discussed.

Start-up/shut down mechanism

After an idle time, as e.g. parking a vehicle for several hours or days, the initially present hydrogen in the anode compartment of a fuel cell stack is removed and the whole anode is filled with air due to imperfect stack sealing as well as air diffusion from the cathode compartment. During a subsequent start-up of the fuel cell stack, hydrogen needs to be introduced to the anode again to start regular operation. Thus, air and hydrogen are present in the same electrode for a certain amount of time. This process is referred to as start-up event or as a so-called air/air start. During an air/air start, the cell can be separated conceptually in two sections: a fuel cell compartment (cf. Figure 2.11a/b below dashed line) and an electrolytic cell (cf. Figure 2.11a/b above dashed line).
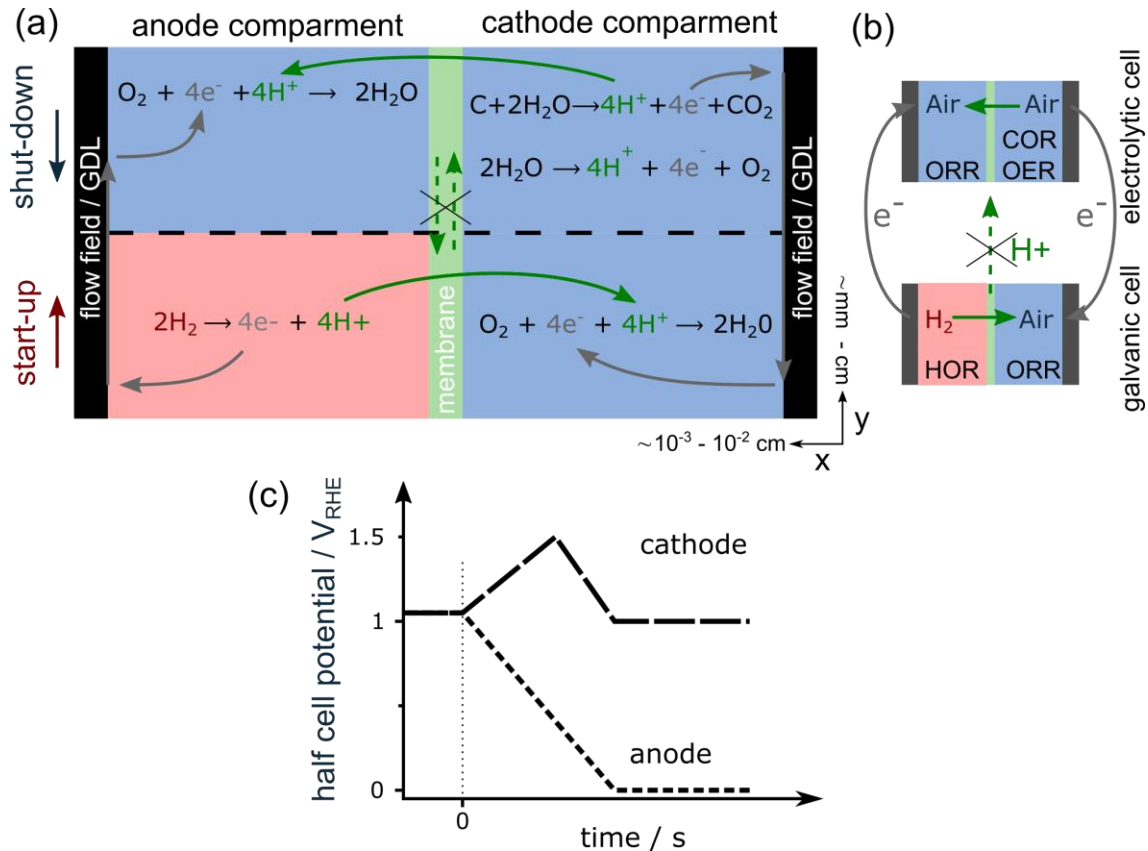
Figure 2.11: Processes during a SUSD event in a PEFC schematically depicted. On the anode compartment a H_2-air front moves through the flow field (in y-direction), whereas the cathode flow field is completely filled with air (H_2: red, air: blue). The direction in which the gas front is moving varies between start-up (red arrow) and shut-down (blue arrow) (a) Electrochemical reactions occurring segment-wise are schematically depicted, with proton pathways across the membrane illustrated as green arrows and electric pathways across electrodes and flow field/GDL as grey arrows. (b) Conceptual separation of the cell during a SUSD event into a fuel cell (galvanic cell) and an electrolytic cell. In-plane proton conductivity (y-direction) is only possible over a short distance (e.g., for a 20 µm thick membrane only ≈ 120 µm) compared to the flow field length (actual range of mm or cm), thus proton migration from the H_2-filled anode compartment to the air-filled anode compartment is negligible (crossed out arrows). Figure adapted from Mittermeier et al. [97] under the terms of the Creative Comments Attribution 4.0. c) Schematic time dependent half-cell potentials during an SU event, according to [131]. The air front enters the cell at t = 0.

The proton conduction between the fuel cell section and the electrolytic cell section is hindered by the high in-plane proton resistance within the electrode and the membrane (in y-direction in Figure 2.11a) due to its large expansion (mm to cm range). Instead, protons migrate across the membrane (thickness commonly ≈ 10 to 20 µm) from anode to cathode and vice versa. Consequently, in the hydrogen filled anode compartment HOR takes place, whereas on the opposite cathode compartment ORR is performed. The protons are migrating from the HOR section to the ORR section across the membrane. In contrast to proton conduction, in-plane electric conduction (y-direction in Figure 2.11a) between the galvanic and electrolytic cell compartment is given (high

electric conductivity of the carbon-based electrode and highly conductive flow fields/GDLs). Therefore, the fuel cell reaction (below dashed line) is supplying the power to the electrolytic cell compartment (above dashed line). In the electrolytic cell compartment ORR takes place in the air-filled anode domain while inducing an oxidative current in the respective cathode domain (so-called reverse-current mechanism). In the cathode compartment opposing the air-filled anode, OER and/or COR is taking place at half-cell potentials > 1.2 V_{RHE}. Whether OER or COR takes place, is dependent on the reaction kinetics (dependent on catalyst and reaction conditions) and the stability of the carbon support. As outlined before, the OER activity for common Pt/C catalysts requires a high onset potential [102]. Consequently, COR is commonly reported as the predominant reaction assumed during an air/air start for Pt/C based PEFCs.

The processes during the shut-down of the cell are conceptually the same as observed during the (air/air) start-up, differing regarding the migration direction of the air-H_2 front.

Without mitigation, the cathode compartment is exposed to high cathode potentials and subsequently severe cathode degradation during these events (cf. Figure 2.11c). Severe carbon corrosion is reported, which can lead to an increased mass transport overpotential by a loss in porosity, culminating in catalyst layer collapse. Additionally, *ECSA* loss due to secondary Pt degradation (e.g. Pt agglomeration or detachment) by carbon corrosion as well as potential driven Pt dissolution (e.g. Ostwald ripening) is commonly observed, increasing the ORR activation overpotential. Due to the harsh cathode degradation, a wide range of research on the topic of start-up/shut-down is available focusing on cathode degradation. Recently, for example the impact of different operating parameters [78, 97] (i.e. varying temperature and relative humidity) as well as locally resolved cathode degradation [132] has been investigated.

In contrast, for SUSD induced degradation investigated in literature, the impact on anode degradation is commonly not focused. However, due to the gas being exchanged in the anode, the anode potential cycles from ≈ 1 V_{RHE} (air) to ≈ 0 V_{RHE} (H_2) during an air/air start (see Figure 2.11c). Therefore, significant degradation can occur either by Pt dissolution or carbon corrosion (cf. section 2.6.4). Engl et al. first reported significant anode degradation for high temperature PEFCs due to SUSD events [96]. Schwämmlein et al. recently observed a significantly increased overpotential for the HOR after applying SUSD events on the respective MEA [35]. However, both studies were investigating Pt/C based anode designs. The introduction of an OER co-catalyst to the anode, to achieve a reversal tolerant anode, adds complexity to the degradation mechanism. For anode catalyst layers containing Ru to mitigate CO poisoning from fuel gas impurities, the dissolution of Ru and subsequent crossover to the cathode compartment has been reported. Crossed-over Ru can cause poisoning of the ORR catalyst [92, 94]. For an RTA containing IrO_2, Tovini et al. most recently revealed a comparable dissolution for

IrO_2 as well as subsequent redeposition of Ir on the cathode, imposed by an in-situ SUSD AST. Ir crossover was investigated via ex-situ X-ray photoelectron spectroscopy (XPS) measurements The degradation was shown to go along with a significant decrease of MEA performance and reversal tolerance [70].

This highlights the need for in-situ characterization methods to investigate the degradation of OER based reversal tolerant anodes for commercial applications due to SUSD events, considering the ageing impact on the reversal tolerance and fuel cell performance due to transient anode conditions. Only if these RTA degradation effects are considered, highly durable anodes over the entire targeted lifetime of commercial PEFC applications can be developed, while maintaining a required high fuel cell performance.

Start-up/shut down mitigation

Within automotive applications, air/air starts are occurring after the vehicle had not been used for a certain amount of time. Mitigation strategies for start-up/shut-down events can either aim for complete avoidance of the events or lowering their degradation impact. To avoid SUSD events, H_2 can be maintained in the anode compartment as long as possible [133]. For example, an improved sealing concept or active hydrogen purging during idle mode can be implemented. Consequently, the shut-down mechanism is suppressed as long as sufficient hydrogen is present in the anode compartment. Simultaneously, no H_2-air front would be formed during a subsequent start-up while hydrogen is maintained in the anode. Mitigation strategies aiming for lower cathode degradation can target the operating conditions, e.g. shortening the residence time of the H_2-air front [134] or aiming for lower temperatures [97] and relative humidity [78] during the SUSD. Fortunately, the commonly long idle times before an air/air start is performed are also ensuring low temperatures (close to ambient temperature). Thus, the rate of carbon corrosion is most likely low [77]. Beside operating strategies, material-based mitigation strategies are suggesting either cathode support materials with improved corrosion resistance [91] or the introduction of an OER catalyst to the cathode [135] to promote OER over COR during SUSD events.

However, these mitigation strategies are again mostly aligned with cathode degradation, therefore their application could come down to an increased amount of air/air starts permitted, whereas the anode degradation might not be considered. To the best of the author's knowledge, mitigation strategies for lowering the HOR or OER degradation impact on the anode have not been reported yet.

Local fuel starvation

In contrast to gross fuel starvation events (cf. section 2.7.1), local H_2 starvation in a single cell can result in a reverse-current event similar to the mechanism observed during SUSD events [101]. During a local fuel starvation, hydrogen is only provided to a certain part of the anode (e.g. due to water droplets blocking the channels) whereas the

oxygen O_2 for the ORR performed in the starved anode compartment is provided by O_2 crossover through the membrane from the cathode side. As a result, the same conceptual separation of the cell into a fuel cell compartment and an electrolytic cell as for the SUSD is valid. Consequently, high cathode potentials are observed in the section opposing the starved anode side. And anode potential undergoes a transition from ≈ 1 V_{RHE} (air) to ≈ 0 V_{RHE} (H_2) in the starved region at a subsequent normal operation.

A major concern for local fuel starvation is the mostly unpredictable occurance during operation. Therefore, the degradation effect on the cathode is strong, i.e. due to elevated temperatures. This high risk for cathode degradation highlights the importance of an elaborate flow field design and operating strategy, to avoid local fuel starvations.

As the controlled and precise simulation of local fuel starvation events leading to reverse-current effects is difficult to implement on single cell tests, local fuel starvation impact is not studied in the framework of this thesis. To simulate transient anode conditions and investigate resulting anode degradation, SUSD based ASTs are performed. These ASTs offer easy control of operating parameters and implementation while the conceptual degradation effects are comparable to local fuel starvation events. In addition, local fuel starvation events are mainly occuring spontaneous during field operation, whereas air/air starts cannot be prevented.

This concept of local fuel starvation leading to a reverse-current effect should not be confused with 'partial' fuel starvation events resulting in a cell reversal operation, as reported by Taniguchi et al [98]. The latter can occur if hydrogen is supplied at a sub stochiometric flow to the affected cell, leading to negative cell potentials and consequently to cell reversal events as described in section 2.7.1, where the electric power for electrochemical reactions within the anode is supplied by adjacent cells.

3   Characterization methods

The relevant experimental techniques used in this thesis are introduced within this chapter.[1] The basis for the following sections can be found in comprehensive scientific literature [21, 41, 43–47, 136–138].

3.1   Electrochemical in-situ measurements

3.1.1   Cyclic voltammetry

Cyclic voltammetry is a common electrochemical technique and can be used to determine the electrochemical surface area (*ECSA*) of fuel cell catalysts in-situ on MEA level. The *ECSA* is commonly used to characterize catalyst layers as well as to analyze and monitor their degradation, as catalyst layer degradation is commonly coupled to *ECSA* decrease (see section 2.6.4). In cyclic voltammetry (CV), the current response of a voltametric cell is measured as a function of an applied triangle-shaped potential change with constant positive and negative sweep rates. Typical CV curves for fuel cell catalyst layers are shown in Figure 3.1. The current response is a combination of the constant capacitive charging current by the linearly changing voltage and the currents due to electrochemical surface reactions. In a single cell setup, the electrode of interest is acting as working electrode, typically supplied with inert gas such as N_2. The opposite electrode is acting as counter electrode and pseudo-reference electrode which is commonly supplied with H_2. To determine the *ECSA*, the charge associated with the reduction or oxidation of a monolayer of ad- or desorbed species is measured. For PEFCs typically hydrogen or carbon monoxide is used as ad- or desorbed species, as their ad/desorption on Pt/C is fully reversible and no persistent contamination or degradation of PEFC components is expected.

Prior to the CV measurement, commonly a cleaning CV is performed (typically under H_2/N_2 atmosphere on the counter/working electrode) to clean the catalyst's surface and to achieve reproducible results. During the potential cycling, the catalyst surface is repeatedly reduced and oxidized which results in the removal of present adsorbates (e.g. organic contaminants) and the defined reorganization of the catalyst surface.

Exemplary CVs of a Pt/C based PEFC electrode are illustrated in Figure 3.1.
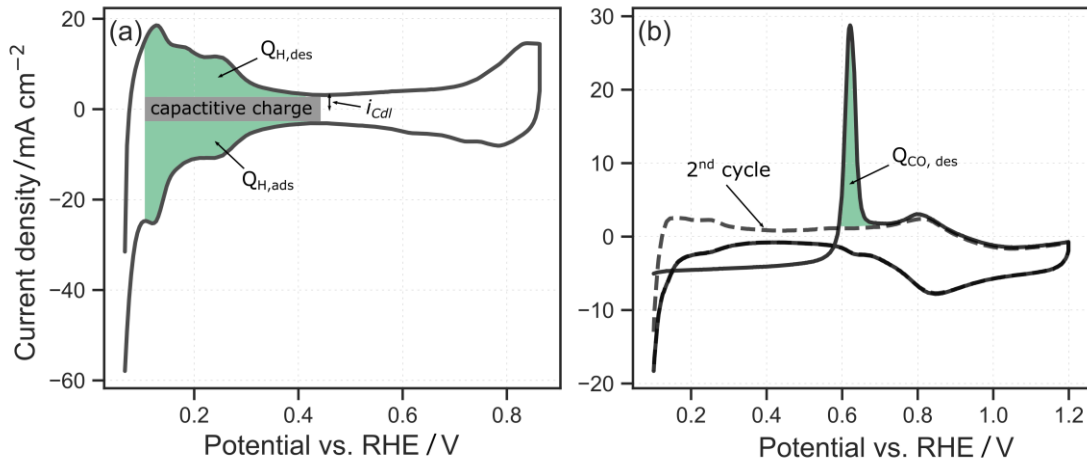
Figure 3.1: (a) Illustration of the *ECSA* evaluation method by H_{upd}. The anodic ($Q_{H,\,des}$, positive current; green area) and cathodic ($Q_{H,\,ads}$, negative current) charge from the cyclic voltammogram between 0.1 and 0.4 V_{RHE} is integrated after double layer capacitance (i_{Cdl}) correction. **(b) Illustration of the *ECSA* determination via CO stripping method. The first cycle shows a distinct CO oxidation peak at 0.62 V_{RHE}, which is integrated (green area, $Q_{CO,\,des}$) after baseline correction by the subsequent cyclic voltammogram.**

ECSA determination by H_{upd}

The *ECSA* estimation by the ad-/desorption of hydrogen on the electrode is depicted in Figure 3.1a. Around 450 mV the obtained current is constant during the anodic and cathodic potential sweep. This behavior is indicating charging/discharging of the electrochemical double layer between working electrode and the electrolyte rather than chemisorption. The double layer capacitance is an additional important indicator obtained by CV, which can be used to investigate structural changes within the catalyst layer (e.g. due to carbon corrosion). Platinum is oxidized between 650 and 800mV during the anodic sweep:

$$Pt + H_2O \rightleftharpoons Pt\text{-}OH + H^+ + e^-\,, \tag{3.1}$$

$$Pt - OH \rightleftharpoons Pt\text{-}O + H^+ + e^-\,. \tag{3.2}$$
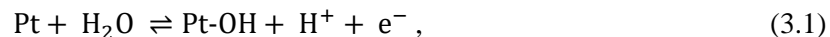
After reaching the upper potential limit (typically between 0.850 and 1.2 V), the direction of the potential sweep is reversed and the oxygenated species covering the platinum are reduced at potentials between 900 and 500 mV, followed again by a double layer charge dominated regime. For potentials < 350 mV during the cathodic sweep, hydrogen adsorption on the surface sites of the working electrode is occurring:

$$Pt + H^+ + e^- \rightleftharpoons Pt\text{-}H\,. \tag{3.3}$$

This process is also referred to as underpotential deposition of hydrogen (H_{upd}). At potentials close to zero high hydrogen evolution currents are measured. When the potential sweep is again reversed, the adsorbed hydrogen is oxidized and desorbed impos-

ing anodic currents (cf. green area Figure 3.1a). The available platinum area A_{Pt} determined via H$_{\text{upd}}$ method is calculated according to the following equation:

$$A_{\text{Pt}} = \frac{Q_{\text{H}_{\text{upd}}}}{210 \, \frac{\mu C}{cm_{\text{Pt}}^2}} \tag{3.4}$$

where $Q_{\text{H}_{\text{upd}}}$ is the electrical charge required to ad-/desorb a hydrogen monolayer from the platinum surface. The conversion factor of $210 \, \frac{\mu C}{cm_{\text{Pt}}^2}$ corresponds to the required charge to ad-/desorb a monolayer of hydrogen from a platinum surface [139]. The electrical charge $Q_{\text{H}_{\text{upd}}}$ is calculated by integrating the corresponding ad- and desorption peaks, averaged and divided by the scan rate $\frac{dE}{dt}$.

$$Q_{\text{H}_{\text{upd}}} = \frac{Q_{\text{H, ads}} + Q_{\text{H, des}}}{2} = \frac{\int I_{\text{H, ads}} \, dE + \int I_{\text{H, des}} \, dE}{2 \, \frac{dE}{dt}} \tag{3.5}$$

The lower integration limit is chosen carefully so as not to overestimate the adsorption charge by the superimposed hydrogen evolution reaction.

In order to calculate the *ECSA* (typically given in units of $[\text{m}_{\text{Pt}}^2 \, \text{g}_{\text{Pt}}^{-1}]$), the available Pt area A_{Pt} is commonly divided by the mass of platinum m_{Pt}. The latter is equal to the electrode's geometrical platinum loading $L \, [\text{g}_{\text{Pt}} \, \text{cm}_{\text{electrode}}^{-2}]$ multiplied with the electrode area $A_{\text{electrode}}$.

$$ECSA = \frac{A_{\text{Pt}}}{m_{Pt}} = \frac{A_{\text{Pt}}}{L \cdot A_{\text{electrode}}} \tag{3.6}$$

The platinum loading is commonly determined for the pristine electrodes, either by calculating the (theoretical) initial catalyst layer loading dependent on the incorporated raw catalyst powder (assuming homogeneous distribution within the electrode) or via X-ray fluorescence spectroscopy of the pristine electrode. As the electrode's platinum loading can decrease over lifetime (e.g. due to washing-out of platinum, resulting in gravimetric platinum loss), sometimes the available Pt area A_{Pt} normalized to the respective geometrical electrode area is reported, referred to as roughness factor *rf* (commonly reported in $[\text{m}_{\text{Pt}}^2 \, \text{cm}_{\text{electrode}}^{-2}]$):

$$rf = \frac{A_{\text{Pt}}}{A_{\text{electrode}}} = ECSA \cdot L \, . \tag{3.7}$$

ECSA determination by CO stripping

The *ECSA* determination via desorption of CO, also referred to as CO stripping voltammetry, is shown in Figure 3.1b. CO molecules are showing a much higher tendency

to bind on platinum than hydrogen. Besides, the adsorption is less surface sensitive. Therefore, the CO stripping method is regarded as more robust to determine the electro-chemical surface area for Pt/C catalysts and less prone to varying fuel cell conditions (e.g. temperature or relative humidity) [140]. To perform the CO stripping method, in a preceding step prior to the CV, CO within the feed gas of the working electrode is adsorbed on platinum:

$$Pt + \; CO \rightarrow Pt\text{-}CO_{ads} \tag{3.8}$$

The subsequent CO desorption by electro-oxidation takes place at higher potentials than hydrogen desorption (cf. Figure 3.1) and can be described by the following equation:

$$Pt\text{-}CO_{ads} \; + \; H_2O \; \rightleftharpoons Pt + CO_2 + 2H^+ + \; 2e^- \; . \tag{3.9}$$
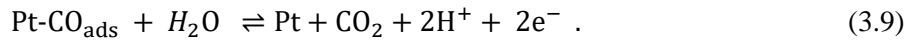
Due to the two-electron transfer, the conversion factor to calculate the *ECSA* via CO stripping is $420 \, \frac{\mu C}{cm_{Pt}^2}$. The platinum area is derived via Equation 3.10.

$$A_{Pt} = \frac{Q_{CO}}{420 \, \dfrac{\mu C}{cm_{Pt}^2}} \tag{3.10}$$

The electrical charge Q_{CO} is calculated by integrating the corresponding CO desorption peak of the 1st scan (cf. Figure 3.1b) divided by the scan rate $\frac{dE}{dt}$.

$$Q_{CO} = \frac{\int I_{CO,\,des} \, dE}{\dfrac{dE}{dt}} \tag{3.11}$$

As integration baseline, to distinguish the CO desorption peak, a subsequent 2nd CV scan is used. During this 2nd CV scan the H$_{upd}$ features are becoming noticeable again (cf. Figure 3.1b). During the 1st scan, the suppression of the H$_{upd}$ features is an indicator for complete platinum coverage by CO.

In contrast to Pt/C based electrodes, the in-situ *ECSA* determination for electrodes incorporating OER catalysts as IrO$_x$ or Pt-alloys is quite challenging [141]. Ir and IrO$_x$ species show diverging H$_{upd}$ and CO features compared to Pt. For metallic Ir, H$_{upd}$ and CO features can be observed, whereas for IrO$_x$ commonly only capacitive behavior is observed instead of surface reactions [142]. In addition, metallic Ir is typically electro-oxidized to IrO$_x$ within only a few CV cycles. Therefore, in-situ *ECSA* determination methods for electrodes containing IrO$_x$ are under research, in particular for PEMWE applications. Recently, Watzele et al. introduced a method based on determining the adsorption capacitance of intermediates within the onset potential of OER via electro-chemical impedance spectroscopy [143]. Alternatively, *ECSA* estimation of IrO$_2$ can be performed via double layer capacitance (only rough estimation due to superimposed

influences, e.g. support materials) or via mercury underpotential deposition [142]. However, the introduction of mercury is hard to implement in single cell fuel cell test stations and includes the risk of contamination effects.

Consequently, for OER based reversal tolerant PEFC anodes incorporating supported IrO_2, commonly still H_{upd} and CO methods are state-of-the-art [37, 70, 114, 125] to determine the *ECSA*. Thus, this thesis also focuses on these *ECSA* methods, predominantly determining the *ECSA* of the Pt-based HOR catalyst, while neglecting the OER co-catalyst's *ECSA*. However, the available catalyst area for OER was nevertheless estimated via the respective OER activity of the electrode.

3.1.2   Hydrogen crossover

The determination of hydrogen crossover can help to detect membrane degradation as well as the presence of electrical short circuits. An increase in hydrogen crossover can indicate chemical or mechanical membrane degradation, e.g. by membrane thinning or pinhole formation.
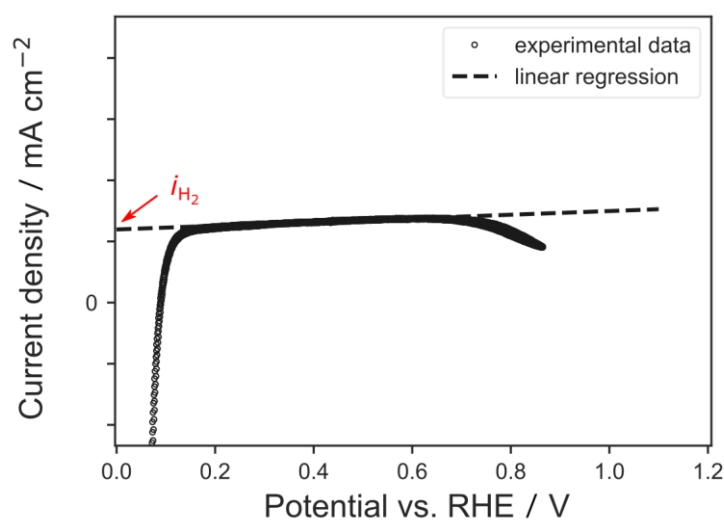
Figure 3.2: Measurement to determine the crossover current density. A single CV between 0.065 and 0.865 V at a scan rate of 2 mV s^{-1} was performed, with a linear regression between 0.35 and 0.6 V. The linear regression intercept at 0 V is equal to the crossover current density, whereas the ohmic short resistance of the membrane is proportional to the inversed slope of the linear regression. (N$_2$/H$_2$ on cathode/anode, T=68° C; p=1 bar$_g$, RH=100%, flow rate=1 l$_n$ min^{-1})

The hydrogen crossover can be measured in-situ comparable to the measurement of CVs. Hydrogen flows on one side of the cell, acting as reference and counter electrode. Subsequently, hydrogen crosses over the membrane to the opposing electrode, acting as working electrode, where the hydrogen gets oxidized. The resulting oxidating current is measured. A typical measurement of the hydrogen crossover current density i_{H_2} is

59

depicted in Figure 3.2. The current is commonly measured over a potential range (i.e.: between 0.065 and 0.865 V), similar to a CV but at significantly lower scan rates (< 5m V s^{-1}). After an initial increase in current density for voltages < 0.1 V$_{RHE}$, a plateau is reached as the current is now limited by the hydrogen permeation rate of the membrane rather than imposed by hydrogen evolution. Subsequently, a linear regression of the plateau region (typically in the region between ≈ 0.35 and ≈ 0.6 V, for up and down sweep) can be performed. The regression line intercept at a current density equal to zero is typically reported as the crossover current density i_{H_2} at the prevailing operating conditions. The slope of the regression line corresponds to the reciprocal value of the electrical short current R_{short}.

3.1.3 Polarization curves

The electrochemical performance of a fuel cell is commonly measured by a polarization curve. An exemplary polarization curve and the occurring overpotentials, dependent on the current density, were introduced in Figure 2.1.The fuel cell's power output can be directly obtained from the polarization curve. Polarization curves can be performed at different operating conditions and gas supply (e.g. varying H$_2$ and O$_2$ concentrations), commonly related to certain application-relevant operating windows.

As overpotentials increase due to degradation, the performance declines with ageing of the fuel cell. For commercial applications, a maximum threshold in performance loss is defining the end-of-life (EOL) state. When this threshold is exceeded, operation within the initial application is no longer reasonable, as either the system efficiency or the maximum power is not sufficient anymore for the respective application (e.g. hill climb for heavy duty trucks). In addition, secondary issues could arise for certain applications, e.g. due to the increased overpotentials the amount of waste heat increases, exceeding the cooling capacity of the fuel cell system. However, the fuel cell system could still meet the requirements for deviating applications, resulting in second-life applications, as known from battery electric vehicles [144].

In addition to application relevant insights, polarization curves provide insights regarding the severity and type of MEA degradation at the chosen operating conditions. Severity can be estimated directly by the voltage or power loss compared to previous operation. As different overpotentials dominate at different current density regimes (cf. section 2.3), a distinction between activation, ohmic or mass transport overpotential increase contributing to performance loss can be derived.

Polarization curves can in principle be performed either in potentiostatic (voltage setpoint, monitoring current) or galvanostatic mode (current setpoint, monitoring voltage). In addition, a distinction is made between steady-state performed polarization curves, where each respective potential or current density within the polarization curve is held

for a certain time period to achieve stable values, and transient polarization curves with constant sweep rates.

3.1.4 OER activity

The catalytic activity of a catalyst corresponds to the rate at which a particular reaction takes place. The activity of a catalyst layers towards OER can be gained by applying potentials where the corresponding water splitting reaction (c.f. Eq. 2.19) takes place at the respective OER catalyst. The reversible equilibrium potential E^0 for the water splitting reaction is equal to 1.23 V_{RHE} [39]. In acidic environment, the activity towards OER for catalysts as Ru, Ir and Pt are commonly investigated at potentials between 1.3 and 2 V_{RHE} [145, 146]. The OER activity series in liquid acidic electrolytes is reported as $Ru > Ir > IrO_x > Pt$ [145, 146]. As the activity of Pt based catalysts towards OER is significantly lower as for Ir or IrO_x [145], the derived OER activity at potentials below 1.5 V should be a figure-of-merit to distinguish the presence of Ir or IrO_x in the investigated catalyst layer.
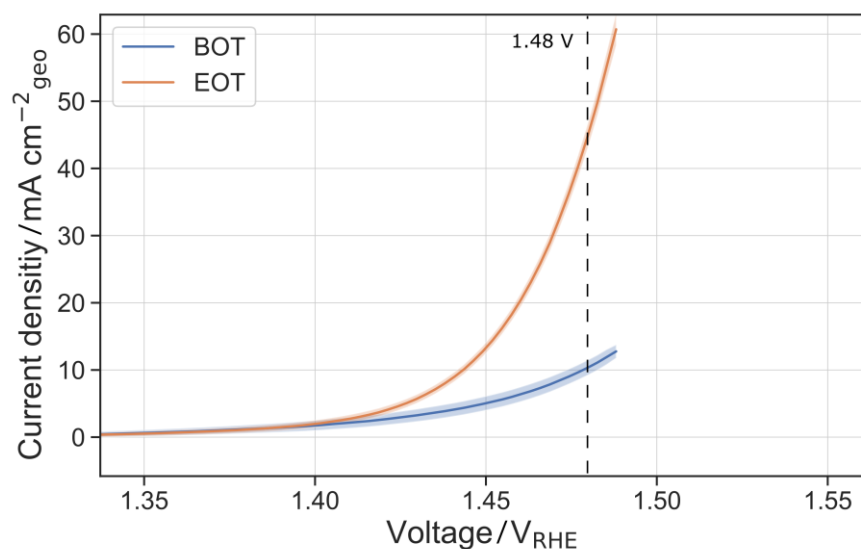
Figure 3.3: Oxygen evolution reaction polarization curves recorded from the anodic sweep of a cathode CV performed at 20 mV s^{-1} between 0.1 and 1.490 V, before (beginning-of-test, BOT) and after (end-of-test, EOT) the reversal tolerant MEA was exposed to a SUSD AST. The solid line corresponds to the mean values and the shaded area to the standard deviations of 9 subsequent CVs (shaded region EOT fully covered by solid line). The current density was corrected for the capacitive current density observed at 1.3V to achieve a comparable baseline for different measurements. Operating conditions: N$_2$/H$_2$ with a flow rate of 3.5/5 l$_n$ min^{-1} on cathode/anode, T=68° C; p=1 bar$_g$, RH=100%.

Typically, the catalytic activity is normalized either to the mass or the *ECSA* of the catalyst, to provide comparable parameters to results of differing materials or research groups [147]. However, in this thesis the derived catalytic activity of the cathode catalyst layer is investigated to evaluate the crossover of migrated OER catalyst from the

61

anode catalyst layer to the cathode. Therefore, neither the *ECSA* nor the OER catalyst loading on the cathode can be determined in this thesis, but the catalytic activity is normalized to the geometrical electrode area. In Figure 3.3 an exemplary OER polarization curve of a cathode is depicted, before (beginning-of-test, BOT) and after (EOT, end-of-test) an SUSD AST was performed with the MEA. The catalytic activity of the electrode is estimated from the current response at a defined potential (i.e. 1.48 V_{RHE}).

3.1.5 Electrochemical impedance spectroscopy

Electrochemical impedance spectroscopy (EIS) is a frequently used method in research for characterizing electrochemical systems. It is capable of resolving individual internal processes of electrochemical systems on the basis of different relaxation times and thus allowing their investigation. EIS can be considered as non-destructive in-situ method giving insights in physical processes within the investigated system.

For EIS, a sinusoidal perturbation signal (input signal) is applied while the corresponding system response to the perturbation (output signal) is measured. The system's response is observed at the same frequency but different amplitude and shifted phase. The impedance can be calculated from the relationship between the input and output signals. When a single frequency is examined, it is referred to as impedance analysis. Impedance spectroscopy analyzes the behavior over a range of frequencies. The applied perturbation signal can be either a current wave at galvanostatic or a potential wave at potentiostatic measurements. In fuel cell environment, galvanostatic EIS is commonly performed under normal operation (H_2/air) and under applied load, where the fuel cell acts as galvanic cell. In contrast, potentiostatic EIS is typically performed under N_2/H_2 supplied to the working/counter electrode.

In this thesis, potentiostatic EIS was used to determine the high frequency resistance overpotential η_{HFR}, which adds up the ohmic overpotentials $\eta_{membrane}$ and $\eta_{contact}$. In addition the effective proton resistance overpotential $\eta_{H^+,\,electrode}^{eff}$ of the catalyst layers can be derived from this measurement. Tracking the temporal evolution of overpotentials can be used to monitor the degradation of MEA components and to allow for overpotential distribution analysis.

HFR determination by EIS

In this thesis potentiostatic EIS measurements under N_2/H_2 atmosphere where performed to investigate the HFR and the proton resistances of the electrode. A typical Nyquist plot is shown in Figure 3.4.
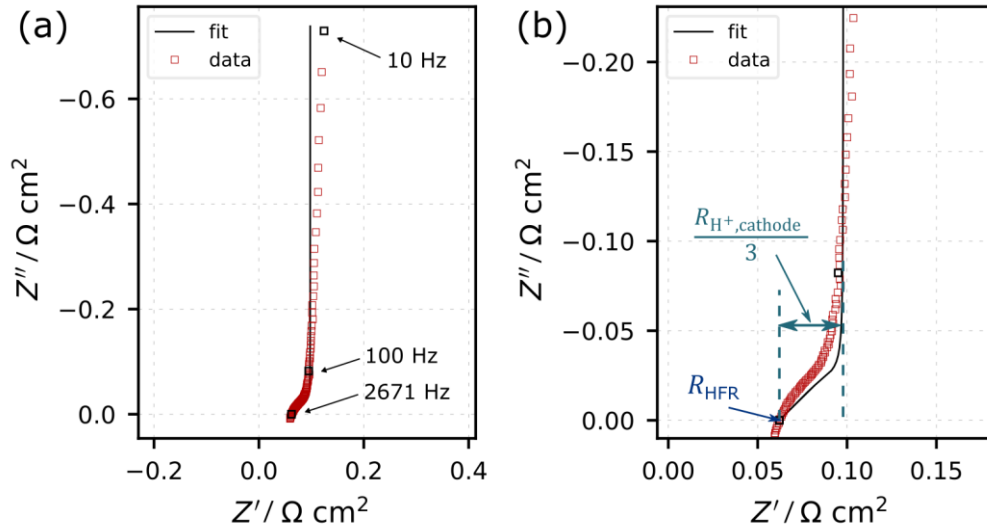
Figure 3.4: Exemplary Nyquist plot of an EIS measurement for a pristine MEA (i.e. MEA-2, cf. section 4.1). Measurement was performed with humidified N₂/H₂ (80% *RH*) at 30° C applying a flow rate of 10 lₙ min⁻¹ and pressures of 1 barₘ on the cathode and anode, respectively. Spectrum was recorded applying a 10 mV perturbation (100 kHz to 10 Hz) at 0.45 V_RHE. Experimental data are shown in red open squares, the corresponding fitting result of an equivalent circuit model (see Appendix-Figure 1) adopted from Makharia et al. [148] is shown as black solid line. Data were fitted using the python library developed by Murbach et al. [149]. (a) Full EIS spectrum with highlighted frequencies. (b) Enlarged section including R_HFR and graphical $R_{\text{H}^+,\text{cathode}}$ determination.

To determine the high frequency resistance R_HFR, the real axis intercept of the impedance is taken, where the imaginary impedance is equal to zero. R_HFR predominantly corresponds to the membrane resistance and the contact resistances along the electric pathways (flow fields, GDLs and catalyst layers interfaces). As the overpotentials for the membrane and contact resistances are showing ohmic behaviour, the overpotential η_HFR is dependent on the applied current density i and the corresponding resistance R_HFR (cf. Equation 3.12) .

$$\eta_\text{HFR} = \eta_\text{membrane} + \eta_\text{contact} = i \cdot R_\text{HFR} \qquad (3.12)$$

Proton resistance determination in the catalyst layer

By determining the effective proton conductivity in the electrodes, the voltage loss due to proton transport within the electrode can be derived. Due to the fast HOR kinetics, the platinum loading and thus the electrode thickness of the anode is significantly lower than that of the cathode. Therefore, the proton conducting pathways in the anode are comparatively short and the corresponding overpotential $\eta_{\text{H}^+,\text{anode}}^\text{eff}$ is typically neglected. In contrast, for MEA voltage loss analysis, the cathode effective proton conduction

overpotential $\eta_{\mathrm{H^+, cathode}}^{\mathrm{eff}}$ must be considered. Due to the ohmic dependence, the effective proton conduction overpotential can be calculated as follows:

$$\eta_{\mathrm{H^+, electrode}}^{\mathrm{eff}} = i \cdot R_{\mathrm{H^+, electrode}}^{\mathrm{eff}} = i \cdot \frac{R_{\mathrm{H^+, electrode}}}{3 + \zeta} \tag{3.13}$$

with the effective proton conduction resistance $R_{\mathrm{H^+, electrode}}^{\mathrm{eff}}$, the electrode sheet resistance $R_{\mathrm{H^+, electrode}}$ and the correction factor ζ, which is dependent on the applied current density i and the Tafel slope of the reaction (for a further explanation, the reader is referred to Neyerlin et al. [150]). In the first approach, ζ is set equal to zero assuming small potential gradients within the electrolyte phase.

The proton conduction resistance can be determined via potentiostatic EIS in N_2/H_2 atmosphere on the working and reference electrode, respectively. To evaluate $R_{\mathrm{H^+, electrode}}$, the EIS spectra can be fitted numerically, assuming an equivalent circuit model including a transmission line model, or a graphical estimation from the Nyquist plot can be performed, considering the length of the observed 45° line (see Figure 3.4b) [148]. For measurements performed on the anode catalyst layer, commonly no 45° line characteristics is observed due to the low proton resistance. The resulting Nyquist plot is showing a straight 90° line for frequencies lower than the frequency where the high frequency resistance is observed.

3.1.6 Hydrogen pump experiment

This section provides an overview of the so-called hydrogen pump experiments which are used for HOR overpotential distribution analysis. A schematical cell setup for the hydrogen pump experiment is depicted in Figure 3.5a.
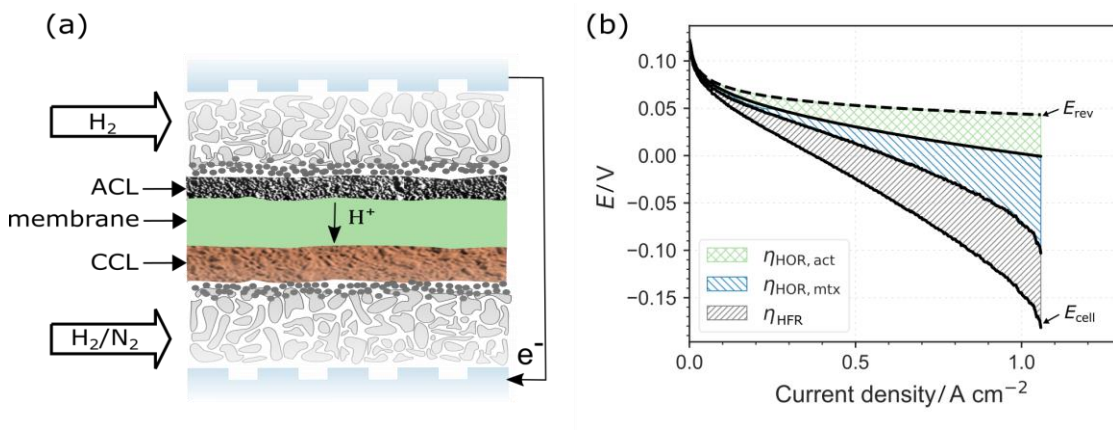

Figure 3.5: (a) Scheme of the hydrogen pump experiment on a single fuel cell. (b) Current density dependent cell voltage and calculated potentials during a hydrogen pump experiment with flowing H$_2$ on the anode and N$_2$ on the cathode, after the MEA underwent significant anode degradation due to a cell reversal AST (see section 1).

During the hydrogen pump experiment, hydrogen is supplied to the anode and nitrogen or hydrogen is supplied to the cathode. On the anode, hydrogen is oxidized during HOR (cf. Equation 3.14), whereas the migrating protons through the membrane are reduced to hydrogen on the cathode during hydrogen evolution reaction (HER, cf. Equation 3.15).

$$H_2 \rightarrow 2H^+ + 2e^- \tag{3.14}$$

$$2H^+ + 2e^- \rightarrow H_2 \tag{3.15}$$

Besides the applicability as diagnostic procedure for PEFCs, this procedure finds commercial application in fuel purification, where hydrogen can be extracted from a polluted/diluted feed gas stream and simultaneously compressed. In the context of PEFCs, hydrogen pump experiments are typically used to i) evaluate the HOR/HER exchange current density of different catalysts [95, 151] and ii) to investigate the anode's contribution to the fuel cell overpotential [35, 152]. The latter enables an in-depth analysis of anode degradation with respect to the application relevant HOR performance.

The cell voltage E_{cell} during the hydrogen pump experiment can be described as [95]:

$$E_{cell} = E_{rev} - \eta_{HFR} - \eta_{HER} - \eta_{HOR} - iR^{eff}_{H^+, anode} - iR^{eff}_{H^+, cathode} \tag{3.16}$$

According to the Nernst equation, E_{rev} during hydrogen pump is dependent on the H_2 partial pressures on the electrodes, the temperature and the equilibrium potential of the HOR/HER (cf. Equation 2.9). Therefore, E_{rev} can show a strong current dependency when pure nitrogen is flown on the cathode, as the partial pressure of hydrogen is dependent on the hydrogen evolution rate according to Faradays law. While this setup satisfies safety aspects of the fuel cell test station, the analysis becomes error prone due to the partial pressure dependency of hydrogen on the cathode. However, the supply of (N_2 diluted) hydrogen on the cathode has the advantage of negligible partial pressure dependency of hydrogen imposed by HER. Within typical fuel cell setups, where the cathode catalyst loading and thus the *ECSA* is significantly higher than on the anode, η_{HER} can be neglected [95, 152, 153]. Also $R^{eff}_{H^+, anode}$ is commonly neglected due to minor proton resistance within the anode catalyst layer. Furthermore, $R^{eff}_{H^+, cathode}$ was shown to be negligible as well during hydrogen pump experiments [95]. As the cathode loading is significantly higher, a substantial proton resistance within the cathode would result in the cathode current distribution shifting closer to the membrane at small overpotential increase, induced by the high catalyst loading and fast HER kinetics [148]. Thus, Equation 3.16 can be simplified to:

$$E_{cell} = E_{rev} - iR_{HFR} - \eta_{HOR}. \tag{3.17}$$

65

The HOR overpotential subsequently can be separated in kinetic and mass transport contributions [152].

$$E_{\text{cell}} = E_{\text{rev}} - iR_{\text{HFR}} - \eta_{\text{HOR,act}} - \eta_{\text{HOR,mtx}}. \tag{3.18}$$

R_{HFR} can be determined by the above presented EIS method. The kinetic overpotential can be derived from fitting the HOR overpotential within a mass transport free domain (i.e. at low current densities) based on a simplified Butler-Volmer approach (also cf. Equation 2.10):

$$i = i_0 \, L \, ECSA \, \left(e^{\frac{\beta F}{RT}\eta_{\text{HOR,act}}} - e^{-\frac{(1-\beta)F}{RT}\eta_{\text{HOR,act}}} \right) \tag{3.19}$$

with the symmetry factor β. Subsequently, the HOR overpotential distribution analysis can be performed. This analysis is illustrated in Figure 3.5b for an MEA with a severely degraded anode catalyst layer. The hydrogen pump polarization curve was recorded after a reversal AST at 30° C, 80% *RH* and $p = 1$ bar$_\text{g}$ was performed.

3.2 Ex-situ characterization methods

3.2.1 SEM/EDX

Scanning electron microscopy (SEM) MEA cross-section images were taken to evaluate the anode, cathode and membrane thickness of MEAs after an AST was performed. To investigate the element composition within catalyst layers and precipitated band formation in the membrane, Energy dispersive X-ray spectroscopy (EDX) was performed. Further information on these characterization methods can be found in standard textbooks [154].

4 Experimental

This chapter provides detailed information on the experimental methods and procedures applied in this thesis, from sample preparation over single cell testing up to ex-situ characterization methods. This chapter contains excerpts from an published article (Bentele et al. [40]). In particular, the accelerated stress test procedures developed within this thesis are introduced.

4.1 Materials and MEA fabrication

Within this work different MEAs were investigated to develop application-relevant stress tests in combination with special electrochemical characterization methods. This allows to derive further insights into the degradation of OER based reversal tolerant anodes.

A general lab-scale manufacturing scheme applied for MEAs investigated in this thesis is depicted in Figure 4.1, from catalyst ink mixing to single cell hot pressing.
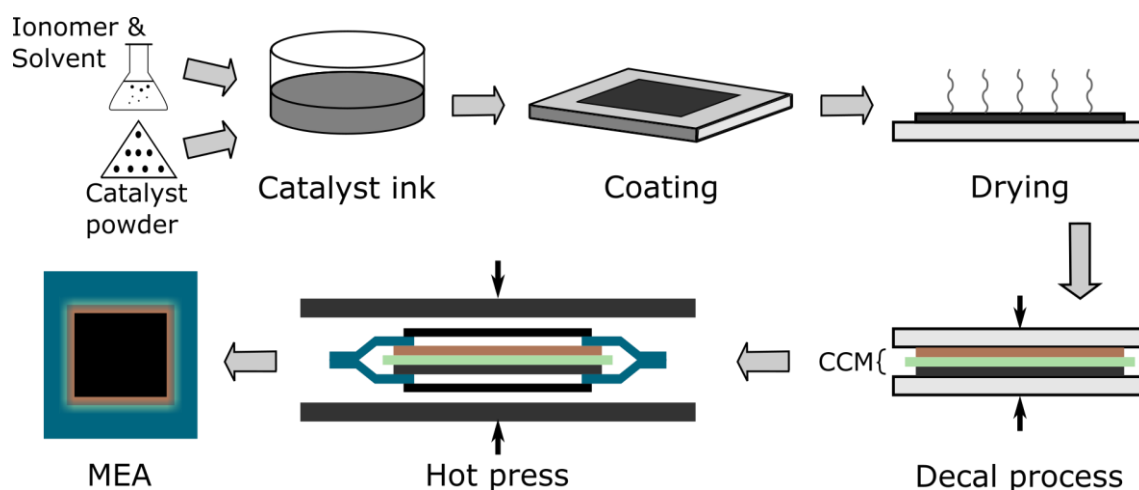
Figure 4.1: Lab-scale Manufacturing process from catalyst powder to PEFC single cell schematically depicted. Upper row (from left to right): catalyst layer manufacturing from ink to catalyst layer supported on a decal foil. Lower row (from right to left): CCM manufacturing via decal process and MEA manufacturing via hot pressing CCM, frame (blue) and GDLs (black) to final framed single cell MEA.

The most relevant information about the used MEAs is given in the following section. However, due to the cooperation with an industry partner, certain detailed process and material information cannot be publicly disclosed. As industrial processes of MEA

production were applied within this thesis, lab-scale based reproducibility would certainly be difficult.

The catalyst layers were manufactured by ink mixing of catalyst powder, solvent and ionomer. Subsequently, the ink was coated on a supporting decal foil. The catalyst layers were processed to a CCM via the decal transfer method. In a final step, the CCM was cut, framed and hot pressed with GDLs on anode and cathode, respectively.

An identical cathode catalyst layer (CCL) was used for all MEAs investigated within this thesis. CCLs were in-house fabricated incorporating commercially available Pt/C catalyst powder and ionomer binder. The platinum loading of the cathode electrodes was fixed to 250 μg_{Pt} $cm_{electrode}^{-2}$ with respect to the geometrical electrode area. The ink preparation and subsequent ink coating on a carrier foil were performed according to in-house developed procedures on industrial production lines. For the fabrication of anode catalyst layers, a comparable coating process was used. Reversal tolerant anodes were fabricated using an OER co-catalyst based on heat treated IrO_2 catalyst carried on a metallic support. Commercially available ionomer binder (equivalent weight < 900 g/mol) was used. Besides, different carbon supported platinum HOR catalysts were used, which were differing regarding the graphitization degree of their high surface area carbon support (graphitization degree HOR-1 $<$ HOR-2). The catalyst loading of Pt and IrO_2 was fixed to equal values of 50 $\mu g_{catalyst}$ $cm_{electrode}^{-2}$, respectively. The ionomer to carbon weight ratio (I/C) was set to be equal to one, except for the reference anode catalyst layer without an OER co-catalyst incorporated. For this reference MEA an anode I/C ratio equal to 0.8 was implemented, aiming for a comparable ionomer to catalyst/support surface ratio and resulting ionomer thin film thickness. The anode catalyst layer for MEA-3 was not fabricated in-house but received by a supplier as decal supported catalyst layer. As for the other anode catalyst layers, Pt/C and metal supported IrO_x catalysts were incorporated. Any further insights in catalysts (HOR-3/OER-2) and ionomer properties cannot be provided.

CCMs were manufactured via the decal transfer process by hot pressing anode and cathode catalyst layers, backed on decal foil, to a reinforced PFSA based membrane (membrane thickness: between 20 µm and 10 µm; high frequency resistance: ≈ 63 mΩ cm² at 30° C and 80% *RH*, cf. Figure 5.12). Hereinafter, the CCMs were cut to the required size and subsequently framed with a PEN foil. Afterwards, commercially available GDLs were hot-pressed (100° C, 30 s) to the framed CCMs.

An overview of the different MEA configurations investigated in this thesis is given in Table 4.1.

Table 4.1: Investigated MEA configurations

Property	Unit	MEA-1	MEA-2	MEA-3	MEA-Pt/IrO$_x$	MEA-Pt
				Designation		
Pt loading	[µg cm$_{electrode}^{-2}$]	50	50	*	50	50
IrO$_2$ loading	[µg cm$_{electrode}^{-2}$]	50	50	*	50	0
I/C ratio	[-]	1	1	*	1	0.8
HOR catalyst	[-]	HOR-1	HOR-2	HOR-3	HOR-2	HOR-2
HOR catalyst graphitization degree (Pt/C)	[-]	+	++	*	++	++
OER catalyst	[-]	OER-1	OER-1	OER-2	OER-1	-
GDL	[-]	GDL-1	GDL-1	GDL-2	GDL-2	GDL-2

* unknown or confidential properties; +: medium, ++: high

4.2 Single cell testing

4.2.1 Test station and cell setup

Single cell tests were performed on in-house developed differential single cell test stations. Cell cooling was realized using an ultra-pure water based liquid cooling loop, which allowed cell temperatures in the range of 30° to 90° C. To achieve the desired operating conditions, the supplied dry gases were humidified with ultra-pure water via a combination of mass flow meters (dry gas and water, respectively) and a humidifier. To prevent water from condensing, piping from humidifier to cell inlet was equipped with heat-tubes and heating tapes. The test stations were equipped with a combined electrical load/power supply, enabling normal operation as well as reversal operation of the cell. To ensure the targeted operating conditions, several sensors (e.g. temperature, pressure, humidity, current, voltage) on multiple locations were included within the test station.

Single cell tests were performed using in-house developed cell hardware with an active area < 50 cm², schematically depicted in Figure 4.2.
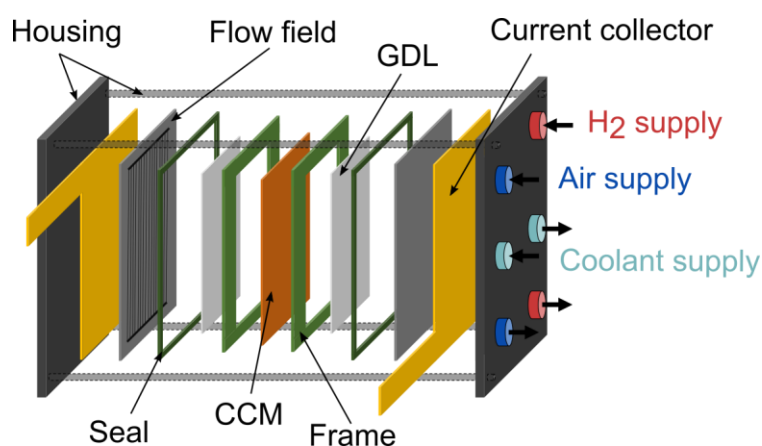
Figure 4.2: Exploded drawing of the cell hardware setup.

The framed MEAs were sandwiched between graphite-based flow fields with parallel gas channels in co-flow arrangement, including internal cooling channels. The metallic current collectors were attached to the flow fields. To prevent gas and coolant leakage, silicone-based seals were incorporated, and a physical leak test of the cell setup was performed prior to any test performed. The cell voltage was monitored by conducting the flow fields directly via sense cables, whereas the current was monitored via shunt measurement within the load cable next to the cathode current collector.

4.2.2 Polarization curves

Pristine MEAs were treated by an in-house developed conditioning procedure prior to each characterization. The fuel cell performance was evaluated at certain points during the test procedures via polarization curves under H_2 and (compressed) air. If not stated otherwise, a recovery procedure including an air- and H_2-soak (10 min each) has been performed prior to the performance evaluation. During the polarization curves, temperature was kept constant at 68 ° whereas pressures, *RH* and gas flow rates (H_2/air) were varied with current density according to Table 4.2.

The fuel cell was allowed to stabilize for 15 min for each current density, whereas data was averaged from the last 60 s. The first investigated current density within the polarization curve was allowed to stabilize for additional 30 min to ensure consistent and stable testing conditions and MEA humidification. If a cell voltage smaller than 0.1 V was observed (e.g. due to severe degradation), the measurement was aborted for the investigated current density as well as for possible subsequent higher current densities.

Table 4.2: Current density dependent operating conditions for polarization curves performed at 68° C

Operating conditions during PEFC performance evaluation at 68° C							
Current density [A cm^{-2}]	0	0.1	0.6	1.0	1.5	2.1	2.4
Pressure anode [bar$_g$]	0.25	0.25	0.6	0.9	1.27	1.7	1.9
Pressure cathode [bar$_g$]	0.07	0.07	0.3	0.59	0.92	1.31	1.5
RH anode [%]	79	79	75	80	85	94	97
RH cathode [%]	52	52	70	69	67	70	71
Anode flow rate [l$_n$ min^{-1}]	0.7	0.7	1.7	2.8	4.3	6.0	6.8
Cathode flow rate [l$_n$ min^{-1}]	1.3	1.3	4.1	6.8	10.2	14.3	16.4

4.2.3 Cyclic voltammetry

Cyclic voltammograms (CVs) were acquired using a *IM6* potentiostat/galvanostat (*Zahner-Elektrik Ingeborg Zahner-Schiller GmbH & Co. KG*, Germany).

If not stated otherwise, CVs were performed at 100% *RH*, 1 bar$_g$ and flow rates of 1 l$_n$ min^{-1} on working (i.e. PEFC cathode for cathode CV) and reference (i.e. anode) electrode, respectively. Cell temperature was set to 60° or 68° C. CVs were recorded block wise for each electrode: i.e. first CO stripping, H$_{upd}$ measurements, H$_2$ crossover and OER performance on the cathode were performed, followed by the corresponding measurements on the anode. Prior to performing CVs, a pre-conditioning was performed at the corresponding CV's temperature and *RH*. For CVs recorded within section 1, MEAs were conditioned by supplying H$_2$/air (reference/working electrode) for 15 minutes at 0.6 V, followed by purging the working electrode with nitrogen for additional 15 minutes. Prior to CVs performed within chapter 6, H$_2$/N$_2$ (reference/working electrode) was supplied for $\geq$ 30 min to allow the MEA to equilibrate. All potentials for CVs are reported with respect to the reversible hydrogen electrode (RHE).

ECSA determination via H$_{upd}$

To evaluate the *ECSA* via H$_{upd}$ the working electrode (i.e. PEFC anode for anode CV) was flushed with N$_2$ whereas the counter/reference electrode (i.e. PEFC cathode for anode CV) was flushed with H$_2$. Flow rates of 1 l$_n$ min^{-1} at 1 bar$_g$ and 100% *RH* were achieved during the CVs for both electrodes. The working electrode was cleaned by four CVs scanned between 0.1 and 1.2 V$_{RHE}$ at 100 mV s^{-1}. Subsequently, four CVs with a potential range from 0.065 to 0.865 V$_{RHE}$ at 100 mV s^{-1} were performed to evaluate the *ECSA* via H$_{upd}$. The hydrogen de- and adsorption charges between 0.1 and 0.4 V$_{RHE}$ were averaged from the 4th CV cycle after correction for the capacitive charge. A conversion factor of 210 μC cm^{-2} was assumed.

Double layer capacitance determination

Double layer capacitance C_{dl} was evaluated from the CV set used for *ECSA* estimation via H_{upd} (potential range of 0.065 to 0.865 V_{RHE}, 100mV s^{-1} scan rate). The capacitive charge was evaluated from the 4th CV cycle at a potential of 0.45 V_{RHE}.

ECSA determination via CO stripping

CO stripping CVs were performed under H_2/N_2 (reference/working electrode) atmosphere at 68° C at 100% *RH* and 1 bar$_g$ on each electrode. To evaluate the cathode *ECSA*, flow rates of 3.5/5 l$_n$ min^{-1} (anode/cathode) were realized, whereas anode CO stripping was performed at flow rates of 1/1 l$_n$ min^{-1} (anode/cathode). These operating conditions were implemented for all substeps within the respective procedure. Prior to the CO stripping CV, two cleaning CVs were performed between 0.1 and 1.2 V_{RHE} at a scan rate of 20 mV s^{-1}, to achieve reproducible results and remove possible contaminants present on the catalyst surface. Subsequently, the working electrode was supplied with 1% CO in N_2 on the working electrode for 3 minutes at a potential of 0.1 V_{RHE} while maintaining the above stated flow rates. To remove CO from the flow field channels, the working electrode was flushed for 5 min with pure N_2 afterwards. Finally, CO stripping measurements were performed by measuring two CVs at a potential range from 0.1 to 1.2 V_{RHE} and a scan rate of 20 mV s^{-1}. *ECSA* was calculated by integrating the CO desorption charge, taking the second CV performed as baseline for integration and assuming 420 µC cm^{-2} as conversion factor.

Preceding any further measurements (e.g. CVs or polarization curves), an additional purging procedure was implemented to ensure the removal of any residual CO from the test station piping.

4.2.4 Hydrogen crossover

Hydrogen crossover measurements were performed with a *IM6* potentiostat/galvanostat (*Zahner-Elektrik Ingeborg Zahner-Schiller GmbH & Co. KG*, Germany) directly after recording the cathode H_{upd} CVs. Therefore, no additional cleaning procedure was implemented. Hydrogen crossover measurements were recorded by performing a single CV with a potential range from 0.065 to 0.865 V_{RHE} at 2 mV s^{-1}. Operating conditions were the same as during the cathode H_{upd} CVs. (H_2/N_2 on anode/cathode at flow rates of 1 l$_n$ min^{-1}, 100% *RH* and 1 bar$_g$). The hydrogen crossover current density was determined by performing a linear regression for the up and down sweep of the CV between 0.35 and 0.6 V_{RHE}.

4.2.5 OER activity

The OER activity was acquired by a *IM6* potentiostat/galvanostat (*Zahner-Elektrik Ingeborg Zahner-Schiller GmbH & Co. KG*, Germany) via cyclic voltammetry. Preceding the measurement, the already equilibrated MEA was flushed with H_2/N_2 (reference/working electrode) for 3 min. The same operating conditions as for the CO stripping measurements were chosen: 68° C, 100% *RH* and 1 bar$_g$ for each electrode. Flow rates of 3.5/5 l_n min^{-1} (anode/cathode) were applied to evaluate cathode OER activity, whereas flow rates of 1/1 l_n min^{-1} (anode/cathode) were applied to investigate anode OER activity. Ten contiguous CVs, each ranging from 0.1 to 1.49 V_{RHE}, were performed at a scan rate of 20 mV s^{-1}. If the upper current limit (3 A) of the potentiostat/galvanostat was exceeded within the chosen potential range, the CV was interrupted, and the CVs were repeated with a decreased upper potential automatically. The first CV performed was considered as a cleaning CV, ensuring a clean catalyst surface and reproducible results. The OER activity was determined from the anodic scans of the subsequent nine CVs at a potential of 1.48 V_{RHE}. To achieve comparable results, the current densities were corrected for the predominantly capacitive charges observed at a potential of 1.3 V_{RHE}.

It should be noted that the reported current densities should be regarded as first approximation of the OER activity of the electrode, rather than the exact OER activity. As the investigated electrodes in this thesis contain Pt/C catalysts (for HOR or ORR) beside OER catalysts, it must be assumed that the measured current density is not solely corresponding to the OER activity of the OER catalyst. It is highly likely that the current density measured is superimposed by the OER activity of platinum as well as by the oxidation of carbon to a certain extend. This applies in particular for cathode catalyst layers, where no OER catalyst was introduced during manufacturing and only traces of migrated OER catalyst should be present. To distinguish the order of magnitude of superimposed currents caused by Pt/C catalysts, an MEA without an incorporated OER co-catalyst on the anode was investigated.

4.2.6 Electrochemical impedance spectroscopy

Electrochemical impedance spectroscopy was performed using a potentiostat/galvanostat (*IM6, Zahner-Elektrik Ingeborg Zahner-Schiller GmbH & Co. KG*, Germany). EIS was performed while supplying the cell with H_2/N_2 (reference/working electrode), keeping cell voltage at 0.45 V_{RHE} and applying a 10 mV perturbation for frequencies ranging from 100 kHz to 10 Hz.

Operating conditions and pretreatment were dependent on the respective purpose and implementation. EIS measurement was included in a standard characterization block, including H_{upd} CVs and hydrogen crossover measurements. Therefore, the operating

conditions were identical to the latter (100% RH, 1 bar$_g$, flow rates of 1 l$_n$ min^{-1}) and no additional conditioning was performed. In addition, EIS was used to evaluate HOR overpotential distribution. Thus, the same operating conditions as during subsequent hydrogen pump experiments were applied to evaluate the HFR and proton resistance of the CCL at these operating conditions. In advance, for these tests a pre-conditioning phase was applied. For section 5 this pre-conditioning included a recovery step (air- and H$_2$-soak, 10 min each), normal operation (H$_2$/air, anode/cathode) at a cell voltage of 0.6 V for 10 min and finally a H$_2$/N$_2$ (anode/cathode) purge for 10 min. For section 6 at each investigated temperature an initial recovery step was performed, including three SUSD cycles, 1 h normal operation at 0.6 V (H$_2$/air) and a H$_2$/N$_2$ (anode/cathode) purge for 1 h. Prior to EIS measurements performed at the same temperature but a lower RH, solely a H$_2$/N$_2$ (anode/cathode) purge for 1 h was performed.

4.2.7 Hydrogen pump experiments

Hydrogen pump measurements in the context of reversal ASTs (section 1)

To quantify and investigate the anode ageing due to repetitive, short-term reversal events, HOR overpotential distribution analysis via hydrogen pump measurements was performed at comparable operating conditions as during the applied reversal AST. Thus, anode and cathode were constantly flushed at 30° C cell temperature, applying humidified gases (80% RH) and pressures of 1 barg, respectively. To enable high limiting current densities, the gas flow rates of N$_2$ (cathode) and H$_2$ (anode) were increased to 10 l$_n$ min^{-1} with respect to the reversal AST. Polarization curves were performed between 0 and 3.75 A cm^{-2} with a sweep rate of 2.5 mA cm^{-2} s^{-1}. The measurement was stopped if the cell voltage reached -0.8 V to prevent the MEA and cell hardware from severe damage. This setup, with no active H$_2$ flow on the cathode, was chosen to enable hydrogen pump measurements without having to adapt the test station piping (e.g. linking anode outlet to the cathode inlet) according to safety regulations. The measurements were performed subsequent to the corresponding EIS measurements (preceding recovery included, see above). Therefore, no additional conditioning was applied prior to the hydrogen pump polarization curves.

To account for the change in equilibrium potential E_{rev} due to a transient hydrogen partial pressure on the cathode, E_{rev} was calculated by the Nernst equation (cf. Equation 2.9). The partial pressure change on the cathode was calculated by the evolving hydrogen due to faradic current. The impact of hydrogen crossover via diffusion was not considered.

The overpotential distribution analysis was determined by applying Equation 3.18, considering the corresponding EIS results (R_{HFR}) and the calculation of E_{rev}. Subse-

quently, the activation overpotential $\eta_{\mathrm{HOR,act}}$ was derived by a non-linear least squares fit to a simplified Butler-Volmer approach (cf. Equation 3.19).

Hydrogen pump measurements in the context of SUSD ASTs (section 6)

To further improve the resolution and accuracy of the HOR overpotential distribution analysis in section 6, the above-described hydrogen pump procedure was adapted. Due to hardware adjustments on the test station, the dilution of hydrogen with nitrogen was implemented as well as implementing the possible flow of (diluted) hydrogen on the reference electrode (cathode). Dilute hydrogen allows a more sophisticated resolution of H_2 mass transport resistance increase at small total HOR overpotentials [35], which in particular is important for decreased anode degradation during SUSD events compared to reversal events. The possibility of flushing the reference electrode (cathode) during the experiment with an identical (diluted) hydrogen gas flow was expected to increase accuracy of the experiment. As for the differential single cell setup, high stoichiometries are implemented. The partial pressures on anode and cathode consequently are facing only small gradients due to hydrogen crossover induced by faradic current and thus can be regarded as constant. Consequently, $E_{\mathrm{rev}} \approx 0$ can be assumed, which simplifies Equation 3.18.

To investigate the HOR overpotential, hydrogen pump measurements were performed at various temperatures, H_2 concentrations and relative humidity. The investigated conditions are shown in Table 4.3.

Table 4.3: Investigated operating conditions for hydrogen pump measurements

H₂ pump operating conditions		
Temperature [° C]	***RH* [%]**	**H₂ concentrations (dry gas) [vol. %]**
35	100, 75	100, 50, 30, 10, 5
70	100, 75, 50, 35	100, 50, 30, 10, 5
86	90, 75, 50, 30	100, 50, 30, 10, 5

For all investigated operating conditions, pressures of 2 bar$_g$ and total dry gas flow rates of 10 l$_n$ min^{-1} were applied on anode and cathode, respectively.[2] To achieve the aimed hydrogen concentrations, dry hydrogen was diluted with the corresponding gas flow rate of dry nitrogen. Subsequently, the dry gas flow was humidified.

---

[2] For 100% H_2 the gas flow rate on the cathode was limited to 5 l$_n$ min^{-1} due to mass flow controller limitations. But due to the still achieved high stoichiometry for this flow rate (> 4.5 at 3.75 A cm^{-2}) and the flow-independent hydrogen partial pressure at the cell inlet, a change in E_{rev} can be regarded as negligible.

Temperatures were investigated in ascending order (35 to 86° C). *RH* was kept stable while varying the respective H$_2$ concentrations. *RH* and H$_2$ concentration were investigated in descending order, respectively (i.e. first 100% *RH* at 30° C for 100, 50, 30, 10 and 5% H$_2$ was investigated, followed by 75% *RH* at 30° C for 100, 50, 30, 10 and 5% H$_2$). For each temperature a pre-conditioning step was performed. After heating the cell to the specific temperature, three SUSDs were performed to clean and recover the catalyst surface. Then the MEA was conditioned under normal operation (H$_2$/air, 100% *RH*) at 0.6 V for 1h. Subsequently, EIS was performed at each investigated *RH* (and temperature) to determine the corresponding R_{HFR}. Prior to each EIS, the MEA was equilibrated for 1 h under H$_2$/N$_2$ (anode/cathode) and two SUSD cycles were performed as recovery procedure. Subsequently, the hydrogen pump polarization curves at the respective temperature and *RH* were recorded with descending H$_2$ concentration.

Prior to each polarization curve, the MEA was flushed with (diluted) H$_2$/H$_2$ at the corresponding temperature, *RH* and H$_2$ concentration for 5 min. Polarization curves were recorded between 0 and 3.75 A cm^{-2} with a sweep rate of 10 mA cm^{-2} s^{-1}. The polarization curve was aborted if the voltage fell below −0.6 V or a stoichiometry of ≤ 2 was achieved, to prevent MEA and cell hardware damage.

Overpotential distribution analysis was performed by applying Equation 3.18, considering the corresponding EIS results (R_{HFR}) and assuming $E_{\mathrm{rev}} = 0$. The activation overpotential $\eta_{\mathrm{HOR,act}}$ was derived by a non-linear least squares fit to a simplified Butler-Volmer approach (cf. Equation 3.19).

4.2.8 Reversal ASTs

For durability estimations and investigations of certain degradation phenomena, so-called accelerated stress tests (ASTs) for differential cells have been established within fuel cell research and development [155, 156]. On the one hand, by applying only a certain degradation stressor intensively within the AST (commonly aiming for solely stressing a specific MEA component), the degradation phenomena and its impact can be investigated more isolated as during lifetime testing. The latter can suffer from significantly increased complexity, e.g. by increased gradients on higher integration levels (e.g. stack) or mutually influencing stressors (e.g. transients imposed by system components). Simultaneously, the reduced test complexity of ASTs on differential cells often is concomitant with simplifying and improving test comparability. On the other hand, ASTs enable a fast and efficient material and degradation evaluation due to low material and testing costs (e.g. small active area in differential cells resulting in low media and energy consumption).

Within this thesis two different accelerated stress tests for reversal events were investigated. A state-of-the-art accelerated stress test, applying a prolonged reversal event at

constant current until cell voltage falls below a certain threshold, is referred to as non-cyclic reversal (NCR) AST. For the NCR AST investigations, a constant current of 0.62 A cm^{-2} is drawn under H$_2$/air condition. Subsequently, the hydrogen supply on the anode is switched to N$_2$, resulting in fuel starvation conditions (N$_2$/air on anode/cathode). This reversal state was kept until the cell voltage reached a threshold of −1.5 V. The performed test scheme and resulting cell voltage is depicted in Figure 4.3a and b. Comparable ASTs are reported in literature to investigate the reversal tolerance of OER co-catalyst based reversal tolerant MEAs [37, 39, 100, 103, 106, 118, 128].
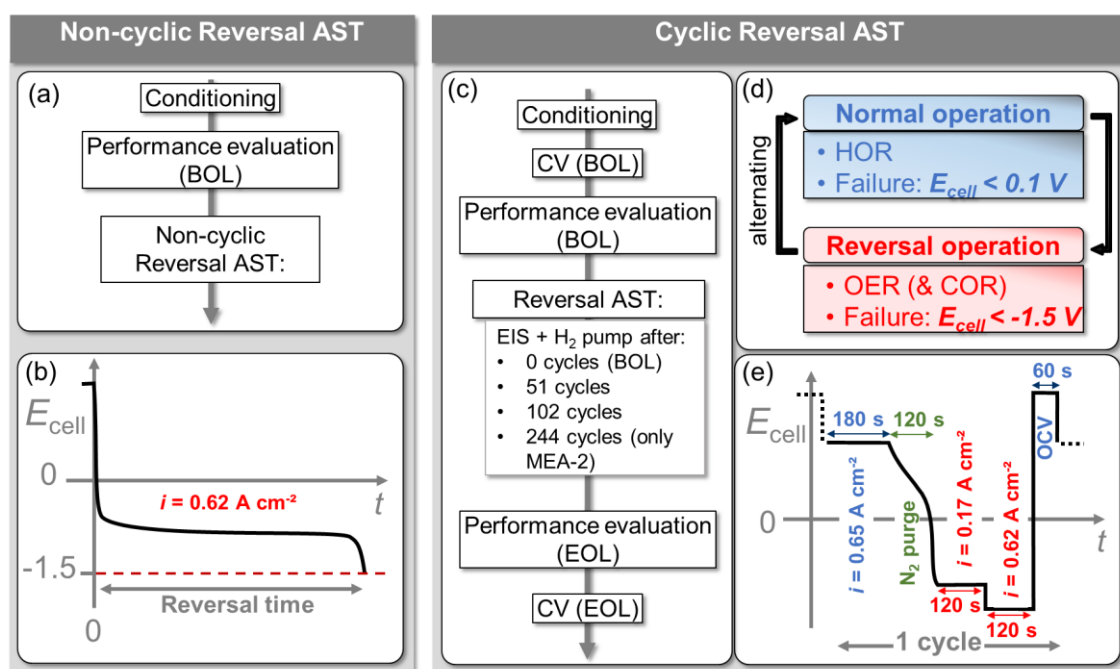
Figure 4.3: Test procedures for non-cyclic reversal (NCR) AST and cyclic reversal (CR) AST. (a) Schematic MEA testing procedure for NCR AST. (b) Schematic cell voltage profile for NCR AST due to a prolonged reversal event. (c) Schematic MEA testing procedure for CR AST. (d) Schematic representation of cycled operation during CR AST including ACL reactions and failure criteria defined for each operation. (e) Schematic CR AST cell voltage profile within one CR AST cycle, alternating normal and cell reversal operation.

In this work, a cyclic reversal (CR) AST was developed, alternating normal and reversal operation (cf. Figure 4.3d). ASTs with short-term reversal events are mimicking field operation more realistic, but are rarely described in literature [114, 120, 157]. Normal operation, N$_2$-purge, reversal operation (two current densities) and open circuit voltage were cycled within CR AST (cf. Figure 4.3e) until a failure criterion was met. For normal operation the failure criterion was set to cell voltages < 0.1 V, whereas cell voltages < −1.5 V were chosen as failure criterion during reversal operation. Normal operation (180 s) was implemented by flowing H$_2$/air (anode/cathode) and drawing a current of 0.65 A cm^{-2}. During the subsequent N$_2$-purge the cell was flushed with N$_2$/air for 120 s while no current was drawn. Reversal operation was performed at 0.17 and 0.62 A cm^{-2}

for 120 s respectively, while supplying N_2/air. OCV was held for 60 s while switching back to H_2/air supply.

Both ASTs were performed at the following operating conditions: 30 °C, 80/80% *RH*, 5/12 l_n min^{-1} gas flow and pressures of 1.7/1.5 bar$_g$ on the anode and cathode, respectively.

The testing conditions were chosen to simulate degradation due to cell reversal events in the context of the automotive startup-phase, where fuel starvation events can occur due to blockage either by icing (during freeze start-ups) or (residual) liquid water at temperatures close to ambient temperatures. The chosen temperature of 30° C simulates both cases satisfactorily. During a fuel starvation event caused by icing, stack temperatures of 30° C can be achieved before the ice blockage is removed by heat input (coolant loop or waste heat). At higher temperatures icing and consequently blockage of the flow field channels within the stack becomes highly unlikely, whereas at lower temperatures (<20° C) anode degradation is significantly decelerated by sluggish carbon corrosion rates [118]. In addition, lower temperatures (<20° C) would require a more complex test setup due to the test station requirements (e.g. cooling loop). Besides simulating fuel starvation events due to icing, the blockage of flow field channels by residual liquid water during a regular start-up is also possible at the chosen temperature of 30° C. Residual water could condense during cooling down in idle mode and could subsequently cause blockage. However, at elevated stack temperatures after start-up, residual liquid water becomes unlikely due to an increasing dew point.

Within this study, reversal tolerance is referring to the amount of applied time or cycles in reversal mode before a failure criterion was met for the respective MEA. However, when comparing both performed reversal ASTs among each other, it should be noted that within CR AST two reversal current densities were investigated within each cycle, whereas for the prolonged reversal events during NCR AST only the higher current density (0.62 A cm^{-2}) was drawn.

To further analyze the failure observed during CR AST, additional characterization methods as CVs, EIS and hydrogen pump experiments were performed. The overall test schemes for both reversal ASTs are depicted in Figure 4.3a/c.

Within this work, no repeating measurements for the investigated MEA designs were shown. However, during intensified testing of various MEA and ACL designs, a sample-to-sample variation of $\leq 4\%$ regarding reversal tolerance was found for CR AST. The high reproducibility is also dependent on MEA processing. All investigated MEAs were produced using an industrialized production line and industrial processing, leading to highly reproducible MEAs.

4.2.9 SUSD ASTs

Within this thesis, two SUSD ASTs were developed to investigate the anode ageing during transient conditions for reversal tolerant anode concepts based on a OER co-catalyst. The main purpose was the development of a time- and cost-effective AST on single cell level to simulate anode aging and investigate the occurring anode degradation and imposed degradation effects on other MEA components.

The performed ASTs were embedded in a series of procedures to further characterize the achieved degradation and ensure reproducible results. The corresponding overall test procedure is depicted in Figure 4.4a.
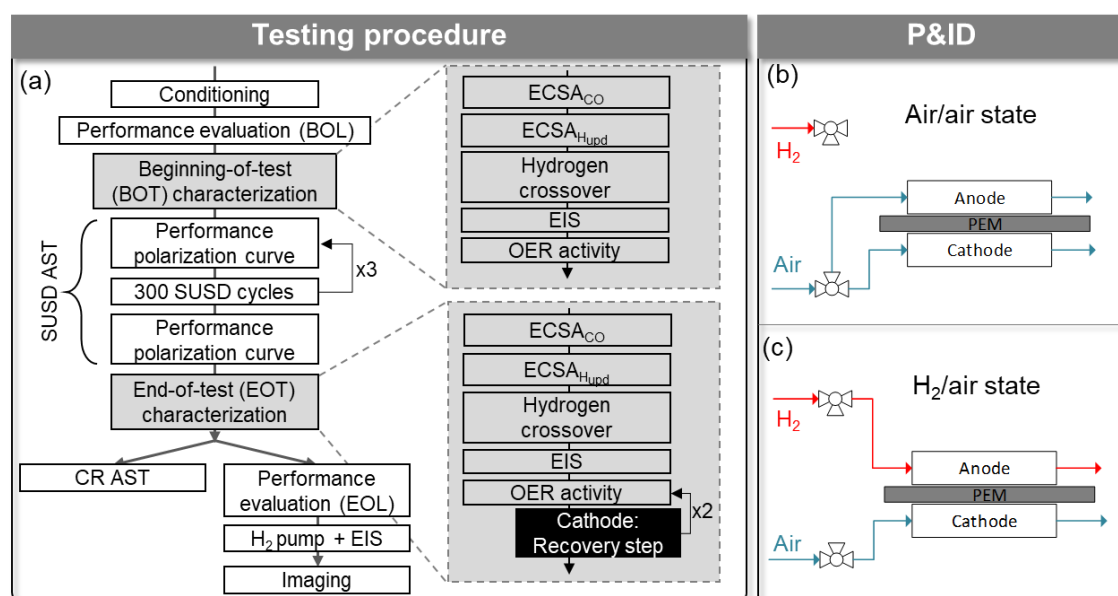
Figure 4.4: (a) Test flow chart for the SUSD AST investigations. Two SUSD AST variations were investigated. After EOT characterization either CR AST or performance evaluation/H₂ pump/imaging was performed with the respective MEA. End-of-test (EOT) the OER activity on the cathode was evaluated two additional times after performing a recovery procedure (black box). (b)-(c) Simplified piping and instrumentation diagram for the anode gas switch. Arrows indicate active gas flow of hydrogen (red) and air (blue).

First the MEA was conditioned. Afterwards, normal operation polarization curves (H₂/air) were recorded to evaluate the PEFC performance. A characterization procedure was performed to investigate the properties of the MEA and its subcomponents. This characterization procedure included: *ECSA* determination via H_{upd} and CO stripping method, hydrogen crossover measurement, EIS and OER activity determination. First the cathode was analyzed followed by the corresponding anode characterizations. All steps within the characterization procedure were performed at $68°\,C$, 100% *RH* and $1\,bar_g$ (for further information see corresponding sections above).

To simulate anode ageing via the developed AST, 1200 SUSD cycles were performed, switching the anode gas supply from air to H₂ (SU) and vice versa (SD). During SUSD

events cell temperature was set to 35 °C while fully humidifying the supplied gases (100/100% *RH*) and applying pressures of 1.42/1.05 bar$_g$ and flow rates 5.87/14 l$_n$ min^{-1} (anode/cathode). The anode gas supply was switched every 30 s. The corresponding, simplified piping and instrumentation diagram of the test station during SUSD states is depicted in Figure 4.4b-c. The PEFC performance at 68° C was evaluated initially (beginning-of-test, BOT) as well as recurrently after 300 consecutive SUSD cycles (cf. Figure 4.4a) via a H$_2$/air polarization curve (operating conditions see Table 4.1). Transition between SUSD operating conditions (at 35° C) and performance evaluation (68° C) was implemented by applying a N$_2$/N$_2$ purge. To reveal any possible reversible performance impact, no recovery procedure was performed prior to each performance evaluation.

The above-described characterization procedure was repeated End-of-test (EOT). Deviating from the initial procedure, EOT the OER activity for the cathode was additionally evaluated twice subsequent to a recovery procedure (cf. Figure 4.4a). As recovery step, normal operation under H$_2$/air for 1.5 h was performed, applying a current density of 1.5 A cm^{-2} and the corresponding operating conditions according to Table 4.1. Deviating from Table 4.1, the first hour was performed at 100% *RH* on both electrodes to facilitate washout of volatile species (e.g. cations). After finishing the EOT characterization procedure, either CR AST (cf. section 4.2.8) was performed to analyze the impact of anode aging on reversal tolerance or the end-of-life (EOL) performance was evaluated via additional polarization curves and H$_2$ pump experiments (cf. section 4.2.7). After the latter, imaging via SEM and TEM was performed to validate the expected degradation indicated by in-situ results.

Two varying SUSD ASTs were developed within this thesis, depicted in Figure 4.5. Due to the realistic simulation of the electrochemical processes appearing during field operation, a H$_2$-Air front based SUSD AST was preferred over a voltage cycling AST. However, the main intention was to suppress H$_2$-Air front induced cathode degradation to better resolve anode degradation and subsequent degradation effects on other MEA components. Thus, high gas flow rates aiming for a very short residence time (≈ 0.014 s, estimated via the equation provided by Schwämmlein et al. [35]) were implemented. In addition, cell temperature was set to 35° C to minimize the impact of carbon corrosion while still maintaining an automotive relevant operating window for start-up events at mediocre to elevated ambient temperatures. Both SUSD ASTs were performed at identical operating conditions (see above), differing solely in the application of an external load bank. For the AST referred to as SUSD-pot, the cell voltage during the AST was kept ≤ 0.5 V via potentiostatic controlled load mode. In this mode, the load bank is drawing a corresponding current to achieve 0.5 V, if the cell voltage would exceed the voltage setpoint in OCV condition. However, if the voltage is lower as the setpoint, no current is drawn. Both, during H$_2$/air as well as during air/air state, potentiostatic mode was maintained to avoid cell voltages > 0.5 V, arising from a time delay between

switching the supplied gas at the corresponding valve and the time when the H_2-Air front passes the flow field. The cell voltage and the expected corresponding half-cell potentials for the SUSD-pot are depicted in Figure 4.5a-b. The half-cell potentials were taken from literature values [35, 131, 158].

Cell voltage during SUSD-pot AST is cycling between ≈ 0 V (air/air state) and ≈ 0.5 V (H_2/air state). Voltage clipping via potentiostatic mode was shown to decrease cathode potential during SUSD, resulting in decreased cathode degradation [159]. Furthermore, drawing load under H_2/air atmosphere for 30s might impact crossover of anode co-catalyst species to the cathode (cationic migration proportional to the transferred charge in the electric circuit) or the redeposition of crossed-over species (by varying cathode potentials) [70].
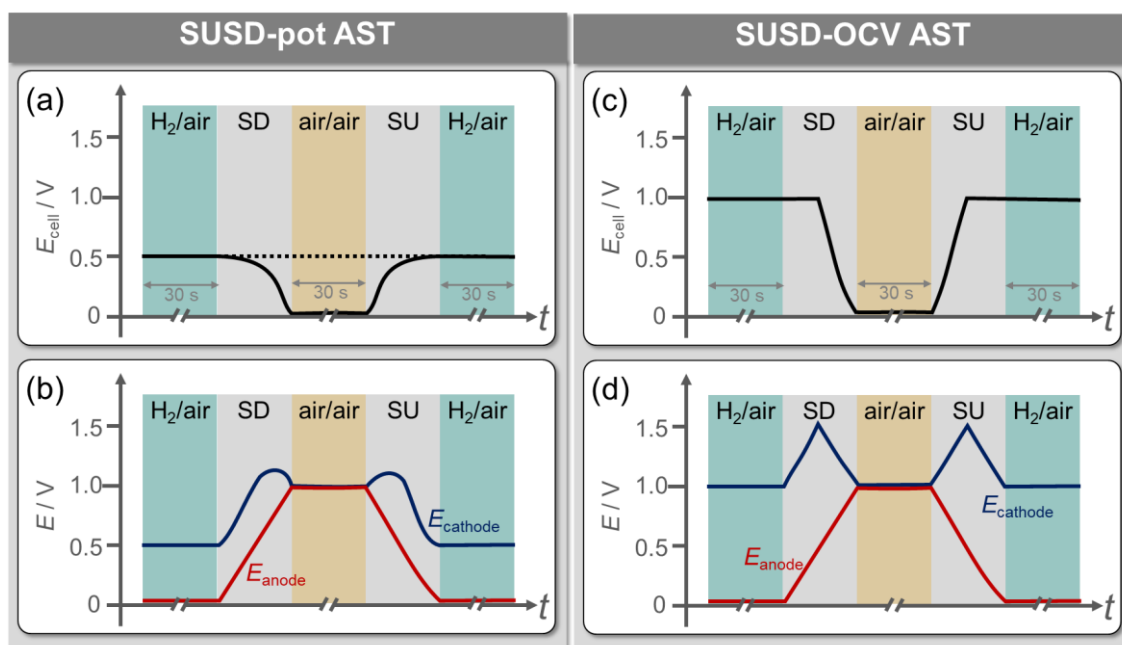
Figure 4.5: Schematic presentation of time dependent (half-)cell potentials during a SUSD cycle within the investigated SUSD ASTs. All voltages should be considered as hypothetic guiderails rather than exact values, representing averaged voltages across the whole electrode area. Left column: SUSD-pot AST. Right column: SUSD-OCV AST. (a)/(c) Cell voltage (black) during the corresponding SUSD steps. The dashed line is indicating potential limitation to ≤ 0.5V. (b)/(d) Corresponding anode (red) and cathode (blue) potential during the SUSD steps. Half-cell potentials based on literature values [35, 131, 132, 158].

The second AST is referred to as SUSD-OCV, as no load is drawn and the cell is kept at OCV condition during the gas switching. The cell voltage and the expected corresponding half-cell potentials during SUSD-OCV AST are depicted in Figure 4.5c-d. Cell voltage during this AST is cycling between ≈ 0 V and ≈ 1 V (cf. Figure 4.5c). However, as the transient anode potential from ≈ 0 to ≈ 1 V_{RHE} during SUSD is induced by the gas switch between H_2 and air, the predominant stressor for the anode catalyst layer should be similar for both developed SUSD ASTs.

4.3 Ex-Situ characterization methods

4.3.1 SEM/EDX

Scanning electron microscopy (SEM) images were taken on a *SU8030* (*Hitachi*, Japan), investigating MEA cross-sections. From each investigated MEA six different cross-section samples were manufactured, distributed over the entire active area. Per cross-section sample 5 SEM images were recorded, providing a 125 µm field-of-view. Therefore, for each MEA 30 SEM images were recorded to assure reliable results. Layer thickness of respective CCM components were evaluated using *ImagePro 7* (*Media Cybernetics Inc.*, USA) software, executing 100 individual thickness measurements for each SEM image.

Elemental identification by Energy dispersive X-ray (EDX) spectra was performed using attached *Xflash* and *QUANTAX FlatQUAD* (*Bruker Corp.*, USA) detectors. Per spectrum 1 million counts were recorded at an accelerating voltage of 5 kV, providing a penetration depth of ≈ 100 nm. EDX spectra were evaluated using *Espirit 1.9* (*Bruker Corp.*, USA) software. A coating correction for carbon has been performed to improve the EDX analysis with respect to additional carbon originating from the sample preparation process.

5 Reversal tolerance of OER based PEFC anodes

In this chapter the reversal tolerance of PEFC anodes containing an OER co-catalyst is investigated and discussed. Different accelerated stress tests and the impact of the incorporated HOR catalyst are discussed. In addition, in-situ characterization methods are presented to further investigate the failure modes of MEAs due to short-term reversal events.[3]

To achieve competitiveness among other technologies such as internal combustion engines and battery powered electric motors, durability is a key lever for PEFC systems [34]. Amongst other degradation phenomena, MEA degradation caused by hydrogen fuel starvation is recognized as major lever for durability and recently gained much attention in scientific research [37, 38, 70, 100]. In stack configuration, (gross) fuel starvation can lead to so-called cell (voltage) reversal events in the affected cell(s). The mechanism of cell reversal events, root causes and possible mitigation strategies are discussed in detail in section 2.7.1.
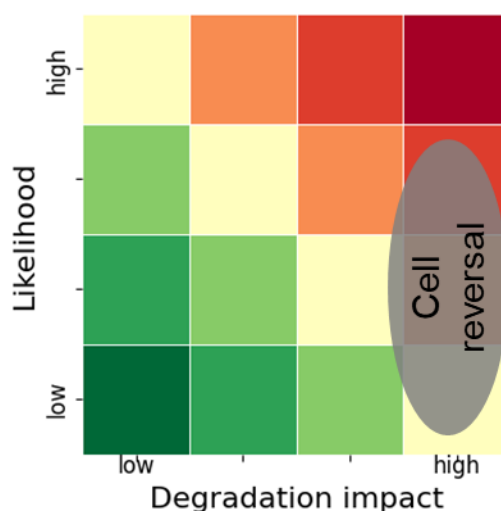
Figure 5.1: Schematic classification of cell reversal events within a risk matrix.

As outlined in section 2.7.1. and depicted in Figure 5.1, the degradation impact of a cell reversal event is high. Reversal intolerant MEA designs can fail within (milli-)seconds if no mitigation strategy is applied. On the other hand, the likelihood of reversal events

can vary from low to medium-high and is dependent on the specific fuel cell system, its components and operating strategies. The risk of reversal events occurring can be minimized to a certain extend if the operating conditions of a fuel cell system and stack design choices are adapted and optimized for the aimed application and other boundary conditions (e.g. allowed start-up temperatures or allowed system dynamics).

Accelerated stress tests (ASTs) for differential cells have been established within fuel cell research and development to gain insights in durability and degradation phenomena [155, 156]. To investigate the degradation impact of cell reversal events on reversal tolerant anodes (RTAs), an AST variant drawing constant current in the absence of hydrogen within the anode has been established [37, 39, 98, 100, 103, 106, 117, 118, 122, 124]. Consequently, a negative cell voltage can be observed indicating the cell reversal operation. The measurement commonly is continued until a negative voltage threshold, typically −1.5 V or −2 V, is met. The time spent in reversal is used as figure-of-merit for the reversal tolerance of the investigated RTA.
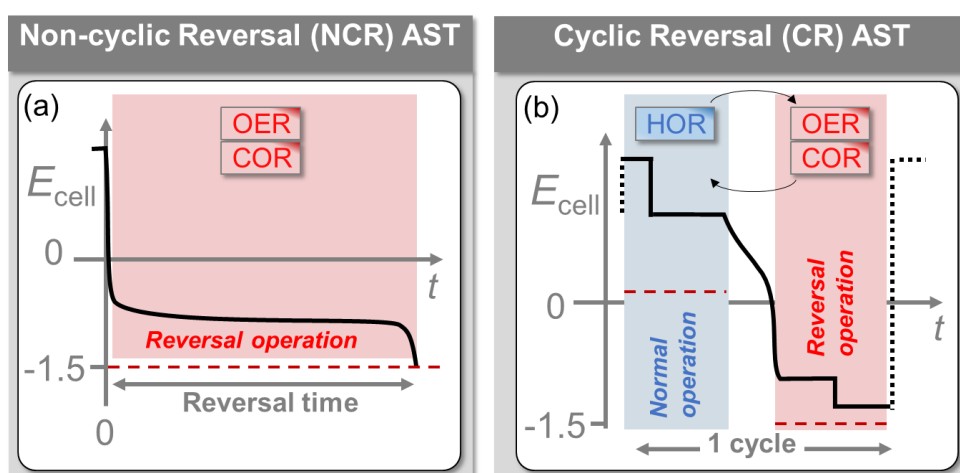
Figure 5.2: Schematic representation of the (a) non-cyclic reversal (NCR) and (b) cyclic reversal (CR) AST. The operating modes (italic) and respective occurring electrochemical reactions (boxes) on the anode are depicted: oxygen evolution reaction (OER), carbon oxidation reaction (COR), hydrogen oxidation reaction (HOR). The resulting cell voltage profiles during the AST are illustrated in black lines. The abortion criteria are indicated by red dashed lines

As outlined in the PEFC Fundamentals section, in the absence of hydrogen either COR or OER can cover the demand for electrons to maintain the requested current within the affected cell(s). During the above-described ASTs, referred to as non-cyclic reversal (NCR) AST in this work, no insights into fuel cell performance decrease can be obtained during the prolonged cell reversal event applied (cf. Figure 5.2a).

Performance decay after meeting the voltage threshold during NCR AST is commonly linked to severe carbon corrosion [37, 100, 122, 124]. However, even before the abortion criterium is met, significant performance decay can be observed during prolonged reversal events [100, 122]. These observations highlight the need for additional charac-

terization methods and test procedures for further insight into the failure modes. Furthermore, hydrogen starvation events appearing in field operation of automotive or stationary fuel cell systems exhibit predominantly short and recurring starvation events. Consequently, degradation events mimicked within non-cyclic reversal ASTs could differ significantly from degradation occurring for real life applications. In addition, the aspect of a possible deactivation of IrO_2 co-catalysts in the presence of carbon species during prolonged reversal operation [117] needs to be considered within reversal AST design.

The development of the cyclic reversal (CR) AST (cf. Figure 5.2b) is trying to bridge the gap between an artificially applied reversal AST and the expected stressor during field operation. Furthermore, the developed CR AST allows the application of recurring reversal events on fuel cells incorporating reversal tolerant anodes while allowing normal fuel cell performance decay investigation simultaneously (cf. Figure 5.2b). Therefore, distinction between OER and HOR degradation is possible. Comparable degradation tests investigating recurring reversal events have been reported for high temperature PEFCs and unsupported PEFC catalysts [152, 157]. However, for low temperature reversal tolerant PEFCs based on IrO_2 co-catalysts, the investigation of these characterization methods are rarely seen, but their necessity was addressed most recently [40, 114].

To account for the interactions of the anode components on reversal tolerance, two different MEAs, solely differing regarding their incorporated HOR catalyst, were investigated within this chapter. Apart a differing HOR catalyst graphitization degree, identical MEA components and catalysts loadings were incorporated (cf. Table 4.1). It is well known that a low onset potential of the incorporated OER catalysts prevents the anode from reaching high half-cell potentials and consequently increases reversal tolerance [100, 125, 126, 128, 160]. Consequently, improving this OER characteristic is under intensified research. The impact on reversal tolerance by the other anode components as well as crosslinks and interactions between these components appear to be less in focus. The investigation of two differing RTA catalyst layers ensures the validity of the gained results for varying MEAs based on OER co-catalysts.

This chapter aims to reveal insights regarding MEA failure during CR AST, which is considered more realistic with respect to expected degradation during field operation caused by reversal events. In-situ diagnostic procedures were developed to enable an HOR overpotential distribution analysis and validation via ex-situ imaging.

5.1 Electrochemical in-situ results and discussion

5.1.1 Reversal AST comparison

In Figure 5.3, a comparison between CR and NCR AST is depicted (for details see Experimental section). For both investigated MEAs the cell voltage during reversal operation at 0.62 A cm^{-2} is shown. A pristine beginning-of-life (BOL) sample after conditioning was investigated for each test.
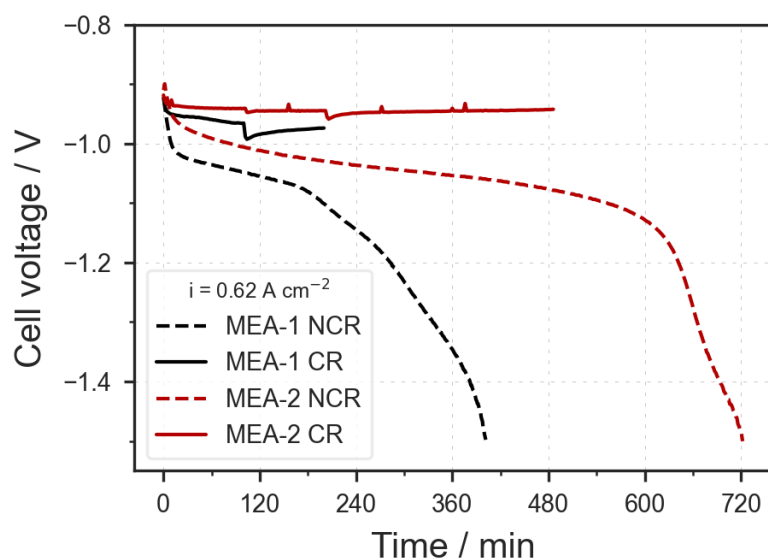
Figure 5.3: Cell voltage during reversal operation at 0.62 A cm^{-2}, 30° C, 80% *RH*, 1.5/1.7 bar$_g$ (anode/cathode) for MEA-1 and MEA-2. Cell potentials during NCR AST are depicted as dashed lines. Accumulated reversal time at 0.62 A cm^{-2} during CR AST is shown as solid lines (averaged from the last 30 s within each cycle). Triggered failure criterion: cell voltage < −1.5 V during reversal within NCR AST; cell voltage < 0.1 V during normal operation within CR AST (not shown).

The voltage profile during NCR AST corresponds to reported characteristics during prolonged fuel starvation events while drawing a constant current [39, 98, 100, 103, 128]. For both MEAs initial cell potential drops to values < −0.9 V for reversal operation during NCR AST. Subsequently, a potential plateau is reached, also referred to as water electrolysis plateau. Afterwards, cell potential decreases to < −1.5 V. Cell voltages during reversal in the range of 0 to −1.6 V are considered to be dominated by the OER reaction. Severe carbon corrosion due to COR has been reported to occur at more negative cell voltages, presumably initiated by the onset of IrO$_2$ deactivation by carbon species [100, 103, 117].

The cathode potential was shown to remain almost constant during reversal operation [100, 161]. Therefore, decreasing cell voltages during reversal operations at non-freezing conditions can be attributed to increased anode potentials.

As a consequence, higher anode potentials for MEA-1 are indicated during prolonged reversal events, with respect to MEA-2 (cf. Figure 5.3). A decreased reversal tolerance for MEA-1 is strongly indicating an increased anode potential during reversal operation, which in turn could cause an increased COR rate [100]. As both MEAs vary solely regarding the incorporated HOR catalyst, an HOR dependency on anode potential during reversal operation is likely. The impact of the HOR catalyst on the resulting anode potential during reversal operation is corroborated by the results for the cyclic reversal AST (cf. Figure 5.3, solid lines). MEA-1 shows a comparable lower cell voltage during recurring, short-term reversal events within CR AST compared to MEA-2.

In conclusion, an increased anode potential for MEA-1 during reversal events can be assumed, independent of the applied reversal duration within the AST. Most likely the individual HOR catalyst's vulnerability to carbon corrosion during fuel starvation events is significantly affecting the anode potential as well as the reversal tolerance of the respective MEA. Besides illustrating the effect of the chosen HOR catalyst on reversal tolerance, this observation is highlighting the necessity of a complementary consideration of all incorporated anode components and their interactions with respect to reversal operation. To achieve an optimized reversal tolerance, the composition of all incorporated anode components should be tailored.

Besides the material induced differences in voltage signals for both investigated MEAs, a substantial difference between NCR and CR AST is indicated by Figure 5.3, independent of the investigated MEA.

NCR AST:
A significant time dependent cell voltage decrease can be observed, culminating in triggering MEA failure by achieving a cell voltage of < -1.5 V during reversal operation. After reaching a cell voltage of < -1.5 V, commonly severe carbon corrosion, irreversible MEA degradation and furthermore insufficient subsequent reversal mitigation capability are reported [103, 124].

CR AST:
Cell potential during reversal operation exhibits minor change (cf. Figure 5.3). MEA failures during normal operation (< 0.1 V, H_2/air) are observed, instead of triggering cell voltages of < -1.5 V during reversal operation. The voltage profiles during reversal operation are indicating an unaffected OER activity. This behavior is indicating a repetitive OER catalyst recovery effect during cycled short-term reversal operation and normal operation. The OER recovery effect potentially affects MEA degradation caused by reversal operation. As outlined above, the ability for mimicking real occurrence of fuel

starvation within automotive applications is more realistically represented alternating normal operation and short-lived reversal events than by a single prolonged reversal event. Consequently, due to the absence of an OER recovery effect test procedures comparable to NCR AST might overestimate OER catalyst deactivation compared to field operation. Thus, the degradation of RTAs with respect to field applications could be overestimated by respective NCR accelerated stress test procedures.

This highlights the importance of applying ASTs which are mimicking field reversal characteristics as realistic as possible and simultaneously achieve further understanding on degradation phenomena occurring during these ASTs. Therefore, the comprehensive test results during CR AST are illustrated and discussed in the following. In addition, the observed MEA failure mode and degradation phenomena are investigated via further characterization methods.

5.1.2 Cyclic reversal AST

5.1.2.1 AST Voltage Profiles
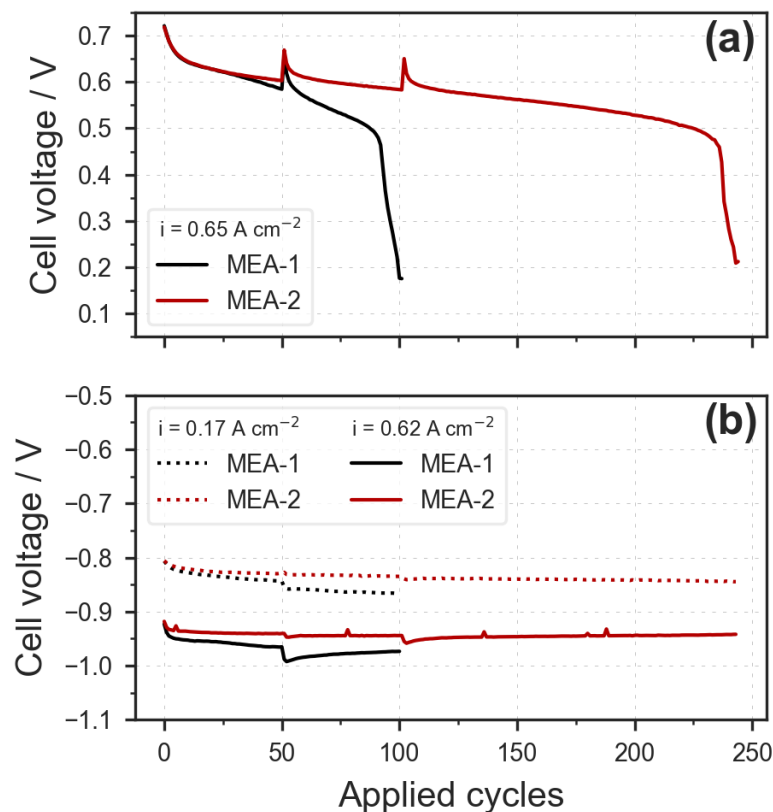
Figure 5.4: Cell voltage for the investigated MEAs during CR AST at 30° C, 80% *RH*, 1.5/1.7 bar$_g$ (anode/cathode). Cell voltage is averaged from the last 30 s within each cycle. (a) Normal operation under H$_2$/air atmosphere at 0.65 A cm^{-2}. Failure for both MEAs observed within this step (failure criterion: cell voltage < 0.1 V). Threshold of 0.1 V is not attended in this graph due to averaging. (b) Reversal operation in N$_2$/air atmosphere at 0.17 (dotted) and 0.62 A cm^{-2} (solid).

To further analyze degradation for recurring short-term reversal events, more comprehensive results are depicted in Figure 5.4. Normal operation at 0.65 (cf. Figure 5.4a) and reversal operation at 0.62 and 0.17 A cm^{-2} (cf. Figure 5.4b) are shown.

Both investigated MEAs fail because of performance decrease in normal operation mode. A cell voltage below 0.1 V was set as failure criterion within normal operation.

Further insights can be provided on voltage degradation caused by reversal operation as a function of the applied number of cycles, corresponding also to the number of reversal events applied. First, the normal operation cell voltage is discussed. For both MEAs normal operation voltage decreases exponentially by ≈ 76 mV within 10 applied reversal events (cf. Figure 5.4a). Subsequently, a voltage decrease with an approximate linear progression can be observed. With exceeding 25 cycles, MEA-1 is showing an increased voltage decay compared to MEA-2. The interposed EIS and H$_2$ pump measure-

89

ments, performed between cycles 51/52 and 102/103 to enable HOR overpotential distribution analysis, lead to a voltage increase in normal operation for both MEAs. A recovery procedure was performed preceding EIS measurements (cf. Experimental section 4.2.6 for details). Consequently, the voltage increase during normal operation can potentially be attributed to reversible losses being recovered by the performed air- and hydrogen soak. However, voltage increase is not expected to have a positive effect on the overall reversal time for the respective MEA, as within the following reversal events a sharp initial voltage decay is observed (cf. cycle 52 to 62 Figure 5.4a). Thereafter, cell voltage loss shows a linear behavior again. For both MEAs, the linear voltage decrease is succeeded by a sharp voltage decrease within the last 10 cycles before the EOL criterion is met. For MEA-1 the EOL criterion is met after 102 cycles, whereas MEA-2 can withstand 244 cycles before cell voltage drops below 0.1 V during normal operation.
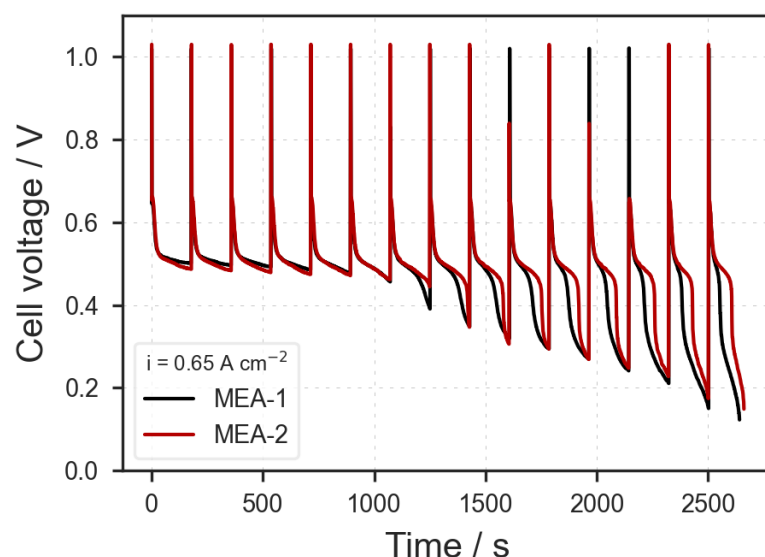
Figure 5.5: Last 15 steady-state normal operation cycles before EOL criterion is met during CR AST at 30° C, 80% *RH*, 1.5/1.7 barg in H$_2$/air (anode/cathode) at 0.65 A cm^{-2}. Voltage peak indicates cycle start. Subsequent measurements in each cycle (N$_2$ purge, cell reversal operation and OCV) are not shown.

The time dependent, non-averaged cell voltages from the last 15 cycles during normal operation are depicted in Figure 5.5. Within each cycle, steady-state normal operation is performed for 3 min. Each cycle is initiated by a OCV potential ≈ 1 V, followed by a voltage drop due to the drawn current (0.65 A cm^{-2}). The cell voltage shape changes from a predominantly linear decrease within each steady-state cycle (mean value ≈ 550 to 500 mV) to a transient cell voltage shape. For the last 10 cycles, cell voltage drops to < 400 mV followed by a drop below 100 mV in the last cycle. This cell voltage characteristic indicates a substantial degradation within the MEA, which makes a subsequent

stable steady-state operation at these operating conditions no longer possible. Despite the significantly different reversal tolerance and reversal cycles, both MEAs are showing comparable time-resolved voltage signals for normal operation within the last cycles. This characteristic is indicating, the observed failure mode is independent of the investigated MEA.

As mentioned above and in contrast to the HOR performance, the OER catalyst exhibits stable performances for both MEAs (cf. Figure 5.4b) within the CR AST. A stable cell voltage plateau is reached upon reversal operation, for both investigated current densities and MEAs, with minor fluctuations (< 50mV) most likely induced by the performed EIS and H_2 pump measurements (between cycles 51/52 and 102/103). The OER performance can be maintained until the EOT criteria is met.

This stable OER voltage plateau during reversal operation is in contradiction to the reversal voltage decrease during a prolonged reversal event (cf. NCR AST Figure 5.3) which is commonly reported in literature [37, 39, 100, 103, 118, 128]. The voltage decrease during prolonged reversal operation is typically attributed to OER catalyst deactivation [103, 117]. Therefore, the constant OER activity during CR AST is indicating an OER catalyst recovery effect due to alternating normal and reversal operation.

Two possible mechanisms could explain the observed OER recovery effect:

- Suppression of OER deactivation
- Surface reduction from IrO_2 to metallic Ir (higher OER activity)

As proposed by Joo et al., carbon oxidation products (from the HOR catalyst or GDL) can potentially cause an OER catalyst poisoning and subsequent OER deactivation for RTAs containing IrO_2 during prolonged reversal operation [117]. Carbon oxidation products could be reduced during each normal operation. As the anode potential is cycling between > 1.3 V_{RHE} (N_2/air, reversal operation) and ≈ 0 V_{RHE} (H_2/air, normal operation) during CR AST, carbon oxidation products could be reduced electrochemically. Additionally, the reductive atmosphere of hydrogen during normal operation can result in chemical reduction of carbon oxidation products. The hypothesis would be consistent with most recent research. Marić et al. found a higher ratio of surface oxide formation on the carbon support with increasing uninterrupted reversal time. For cycled, short-term reversal events the amount of surface oxide formation was found to be decreased [114]. This would lead to a decreased OER catalyst deactivation for short-term reversal events compared to prolonged reversal stress tests.

Alternatively, the OER recovery effect can arise, at least partially, from a mechanism recently proposed by Tovini et al. [70]. During normal operation of a fuel cell, the IrO_2 co-catalyst surface within the anode catalyst layer can be reduced to metallic Ir in the presence of hydrogen. As metallic Ir exhibits a higher activity towards OER [146], the

anode potential within a subsequent reversal event is decreased. This can compensate OER catalyst deactivation by carbon oxidation products when reversal and normal operation are alternated.

The observed OER recovery effect is most likely a combination of both proposed mechanisms. Furthermore, the OER recovery aligns with the absence of increasing OER mass transport phenomena during CR AST. The onset of OER mass transport limitation, e.g. due to a loss of active OER catalyst sites and subsequently increased diffusion pathways, would be indicated by an increased OER overpotential at increased currents (cf. section 2.3). Therefore, the onset of increased OER mass transport with increasing reversal events would result in an increasing cell voltage gap between higher (0.62 A cm^{-2}) and lower (0.17 A cm^{-2}) reversal current density.
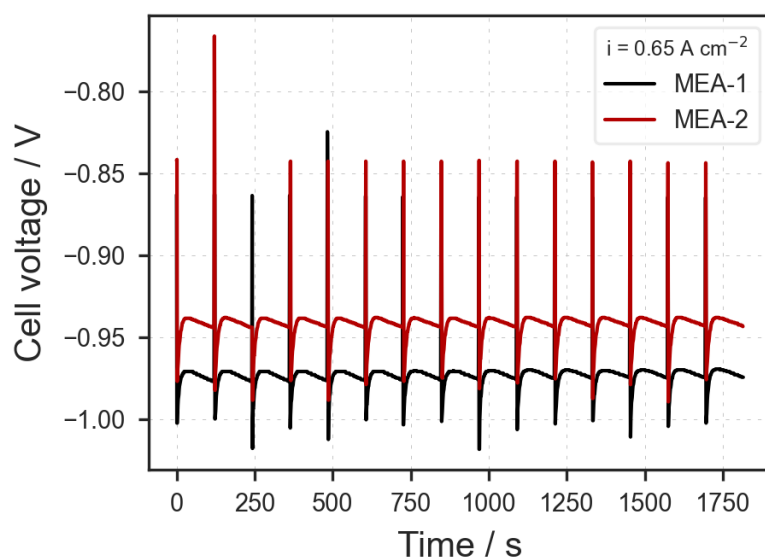
Figure 5.6: Last 15 reversal operation cycles before EOL of each MEA during CR AST at 30° C, 80% *RH*, 1.5/1.7 bar$_g$ (N$_2$/air on anode/cathode) at 0.62 A cm^{-2}. Voltage peak indicates new cycle. Subsequent measurements in cycle (OCV, normal operation, N$_2$ purge, and reversal operation at 0.17 A cm^{-2}) are not shown.

The proposed OER catalyst recovery during CR AST is corroborated by the time dependent cell voltages during reversal operation depicted in Figure 5.6. The last 15 cycles for reversal operation at 0.62 A cm^{-2} are depicted before the respective test failure criterion during normal operation was met. Each cycle is indicated by an initial vertical voltage drop, due to the reversal current increase from 0.17 A cm^{-2} to 0.62 A cm^{-2}. As illustrated in Figure 5.6, after equilibration during the first couple of seconds, the cell voltage during a reversal event slightly decreases within the 120 s of reversal operation. The cell voltage decrease can be recovered for each subsequent cycle, indicating a constant OER activity.

OER based reversal tolerant MEAs were shown to fail during normal operation when performing CR AST, whereas the OER catalyst simultaneously exhibits good functionality even during the last cycle. This observation was valid for both investigated MEAs, independent on the incorporated HOR catalysts. To the best of the author's knowledge, no such behavior has been reported in literature so far.

To further investigate the MEA failure modes during CR AST, additional characterization methods were performed. These methods can also help to better understand the HOR catalyst's influence on reversal tolerance. As the observed MEA failure occurred during normal operation, mass transport, activation overpotential and/or ohmic resistance increase for the anode (HOR) could be responsible for MEA failure. In addition, cathode catalyst degradation or ohmic resistance increase (e.g. increased contact resistances) induced by other MEA components could contribute to MEA failure. Consequently, EIS, CV and hydrogen pump experiments were performed to investigate the corresponding overpotentials of all MEA components.

5.1.2.2 Cyclic voltammetry
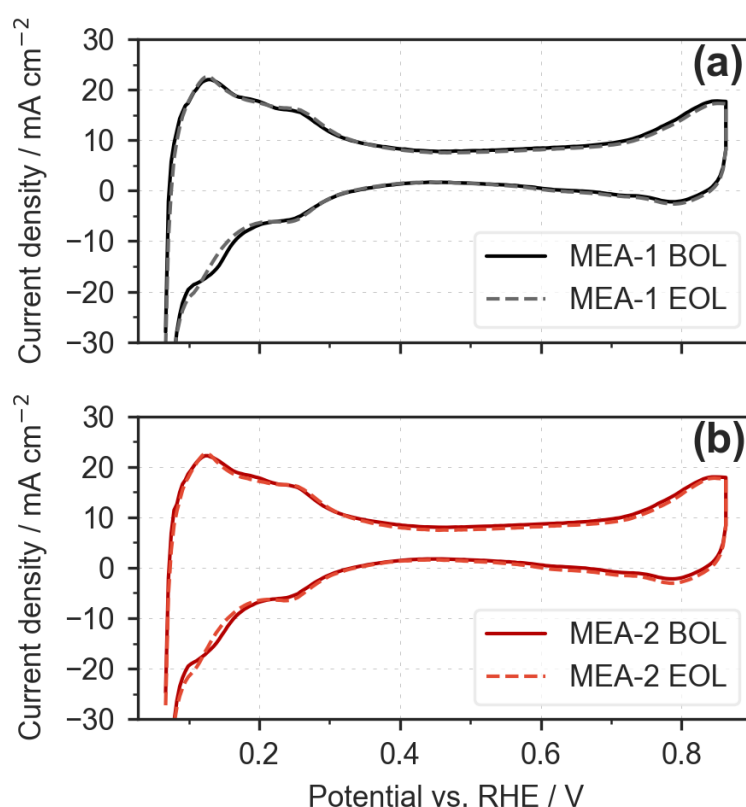
Figure 5.7: Cathode CVs prior (BOL) and following (EOL) CR AST at 60° C, 100% *RH* and recorded with a scan rate of 100 mV s^{-1}: (a) MEA-1 and (b) MEA-2

To analyze ORR and HOR catalyst degradation, anode and cathode *ECSA* measurements based on the H$_{upd}$ method were performed. Consequently, anode and cathode

CVs were recorded before and after finishing the cyclic reversal stress test at 60° C (for further details see section 3.1.1). The corresponding cathode CVs are depicted in Figure 5.7.

Peak characteristics which are typical for Pt/C catalysts were achieved for the cathode CVs: hydrogen ad-/desorption features at a potential range between 0.1 and 0.3 V_{RHE} and Pt oxidation/reduction peaks at potentials above 0.6 V_{RHE} [48]. The applied cyclic reversal AST does not induce any significant *ECSA* loss or change in double layer capacitance. As both platinum dissolution and carbon corrosion would cause a significant change in the H_{upd} feature and/or double layer capacitance, insignificant cathode degradation is assumed during CR AST. The absence of cathode degradation is corroborated by the constant cell voltages observed during reversal operation within CR AST. During reversal operation ORR takes place on the cathode and OER on the anode. Therefore, a decrease in cathode potential would require a compensating OER activity increase to maintain constant cell voltages during reversal operation.

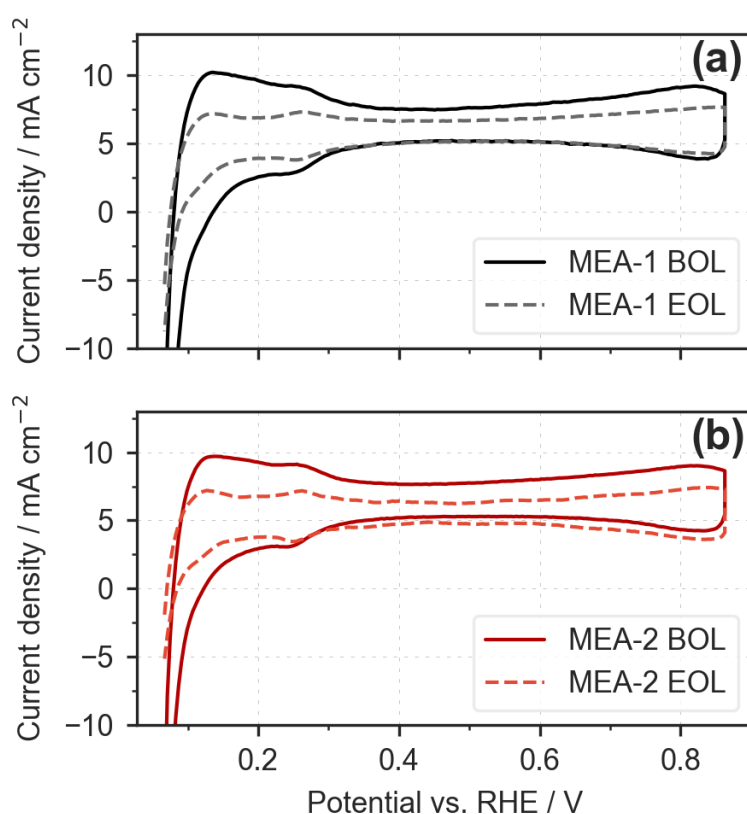**Figure 5.8: Anode CVs prior (BOL) and following (EOL) CR AST at 60° C, 100% *RH* and recorded with a scan rate of 100 mV s^{-1}: (a) MEA-1 and (b) MEA-2**

The corresponding anode CVs are depicted in Figure 5.8. As for the cathode CVs, typical Pt/C electrode characteristics are exhibited, despite the present IrO$_2$ catalyst. This observation aligns with former results by other research groups investigating com-

parable reversal tolerant electrodes incorporating an IrO_2 co-catalyst [37, 100, 103, 114]. After reaching the EOL state within CR AST, the anode CVs exhibit a significant decrease in hydrogen ad-/desorption and platinum oxidation peaks.

As depicted in Figure 5.9, anode *ECSA* decreases during CR AST by 59% and 49% for MEA-1 and -2, respectively. Commonly, H_2 desorption/adsorption is not observed on IrO_2 catalysts [142]. Assuming the ratio of metallic Ir species on the OER catalyst surface is minor, *ECSA* loss is presumably dominated by a loss of the Pt based HOR catalyst. Tovini et al. found minor metallic Ir in as-received supported IrO_2 OER catalyst powder. However, the ratio was found to increase under hydrogen atmosphere and elevated temperatures (120 °C) [70].

Besides *ECSA* loss, the CVs recorded EOL are showing a shift to lower currents across a wide potential range (cf. Figure 5.8), indicating changes in hydrogen crossover [141], and corroborated by the performed hydrogen crossover measurements (cf. Figure 5.9) determining the crossover current density i_{H_2}. The latter showed a decrease in hydrogen crossover by 2.8% and 5.7% for MEA-1 and MEA-2, respectively. This difference is likely a result of varying membrane water content caused by the potentiostatic preconditioning performed prior to the CV and hydrogen crossover measurements (15 minutes normal operation at 0.6 V, cf. section 4.2.3). Consequently, membrane water content could vary between BOL and EOL state, resulting in H_2 crossover changes. Commonly, H_2 crossover increases with increasing water content [141]. In addition, the decrease in hydrogen crossover is indicating the absence of chemical (or mechanical) membrane degradation with membrane thinning or puncture, which would increase hydrogen crossover.
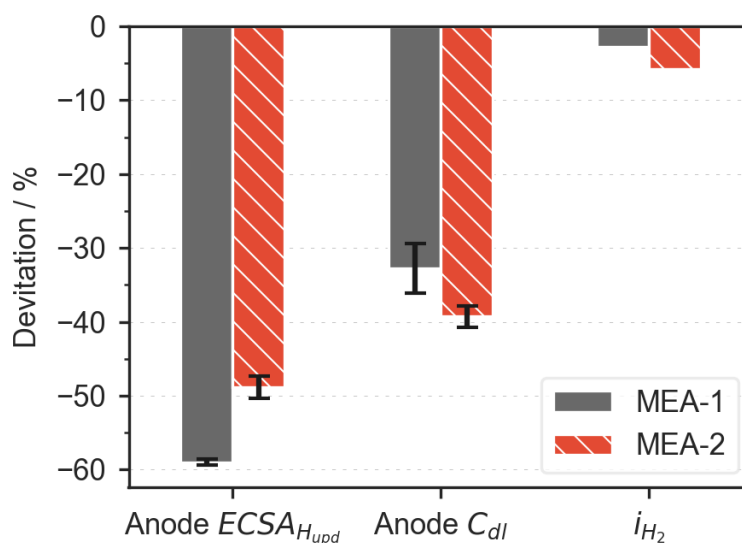
Figure 5.9: Change in anode *ECSA*, anode double layer capacitance C_{dl} and hydrogen crossover current density i_{H_2} due to CR AST. Standard deviation is calculated from the corresponding last three H_{upd} CVs performed within each CV set. For hydrogen crossover, no repeated measurements were performed, therefore no standard deviation is reported.

Furthermore, a significant decrease in double layer capacitance C_{dl} caused by CR AST can be observed (cf. Figure 5.8 and Figure 5.9). The double layer capacitance decreases by 33% and 39% for MEA-1 and MEA-2, respectively. This effect indicates a loss of carbon surface area [162], due to carbon corrosion at the ACL. The decrease in double layer capacitance is in contrast to findings from other groups, commonly reporting hydroquinone-quinone peaks after performing reversal stress tests [37, 100, 103]. These hydroquinone-quinone peaks are a result of the formation of surface oxides on the carbon and are also indicating carbon corrosion [83, 163]. Within this work, no hydro-quinone-quinone peaks were found during cleaning or subsequent CVs. This behavior can be caused:

- by the preceding recovery steps performed
- or due the suppressed formation of surface oxides for short-term reversal events, most recently reported by Marić et al [114].

Summarizing the results shown above, MEA failure during normal operation due to cathode degradation can be neglected and the absence of membrane degradation is indicated. Severe anode degradation is observed, indicated by a loss of platinum catalyst and carbon support corrosion. To quantify the impact of the observed Pt loss and carbon corrosion on the anode overpotential, an HOR overpotential distribution analysis was performed.

5.1.2.3 Electrochemical impedance spectroscopy
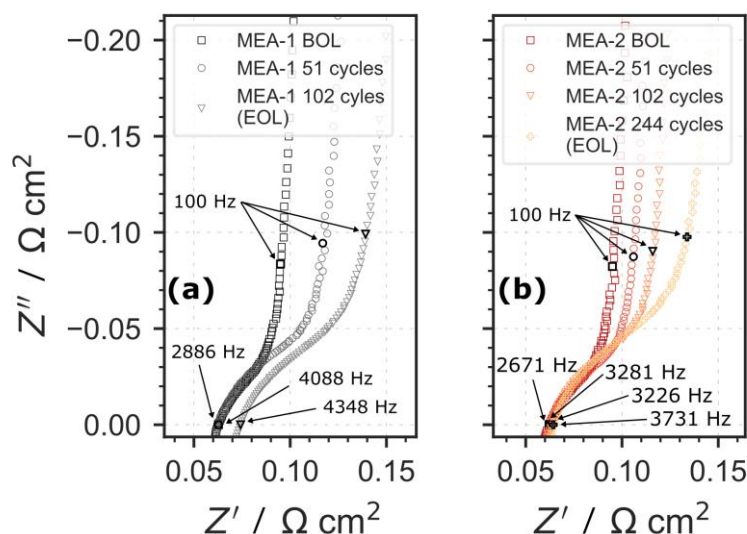
Figure 5.10: Impedance spectra comparison of (a) MEA-1 and (b) MEA-2. Measurements were performed prior (BOL), during and following (EOL) CR AST at 30° C, 80% *RH* and 1 bar$_g$. Potentiostatic EIS was performed at 0.45 V$_{RHE}$. The highlighted frequencies at the real axis intercept and 100 Hz are annotated for orientation purposes.

Potentiostatic EIS measurements under H_2/N_2 atmosphere were performed preceding, during and subsequent CR AST to quantify the high frequency resistance R_{HFR}. The high frequency resistance was obtained by the real axis intercept of the Nyquist plot. The corresponding Nyquist plots at hydrogen pump operating conditions (30° C, 80% *RH* and 1 barg) are shown in Figure 5.10. Flow rates were set to $10 \, l_n \, min^{-1}$ as during the hydrogen pump experiments. R_{HFR} shows a minor increase with increasing number of reversal events applied. Solely for MEA-1 EOL a sligth increase is observable (11 mΩ cm^2 BOL vs. EOL), corresponding to an ohmic overpotential increase equal to 7.15 mV (at 0.65 A cm^{-2}). Therefore, MEA failure during cyclic reversal AST cannot be attributed to an increased high frequency resistance, as the increase only has a negligible impact on voltage degradation during normal operation. As outlined in the fundamental section, R_{HFR} is summarizing the membrane resistance $R_{membrane}$ and contact resistances $R_{contact}$. Consequently, the negligible high frequency resistance increase is corroborating the absence of membrane degradation, already indicated by hydrogen crossover measurements.

The performed EIS measurements allow for estimation of the effective proton resistance $R_{H^+, electrode}^{eff}$ and the corresponding overpotential $\eta_{H^+, electrode}^{eff}$. within the investigated electrode (for further details see section 3.1.5). As depicted in Figure 5.10, a increase in effective proton resistance on the cathode, $R_{H^+, cathode}^{eff}$, is indicated by the extension of the 45° line after reversal operation. The intrinsic air/air start within each reversal cycle

could be responsible for the observed protonic resistance increase. During each reversal event oxygen is evolved within the anode. The subsequent reintroduction of hydrogen is causing an air/air start event (cf. section 3.1.5). The observed increase in $R_{\mathrm{H^+,\,cathode}}^{\mathrm{eff}}$ is resulting in an corresponding overpotential increase at 0.65 A cm^{-2} of 19 and 23 mV for MEA-1 and -2, respectively. Consequently, the overpotential increase cannot be accounted for MEA failure ($>$ 600 mV, cf. Figure 5.4). The minor resistance increase is in alignment with the prior discussed negligible cathode degradation. As outlined in section 3.1.5, the proton resistance within the anode is also negligible due to the small catalyst layer thickness. Commonly, no 45° line is observed within the Nyquist plot for potentiostatic EIS performed on the anode. Therefore, only measurements for the cathode catalyst layer were performed.

5.1.2.4 HOR overpotential distribution analysis

In conclusion, MEA failure during normal fuel cell operation can be mainly attributed to anode kinetic and mass transport resistance increase (cf. section 2.3 and Figure 2.1). These overpotentials can be quantified using hydrogen pump measurements [152]. Hydrogen pump polarization curves were recorded from 0 to 3.75 A cm^{-2} prior, during and following the reversal stress test. The obtained polarization curves were corrected for high frequency resistance R_{HFR}. As outlined in section 3.1.6, the effective proton resistances of anode and cathode were not considered for the hydrogen pump analysis. Following the argumentation of Makharia et al. for determining $R_{\mathrm{H^+,\,cathode}}^{\mathrm{eff}}$ via EIS, a significant contribution or increase of $R_{\mathrm{H^+,\,cathode}}^{\mathrm{eff}}$ would result in shifting the cathode current distribution closer to the membrane. For the incorporated cathode catalyst layer with a significant higher Pt loading as the anode, this is resulting in negligible cathode overpotential during the hydrogen evolution reaction [148]. Therefore, the assumptions for Equation 3.17 are still valid and R_{HFR}-corrected cell voltage is solely dependent on E_{rev} and η_{HOR}.
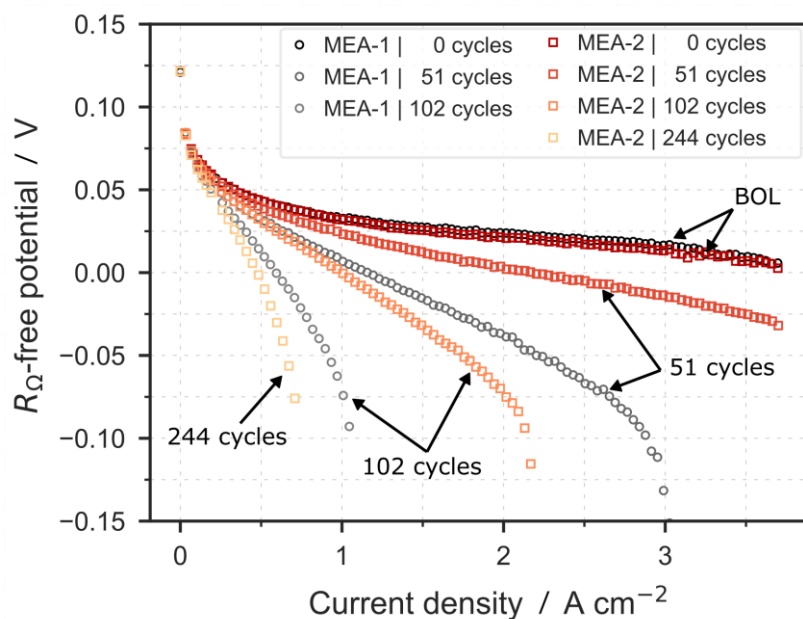
Figure 5.11: R_{HFR}-corrected hydrogen pump polarization (H$_2$/N$_2$ on anode/cathode) curves during CR AST at BOL and after 51, 102 and 244 reversal events.

The corresponding R_{HFR}-free polarization curves are depicted in Figure 5.11. The temperature is kept constant during the measurement, consequently only hydrogen partial pressures contribute to changes in E_{rev}. The occurring hydrogen partial pressures are most likely not affected by occurring degradation effects or increased overpotentials (anode: high stoichiometry; cathode: hydrogen partial pressure is dependent on HER, but negligible cathode degradation is observed). Consequently, a decrease in R_{HFR}-corrected cell potential can be fully attributed to an increase in the HOR overpotential η_{HOR}. The pristine MEAs are showing comparable polarization curves BOL, indicating a comparable HOR performance. As the Pt loading is equal for both MEAs and only the Pt support varies, this result is as expected. Even for high current densities > 3 A cm^{-2}, no change of the linear voltage decrease is observed. Therefore, there is no indication for HOR mass transport limitations in the pristine catalyst layers. After 51 reversal events MEA-2 still exhibits a linear voltage decrease characteristic with a small HOR overpotential increase compared to BOL. In contrast, MEA-1 is already showing mass transport limiting behavior for current densities above 2.7 A cm^{-2}. The polarization curves after 102 cycles are showing mass transport limiting behavior for both investigated MEAs. The overpotential for MEA-1 is significantly increased compared to MEA-2, indicating a significantly higher HOR catalyst degradation for MEA-1 at this state. The strong increase in HOR overpotential for MEA-1 is corroborating the previous observation of the strong HOR catalyst contribution on the resulting reversal tolerance of the anode catalyst layer.

The hydrogen pump polarization curves indicate that HOR mass transport overpotential might be responsible for MEA failure during normal operation independent on the

incorporated HOR catalyst in the anode catalyst layer. To verify the above stated assumption, an HOR overpotential distribution analysis was performed. As outlined in section 3.1.6, the theoretical kinetic overpotential can be estimated and calculated based on a simplified Butler-Volmer approach (Equation 3.19).

As shown by previous research of other groups, very low platinum loadings are required (in the order of 1 to 10 $\mu g_{Pt}\,cm_{electrode}^{-2}$) to determine the exchange current density i_0 of a catalyst on MEA level [95, 151]. High catalyst loadings lead to small total overpotentials for HOR/HER. Consequently, the estimation of i_0 becomes extremely sensitive to small inaccuracies within the performed measurement (e.g. R_{HFR} determination). Therefore, in this work the values for the exchange current density i_0 are solely derived for validating the experimental approach. They should be regarded as apparent values, which are not describing the exact catalyst kinetics. Beside HOR polarization curves, *ECSA* measurements are mandatory to calculate the exchange current density i_0. To prevent unintended catalyst layer recovery and cleaning within the AST, CVs were only performed before and after the CR AST. For MEA-1 and -2 values of 103 and 93 mA cm_{Pt}^{-2} for i_0 are derived BOL by a non-linear least squares fit. A symmetry factor of 0.5 was assumed and only current densities below 1 A cm^{-2} were considered. At BOL the chosen upper current density is below the onset of mass transport limitation (cf. Figure 5.11). The experimentally determined *ECSA* values (see above) were used to estimate the Pt surface area. The resulting exchange current densities are consistent with literature results for Pt/C electrodes at 30 °C [151], validating the experimental approach. The numerical Butler-Volmer fitting results for all polarization curves are depicted in the Appendix (cf. Appendix-Figure 2).

Considering that the kinetic overpotential can be estimated via the chosen Butler-Volmer approach, all terms in Equation 3.18 can be determined. A resulting overpotential distribution for the polarization curve of MEA-1 after 102 cycles is depicted in Figure 3.5b. The measured cell voltage E_{cell}, the cell voltage corrected for the high frequency resistance $E_{R_{HFR},free}$, the reversible cell voltage E_{rev} and the derived kinetic Butler-Vollmer voltage E_{BV} are depicted. In addition, the corresponding overpotentials are shown: the HFR overpotential η_{Ω}, the activation/kinetic overpotential $\eta_{HOR,act}$ and the mass transport overpotential $\eta_{HOR,mtx}$. From Figure 3.5b further insights in the failure mode of MEA-1 after the CR AST can be derived. The individual overpotential contributions for the ohmic, kinetic and mass transport losses are in the same order of magnitude for current densities < 1 A cm^{-2}. For current densities exceeding 1 A cm^{-2}, the mass transport overpotential is significantly increased. MEA failure during CR AST for MEA-1 therefore can be mainly attributed to an increased HOR mass transport resistance.
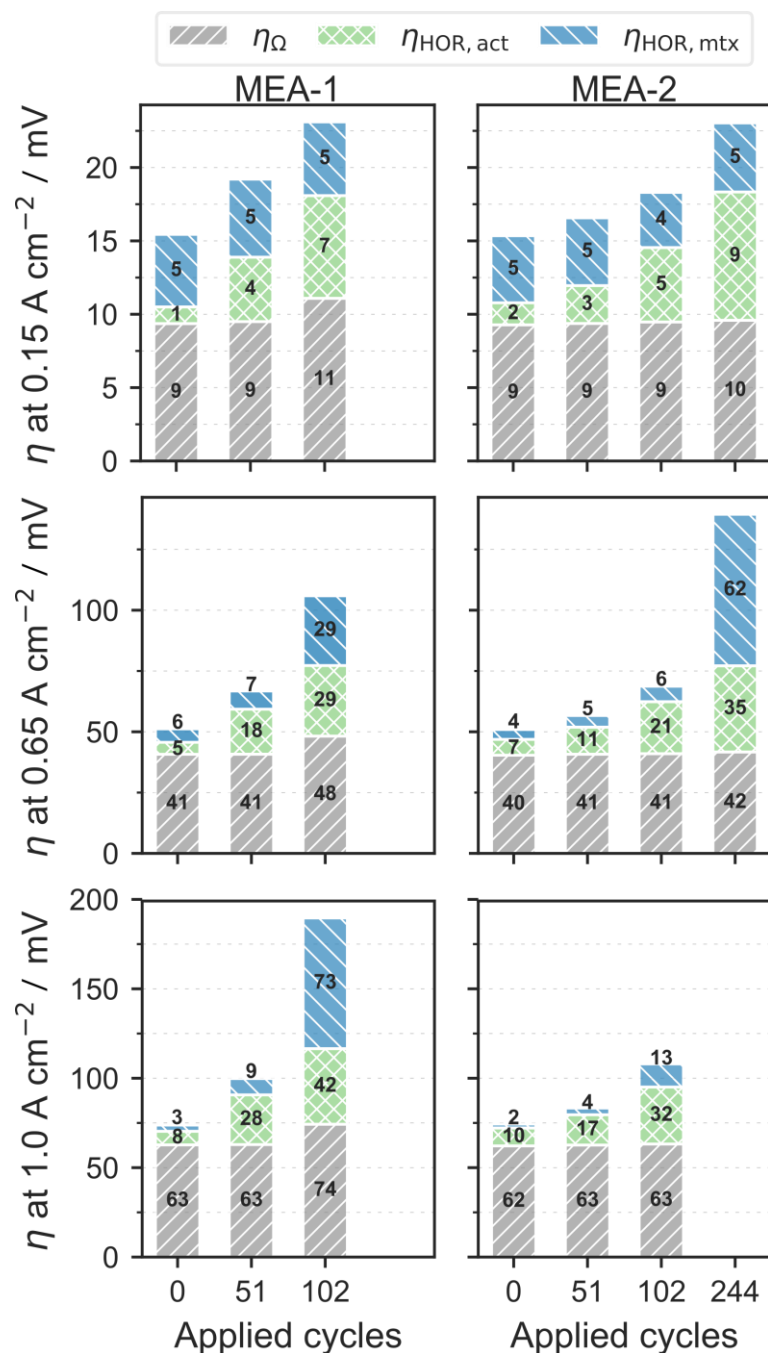
Figure 5.12: Overpotential contributions for 0.15 A cm^{-2} (first row), 0.65 A cm^{-2} (second row) and 1 A cm^{-2} (third row) obtained by H$_2$ pump polarization curves during CR AST for MEA-1 (first column) and MEA-2 (second column). The EOL corresponds to 102 and 244 cycles for MEA-1 and -2, respectively. A current density of 1 A cm^{-2} could not be achieved for MEA-2 EOL.

To validate this assumption and gain further insights, the corresponding overpotential distribution analysis for all hydrogen pump polarization curves recorded are depicted in Figure 5.12. This enables further analysis of the failure mode observed during CR AST as well as quantitative comparison. The high frequency resistance overpotential η_{HFR} is dominating the overpotential losses for both MEAs during HOR/HER operation. This appears reasonable as ohmic resistances from all MEA components are summed up

101

within the high frequency resistance, e.g. the membrane resistance and all ohmic cell resistances along electric pathways (e.g. across GDLs, flow fields, current collectors). This is in alignment with commonly reported negligible anode overpotentials for MEAs in an undegraded state and comparably high Pt loadings ($\geq 50\,\mu g_{Pt}\,cm_{electrode}^{-2}$) [95]. Figure 5.12 illustrates that the recurring application of reversal events only leads to a minor increase in the high frequency resistance. But as discussed above, the increase is small compared to the general overpotential increase. For MEA-1, where the highest increase for R_{HFR} EOL is observed, η_{HFR} only contributes 9% to the total overpotential increase observed at $1\,A\,cm^{-2}$ (see first cloumn, last row in Figure 5.12). Therefore, increasing ohmic resistances during short-term reversal events cannot be accounted for MEA failure during normal operation.

As illustrated by Figure 5.12, the kinetic HOR activation overpotential $\eta_{HOR,act}$ exhibits a significant increase during the applied CR AST, caused by the recurring cell reversal events. The HOR activation overpotential increase aligns with the above discussed *ECSA* loss observed for the anode and is simultaneously confirming the assumption, that the measured *ECSA* loss can be linked predominantly to a loss in platinum rather than being induced by a loss in surface area of the IrO$_2$ co-catalyst or resulting species from IrO$_2$ (e.g. metallic Ir). During the applied cyclic reversal stress test, the activation overpotential exhibits an approximately linear increase with slopes of 0.24 and 0.17 mV/cycle at $0.65\,A\,cm^{-2}$ for MEA-1 and -2 respectively.

In contrast to the ohmic and kinetic overpotential, the HOR mass transport overpotential $\eta_{HOR,mtx}$ exhibits an exponential voltage increase for current densities $> 0.15\,A\,cm^{-2}$. Lower current densities are commonly assigned to the kinetically dominated current density regime (cf. Figure 2.1). Within the first investigated increment between 0 and 51 reversal cycles, the HOR mass transport overpotential for MEA-1 at $1\,A\,cm^{-2}$ increases by a factor of three. Within the subsequent increment from 51 to 102 cycles, the $\eta_{HOR,mtx}$ increases by a factor of eight, illustrating the exponential overpotential increase. For MEA-2 the same pattern can be recognized at $0.65\,A\,cm^{-2}$, which corresponds to the respective EOL limiting current density for this MEA (cf. Figure 5.11) after 244 cycles. A current density of $1\,A\,cm^{-2}$ cannot be achieved EOL for this MEA. The HOR mass transport overpotential increases by factors of 1.3, 1.2 and 10.3 within the investigated increments (0 to 51, 51 to 102, 102 to 244 cycles). Consequently, the HOR mass transport increase also exhibits an exponential increase.

However, a quantitative discrepancy between the overpotential increase observed during CR AST's normal operation (> 600 mV, cf. Figure 5.4) and the respective overpotential increase determined within H$_2$ pump polarization curves becomes apparent. This can at least partly be explained by differing operating conditions. The applied pressures and gas flow rates on anode and cathode differed between hydrogen pump polarization curve and normal operation, which can have a significant impact on mass transport

losses [164]. During hydrogen pump experiments the pressure was set to 1 bar_g on the anode and cathode to minimize cross pressures between anode and cathode compartment during the polarization curves. In addition, higher flow rates were chosen during hydrogen pump experiments to allow for the investigation of higher current densities while still achieving high stoichiometries. Furthermore, membrane humidification and consequently the resulting HFR differs between normal operation and hydrogen pump mode due to the produced water on the cathode during normal operation. Consequently, the ohmic resistance between both operating modes most likely differs. In addition, hydrogen pump polarization curves were recorded applying a transient current whereas normal operation during CR AST was performed at steady state operating conditions. The steady state normal operation exhibited a time-dependent voltage loss EOL (cf. Figure 5.5) while the reported cell voltages in Figure 5.4 are averaged within each cycle. All these differences contribute to a difference in overpotential. Additionally, catalyst layer treatment by performing recovery procedures might also contribute for the misalignment. Preceding the H_2 pump experiments, Air- and H_2-soaks were performed.

Consequently, the overpotential deviations are not contradicting the general findings regarding MEA failure obtained by hydrogen pump polarization curves. In conclusion, the increase of the HOR mass transport can be identified as a major contributor to MEA failure during cyclic short-term reversal events, independent on the MEA variant.

But the question remains, where the increase in HOR mass transport overpotential is originating from. The observed exponential increase in HOR mass transport increase is strongly indicating a substantial structural change within the anode catalyst layer during CR AST. Schwämmlein et al. have reported, that an HOR mass transport increase within the anode is most likely caused by carbon corrosion and a consequential loss of void volume within the catalyst layer [35]. Therefore, the loss of void volume within the ACL or even complete ACL collapse during CR AST is indicated. In addition to the findings within the HOR overpotential distribution analysis, the substantial decrease in double layer capacitance by 30-40% (see Figure 5.9) is corroborating the assumption of severe carbon corrosion and ACL collapse as major failure mechanism during CR AST. It should be highlighted, that significant carbon corrosion occurs even though a low temperature was applied at the chosen cyclic reversal testing conditions, resulting in a kinetically suppressed carbon oxidation rate. Furthermore, severe carbon corrosion induced by reversal events is commonly attributed to cell potentials < -1.6 V during reversal operation [37, 100, 103, 117]. In contrast, the cell potentials during cyclic reversal operation were shown to be constant and above a threshold of -1 V (cf. Figure 5.4).

5.1.2.5 Performance loss during normal operation
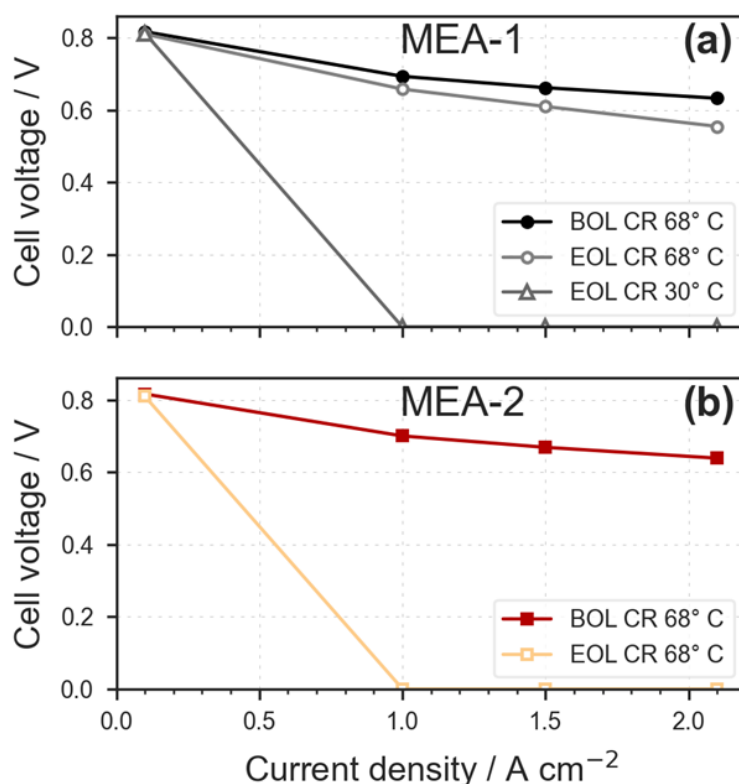
Figure 5.13: Normal operation polarization curves for (a) MEA-1 and (b) MEA-2 prior and proceeding CR AST (BOL: filled markers; EOL: empty markers). Circles and squares represent normal operation performance at 68° C, whereas triangles represent performance at 30° C. If current density cannot be achieved, a cell voltage equal to zero is depicted. For detailed operating conditions see Experimental section (68° C: see Table 1; 30° C: operating conditions of CR AST were applied).

To validate the previous results during CR AST, steady-state polarization curves at 68° C were performed BOL and EOL for both MEAs. The operating conditions are described in the Experimental section (cf. Table 4.2; but only the current densities shown in Figure 5.13 were investigated). The resulting polarization curves are depicted in Figure 5.13. The polarization curves were recorded with increasing current density. If the cell voltage dips below 0.1 V the corresponding steady-state step was aborted, and subsequent higher current densities were not investigated. As illustrated in Figure 5.13b, MEA-2 cannot achieve current densities of 1 A cm^{-2} and higher after its EOL state has been achieved within CR AST. This is in alignment with the results observed at 30° C during steady-state normal operation (CR AST, cf. Figure 5.4) and hydrogen pump polarization curves (cf. Figure 5.11). In contrast, for MEA-1 normal operation at 68° C up to 2.1 A cm^{-2} was possible with a comparably small performance decay. At 2.1 A cm^{-2} a voltage loss of 78 mV was observed (cf. Figure 5.12). The observed cathode proton resistance and HFR increases cause an estimated overpotential of 38 mV at this current density. Consequently, an HOR overpotential resistance increase of 40 mV can

be estimated. This comparatively small HOR overpotential increase is clearly contradicting the results of both CR AST and hydrogen pump polarization curves, where MEA failure due to an HOR mass transport overpotential increase was found. Therefore, a subsequent steady-state polarization curve at the operating conditions of the cyclic reversal stress test (30° C, 80% *RH*) was recorded for MEA-1. This additional polarization curve is depicted in Figure 5.13a (open triangle marker) and exhibits MEA failure for current densities of 1 A cm^{-2} or higher. This failure aligns with failure during normal operation at a current density of 0.65 A cm^{-2} (cf. Figure 5.4 and Figure 5.5). This is validating MEA failure triggered and observed during CR AST, even if a subsequent recovery procedure is applied (air and hydrogen soak without load preceding the steady state polarization curve). Additionally, this result is corroborating the collapse of the anode catalyst layer. At a higher temperature water condensation becomes less likely, induced by the non-linear saturation vapor pressure dependency on temperature. Consequently, at lower temperatures water condensation is leading to more dominant mass transport limitations caused by a collapsed anode structure. If the catalyst layer collapses due to carbon corrosion, only few open pores remain in the catalyst layer. At lower temperatures these remaining pores are more likely blocked by condensed water. Thus, the supplied gaseous hydrogen is no longer able to diffuse to the active HOR catalyst sites. This substantial temperature dependence on performance highlights catalyst layer flooding. Simultaneously, the substantial temperature dependence is weakening the hypothesis of local Pt loading decrease being mainly responsible for the sharp HOR mass transport overpotential increase. Such local Pt decrease phenomena was reported by Weber et al [165]. Certainly, this effect also contributes to the observed mass transport in this study, indicated by the substantial *ECSA* loss on the anode. However, the intense temperature dependence is strongly indicating ACL collapse as the major lever for HOR mass transport increase and MEA failure during CR AST.

Additionally, the severe performance dependence on temperature is highlighting a possible underestimation of degradation for reversal stress tests performed at higher temperatures. Whereas the performance results at 68° C are indicating a low MEA degradation level for MEA-1, substantial performance decay at lower temperature is observed. However, for automotive applications the low temperature fuel cell performance is crucial to ensure a robust cold-start ability, e.g. after long idle times which occur periodically. Besides, a collapsed anode structure within a cell in an automotive stack would have a self-reinforcing effect: reversal events would become more likely in the affected cells due to mass transport limitations.

The indicated ACL collapse contributes mainly to MEA failure during CR AST. This highlights the advantage of such ASTs, applying short-term reversal events alternating with normal operation, compared to non-cyclic reversal ASTs where a single, prolonged reversal event is applied. During non-cyclic reversal ASTs predominantly the activity of the oxygen evolution reaction is monitored, while simultaneously the COR contribution

to the total faradic current is masked due to its smaller reaction rates within reversal events [100, 114]. However, the results for CR AST have proven that even when the anode structure collapsed already and substantial HOR overpotentials arise, OER can be performed without significant overpotential increase (cf. Figure 5.4). OER mass transport is more likely dependent on ionic pathways (ionomer) within the ACL than on diffusive gas transport in the catalyst layer's pores (e.g. diffusive transport of oxygen to the active OER catalyst sites). Consequently, OER could still be performed during a single prolonged reversal event (non-cyclic), whereas significant mass transport limitations and catalyst layer collapse are already present, inhibiting the HOR. This is highlighting that cell voltage monitoring during reversal operation, mainly indicating OER activity, is insufficient to evaluate the integrity of the anode catalyst layer. In contrast, monitoring the fuel cell performance on a regular basis is crucial to evaluate MEA degradation caused by reversal events. Preferably, fuel cell performance is evaluated at low cell temperatures to reveal substantial structural changes in the ACL at an early stage.

5.1.2.6 OER recovery effect at elevated temperatures

In literature, reversal tolerance is commonly determined via NCR ASTs at temperatures between 60 and 80 °C and a current density of 0.2 A cm^{-2}. For CR AST development, operating conditions representative for a start-up procedure occurring on stack level were approximated. Reversal events in automotive applications most likely occur due to icing on a cell inlet and appear at stack temperatures < 0°C. Ice blockages can still exist during warm-up but become highly unlikely at stack temperatures above 30 °C. Therefore, 30 °C is regarded as a worst-case scenario for gross fuel starvation events caused by icing. In addition, reversal events due to liquid water accumulation during start-up events above freezing temperatures are covered by this operating point. The current density of 0.62 A cm^{-2} was introduced as current densities of 0.2 A cm^{-2} are probably exceeded before the fuel starvation root cause is mitigated in field operation. Consequently, the successive increase of the investigated current density from 0.17 to 0.62 A cm^{-2} during CR AST is realistically simulating current densities occurring during stack start-up procedures in field operation. An additional positive side effect of the second current density is the ability to determine the onset of OER (or COR) mass transport increase during reversal operation.

To illustrate and further validate the discussed OER recovery effect, two identical and pristine reversal tolerant MEAs (MEA-3, cf. Table 4.1) based on a IrO$_2$ co-catalyst were investigated. The incorporated cathode catalyst layer, and membrane were identical as for MEA-1 and -2. The pristine MEAs were investigated within an adopted NCR and CR AST experiment, where during CR AST only a single current density was investigated. In addition, the operating conditions were customized to represent commonly applied temperatures and *RH* in literature. Both ASTs were performed at a reversal

current density of 0.2 A cm^{-2}. Consequently, within each cycle 240 s of reversal operation at 0.2 A cm^{-2} was applied within the adapted CR AST. Cell temperature was set to 60 °C at 100% *RH* and gas flow rates of 2/12 ln min^{-1} on anode/cathode respectively. All other operating parameters were not varied (cf. Experimental section). The results are depicted in Figure 5.14.
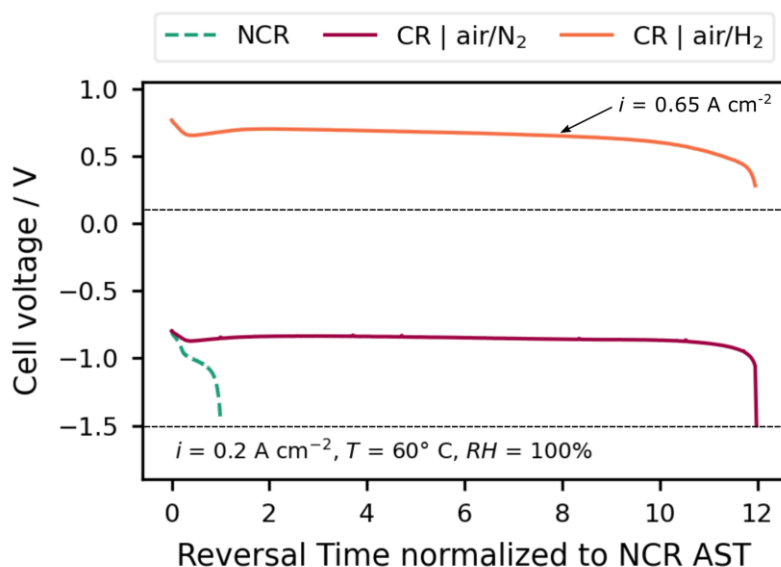
Figure 5.14: Two identical, pristine MEAs (MEA-3, cf. Table 4.1) were investigated within an adapted NCR (dashed line) and CR AST (solid lines). Both ASTs were adapted to the following operating conditions: 60° C, 100/100% *RH*, 2/12 ln min^{-1}, 1.7/1.5 barg (anode/cathode). CR AST was modified investigating solely a reversal current density of 0.2 A cm^{-2} for 240 s within each cycle applied.

Due to the OER recovery effect, the reversal time (or tolerance) before a failure criterion was triggered is 12-fold increased for the cyclic reversal AST. Cell voltage profiles are comparable to Figure 5.3. During NCR AST a rapid cell voltage decrease is observed, triggering MEA failure for cell voltages < -1.5 V. For CR AST the cell voltage during reversal operation is forming a stable plateau upon a few cycles before failure criterion is triggered (during reversal). Normal operation during adapted CR AST is showing minor decrease upon a few cycles before the reversal failure criterion is triggered. At the EOL state severe performance decay during normal operation is observed.

In contrast, for regular CR AST (30° C, two reversal current densities) MEA failure was triggered due to normal operation whereas during reversal operation no OER performance decay was observed, even EOL (cf. Figure 5.4). For the adapted AST at 60 °C (cf. Figure 5.14) undetected anode collapse before a failure criterion is met should be considered, as the increased temperature is most likely concealing severe HOR mass transport increase (discussed above). This aspect might explain the differing EOL failure criterion for the adapted CR at 60 °C (reversal failure), where HOR is still possible

with a collapsed anode structure, compared to the regular CR AST at 30° C (HOR failure).

5.2 Ex-situ imaging analysis

To further validate the assumed anode collapse via in-situ measurements on MEA level, cross sectional images were taken via SEM prior and after CR AST from MEA-2. The acquired images representative for the anode thickness decrease and degradation are shown in Figure 5.15.
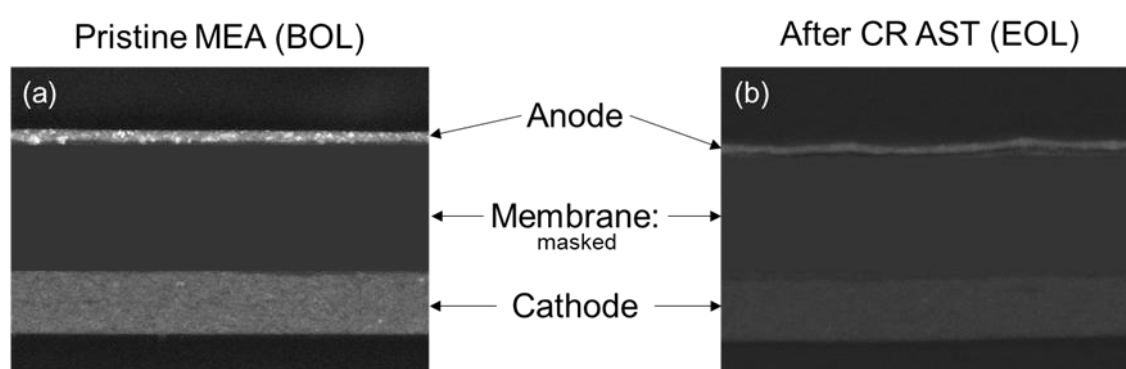
Figure 5.15: Cross sectional SEM images for MEA-2 to investigate anode degradation and thickness. (a) pristine, as-produced CCM. (b) MEA-2 after CR AST was performed. SEM taken with an acceleration voltage of 5 kV. The membrane cross-sections cannot be disclosed, and therefore were masked.

SEM images illustrate how the anode thickness decreases during the applied reversal stress test homogeneously along the anode catalyst layer. Anode collapse after the cyclic reversal AST becomes apparent. The average anode thickness decreases by 27 % (BOL standard deviation: 9%). For the CCL and membrane no significant change in layer thickness change could be observed. The thickness change was calculated from 30 locations within 6 cross-sections (evenly distributed over the active area) per MEA. End-of-life disconnection of the anode from the membrane can be observed. Whether the disconnection is originating from a sample preparation artifact or a disconnection caused by the AST cannot be evaluated.

The results obtained via in-situ measurements are corroborated by imaging:

- No cathode catalyst layer and membrane thinning observed.
- ACL collapse is the major contributor to MEA failure. This results in substantial increased HOR mass transport, amplified at low temperatures.
- HOR catalyst is still present EOL, leading to the measurable performance at high temperatures.

- OER catalyst is still present EOL (bright spots in SEM images). However, qualitative comparison is complicated due to differing image contrasts.

5.3   Conclusion

The reversal tolerance of PEFCs based on OER co-catalysts can be attained via different AST approaches. A novel cyclic reversal (CR) AST was developed, which is alternating short-term reversal operation and normal operation at low temperatures. The AST is used to approximate the occurrence of realistic cell reversal events occurring during field operation. Predominantly, the developed AST procedure is aimed at mimicking degradation caused by reversal events within freeze start-ups of automotive applications. The degradation caused by CR AST was compared to state-of-the-art non-cyclic reversal (NCR) ASTs, commonly applied for determining the reversal tolerance of reversal tolerant anodes (RTAs) based on OER co-catalysts.

Further insights in degradation mechanisms were obtained by combining the developed cyclic reversal stress test with additional characterization methods such as cyclic voltammetry, EIS and hydrogen pump polarization curves.

Cyclic reversal AST: The possibility of MEA failure during normal operation was observed. At the same time OER activity stays intact during reversal operation for the investigated MEAs. Consequently, this result indicates an OER recovery effect for recurring short-term reversal operation, whereas commonly OER deactivation is reported for non-cyclic reversal ASTs. The OER recovery effect was validated at elevated temperatures as well and was shown to increase reversal tolerance significantly.

The occurring failure mode was analyzed by further investigating the observed increased overpotentials during normal operation. The increase of ohmic resistances and cathode overpotential was proven to be negligible for MEA failure due to the reversal stress test. In contrast, normal operation failure was attributed to a significant increase in HOR overpotential on the anode. Despite a significant increase in kinetic HOR overpotential, HOR mass transport overpotential increase was identified as major contributor for voltage loss during normal operation and subsequent MEA failure. The increase in mass transport overpotential strongly indicates a substantial change in the ACL structure with increasing reversal events, most likely due to ACL collapse caused by carbon corrosion. Additional in-situ results of EOL polarization curves and anode CV measurements corroborate these assumptions. Severe performance decay was observed, amplified for low temperatures. The structural change and anode collapse indicated by in-situ measurements were confirmed via SEM imaging. Consequently, the presented characterization methods were proven to allow fast and cost efficient in-situ determination of MEA failure during CR AST which can be easily implemented during the testing of reversal tolerant anodes.

The reversal tolerance of RTAs based on IrO_2 OER co-catalysts was shown to be significantly dependent on the HOR catalyst, despite introducing an identical, highly active OER catalyst. Two MEAs differing solely in the incorporated HOR catalyst were investigated. For both MEAs platinum supported on graphitized carbon was used, with varying graphitization degree. An increase in reversal tolerance by a factor of ≈ 2.4 due to the differing HOR catalyst was observed for both investigated ASTs.

Furthermore, OER can be performed without significant voltage loss in the presence of a strongly corroded and collapsed ACL. This highlights that OER activity is not sufficient evidence for intact anode catalyst layers. Consequently, state-of-the art non-cyclic reversal stress tests, predominantly monitoring OER activity, are a fast and effective testing method to screen multiple OER catalysts or concepts for RTAs. However, different testing methods and further scientific research is necessary to investigate the reversal tolerance of ACLs realistically and to obtain further insights on complementary intrinsic degradation effects within the ACL as well as deriving correlations between incorporated ACL components (e.g. HOR and OER catalyst). The reported dependence of reversal tolerance on HOR catalyst used within the anode exemplifies this aspect. Whether this is based on a primary effect due to HOR catalyst properties itself or a secondary effect, for example due to a changed ACL structure, is beyond the scope of this thesis.

The developed cyclic reversal AST in combination with hydrogen pump experiments set an optimal framework to allow for investigations on OER based RTAs, which are crucial for PEFC durability and thus commercial implementation of the sustainable PEFC technology across all sectors.

6 Durability of OER based RTAs under transient conditions

In this chapter the ageing of PEFC anodes containing an OER co-catalyst during regular fuel cell operation is investigated and discussed. In the absence of reversal events, the anode catalyst layer can be exposed to significant degradation caused by transient conditions. Besides ageing of the incorporated HOR catalyst, the OER co-catalyst can degrade substantially, inducing additional degradation effects. Two varying start-up/shut-down ASTs were developed to simulate anode degradation. In addition, in-situ characterization methods were developed to allow for in-depth analysis of the resulting degradation effects on the anode catalyst layer and MEA.

Anode degradation during start-up/shut-down (SUSD) transient conditions or local fuel starvation events is believed to be mainly induced by the anode potential cycling from ≈ 0 to ≈ 1 V_{RHE} [35]. Probably the most efficient way to perform potential cycling on single cell level is by applying potential on the working electrode (i.e. PEFC anode) by an external power supply under inert gas atmosphere, while the counter electrode (i.e. PEFC cathode) acts as reference electrode in hydrogen atmosphere. This maintains the respective electrode potential close to zero. However, ASTs imposing a cycling anode potential cannot reproduce SUSD events as they would occur during field operation. Potentiostatic tests may simulate the degradation of the HOR catalyst sufficiently [35]. But in a real-world scenario, the impact of chemical reactions by reactant gases (e.g. reduction of IrO_2 in hydrogen atmosphere) as well as ionic and electric pathways within the MEA most likely impact the dissolution, migration and redeposition of OER catalyst. Therefore, more realistic SUSD ASTs based on cycling the anode gas supply between hydrogen and air are used within this work.

Besides HOR induced anode degradation, the SUSD degradation of anode catalyst layers including IrO_2 based OER co-catalysts was recently investigated [70, 128]. Due to the reductive hydrogen atmosphere during normal fuel cell operation, IrO_2 on the anode can be reduced to metallic iridium on the catalyst surface [70]. During the chemical reduction from IrO_2 to Ir, according to the respective Pourbaix diagram [166], soluble Ir^{3+} can be formed as an intermediate. Subsequently, these soluble Ir^{3+} can migrate to the cathode, referred to as iridium crossover, resulting to reduced reversal tolerance by a loss of OER activity on the anode and detrimental effects on the cathode ORR performance [70, 128].

Moore et al. investigated the dissolution of IrO_2 catalysts during a novel ex-situ stress test and the stabilizing impact of OER supports [128]. The dissolution of IrO_2 during the

developed ex-situ AST was investigated by determining the dissolved species in the electrolyte via inductively coupled plasma mass spectrometry. The measured dissolution of IrO_2 correlated with a loss in reversal tolerance after SUSD AST. Tovini et al. investigated the chemical reduction of supported IrO_2 catalysts to metallic iridium in hydrogen atmosphere and showed that Ir crossover in MEAs can be caused by SUSD events, leading to redeposition of Ir species on the cathode and a decrease in fuel cell performance [70].

However, the development of in-situ SUSD ASTs, based on gas-switching and focusing primarily on anode induced degradation in the presence of IrO_2 co-catalysts, has not been reported yet. Furthermore, to the best of the author's knowledge, in-situ characterization methods to investigate Ir crossover and its comprehensive impact on MEA degradation have not been reported so far.

Therefore, the degradation due to transient anode potentials is investigated within this thesis via cycling the anode gas supply between H_2 and air to mimic SUSD events as they would occur during regular field operation. A major scope during the AST development in this work was to suppress the simultaneously occurring cathode degradation during gas switches to highlight the effect of the anode stressor. Typically, SUSD investigations are focused on cathode degradation due to the high cathode potentials ≥ 1.4 V caused by the reverse-current effect, resulting in severe carbon corrosion [38, 97]. However, recent results are considering anode HOR catalyst degradation occurring during SUSD events as an stressor which should be considered [35, 96]. Applying this stressor on reversal tolerant anode concepts containing OER co-catalysts, characterization methods to investigate the comprehensive degradation of PEFC anodes need to be developed. Furthermore, the observed degradation should distinguish between degradation induced by the HOR catalyst (activity and mass transport overpotential) and the incorporated OER co-catalyst (Ir crossover and reversal tolerance).

To implement reduced cathode degradation during the developed SUSD stress tests induced by the reverse-current effect, the residence time of air/hydrogen fronts in the anode compartment was reduced to a minimum, while simultaneously testing at low temperatures (see Experimental section for details). Thereby, the reverse-current induced cathode degradation should be reduced significantly [97] allowing for a better resolution of anode degradation (e.g. HOR overpotential) and cathode degradation induced by Ir crossover. The latter has been reported most recently for reversal tolerant anodes containing IrO_2 co-catalysts [70, 128] and was also reported for Ru-containing anode concepts aiming for increased CO tolerance [92, 94].

To vary the stressor for possible Ir migration and Ir redeposition, two varying SUSD ASTs were developed. During the so-called SUSD-pot AST, cell voltage was kept below 0.5 V by potentiostatic load control. This is expected to result in an increased and/or faster migration of Ir^{3+} species from the anode across the membrane, as the mi-

gration of protons depends on the charge balancing of the external electrical circuit. The potential load control might also impact the electrochemical state of Ir species on the cathode. The cathode potential during SUSD-pot AST cycles between ≈ 0.5 V (H_2/air operation) and ≈ 1.5 V during the SUSD event (cf. Figure 4.5).
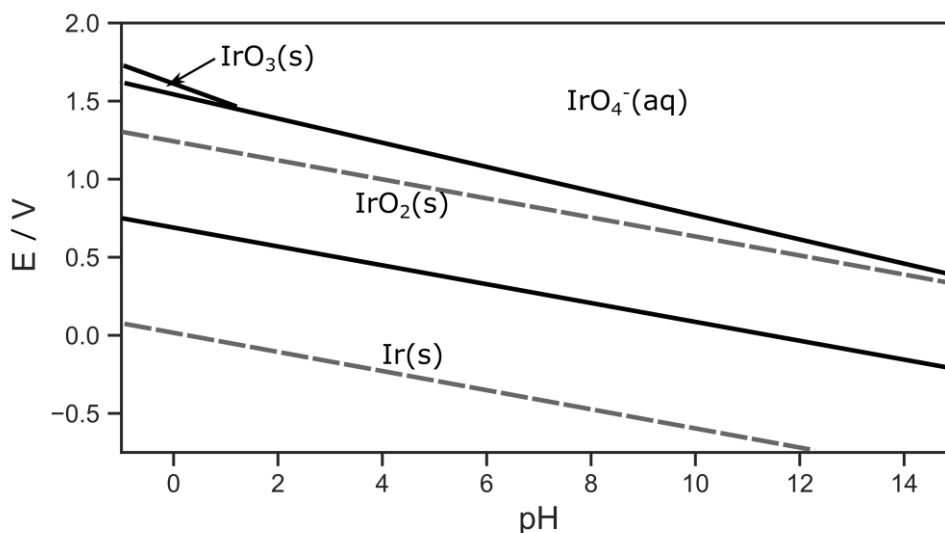
Figure 6.1: Schematic Pourbaix diagram for the electrochemical equilibria of iridium in aqueous electrolyte according to literature (corresponding to an Ir concentration of 10^{-6} M at 25 °C) [166, 167]. The water stability window is shown in grey dashed line.

According to the Pourbaix diagram (cf. Figure 6.1) in acidic media (pH ≈ 0) a thermodynamically stable metallic Ir phase on the cathode should change to a thermodynamically stable IrO_2 phase at voltages above ≈ 0.8 V (and vice versa) [166, 167]. Voltage clipping during SUSD events might further decrease the occurring cathode degradation induced via reverse-current effect [159]. During the AST variation without drawing any current, referred to as SUSD-OCV, the migration of Ir^{3+} across the membrane is expected to be reduced due to the absence of charge transfer via the external electrical circuit. In addition, the cathode half-cell potential should not fall below ≈ 1 V (cf. Figure 4.5) during the AST. Therefore, a phase change from crossed-over IrO_2 to Ir, which in turn might dissolve again on the cathode, is not expected.

For both ASTs the anode stressor via gas switch induced anode potential change is identical (also compare Figure 4.5). Degradation for the two ASTs should vary solely regarding secondary MEA degradation effects induced by possible Ir crossover and subsequent Ir precipitation or deposition within the membrane or the cathode catalyst layer. For both AST variations two identical OER based reversal tolerant MEAs were investigated.

To analyze the SUSD induced degradation, several in-situ characterization procedures were applied before and after the AST (cf. Figure 4.4 and section 4.2.9):

- H_2/air polarization curves (MEA performance loss)
- Cyclic voltammetry
    - H_{upd} (electrochemical surface area)
    - CO stripping (electrochemical surface area)
    - OER activity (OER degradation and Ir crossover)
- Hydrogen crossover (membrane degradation)
- EIS (ohmic and proton resistance increase)

Furthermore, hydrogen pump experiments were performed to assess HOR performance loss and evaluate possible structural changes within the anode catalyst layer. The impact of SUSD induced degradation on reversal tolerance was analyzed by performing cyclic reversal ASTs. Finally, imaging was performed to validate the obtained in-situ results.

A MEA without an OER co-catalyst was used as a baseline sample for better context of the observations during SUSD testing.

6.1 Electrochemical results and discussion

6.1.1 PEFC performance loss
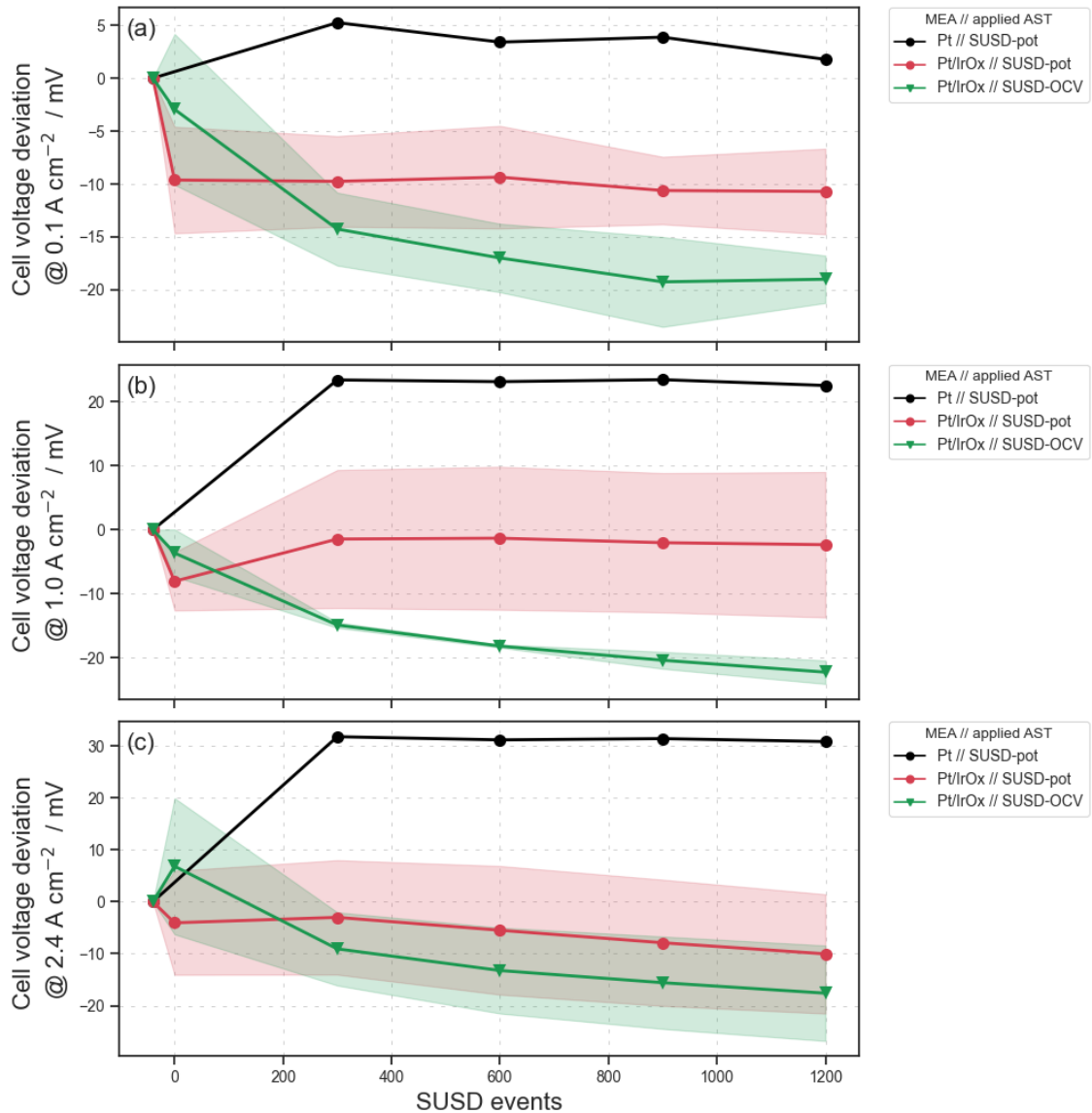
Figure 6.2: (a)-(c) Performance loss at 68° C for varying current densities during the respective SUSD AST compared to BOL performance. SUSD events < 0: BOL performance during conditioning and prior to characterization procedure; SUSD events = 0: BOT performance after characterization procedure and before SUSD AST. Data points: mean values. Shaded region: divergence of two repeated measurements with pristine MEAs. For Pt-MEA only a single MEA was investigated.

To evaluate the impact of SUSD induced fuel cell performance decrease, polarization curves at 68° C were recorded after MEA conditioning, preceding the BOL characterization measurements and after each consecutive 300 SUSD events (see Experimental section Figure 4.4). In Figure 6.2 the respective performance losses with increasing

115

SUSD events are depicted for varying current densities. Current densities are chosen to be representative for the activation, ohmic or mass transport overpotential dominated regime of the polarization curve, respectively (cf. section 2.3). All investigated MEA designs were solely differing regarding the incorporated anode catalyst layer, whereas the employed cathode electrode and membrane were identical. The reversal intolerant ACL, solely containing Pt/C HOR catalyst, is referred to as Pt-MEA and was aged using SUSD-pot AST. The reversal tolerant MEAs, referred to as Pt/IrO$_x$ -MEAs, were investigated within both AST variants.

Table 6.1: SUSD degradation rate derived by linear regression (not considering initial conditioning effects before 300 SUSD cycles).

MEA	AST	Voltage loss at 0.1 A cm^{-2} [μV/cycle]	Voltage loss at 1 A cm^{-2} [μV/cycle]	Voltage loss at 2.4 A cm^{-2} [μV/cycle]
Pt	SUSD-pot	3.32	0.76	0.85
Pt/IrO$_x$	SUSD-pot	1.37	1.12	7.83
Pt/IrO$_x$	SUSD-OCV	5.49	8.08	9.31

Pt-MEA // SUSD-pot AST

During SUSD-pot AST the anode gas supply is switched from air to hydrogen and vice versa every 30 s while the cell voltage is cycling between ≈ 0.5 V (air/H$_2$ on cathode/anode with potentiostatic load control) and ≈ 0 V (air/air). The Pt only MEA is showing an increased PEFC performance after 300 start-up/shut-downs. Subsequently, a more or less stable cell performance is obtained with increasing SUSD events. The performance after 1200 SUSD events still exceeds the initial BOL performance. These observations are valid for all three investigated current densities (cf. Figure 6.2 a-c).

The performance increase can most likely be explained by a conditioning effect (also referred to as break-in) of the cathode catalyst layer within the first 300 SUSDs [168]. At the chosen operating conditions and HOR catalyst loadings, the anode overpotentials for unaged MEAs are negligible (even a substantially degraded and collapsed ACL was showing minor performance decay at this operating conditions, cf. section 1). Therefore, performance increase by a structural change of the cathode catalyst layer rather than by an anode induced effect is indicated. There is ample literature present describing a cathode catalyst layer porosity increase due to carbon corrosion during SUSD and external cathode potential cycling events [84, 91, 133, 169, 170].

While carbon corrosion is generally associated with severe performance degradation, the initial effects on performance are often positive in nature and can be summarized as follows:

- Improved diffusive gas transport and better permeability for product water [169, 171].
- New pathways to previously inaccessible Pt catalyst cluster within the pores of the carbon support [168].
- redistribution of ionomer resulting in a decreased mass transport resistance for oxygen [169, 172].

The assumption that an increased porosity is causing the initial performance increase is corroborated by an increased double layer capacitance for this MEA after the AST, which will be discussed in section 6.1.3.

Furthermore, the results are illustrating the achieved reduction in cathode degradation for the developed SUSD AST. The voltage degradation rates derived via linear regression, not considering initial conditioning effects within the first 300 SUSD cycles, are listed in Table 6.1. For the kinetically dominated voltage loss regime, a voltage loss of 3.32 μV/cycle is observed (cf. Table 6.1). For the 1200 cycles applied this would lead to an overpotential increase of 3.98 mV if a conditioning effect is not considered. Assuming this overpotential loss is mainly dominated by an increase in ORR activation overpotential on the cathode, an *ECSA* loss induced kinetical overpotential estimation can be derived by the Tafel kinetics (cf. Equation 2.11) [97]:

$$\Delta E_{\mathrm{ORR}}^{\mathrm{cathode}} = \frac{R \cdot T}{\alpha_c \cdot F} \ln \left(\frac{ECSA_{\mathrm{EOL}}}{ECSA_{\mathrm{BOL}}} \right) \tag{6.1}$$

where α_c=1. For the apparent cathode *ECSA* loss of 10.4% (mean loss for H_{upd} and CO stripping with respect to the BOL value) a kinetical ORR overpotential increase $\Delta E_{\mathrm{ORR}}^{\mathrm{cathode}}$ of 3.22 mV would be achieved, which is in good agreement with the experimentally derived voltage loss in the kinetically dominated current regime (0.1 A cm^{-2}) of 3.98 mV.

However, this is indicating that the overpotential increase induced by kinetic overpotential is most likely compensated via decreased ohmic or mass transport overpotentials at high current densities. At a current density of 2.4 A cm^{-2} a degradation rate of 0.85 μV/cycle is achieved (cf. Table 6.1, adjusted for conditioning effects), leading to a total voltage loss of 1.02 mV after 1200 cycles. This results in a lower performance degradation than expected by *ECSA* loss and performance at 0.1 A cm^{-2}. Additionally, the total performance increase by 31 mV is an order of magnitude higher as the degradation rates not considering the initial conditioning effect. Consequently, the degradation behavior of the MEA containing only Pt catalyst on the ACL demonstrates, that the

developed SUSD-pot AST has a minor impact on reverse-current induced cathode degradation. This characteristic will allow for a precise monitoring of cathode degradation induced by Ir crossover.

Pt/IrO$_x$-MEA

SUSD-pot AST:

The SUSD-pot AST was also applied on an MEA containing IrO$_2$ as OER co-catalyst. The absolute BOL performance deviation for this MEA design was comparable to the Pt-MEA ($\leq$ 15 mV). However, the performance degradation profile differs significantly when an OER co-catalyst is introduced to the MEA. Despite an identical cathode catalyst layer, no conditioning effect can be observed for this MEA within the initial cycles. In contrast, an initial performance decrease can be observed, most pronounced within low current densities (cf. Figure 6.2). Subsequently, the degradation rates are higher compared to the Pt-MEA (cf. Table 6.1), except for the performance at 0.1 A cm^{-2}. Especially for the high current density the degradation rate is increased by a factor of $\approx$ 9 compared to the Pt-MEA, indicating a co-catalyst dependent degradation behavior

The differing performance degradation during SUSD-pot AST can be either explained by a suppressed conditioning effect or by a OER co-catalyst induced degradation effect superimposing MEA conditioning. The significant increased degradation rate at 2.4 A cm^{-2} is leading to a pronounced, linear voltage loss with increasing SUSD events (cf. Figure 6.2c). Consequently, a continuous and superimposed degradation effect in the presence of IrO$_2$ is observed. The crossover of Ir (discussed in section 6.1.3) has the potential to strongly contribute to the continuous performance loss with increasing SUSD events. The cell performance after 1200 potentiostatic SUSD events is lower as the initial performance at all investigated current densities, which is in contrast to the Pt-MEA results. However, the comparably high divergence between repeated measurements should be noted, which could result from sample-to-sample variations.

SUSD-OCV AST:

For the AST variation SUSD-OCV the anode gas supply was also switched from air to hydrogen and vice versa. In contrast to the potentiostatic SUSD no load was applied during the gas switches, resulting in the cell voltage cycling between $\approx$ 0.95 V (air/H$_2$ on cathode/anode, no load applied) and $\approx$ 0 V (air/air). As outlined before, this could

- decrease Ir crossover (cationic migration across the membrane depends on the charge balancing of the external electrical circuit)
- impact Ir redeposition (cathode potential not below thermodynamically stable IrO$_2$ phase)
- impact cathode degradation (no voltage clipping).

The anode stressor should be similar within both AST variations. The anode stressor is induced by the gas switch on the anode, resulting in cycling the anode half-cell potential between ≈ 0 V_{RHE} (H_2) and ≈ 0.95 V_{RHE} (air). Consequently, a differing performance degradation between both ASTs is an indicator for a differing cathode degradation.

For SUSD-OCV, the performance degradation is again showing a comparable behavior as for the potentiostatic AST. No initial performance increase within the first 300 SUSD cycles is observed. However, a performance decrease is indicative of a negligible or superimposed conditioning effect in the presence of OER co-catalyst.

The performance decreases and degradation rates are higher as for potentiostatic SUSD events, emphasized especially for current densities where kinetic and ohmic overpotentials are dominating (cf. Figure 6.2 and Table 6.1). This substantiates increased cathode degradation:

- either by higher primary cathode degradation (carbon corrosion) due to the absence of voltage clipping during the SUSD events or
- due to increased cathode poisoning induced by a change in Ir crossover and/or redeposition on the cathode electrode.

However, the higher degradation rates at 0.1 A cm^{-2} and 1.0 A cm^{-2} for this AST variation is indicative of Ir poisoning being the major contributor. At the chosen operating conditions (low residence time and low temperature) severe carbon corrosion on the cathode should be suppressed, even in the absence of voltage clipping. Instead, minor accelerated carbon corrosion in the absence of voltage clipping is expected to increase MEA performance due to increased CCL porosity. However, at 2.4 A cm^{-2} no significant performance increase for this AST variant is observed. At high current densities, a porosity increase is anticipated to have the highest performance impact.

To resolve the differences obtained in performance degradation dependent on the incorporated IrO_2 co-catalyst and the AST variation, further characterization methods were performed to investigate the occurring degradation. In the following, degradation is discussed for each CCM component separately.

6.1.2 Membrane degradation

The performed SUSD ASTs were not expected to have a significant impact on membrane degradation.

However, the membrane degradation was monitored via hydrogen crossover and HFR measurements. The results observed within EIS and CV measurements showed no significant change in hydrogen crossover nor HFR after 1200 SUSD events (cf. Appendix-Figure 5 and Appendix-Figure 6). The observed minor changes in HFR can, there-

fore, be explained by varying membrane humidification resulting from potentiostatic pre-conditioning. The minor changes in hydrogen crossover might originate from the same effect and in addition form the Pt band formation found within the membrane after SUSD AST (discussed in section 6.2), which is known to impact hydrogen crossover [173]. Consequently, negligible membrane degradation can be assumed. This assumption is further corroborated by the obtained post-mortem ex-situ results in section 6.2.

6.1.3 Cathode degradation

In the following, the cathode degradation is further investigated and discussed. The section is structured by the performed characterization techniques. The significantly increased performance degradation in the presence of IrO_2 is strongly indicating cathode poisoning by crossed-over Ir species as major contributor.

The Ir crossover mechanism has been reported as following [70, 128]: Soluble Ir^{3+} species are formed on the anode and subsequently migrate within the ionomer phase across the membrane. The cation transport across the membrane is driven by the electric field and the concentration gradient (diffusion). Subsequent redeposition on membrane or cathode is then determined by local chemical and potential conditions within the respective layers [128]. Soluble Ir^{3+} species for IrO_2 based ACL are originating either from the pristine OER catalyst (e.g. residues from catalyst or MEA manufacturing) or are formed by reduction of Ir^{4+} (IrO_2) species during operation [128]. The reduction from Ir^{4+} to Ir^{3+} species is most driven by the so-called transient dissolution, which is also known from common Pt based catalysts [174]. Transient dissolution describes the anodic or cathodic catalyst dissolution originating by applying a transient electrical potential. Therefore, transient dissolution is substantially amplified by potential cycling. In the case of transient dissolution of Ir, the square-wave like voltage cycling during SUSD events are believed to mainly promote Ir dissolution [70, 175, 176]. During an air/air start, the anode potential jumps from ≈ 0 V_{RHE} (H_2) to ≈ 1 V_{RHE} (air) in a stepwise form. For a shut-down event, the anode potential jumps vice versa.

To evaluate the possible Ir crossover from the anode catalyst layer to the cathode, an in-situ method is developed evaluating the OER activity in the cathode catalyst layer. Former works already proved Ir crossover via ex-situ methods. The research group of Tovini et al. most recently found evidence of Ir species present on the cathode catalyst layer after 500 SUSD events applied via XPS measurements [70]. Moore et al. developed an ex-situ AST to simulate Ir dissolution of reversal tolerant anodes realistically. Ir crossover within the ex-situ AST and an in-situ performed SUSD were subsequently quantified via ex-situ measurements of the Ir concentration in liquid electrolyte and via EDX analysis after the in-situ SUSD [128]. However, the application of measurements ex-situ before/after the electrochemical characterization on MEA level is challenging in

terms of testing time, resources and testing complexity. In contrast, in-situ measurements can be easily implemented using single cell test station equipment in the absence of external sample preparation. In addition, in-situ characterization methods allow for intermittent, non-destructive, investigations during ASTs. Therefore, analyzing the OER activity was implemented as in-situ electrochemical characterization method to detect Ir crossover. As the OER activity in acidic media should decrease in the following order Ir > $IrO_2 \gg$ Pt [146, 177], the crossover and redeposition of Ir species to the cathode in any form (Ir or IrO_2) should increase the OER performance on the cathode significantly.

6.1.3.1 OER activity
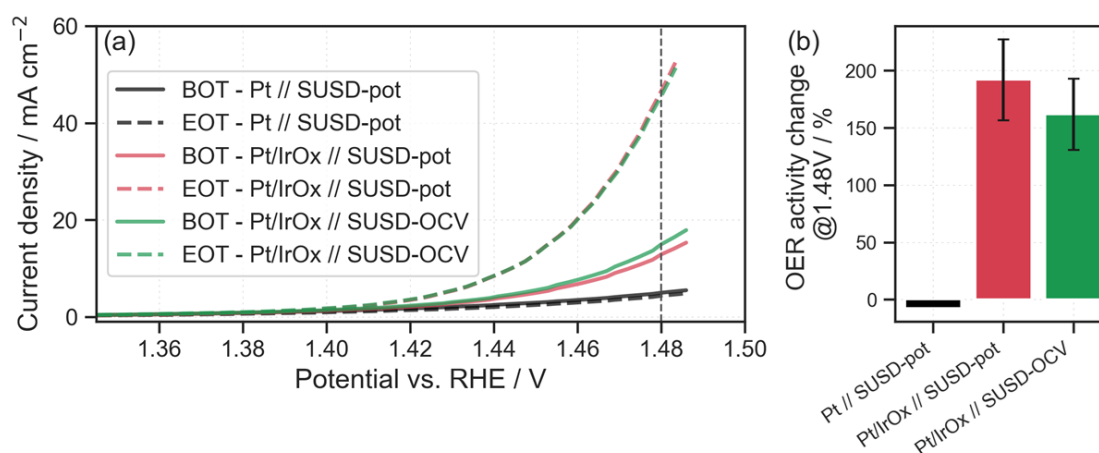
Figure 6.3: (a) Cathode OER polarization curves extracted from the anodic sweep of 9 subsequent cathode CVs at 20 mV s^{-1} between 0.1 and 1.49 V, before (BOT, solid lines) and after (EOT, dashed lines) the respective SUSD AST. Identical pristine cathode catalyst layers, solely incorporating Pt/C as ORR catalyst, were used for all MEAs. The current density was corrected for the capacitive current density observed at 1.3 V. For the Pt/IrO$_x$-MEAs the averaged values from two samples are depicted. Operating conditions: N$_2$/H$_2$ with a flow rate of 3.5/5 ln min^{-1} on cathode/anode, T=68° C; p=1 bar$_g$, RH=100%. EOT the red and green dashed lines are overlapping (cf. blue insert and see Appendix-Figure 3). (b) Cathode OER activity change after the performed SUSD AST extracted from OER polarization curves at 1.48 V$_{RHE}$ with respect to BOT. Error bars represent standard deviation derived from investigating two similar MEAs, respectively.

In Figure 6.3 the cathode OER activity before (BOT) and after (EOT) SUSD AST is depicted.

Pt-MEA:
If no IrO_2 catalyst is embedded as anode co-catalyst, no distinct OER onset potential for the cathode is observed within the investigated potential of $\leq$ 1.49 V$_{RHE}$. Consequently, neither before nor after the performed SUSD-pot AST a significant OER activity can be observed. As the cathode ORR catalyst investigated consists of Pt supported on carbon, the absence of a distinct OER onset activity is in alignment with literature, where the OER onset for platinum in acidic environment was reported for potentials $\geq$ 1.7 V [177]. The very small, apparent OER activity observed for the Pt-MEA extracted at 1.48 V$_{RHE}$ even slightly decreases after the applied SUSD AST (-13%, cf. Figure 6.3b). This can

potentially be explained by the observed cathode *ECSA* loss, which will be discussed later. An *ECSA* loss of Pt would, according to the kinetics, increase the OER overpotential.

Pt/IrO$_x$-MEAs:

When IrO$_2$ is introduced to the anode layer to achieve reversal tolerance, the OER activity on the cathode is increased even before the stress test was performed (cf. Figure 6.3a). Commonly, the OER onset potential of Ir in acidic media is reported to be in the region of 1.45 to 1.55 V$_{RHE}$ [146, 177], which aligns with the observed OER onset for Pt/IrO$_x$-MEAs (cf. Figure 6.3a).

As similar pristine cathode catalyst layers were used for all investigated MEAs, the increase in OER activity is strongly indicating the crossover of iridium. The OER activity increase beginning-of-test, compared to the Pt-MEA design, is remarkable. The incorporated OER catalyst consists of a heat treated IrO$_2$ catalyst carried on a metallic support (see section 4.1). One would expect, that this combination should lead to very low Ir dissolution rates [128]. However, the increased cathode OER activity BOT for the Pt/IrO$_x$-MEAs compared to the Pt-MEA is strongly indicating the presence of Ir or IrO$_2$ catalyst on the cathode already at this stage of the testing procedure, without promoting transient dissolution of Ir by SUSD events. Therefore, Ir crossover presumably occurs already within MEA conditioning and initial polarization curves (cf. Figure 4.4).

Conditioning and performance evaluation procedures included four air- and hydrogen soaks as recovery procedures to ensure reproducible measurements and catalyst layer recovery prior to any performance measurement. During each air-/hydrogen soak combination an air-/air start like behavior is performed, leading to an anode potential cycle from $\approx$ 0 V$_{RHE}$ to $\approx$ 1 V$_{RHE}$ in a square-wave form. This causes transient Ir dissolution, as discussed in the introduction of section 6.1.3. However, the remarkably increased cathode OER activity BOT, after only four air/air starts, is corroborating Ir dissolution by chemical reduction of IrO$_2$ to Ir in the presence of hydrogen as significant contributor. Intermediate soluble Ir^{3+} species can be formed during this chemical reduction [128, 166]. Such a behavior was reported during electrochemical surface oxide reduction of Ir at potentials $\approx$0 V$_{RHE}$ [145], which corresponds to the fuel cell's anode half-cell potential during normal operation in the presence of hydrogen.

Besides, the increase of OER activity after SUSD AST is significant. For both AST variations, an OER activity increase by a factor of $\approx$ 1.5 to $\approx$ 2 is observed (cf. Figure 6.3b), indicating a significant amount of Ir crossover and redeposition during the SUSD ASTs. As described above, Ir redeposition on the cathode after SUSD ASTs was already reported by other groups and validated using ex-situ characterization methods (via XPS measurements [70] and EDX [128]). However, to the best of the authors knowledge no in-situ characterization method to investigate Ir crossover has been reported so far.

The electrochemical state of the OER catalyst surface should be comparable between BOT and EOT state since a cleaning CV was performed prior to the measurement. In addition, the OER activity for each sample was determined from 9 consecutive CVs between 0.1 and 1.5 V_{RHE} to increase reproducibility. Consequently, an increase in OER activity on the cathode should correlate directly with the roughness factor (product of *ECSA* and catalyst loading, cf. Equation 3.7) increase of the present Ir species. Whether the present Ir is in metallic, hydrous or oxide form cannot be answered by the in-situ measurements. However, the low onset potential EOT is indicative of highly active metallic or hydrous species [146, 175, 178].

The kind of AST (SUSD-pot or SUSD-OCV) has a minor impact on the OER activity increase. The activity change illustrated by the bar plot (cf. Figure 6.3b) is predominantly arising by a difference in OER activity beginning-of-test. As the same MEAs and testing procedures prior to the AST were used, this is most likely originating from sample-to-sample variations. Assuming identical electrochemical iridium species present on the cathode after the respective stress test, this should indicate a comparable roughness factor of the OER catalyst after both ASTs. Therefore, the impact on Ir crossover and Ir redeposition by the AST variation seems to be minor, despite the different cathode potentials and ionic charge transfer across the membrane induced by the external electrical circuit. The minor impact of charge transfer could be explained by the periodic polarization curves performed after each 300 SUSD cycles. Soluble Ir species still present on the anode could migrate during these polarization curves, independent on the performed AST.

A comparable Ir crossover and redeposition for both AST variations could imply, that the observed difference in performance decrease is originating from another degradation mechanism. For example, one could speculate of increased cathode degradation by the reverse-current mechanism in the absence of voltage clipping, as discussed in section 6.1.3. In addition, the OER activity measurement might be too imprecise to resolve such small degradation differences quantitatively.

6.1.3.2 Cyclic voltammetry

To further analyze cathode degradation and the impact of the performed AST, *ECSA* measurements were performed via H_{upd} and CO stripping.
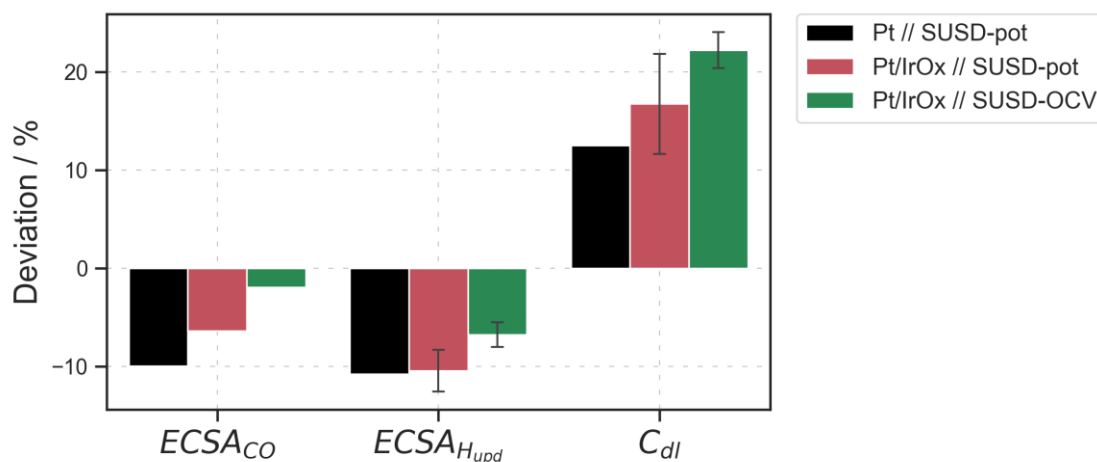
Figure 6.4: Observed changes in cathode *ECSA* by CO stripping and H_{upd} as well as in double layer capacitance C_{dl} after SUSD AST was applied. Operating conditions: T=68° C; p=1 bar$_g$, *RH*=100%. C_{dl} was estimated from the H_{upd} CV at a voltage of 0.45 V_{RHE}.

The observed changes in cathode *ECSA* and double layer capacitance during the ASTs are illustrated in Figure 6.4. For all investigated MEA and AST variations, a cathode *ECSA* loss is observed, both for CO stripping and H_{upd}. However, the *ECSA* loss amplitude for Pt/IrO$_x$-MEAs seems to be dependent on the *ECSA* measurement and the performed AST. Furthermore, a double layer capacitance C_{dl} increase is observed after SUSD AST. The double layer capacitance was estimated from the H_{upd} CVs at a potential of 0.45 V_{RHE}. The increased cathode degradation by *ECSA* loss for the SUSD-pot compared to SUSD-OCV is in contrast to the observed degradation rate during normal operation. The observed losses in *ECSA* and C_{dl} are further discussed in the discussion of the respective cyclic voltammograms.

H_{upd}

The cathode CVs obtained via H_{upd} prior and after the AST are depicted in Figure 6.5. The observed peak characteristics are typical for Pt/C catalysts: hydrogen ad-/desorption features at a potential range between 0.1 and 0.3 V_{RHE} and Pt oxidation/reduction peaks at potentials above 0.6 V_{RHE} [48].
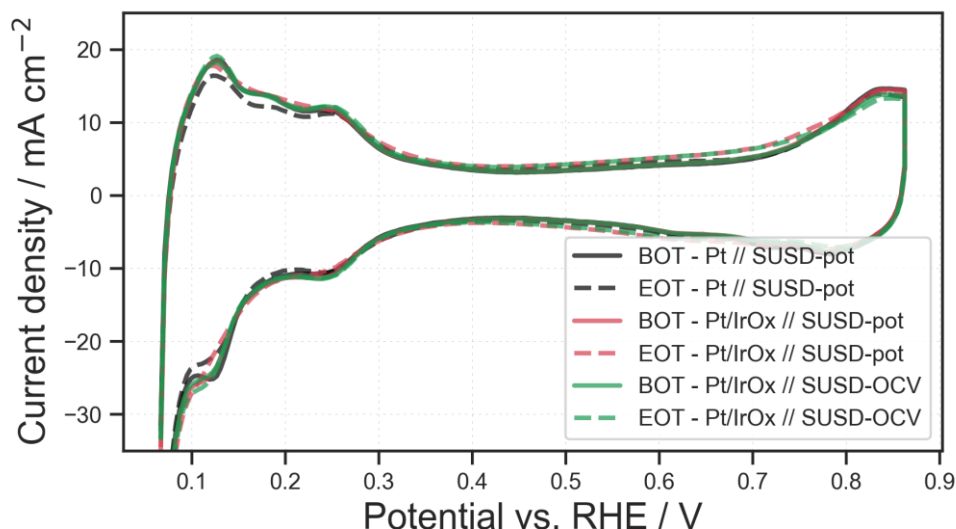
Figure 6.5: Cathode CVs prior (BOT) and succeeding (EOT) the respective SUSD AST. After a cleaning CV four contiguous CVs were recorded at *T*=68° C; *p*=1 bar$_g$, *RH*=100% with a scan rate of 100 mV s^{-1}, from which the last cycle is depicted. For the Pt/IrO$_x$-MEAs the current density is averaged from two investigated samples, respectively. Each CV was corrected by the respective capacitive charge observed at 0.45 V$_{RHE}$ to improve visual comparability. For better illustration of the double layer region see Appendix-Figure 4.

Pt-MEA:

Most distinct is the decrease in H$_{upd}$ features for the Pt-MEA after SUSD-pot AST. The resulting peak decrease is in alignment with the determined *ECSA* decrease (cf. Figure 6.4), most likely caused by a loss of Pt *ECSA* during SUSD AST [97]. In addition, the double layer capacitance increases (better visualized in Figure 6.4). An increase of C_{dl} can be attributed to the onset of carbon corrosion [179]. Commonly, the double layer capacitance within a SUSD AST initially increases due to increasing porosity in the cathode catalyst layer. Subsequently, C_{dl} decreases with contiguous SUSD events applied. The decrease is arising from continuous carbon corrosion leading to structural change with porosity loss and catalyst layer collapse [179]. Therefore, the observed *ECSA* loss and C_{dl} increase (cf. Figure 6.4 and Figure 6.5) are indicating minor cathode degradation, originating from carbon corrosion (inducing also secondary Pt degradation) and Pt dissolution. This is corroborated by the minor degradation rates observed during performance evaluation. This highlights that the developed AST is suppressing cathode degradation by the reverse-current during SUSD cycles.

Pt/IrO$_x$-MEA:

If IrO$_2$ is introduced to the anode, the general peak characteristics of the cathode CVs are not substantially affected, neither before nor after SUSD AST. However, two H$_{upd}$ features are changing for these MEAs after the stress test. The double layer capacitance in the region 0.45 to 0.75 V$_{RHE}$ increases, predominantly at higher potentials. This is again corroborating the crossover of Ir to the cathode, as Ir oxides are commonly show-

125

ing increased double layer capacitance within this potential regions [142, 147]. Furthermore, hydrogen desorption/-adsorption features are showing a slight decrease (cf. Figure 6.5), resulting in the respective *ECSA* decrease of ≈ 7 to 10% (cf. Figure 6.4). SUSD-pot seems to cause a higher *ECSA* loss, whereas the C_{dl} increase is lower (cf. Figure 6.4). This contradicts the observed performance losses. However, as H_{upd} is not solely possible on Pt, but also on metallic Ir, it is very difficult to determine the real *ECSA* loss of the Pt based ORR catalyst after Ir crossover. This could explain to the discrepancy between performance and apparent *ECSA* loss.

CO stripping

Therefore, the second *ECSA* determination method, CO stripping, was applied. CO stripping is commonly regarded as the more robust method for *ECSA* determination of Pt based catalysts, being less prone to changes in temperature and *RH* and allowing to determine the *ECSA* of smaller crystallite sizes [140, 141, 180, 181]. Similar to H_{upd}, metallic iridium was reported to allow chemical adsorption of CO species and subsequent electrochemical desorption during the stripping CV. In contrast, iridium oxides were found to be inactive for CO ad-/desorption [142].
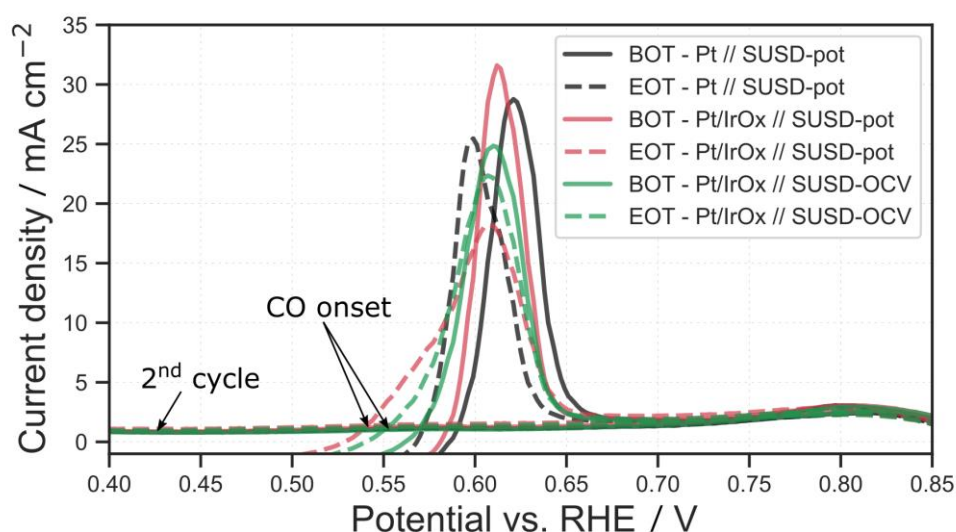
Figure 6.6: Cathode CO stripping measurements prior (BOT) and succeeding (EOT) SUSD AST. After two cleaning CVs, CO was adsorbed on the cathode catalyst sites for 3 minutes. The subsequent stripping CVs at T=68° C; p=1 bar$_g$, RH=100% and a scan rate of 20 mV s^{-1} are depicted. The second cycle after the stripping CV (approximately horizontal lines) was used as integration baseline. For better visual comparison, the CVs were corrected for the capacitive charge obtained at 0.45 V$_{RHE}$ during the second cycle.

Cathode CO stripping results are depicted in Figure 6.6. For each MEA//AST combination only one sample was investigated via CO stripping.

Pt-MEA:

In the absence of IrO_2 on the ACL, the CO peak shifts to lower potentials after 1200 SUSD cycles. Both, the peak potential as well as the CO onset potential, the intersection between the onset of CO desorption and the baseline CV from the 2nd cycle, are moving to lower potentials after the AST. Furthermore, EOT a comparable peak shape is observed as BOT but with a lower maximum current density. The shift in the CO peak is concomitant with an *ECSA* decrease ($\approx 10\%$), which is in alignment with the loss observed for H_{upd} (cf. Figure 6.4) for this MEA. The CO peak shift to lower potentials could originate from the observed cathode degradation [93] or slight changes in hydrogen crossover and/or ohmic resistance (cf. Appendix-Figure 6).

Pt/IrO$_x$-MEA:

If IrO_2 is introduced to the anode, the cathode CO peak beginning-of-test is shifted to lower potentials. As the testing procedure, apart from the SUSD AST, was similar, the BOT deviation for the two Pt/IrO$_x$-MEAs is most likely induced by reproducibility issues or sample-to-sample variations (the absolute *ECSA* deviation for both MEAs was $\approx 0.26 \frac{m_{Pt}^2}{g_{Pt}}$ BOT). However, due to the stress test performed, the shape of the CO peak changes significantly after both stress tests. The cathode CO peak becomes wider and a shoulder at lower potentials (0.54 to 0.58 V_{RHE}) is formed EOT (cf. Figure 6.6). Furthermore, the CO onset potential is shifted to lower potentials. A comparable behavior, a cathode CO peak shift to more negative potentials, was reported after Ru crossover to the cathode for CO-tolerant PEFC anodes containing Ru [92, 94, 182] and direct-methanol fuel cells containing Pt-Ru anodes [183].

As the OER activity measurements are indicating the presence of Ir species EOT, these Ir species most likely have a significant impact on the electrochemical CO desorption. This effect could originate from the following mechanisms:

  i) Ir species are weakening the CO-Pt bond
  ii) The presence of metallic Ir species on the cathode.

A weakening of the CO-Pt bond is commonly reported for Pt catalysts with increasing temperatures [141] or relative humidity [140]. However, CO peak shifts have also been reported for Pt nanoparticles deposited on Ir support [184] and Pt/Ir bifunctional catalysts [147] if the mass ratio of Ir was varied. Consequently, a comparable effect is conceivable for migrated and redeposited Ir species on the Pt/C cathode. The second possible mechanism was also reported in literature: chemical CO adsorption on metallic iridium and subsequent CO desorption during the stripping CV [142, 185]. This effect would superimpose the CO ad-/desorption on Pt and affect the correct *ECSA* determination for the ORR catalyst. It is difficult to conclude which of the proposed mechanisms is responsible for the observed cathode CO peak shift EOT, when IrO_2 was introduced to the pristine anode. However, the observation is corroborating Ir crossover and re-

127

deposition on the cathode after the SUSD ASTs, which was indicated by the OER activity increase.

6.1.3.3 Impact of iridium on ECSA determination

The assumed presence of Ir species on the cathode induced by the SUSD ASTs seems to have a significant impact on *ECSA* determination. Whereas the observed *ECSA* loss for the Pt-MEA aligns for the H_{upd} and CO stripping method ($\approx 10\%$), the *ECSA* losses deviate significantly for the Pt/IrO$_x$-MEAs (cf. Figure 6.4). The *ECSA* loss derived via CO stripping is lower compared to the *ECSA* loss derived via H_{upd}, regardless of the kind of SUSD AST applied.
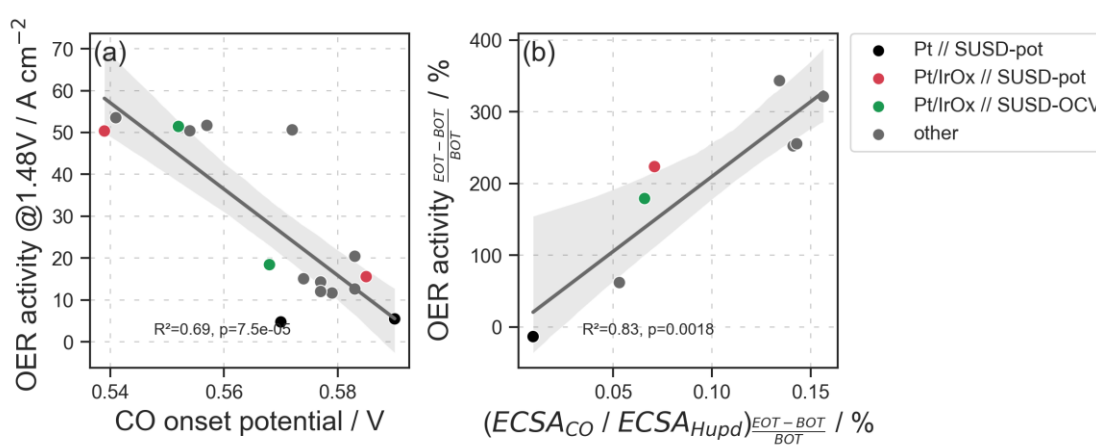
Figure 6.7: Correlations between OER activity and *ECSA* measurements. Besides the investigated MEAs within this work, additional MEA designs are included on which one of the presented SUSD ASTs was performed. All MEA designs use identical CCLs and membranes. Solid line: linear fit; shaded region: 95% confidence interval. (a) OER activity at 1.48 V against respective CO onset potential for the MEA. BOT (before SUSD AST) and EOT (after SUSD AST) values are depicted. R^2 of linear fit: 0.69. (b) Correlation between the SUSD AST induced change in OER activity against the change in *ECSA* ratio (*ECSA*$_{CO}$/*ECSA*$_{Hupd}$). R^2 of linear fit: 0.83.

To further corroborate Ir crossover to the cathode and a subsequent impact on *ECSA* determination, correlations between cathode OER activity and the cyclic voltammetry results are illustrated in Figure 6.7. Besides the MEAs investigated within this work, additional MEA designs were included to further validate these correlations. All MEAs were characterized prior and after one of the here presented SUSD AST and had the same CCL and membrane incorporated as the MEAs investigated within this chapter. Except for the Pt-MEA, all MEAs incorporated an IrO$_2$ based co-catalyst on the anode to achieve reversal tolerance. The data in Figure 6.7a is strongly indicative that an increased OER activity is concomitant with a shift in the CO onset potential to lower potentials. Furthermore, for all investigated MEA designs an increased cathode OER activity was achieved compared to the Pt-MEA, even BOL. This corroborates Ir crossover can already occur during the initial conditioning and performance evaluation procedures.

Figure 6.7b shows the impact of Ir crossover, indicated by increased cathode OER activity, on the *ECSA* determination. Increased OER activity on the cathode is concomitant with an increased ratio of *ECSA*$_{CO}$/*ECSA*$_{Hupd}$ on the cathode. This correlation is highlighting that OER ageing and Ir crossover significantly impact the *ECSA* determination. To the best of the author's knowledge, no such behavior has been reported so far. As a consequence, for IrO_2 based reversal tolerant PEFCs *ECSA* determination via H_{upd} and CO stripping, commonly attributed solely to Pt surface area, should be critically reviewed. This is valid for Pt/C based cathode catalyst layer after (possible) Ir crossover as well as for Pt/IrO_2 based anode catalyst layers. The degradation of the analyzed catalyst layer could be misinterpreted. However, which of the two *ECSA* methods is resulting in a physically more correct *ECSA* after OER aging and crossover cannot be resolved within this work.

Moreover, the correlations between cyclic voltammetry and OER activity on the cathode corroborate that both, the CO onset potential as well as the OER activity measurement are promising in-situ characterization methods to monitor Ir crossover due to transient anode potentials. As the CO ad-/desorption is fully reversible this method could be preferred over the OER activity method. The latter includes the risk of irreversible carbon corrosion in the investigated catalyst layer due to the high potentials applied (≥ 1.4 V_{RHE}).

6.1.3.4 Reversibility of Ir crossover

To analyze the reversibility of Ir crossover to the cathode, the OER activity measurements were repeated twice after a respective recovery procedure. As recovery procedure the cell was operated for 1.5 h at normal operation (68 °C) and 1.5 A cm^{-2} (cf. Table 4.2). Ir species on the cathode could become soluble again at normal operating cathode potentials (≈ 0.6 to 0.8 V_{RHE}). To promote Ir washout of soluble species, the cells were operated for the first 60 min at 100% *RH* on anode and cathode. The operating conditions were adjusted according to Table 4.2.
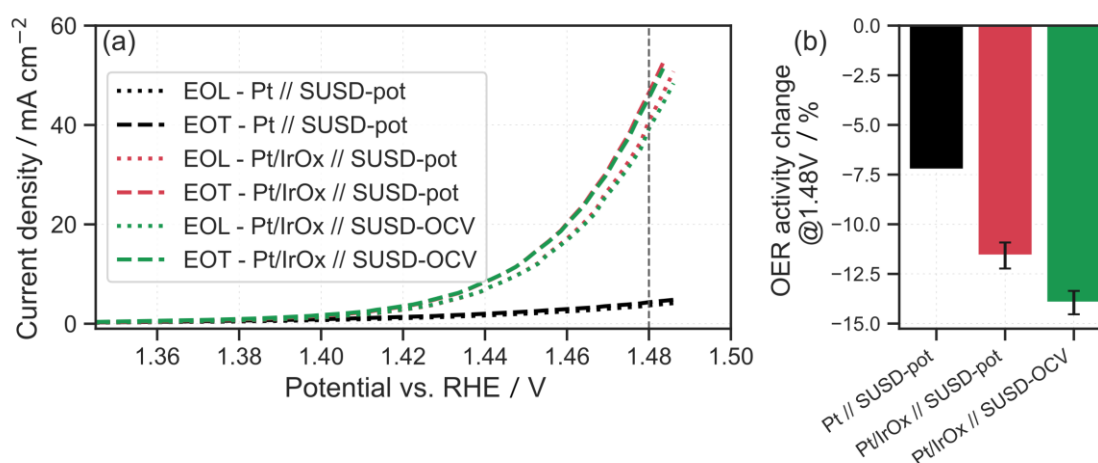
Figure 6.8: Ir crossover recovery. (a) Cathode OER polarization curves extracted from the anodic sweep of 9 subsequent cathode CVs at 20 mV s^{-1} between 0.1 and 1.49 V, after SUSD AST (EOT, dashed lines) and after performing a recovery procedure twice (EOL, dotted lines). Recovery procedure included normal operation for 1.5 h under increased humidification. Identical pristine CCLs, solely incorporating Pt/C as ORR catalyst, were used for all MEAs. The current density was corrected for the capacitive current observed at 1.3 V. For the Pt/IrO$_x$-MEAs the averaged values from two MEAs are depicted. Operating conditions: N$_2$/H$_2$ with a flow rate of 3.5/5 ln min^{-1} on cathode/anode, T=68° C; p=1 bar$_g$, RH=100%. (b) Cathode OER activity change after the performed recovery procedure, extracted from OER polarization curves at 1.48 V$_{RHE}$ with respect to EOT. Error bars represent standard deviation derived from investigating two similar MEAs, respectively.

The OER activities are depicted in Figure 6.8. The EOT curves demonstrate the OER activity after the SUSD AST, whereas the EOL curves represent the OER activity after the recovery procedure was performed twice. The OER activity decreases by 7% to 14% (Figure 6.8b), dependent on the MEA//AST combination. In contrast to the increase by > 150% after the SUSD (cf. Figure 6.3), the OER activity decrease during the chosen recovery procedure is minor. This is a strong indication for the irreversibility of Ir crossover to the cathode. Crossed-over iridium species cannot be washed out easily during normal operation. In addition, the OER activity decrease after the recovery procedure most likely is imposed by concomitant carbon corrosion and Pt loss originating from the high cathode potentials during the OER activity measurements (cf. Pt-MEA OER activity loss).

6.1.3.5 Proton resistance

In order to investigate the proton resistance change in the cathode catalyst layer, EIS measurements were performed. The corresponding Nyquist plots are depicted in Figure 6.9. The length of the 45° line is representative for the proton resistance (cf. experimental section). All MEAs have the same pristine cathode incorporated.
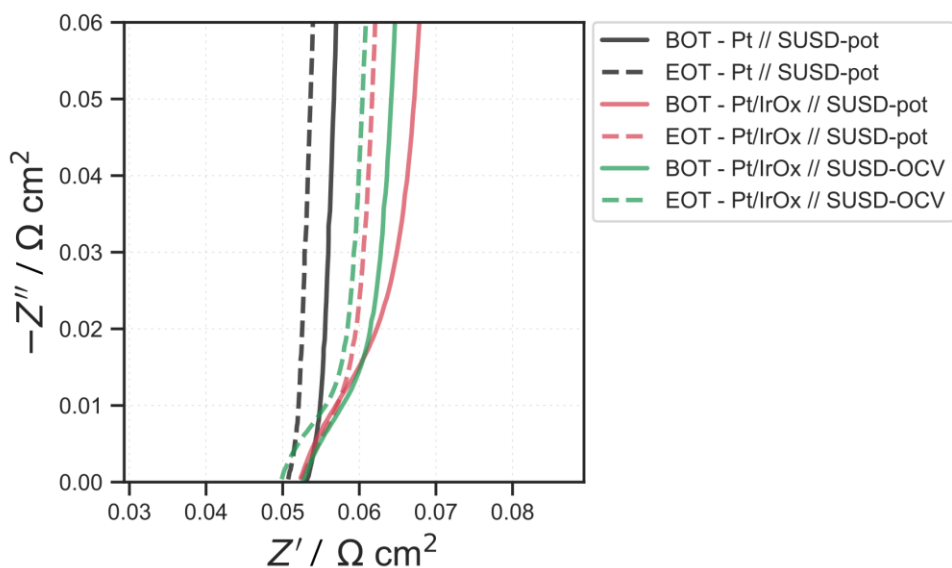
Figure 6.9: Cathode impedance spectra prior (BOT) and succeeding SUSD AST (EOT) for one exemplary sample of each MEA//AST combination. Measurements were performed at 68° C, 100% *RH* and 1 bar$_\text{g}$.

For the Pt-MEA, proton resistance is minor due to the absence of a clear 45° line. In contrast, as soon as IrO$_2$ is incorporated to the CCM, the proton resistance seems to increase significantly, and the spectra feature a 45° line. From this behavior two conclusions can be drawn:

- Ir crossover is corroborated.
- Crossed-over iridium species significantly increase protonic resistance.

The latter could be explained by the (temporary) chemical bond of soluble Ir^{3+} species to the sulfonic acid groups within the ionomer phase of the catalyst layer.

During aging, the change in protonic resistance is not as significant. For the Pt-MEA the spectrum is shifted to lower *Z'*, most likely originating from a differing membrane hydration (cf. section 6.1.2). The proton resistance seems to be unaffected. For the Pt/IrO$_\text{x}$ MEAs the observed decrease in proton resistance after the AST is imposed by the significant BOT variation (cf. Figure 6.9) as well as a huge standard deviation for the repeated measurements (not shown). Consequently, the impact of SUSD AST on proton resistance cannot be fully clarified.

In conclusion, strong indication for Ir crossover to the cathode could be found via in-situ characterization methods. For both SUSD AST variations, comparable Ir crossover was found. In contrast, the cathode degradation for the SUSD-pot AST seems to lead to higher ORR *ECSA* losses and carbon corrosion (indicated by double layer capacitance). But the cyclic voltammetry results should be considered with caution due to the previ-

ously discussed influencing factors of Ir crossover. The indicated higher cathode degradation for SUSD-pot, found by *ECSA* and C_{dl}, is contradictory to the performance degradation rate, which propose a higher degradation rate for the SUSD-OCV.

6.1.4 Anode degradation

Beside cathode degradation, anode degradation induced by SUSD events is significant for PEFC durability and performance. As outlined before, the SUSD stress tests in this work were designed to minimize cathode degradation while emphasizing anode degradation: both for the HOR and OER catalyst.

6.1.4.1 Cyclic voltammetry
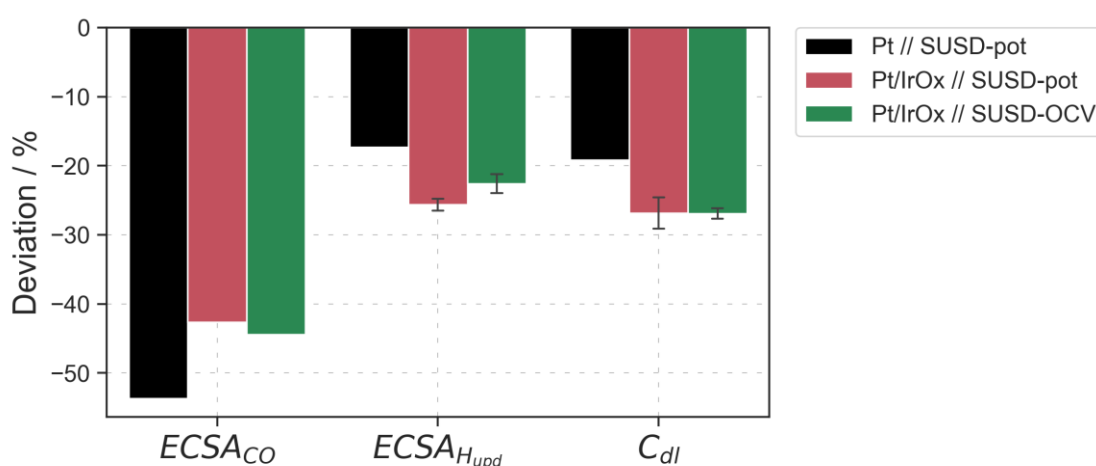
Figure 6.10: Observed changes in anode ECSA by CO stripping and H_{upd} as well as in double layer capacitance C_{dl} after SUSD AST was applied. Operating conditions: T=68° C; p=1 bar$_g$, RH=100%. C_{dl} was estimated from the H_{upd} CV at a voltage of 0.45 V_{RHE}.

In Figure 6.10 the losses in anode *ECSA* and C_{dl} for each MEA//AST combination are depicted. All combinations show significant *ECSA* losses and decrease in double layer capacitance after 1200 SUSD events. These results indicate a substantial loss of HOR catalyst as well as severe carbon corrosion concomitant with ACL porosity loss. However, there is a significant difference between *ECSA* loss obtained via CO desorption compared to hydrogen ad-/desorption. The results are further discussed in the following.

H_{upd}
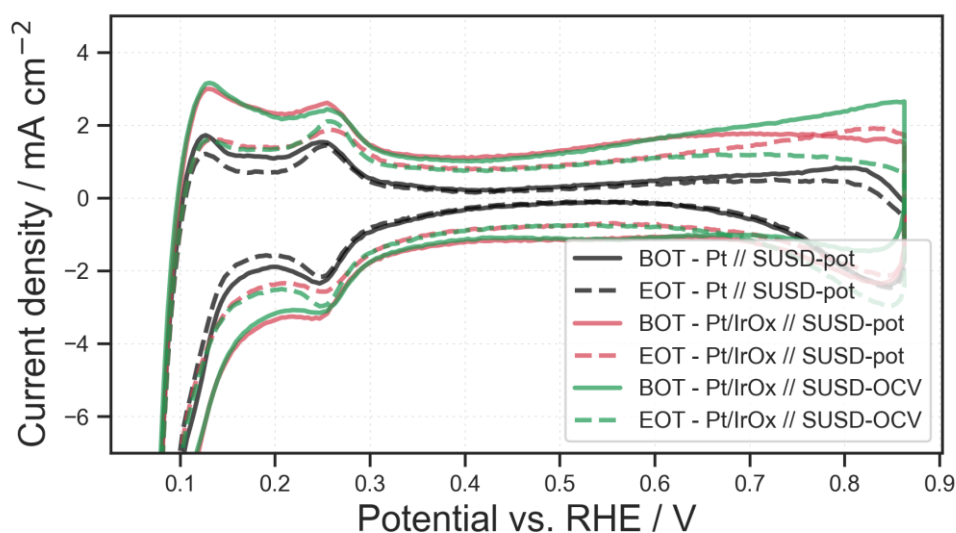
Figure 6.11: Anode CVs prior (BOT) and succeeding (EOT) SUSD AST. After a cleaning CV four contiguous CVs were recorded at $T=68°$ C, $p=1$ bar$_g$, $RH=100\%$ with a scan rate of 100 mV s^{-1}, from which the last cycle is depicted. For the Pt/IrO$_x$-MEAs the current density is averaged from two investigated samples, respectively. Each CV was corrected by the respective capacitive charge observed at 0.45 V$_{RHE}$ to improve visual comparability.

In Figure 6.11 the anode cyclic voltammograms from hydrogen underpotential deposition are depicted. The observed peak characteristics are comparable to the cathode CVs and commonly reported for Pt/C catalysts: between 0.1 and 0.3 V$_{RHE}$ hydrogen ad-/desorption features are found and Pt oxidation/reduction peaks occur at potentials above 0.6 V$_{RHE}$ [48].

Pt-MEA:
The significant lower double layer capacitance in contrast to the ACL containing IrO$_2$ is drastic. Most likely the capacitive behavior of the IrO$_2$ co-catalyst is causing this effect [142]. The difference in absolute C_{dl} values should be considered when discussing the respective C_{dl} losses after 1200 SUSD events (cf. Figure 6.10 and Figure 6.11). The decrease in C_{dl} is indicating carbon corrosion [35, 179] as no IrO$_2$ is present in the MEA. However, the absolute loss in capacitive charge compared to the ACLs containing IrO$_2$ is low. After SUSD AST, the hydrogen ad-/desorption features are shifted to lower currents, signifying HOR catalyst loss which leads to a *ECSA* loss.

Pt/IrO$_x$-MEAs:
As discussed above, a loss of IrO$_2$ catalyst within the ACL is assumed to be the major contributor to C_{dl} loss after 1200 SUSD cycles for the Pt/IrO$_x$-MEAs. As the losses in C_{dl} are comparable, most likely the degree of Ir dissolution between both AST variations is equivalent. These observations are in alignment with the indicated Ir crossover discussed within the cathode characterization section. However, simultaneous carbon

corrosion of the HOR catalyst should not be neglected, as observed for the Pt-MEA. But considering the absolute contribution to capacitance, this effect can be considered as minor contributor.

Hydrogen ad-/desorption features for all investigated MEA//AST configurations are decreasing to lower currents, indicating HOR catalyst loss. However, the *ECSA* losses determined via H_{upd} are significantly smaller as the respective losses measured via CO desorption (cf. Figure 6.10). For the Pt-MEA a similar behavior is observed, despite no OER catalyst present in the MEA, which could impact the *ECSA* measurement (see section 6.1.3). Lindström et al. reported that an increasing overlap of hydrogen evolution and hydrogen adsorption can decrease the *ECSA* accuracy via H_{upd} method [140]. As the hydrogen adsorption/evolution features are only slightly shifting with anode ageing (cf. Figure 6.11), overlapping hydrogen evolution could result in an overestimation of H_{upd} charge (charge was determined via integration between 0.1 and 0.4 V_{RHE} of the ad-/ and desorption after double layer correction). Consequently, one could speculate the *ECSA* loss via H_{upd} could underestimate the anode aging here. For the cathode, such a significant discrepancy in *ECSA* loss between CO stripping and H_{upd} in the absence of IrO_2 was not overserved (cf. Figure 6.4).

When comparing the two AST variations applied on IrO_2 based anodes, only minor differences in anode degradation can be observed. The change in H_{upd} features and concomitant *ECSA* loss varies only slightly (cf. second ad-/desorption peaks EOT at ≈ 0.25 V_{RHE}, cf. Figure 6.11), whereas the double layer capacitance is showing no significant difference. As the anode stressor is expected to be identical for both ASTs, these results meet the presumed expectations.

CO stripping

Beside Hupd measurements, CO stripping has been performed to evaluate *ECSA* losses. The resulting CO stripping CVs are depicted in Figure 6.12.

134
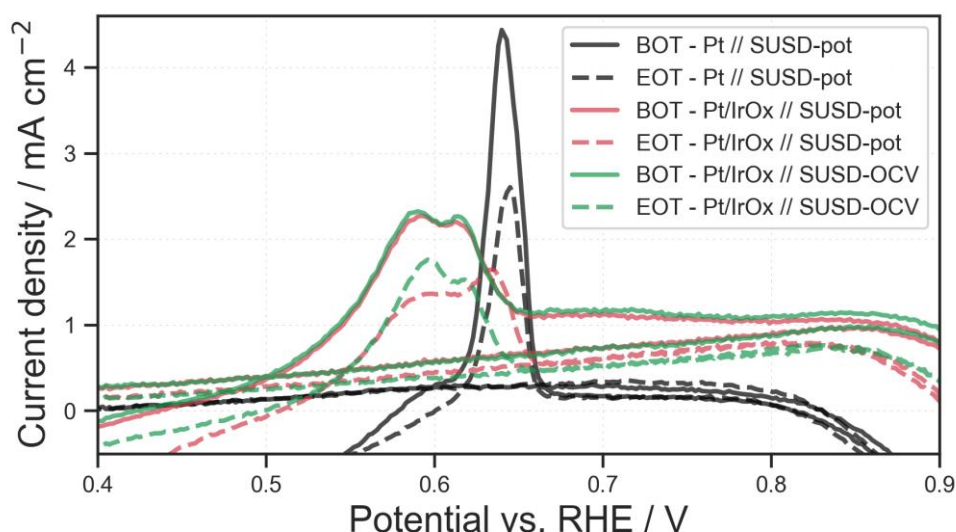
Figure 6.12: Anode CO stripping measurements prior (BOT) and succeeding (EOT) SUSD AST. After two cleaning CVs, CO was adsorbed on the cathode catalyst sites for 3 minutes. The subsequent stripping CVs at T=68° C; p=1 bar$_g$, RH=100% and a scan rate of 20 mV s^{-1} are depicted. The second cycle after the stripping CV (approximately horizontal lines) was used as integration baseline. For better visual comparability, CVs were corrected for the capacitive charge obtained at 0.45 V$_{RHE}$ during the second cycle.

Pt-MEA:

The CO peak is decreasing significantly EOT, whereas the peak is slightly shifted to higher potentials. These findings are in contrast to the cathode CO peaks (cf. Figure 6.6) and could indicate that the CO peak shift to lower potentials on the cathode EOT was an outlier (cf. Figure 6.7). The decreasing anode CO peak illustrates the severe HOR degradation due to the 1200 SUSD cycles. The *ECSA* is decreased by 54%, indicating a significant loss of HOR catalyst induced either by carbon corrosion and/or Pt dissolution. The potential cycling of the anode between ≈ 0 V$_{RHE}$ (H$_2$) and ≈ 1 V$_{RHE}$ (air) during each SUSD cycle is commonly considered to be causing Pt dissolution, e.g. via Ostwald ripening (cf. PEFC Fundamentals). However, Schwämmlein et al. reported, SUSD are also causing significant carbon corrosion [35]. This can also be observed within this work through the anode double layer decrease (cf. Figure 6.10).

Pt/IrO$_x$-MEA:

BOT the CO peaks are showing a different peak shape and a shift to lower potentials with respect to the Pt-MEA. When IrO$_2$ is present on the anode, two distinct peaks are formed, and the CO onset potential is in the range of ≈ 0.5 V$_{RHE}$. This effect is corroborating the observed effect discussed for the CO peak shift after Ir crossover on the cathode. The presence of Ir species in the ACL is either lowering the Pt-CO bond or is indicating the presence of metallic iridium, which is commonly reported to be capable of CO ad-/desorption. Da Silva et al reported a comparable formation of two distinct CO desorption peaks for Pt/IrO$_2$ bifunctional catalysts when IrO$_2$ was introduced [147].

The aging of the ACL during SUSD AST for the reversal tolerant anodes is shifting the CO peak and CO onset potential to higher potentials. In addition, the corresponding peaks decrease. The peak decrease is corroborating the loss of HOR catalyst, in alignment with the H_{upd} results. Following the argumentation for the cathode CO peak shift after Ir crossover, one could speculate the increasing CO onset potential on the anode is demonstrating the loss of Ir species. The loss of OER co-catalyst on the anode is further corroborated by the decrease of double layer capacitance and anode OER activity.

Besides the potential shift after anode aging, the general peak shape is maintained for the Pt/IrO$_x$-MEAs, forming two distinct CO desorption peaks. But, depending on the performed AST, one of the peaks is found to decrease to a shoulder-like shape whereas the other peak is still distinct. After SUSD-pot AST, the second peak at higher potentials remains. The potential regime is indicating this peak is predominantly attributed to CO desorption on Pt (cf. Pt-MEA Figure 6.12). After SUSD-OCV, this corresponding peak almost disappears, simultaneously leading to a narrower CO peak. Da Silva et al. reported the evolution of CO peaks with different characteristics dependent on the respective Pt/IrO$_2$ mass ratio of bifunctional catalysts [147]. Consequently, one could speculate based on the peak characteristics that during SUSD-OCV the loss of Pt area on the anode is more dominant, whereas the OER co-catalyst is simultaneously facing lower degradation with respect to SUSD-pot. However, the exact distinction of HOR and OER impact on the CO peaks is difficult due to the previously discussed interference of Pt and Ir with respect to CO and hydrogen ad-/desorption.

But in alignment with the observed Ir crossover, *ECSA* and double layer loss, severe anode degradation during the developed SUSD ASTs appears evident. Therefore, the developed ASTs are promising to enable the investigation of anode ageing.

6.1.4.2 OER activity

To further analyze anode degradation, anode OER activity was investigated. This should provide further insights in degradation and loss of OER co-catalyst in addition to the *ECSA* measurements discussed above. Furthermore, insights in the reversal mitigation capability of OER based reversal tolerant anodes should be derived, after anodes were exposed to transient anode conditions, causing substantial anode degradation.

In Figure 6.13 the anode OER activity BOT and EOT as well as the respective losses are depicted. In alignment with the cathode results, the carbon supported platinum based HOR catalyst is showing a negligible OER performance in the absence of IrO$_2$, both prior as well as proceeding the performed SUSD AST. In contrast, for the MEAs incorporating an OER co-catalyst a significant OER activity is observed, both BOT and EOT. This observation validates Ir crossover detection via monitoring the OER activity on the cathode, as the pristine OER co-catalyst on the anode is showing distinct OER activity within the investigated potential regime.
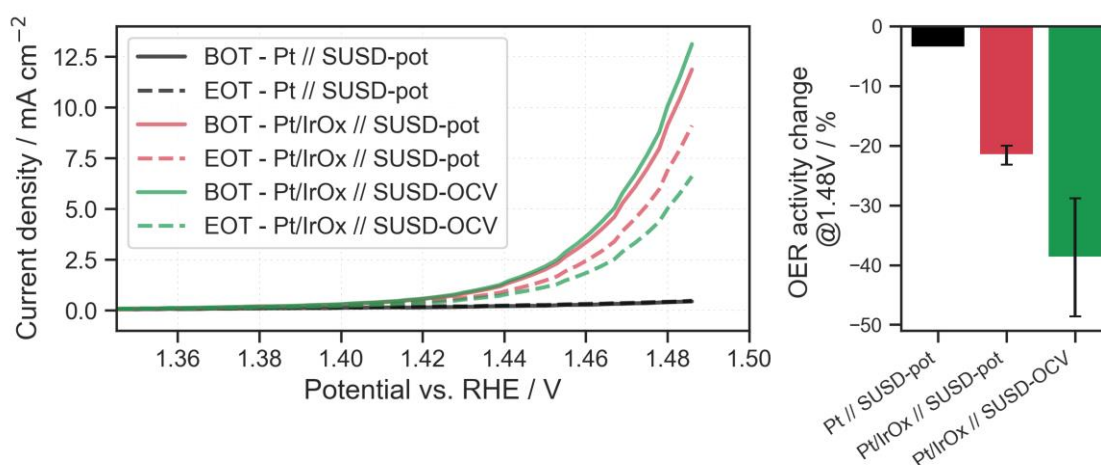
Figure 6.13: (a) Anode OER polarization curves extracted from the anodic sweep of 9 subsequent anode CVs at 20 mV s^{-1} between 0.1 and 1.49 V, before (BOT, solid lines) and after (EOT, dashed lines) the respective SUSD AST was performed. The current density was corrected for the capacitive current density observed at 1.3 V. For the Pt/IrO$_x$-MEAs averaged values from two samples are depicted. Operating conditions: H$_2$/N$_2$ with flow rates of 1/1 ln min^{-1} (cathode/anode), T=68° C; p=1 bar$_g$, RH=100%. **(b)** Anode OER activity change after the performed SUSD AST extracted from OER polarization curves at 1.48 V$_{RHE}$ with respect to BOT. Error bars represent standard deviation derived from investigating two similar MEAs, respectively.

In context with the cathode OER activity it should be considered that the absolute OER activity was found to be higher for the cathode as for the anode electrode EOT (cf. Figure 6.3 and Figure 6.13). Consequently, either the OER *ECSA* and/or the intrinsic OER activity of the crossed-over and redeposited Ir species could be higher as the introduced IrO$_2$ catalyst on the anode.

The anode aging during the SUSD AST is resulting in an anode OER activity decrease by 22% (SUSD-pot) and 39% (SUSD-OCV; cf. Figure 6.13). Assuming the exchange current density of the pristine OER co-catalyst did not change during ageing, the OER activity decrease is indicative of significant IrO$_2$ dissolution. As the anode potential was cycled identically for both AST variants, the transient dissolution of Ir and the respective OER species present on the anode EOT should be identical. However, a higher IrO$_2$ loss on the anode after SUSD-OCV is indicated by the OER activity. This contradicts previously discussed results, which induce either i) a lower (ACL CO stripping) or ii) comparable (ACL double layer decrease and cathode OER activity) Ir dissolution rate for the SUSD-OCV AST. Therefore, quantifying the comprehensive Ir dissolution of an OER co-catalyst via in-situ measurements is not unambiguous, especially as the OER aging could affect the oxidation state of the co-catalyst. This would influence the apparent OER activity (e.g. OER activity of Ir > IrO$_x$ [146, 177]).

Nevertheless, both AST variants seem to induce significant IrO$_2$ dissolution within conditions expected during field application of fuel cell systems. If the *ECSA* and/or the activity of the OER co-catalyst is substantially reduced, the fuel cell's tolerance against

reversal events will decrease. The respective impact is critical for durability and of great importance for the assessment and development of reversal tolerant anodes. RTAs should not only be optimized regarding BOL reversal tolerance but should also ensure reversal tolerance over the entire targeted lifetime. Therefore, the importance of OER co-catalyst stability during transient anode conditions is highlighted and can be investigated via the here proposed SUSD ASTs.

6.1.4.3 Reversal tolerance
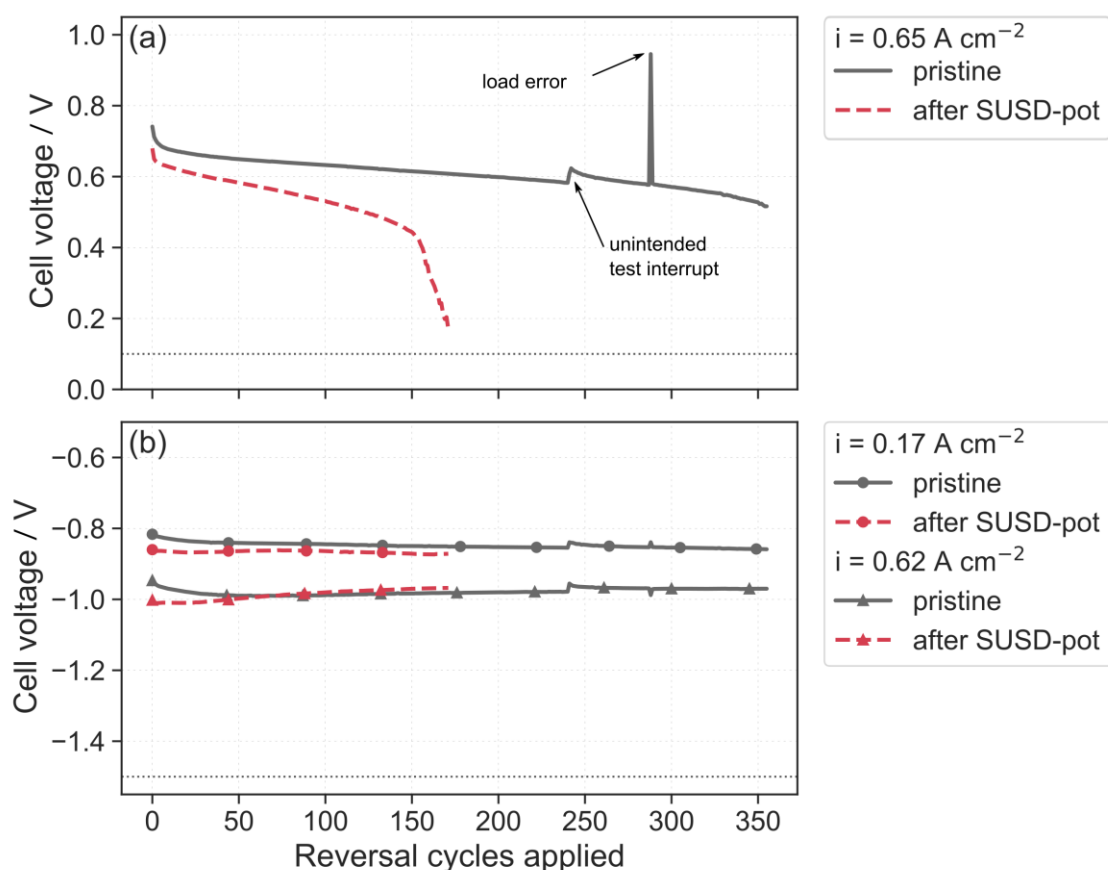
Figure 6.14: Cell voltage for two Pt/IrO$_x$-MEAs during CR AST at 30° C, 80% *RH*, 1.5/1.7 bar$_g$ (anode/cathode). Cell voltage is averaged from the last 30 s within each cycle. Pristine MEA: grey, MEA after SUSD-pot AST: red. Failure criteria are shown in black dotted lines. (a) Normal operation under H$_2$/air atmosphere at 0.65 A cm^{-2}. Failure for both MEAs observed during normal operation (failure criterion: cell voltage < 0.1 V; threshold of 0.1 V is not attended in this graph due to averaging). (b) Reversal operation in N$_2$/air atmosphere at 0.17 (circles) and 0.62 A cm^{-2} (triangles).

To correlate the observed anode ageing and anode OER activity decrease after the SUSD AST with the respective reversal tolerance, cyclic reversal (CR) AST was performed after SUSD-pot AST. Deviating from the test procedure within section 1 (for details see section 4.2.8), no H$_2$ pump polarization curves, EIS and CVs were performed during the CR AST. Normal operation at 0.65 A cm^{-2} (3 min) and reversal operation at two different current densities are alternated during CR AST.

The results for two identical Pt-IrOx-MEAs are depicted in Figure 6.14: a pristine MEA after conditioning (grey lines) and an MEA after SUSD-pot AST (red lines). Both investigated MEAs are failing within normal operation after 171 and 355 cycles, respectively. Therefore, the anode ageing induced by SUSD AST is causing a decrease in reversal tolerance by 51%. This behavior correlates with the substantial anode OER activity decrease after SUSD-pot AST (-21.6%, cf. Figure 6.13).

During normal operation at 0.65 A cm^{-2} (cf. Figure 6.14a) the previously aged MEA is showing a decreased cell performance along the entire AST compared to the pristine MEA. The performance is further decreasing with each reversal cycle applied. Therefore, the overpotential for the aged MEA is higher (beginning-of-test ≈ 61 mV) and increases at higher rates.

During reversal operation (cf. Figure 6.14b) the cell voltage of the aged MEA is slightly lower at CR AST start (0 cycles: ≈ 43 and ≈ 55 mV at 0.17 and 0.62 A cm^{-2}, respectively). However, with increasing reversal events applied, the cell voltage difference between the aged and pristine MEA is decreasing. For the higher current density after 171 cycles the cell voltage of the aged MEA even exceeds the cell voltage of the pristine MEA by ≈ 14mV in reversal mode.

During the SUSD-pot AST the HFR remained approximately constant (≤ 3 mΩ cm^2 at 68° C). In addition, the proton resistance increase on the cathode is minor (cf. section 6.1.3). Consequently, the increased overpotentials during normal operation can be attributed to ORR and HOR activity and/or mass transport overpotentials. During reversal events, ORR and OER are taking place on the cathode and anode, respectively. The cathode *ECSA* loss at 30° C would induce an ORR activity loss equal to 2.75 mV (cf. Equation 6.1). Consequently, the lower cell performance during normal operation (ORR and HOR taking place) within CR AST for the aged MEA can be attributed most likely to an increased HOR overpotential and degradation rate. As shown within section 5, the CR failure during normal operation could be attributed to an increased HOR mass transport overpotential originating from ACL collapse. Simultaneously, the OER performance for the MEA is unaffected from the ACL collapse.

In conclusion, the anode aging originating from the 1200 SUSD events causes significant ageing of the HOR and OER co-catalyst. Furthermore, a significant increase in HOR overpotential is highlighted by the reversal tolerance decrease measured by the CR AST and OER activity measurements after SUSD induced anode ageing.

6.1.4.4 Hydrogen pump experiments

To provide further insights in the HOR overpotential increase after SUSD AST, hydrogen pump experiments were performed at varying temperatures (35, 70, 86 °C), relative humidity, and hydrogen concentrations (100, 50, 30, 10, 5 vol% of dry gas). For further information, the reader is referred to section 4.2.7 and 3.1.6. As the cathode degradation

after SUSD AST is assumed to be low (*ECSA* loss $\leq$ 10% and C_{dl} increase $\approx$ 17 to 22%), the required assumption of negligible HER overpotential is still valid (BOT and EOT $rf_{cathode} \geq 6 \cdot rf_{anode}$). In addition, a change in proton resistance within the catalyst layers can be neglected (for discussion see section 5). For better comparison, an identical pristine MEA was investigated after conditioning. A decreasing cell potential after HFR-correction for the hydrogen pump polarization curves with respect to the BOT MEA is indicating an increased HOR overpotential originating from SUSD aging.

As the anode degradation after SUSD AST is expected to be low with respect to an MEA after a reversal stress test (e.g. CR AST, cf. section 5), polarization curves with lower H_2 concentrations (diluted with nitrogen) were investigated to better resolve HOR mass transport issues. Due to the high exchange current density of Pt for the HOR reaction, weak structural changes and degradation are hard to distinguish using pure hydrogen during polarization.
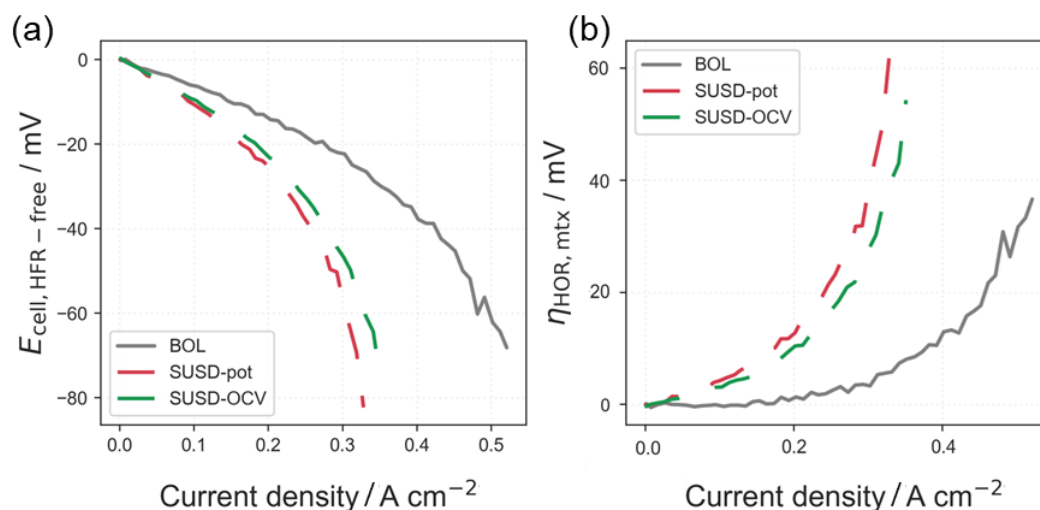
Figure 6.15: Hydrogen pump experiments at 35°C, 100% *RH* and 5 vol% H_2 concentration (2 bar$_g$ on the anode/cathode). Measurements performed for a pristine Pt/IrO$_x$-MEA after conditioning (BOL) and similar MEAs after an SUSD AST was performed. (a) HFR-corrected polarization curves representing the total HOR overpotential (activation and mass transport). (b) Respective HOR mass transport overpotential against current density, considering the HOR activation overpotential by using a simplified Butler-Volmer approach.

To illustrate the HOR overpotential increase during the respective SUSD AST, the HFR-corrected polarization curves at 35° C, 100% *RH* and 5 vol% H_2 are depicted in Figure 6.15a. For the MEAs previously exposed to anode ageing via SUSD AST, a decreased cell voltage over the complete current density range is observed. As pressure, flow rate and hydrogen concentrations were equalized for anode and cathode within this test procedure, the equilibrium potential E_{rev} should be $\approx$ 0 V.

According to Equation 3.18 consequently the HFR-corrected cell voltage $E_{\text{cell,HFR−free}}$ directly correlates with the HOR overpotential:

$$E_{\text{cell,HFR−free}} = -\eta_{\text{HOR}} = -\eta_{\text{HOR,act}} - \eta_{\text{HOR,mtx}}. \tag{6.2}$$

Therefore, the hydrogen pump polarization curves in Figure 6.15a are strongly indicating an increased HOR overpotential after SUSD AST. This observation corroborates the CR AST results with an aged MEA after SUSD AST. To resolve the overpotential distribution, the kinetic HOR overpotential was calculated using a simplified Butler-Volmer approach. The resulting HOR mass transport overpotentials are shown in Figure 6.15b.

At the depicted hydrogen concentration (5%), the HOR mass transport overpotential contributes predominantly to the overall HOR overpotential. In addition, $\eta_{\text{HOR,mtx}}$ increases in the same order as the overall HOR overpotential: BOL < SUSD-OCV < SUSD-pot. Consequently, the aging originating from SUSD events increases the HOR mass transport overpotential significantly, indicating a loss in ACL porosity. This is corroborating the observations derived from C_{dl} change after SUSD events.

The complete set of operating conditions investigated via hydrogen pump experiments is depicted in Figure 6.16. The resulting HOR overpotential observed at the common limiting current for all MEAs within a certain temperature/relative humidity combination is dependent on the *RH*. For 35° C the respective overpotentials observed at 100% *RH* are allowing for the best distinction in kinetic and structural anode ageing after the respective SUSD stress test. At higher temperatures (70° and 86° C) and application relevant *RH* (> 60%) the HOR overpotential becomes minor and the distinction becomes difficult, especially BOL. For *RH* < 60% distinct HOR overpotentials can be observed but are most likely impacted by a significant increase in proton resistance in the catalyst layers. As a consequence, performing hydrogen pump experiments at low temperatures and high *RH* are the most promising operating conditions to investigate anode ageing and the respective impact on structural degradation. Lowering the hydrogen concentration can further improve the distinction of anode ageing. Using higher hydrogen concentrations, higher current densities must be applied to resolve overpotential increases. Higher current densities are increasing noises arising from the HFR determination, which is always subjected to small errors and can change with the current density applied [36].
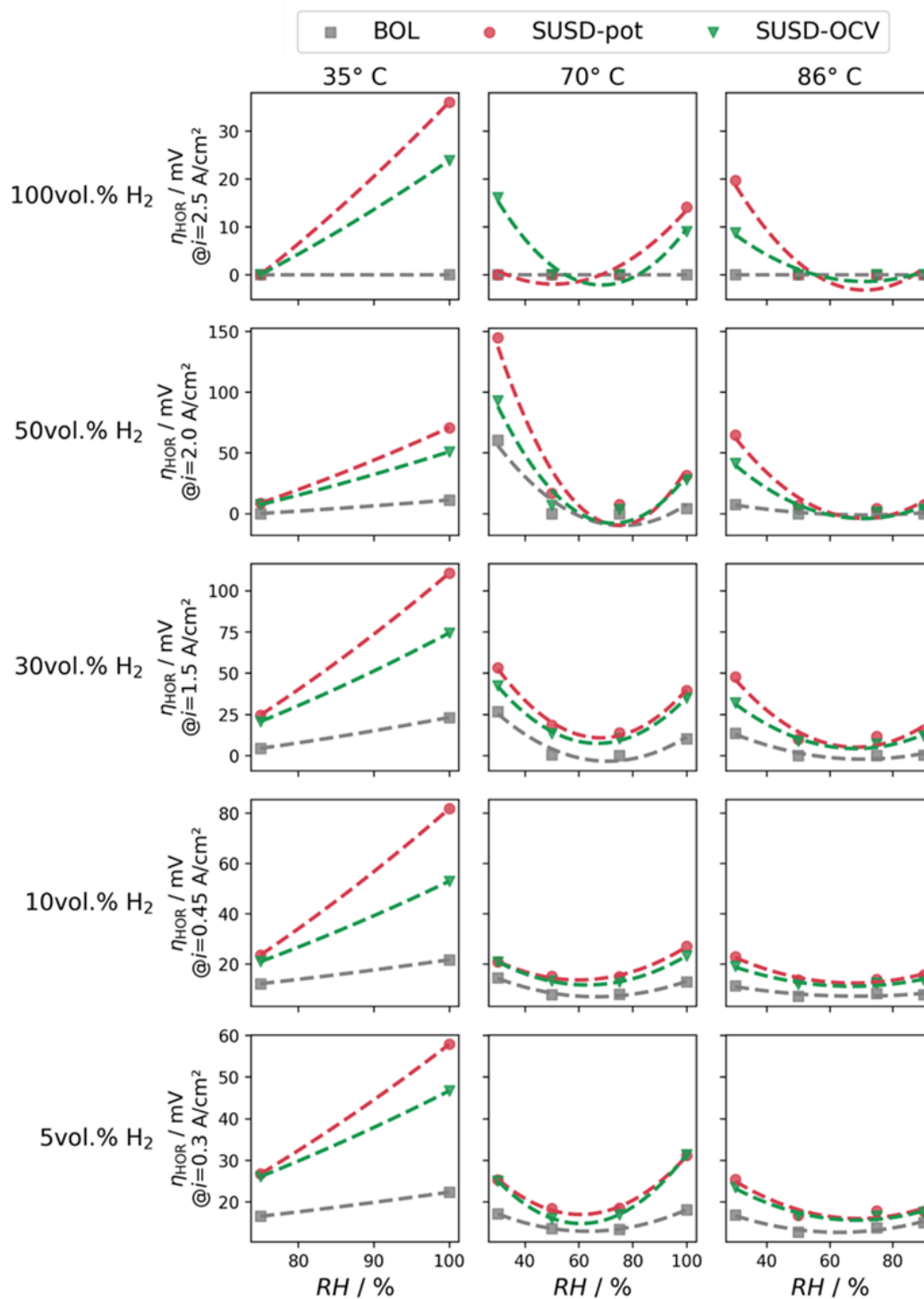
Figure 6.16: HOR overpotentials η_{HOR} at the respective limiting current against relative humidity at varying temperatures (columns) and hydrogen concentrations (rows) derived from hydrogen pump polarization curves. For each *T*/*RH* combination the common limiting current density of the HFR-corrected hydrogen pump polarization curve for all MEAs was determined. Dashed lines represent linear or non-linear regression which should be regarded as guide-to-the-eye. Apparent negative values for η_{HOR}, most likely induced by inaccuracies arising from current independent HFR determination (cf. Experimental section), were set equal to 0.

6.1.4.5 Performance loss at low temperatures

The hydrogen pump experiments are indicating an increased HOR overpotential for SUSD-pot compared to SUSD-OCV, especially at low temperatures and high RH. Comparable behavior is observed for H_2/air polarization curves at 40° C and oversaturated anode gas (RH_{anode} = 104 to 139%; increasing with increasing current density).
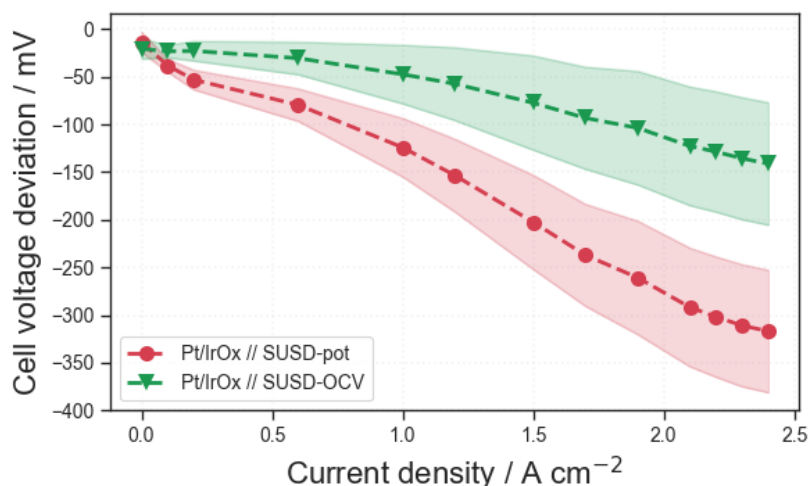
Figure 6.17: Performance loss obtained from polarization curves (H_2/air) at 40° C after 1200 SUSD cycles performed. Shaded region: standard deviation derived from current dependent BOL performance variation from all Pt/IrO$_x$-MEAs investigated. Pressure, flow rates and RH were dependent on current density: p = 0.3 to 1.9/0.2 to 1.5 bar$_g$, flow rates = 0.9 to 6.8/1.7 to 16.4 l$_n$ min^{-1}, RH = 104 to 139/73 to 50% (on anode/cathode).

Polarization curves were recorded during performance evaluation prior and post SUSD AST. The observed performance losses are illustrated in Figure 6.17. The reproducibility of this test suffers from a high standard deviation for high current densities, even for BOL MEAs. In addition, catalyst layer degradation between SUSD AST and the polarization curves should be considered. During the characterization sequence EOT, in total three sets à 10 CVs up to 1.49 V$_{RHE}$ at 68 °C were performed (cf. section 4.2.9) to evaluate cathode OER activity and the reversibility of Ir crossover. For these conditions, accelerated carbon corrosion is reported [97].

Nevertheless, the polarization curves shown in Figure 6.17 are corroborating the previous results. The increased degradation of the HOR catalyst during SUSD-pot AST is highlighted. As load is applied during this AST variant within each SUSD cycle under H_2/air, water is produced by ORR on the cathode. Therefore, one could hypothesize a higher water content in the whole MEA during SUSD-pot, not only in the cathode but also within membrane and ACL via water diffusion. As carbon corrosion is known to be strongly dependent on water content [78, 79], this could be an explanation for the increased degradation in contrast to SUSD-OCV.

In conclusion, substantial ageing of the ACL and substantial HOR mass transport over-potential increase are present after SUSD AST. At normal fuel cell operating conditions (60 to 90 °C, high *RH*) the increased HOR overpotentials become negligible (cf. Figure 6.16). This observation is corroborated by the H_2/air performance evaluation at 68° (cf. Figure 6.2) and results within section 5. However, as discussed within section 5, the operation at low temperatures is crucial during the start-up phase of automotive fuel cell systems. Subsequently, the performance under these operating conditions is application relevant and should be considered.

In addition, the increase of HOR overpotential and the concomitant decreased OER activity on the anode by IrO_2 aging were found to result in a significant loss in reversal tolerance. To achieve highly durable reversal tolerant ACLs, the ageing impacts during SUSD events or comparable transient anode conditions have to be considered for product development.

6.2   Ex-situ imaging analysis

To validate the observed in-situ characterization results for reversal tolerant anodes, imaging via SEM and EDX analysis was performed.

6.2.1.1   SEM imaging

To evaluate the catalyst layer and membrane degradation, thickness was qualitatively and quantitatively analyzed via SEM images.
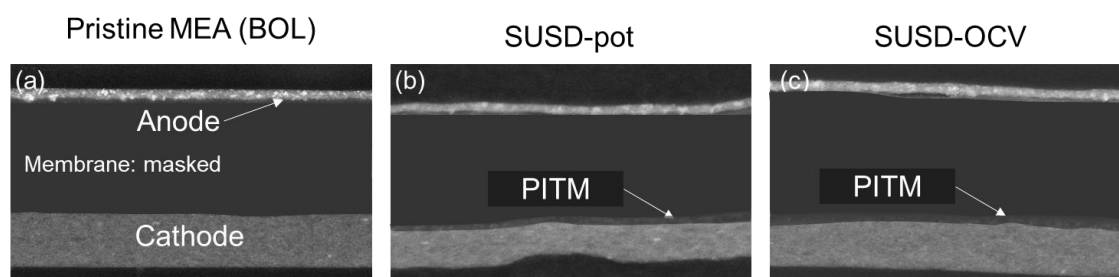
Figure 6.18: SEM images were made at 5 kV taken from (a) pristine and (b)-(c) aged MEAs after SUSD AST. Bright spots in the ACL were identified as IrO_x by EDX analysis (Appendix-Figure 7), in alignment with literature [114]. The band formation (PITM: platinum in the membrane) close to the cathode after SUSD AST (b)-(c) was identified as platinum precipitation by EDX analysis (see Appendix-Figure 8). The membrane cross-sections cannot be disclosed, and therefore were masked.

SEM images were taken from a pristine Pt/IrO_x-MEA and from identical MEAs after SUSD-pot and -OCV AST. Representative images are depicted in Figure 6.18. The quantitative thickness results are illustrated in Table 6.2.

144

Table 6.2: Layer thicknesses change after SUSD AST for Pt/IrO$_x$ MEAs with respect to a similar BOL MEA. Standard deviation derived from evaluating 30 spots within 6 cross-sections for the BOL MEA written in brackets.

AST performed	ACL thickness deviation [%]	CCL thickness deviation [%]	PEM thickness deviation [%]
SUSD-pot	-13 (9)	-27 (2)	-2 (1)
SUSD-OCV	-17 (9)	-18 (2)	+2 (1)

For the membrane, no significant degradation was found after SUSD AST via in-situ characterization. In alignment with these results, no significant membrane thinning was observed by SEM imaging. However, the formation of a Pt band (validated via EDX) was found to evolve after both SUSD AST variants next to the cathode/membrane interface (cf. Figure 6.18). Depleted areas within the cathode catalyst layer indicate the Pt band is formed by dissolved Pt from the cathode. The band formation presumably contributes to the slight changes in hydrogen crossover (cf. 6.1.2) [173].

For the cathode catalyst layer, significant thinning was observed via SEM images. In general, the cathode thinning supports the observed cathode degradation observed via in-situ characterization after the SUSD ASTs. However, the thinning is higher than expected. Subsequent to the SUSD AST, the normal performance loss is ≤ 25 mV, the cathode double layer capacitance is indicating solely the onset of carbon corrosion and the cathode *ECSA* loss is ≤ 10 %. However, as discussed within section 6.1.4, the repetitive OER activity measurements between SUSD AST and the following characterizations, as e.g. SEM, could cause significant carbon corrosion. Consequently, the cathode thinning observed by SEM imaging could overestimate the contribution of the SUSD AST. The cathode thinning for the OCV AST was lower compared to the potential SUSD variant. This observation is in alignment with the increased cathode degradation indicated by *ECSA* loss.

For the anode, significant thinning is observed via SEM imaging, confirming the structural change indicated by HOR overpotential increase at low temperatures (cf. 6.1.4). Catalyst layer thinning commonly is concomitant with a porosity loss, leading to increased mass transport overpotentials. The HOR overpotential indicated a higher degradation rate for SUSD-pot AST. This correlation cannot be found via ex-situ thickness characterization. However, due to the high standard deviation for anode thickness, the correlation between AST variation and the respective anode thinning is flawed. In addition, anode disconnection from the membrane can be observed after SUSD stress tests. Whether the disconnection is originating from a sample preparation artifact or from the AST cannot be evaluated. If the disconnection was already present during operation, an influence on the measurements caused by inhomogeneous current distribution could be possible.

6.2.1.2 Energy dispersive X-ray spectroscopy analysis

In order to achieve insights in elemental composition, EDX analysis was performed. The band formation in the membrane next to the cathode was found to be based on platinum. No Ir precipitation was found within the membrane in any cross section, neither BOL nor after SUSD events (Ir detection limit: 0.5 atomic %).

In addition, the presence of Ir on the cathode catalyst layer was investigated. During operation Ir crossover was strongly indicated by:

- cathode OER activity increase
- change in CO desorption characteristic
- significant double layer capacitance increase at high potentials.

However, via EDX no Ir was found in any cathode cross section. Representative EDX spectra for the CCLs are depicted in Figure 6.19.
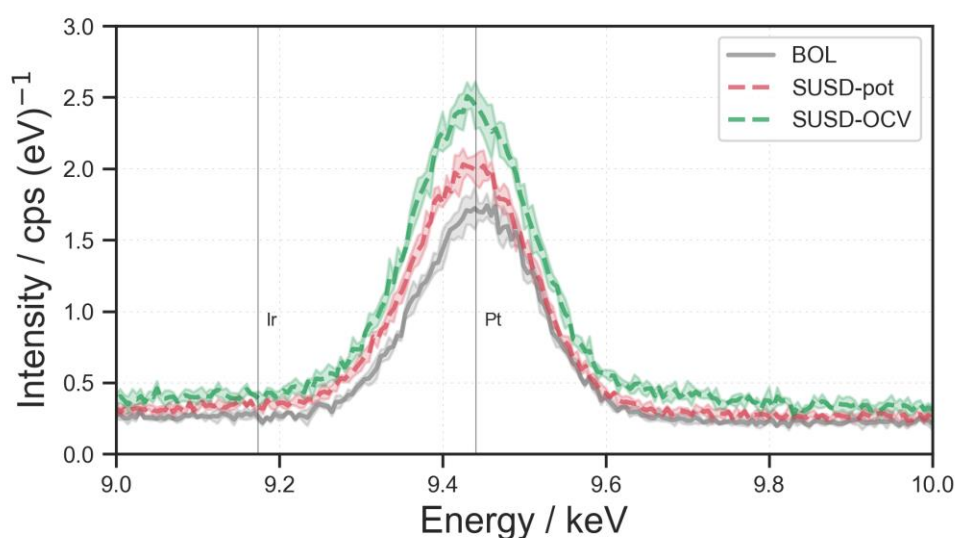
Figure 6.19: Cathode catalyst layer EDX spectra for Pt/IrO$_x$ MEAs prior (BOL) and after SUSD AST. Shaded region: standard deviation. Vertical grey lines: characteristic X-ray energy for iridium and platinum (source: Bruker Espirit 1.9 software documentation and other sources [186, 187]).

As the evidence of Ir crossover during operation was substantiated by various characterization methods, one could speculate about the lack of evidence via EDX. Ir redeposition is dependent on local chemical and potential conditions within the respective layers [128] and therefore could result in in a very inhomogeneous distribution on the cathode, resulting in not being traceable within the investigated cross sections. As the penetration depth for the EDX setup was low ($\approx$ 100 nm), the total amount of investigated catalyst layer volume could be below the threshold of a statistically robust evidence and Ir redeposition spots could be missed. In addition, the signal of deposited Ir species could be below the EDX detection limit (0.5 atomic %), while being electrochemically active. In

conclusion, Ir crossover could not be corroborated by EDX measurements. However, due to the broad indicative signals found during operation and in literature, the appearance of Ir crossover seems to be reliable evident. This assumption is highlighting the importance of in-situ characterization methods to investigate Ir crossover.
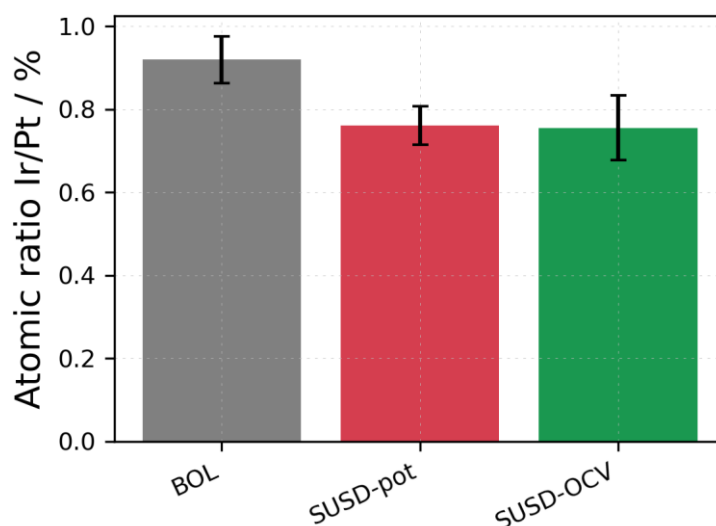
Figure 6.20: Ir/Pt atomic ratio for the anode catalyst layer of Pt/IrO$_x$ MEAs derived by EDX analysis. A pristine (BOL) and aged MEAs after SUSD AST were investigated.

EDX analysis was also performed on the anode. The elemental composition change on the anode is depicted in Figure 6.20. The atomic ratio for Ir/Pt decreases after SUSD AST. This result is indicating a significant loss of OER co-catalyst on the anode, corroborating the results obtained for anode OER activity and reversal tolerance after SUSD events. In addition, no reliable difference for both AST variants was found via EDX analysis.

6.3 SUSD AST comparison

The two developed SUSD ASTs are both leading to comparable degradation effects for OER based reversal tolerant anodes, with minor differences regarding the respective component degradation. A comprehensive overview of the most relevant degradation key aspects, dependent on the performed AST, is given in Table 6.3.

For both AST variants the cathode degradation was minimized and significant anode degradation (OER and HOR catalyst) due to transient anode conditions was achieved. As for SUSD-pot the PEFC performance loss is decreased and a comparable Ir crossover indicates that this AST has a slight advantage in effectively simulating anode aging by transient conditions. Furthermore, this AST should promote the migration of dissolved Ir species from the anode to the membrane/cathode due to the applied current

during the AST. However, within the presented characterization methods this effect could not be confirmed, as for both ASTs comparable Ir crossover to the cathode was measured by cathode OER activity and a shift in cathode CO onset potential.

Table 6.3: SUSD AST comparison. Mean changes during the AST with respect to BOL values are depicted. Higher degradation indicated by value is highlighted in red.

Aspect	Key value	SUSD-pot	SUSD-OCV
Performance	0.1 A cm^{-2}	-1.12 mV	-8.08 mV
	2.4 A cm^{-2}	-7.83 mV	-9.31 mV
Membrane degradation	i_{H_2}, HFR	-	-
Cathode degradation	$ECSA_{Hupd}$	-10.5%	-6.8%
	$ECSA_{CO}$	-6.4%	-1.97%
	C_{dl}	+16.7%	+22.2%
	Cathode thinning (SEM)	-27%	-18%
Ir crossover	Cathode OER activity	+194%	+165%
	Cathode CO peak shift	-46 mV	-18 mV
	EDX analysis	-	-
Anode degradation	$ECSA_{Hupd}$	-25.6%	-22.6%
	$ECSA_{CO}$	-42.6%	-44.4%
	C_{dl}	-26.8%	-26.9%
	OER activity	-21.6%	-39.4%
	Ir/Pt ratio (EDX)	-15.8%	-16.4%
	η_{HOR} (35°C, 100%RH, 5% H2, $i = 0.3$ A cm^{-2})	+ 36 mV	+ 24 mV
	Anode thinning (SEM)	-13%	-17%

6.4 Conclusion

The aging of OER based reversal tolerant anodes by transient anode conditions was investigated under field relevant conditions by developing two start-up/shut-down (SUSD) accelerated stress tests (ASTs). The developed SUSD ASTs were designed to investigate the MEA aging by transient anode potentials due to gas switches, as commonly occurring during PEFC start-up/shut-down events. Tests were performed on time- and resource-saving single cell level. Simultaneously, the SUSD induced major cathode degradation, caused by the so-called reverse-current effect, could be kept on a moderate level (*ECSA* loss ≤ 10%). This allows for better distinction of the occurring anode degradation and subsequently induced secondary degradation effects. In addition, in-situ characterization methods were established, which allow for fast and efficient analysis of the dissolution and subsequent crossover of Ir species from the initially employed anode OER co-catalyst.

A significant PEFC performance decrease during and after 1200 SUSD events was found if an OER co-catalyst was embedded to achieve RTAs. The performance decrease was presumably induced by Ir crossover poisoning the ORR catalyst on the cathode. When no OER co-catalyst was introduced to the MEA, a general performance increase by a conditioning effect and a very low degradation rate was observed during potentiostatic SUSD AST.

The Ir crossover to the cathode catalyst layer during the SUSD ASTs was shown to be measurable via OER activity monitoring on the respective electrode. Furthermore, the onset potential of electrochemical CO desorption was found to correlate with the Ir crossover indicated by the cathode OER activity. Consequently, Ir crossover can be investigated by monitoring OER activity and perform CO stripping on the cathode electrode. Additionally, a significant disturbance of ECSA determination via CO stripping and H_{upd} was found in the presence of Ir crossover, resulting in a shifting *ECSA*-$_{CO/Hupd}$ ratio. Therefore, in the presence of IrO_2, derived *ECSA* values should be reviewed carefully, both, for Pt based HOR as well as ORR catalysts.

For the developed SUSD ASTs, a significant anode ageing was attained. The ageing of the OER co-catalyst was found to result in a decreased anode OER activity. Additionally, a significant HOR catalyst degradation was observed. A substantial loss in anode *ECSA* was observed, especially by the commonly more robust CO stripping method. In addition, a loss in ACL porosity by carbon corrosion during SUSD AST was indicated by the increase of HOR mass transport resistance, evaluated via hydrogen pump experiments using diluted hydrogen feed gas (H_2 in N_2). The substantial ageing of the HOR and OER catalyst was found to lead to significantly reduced reversal mitigation capability. The loss in reversal tolerance should be considered for application as well as during

149

scientific research and development on OER based RTAs. The degradation effects investigated during operation could be corroborated via SEM and EDX analysis.

The developed SUSD ASTs were found to be a good basis to investigate the durability of the ACL and its components during transient anode conditions on single cell level. The resulting SUSD induced degradation was found to be comparable for both AST variants. However, as Ir migration of dissolved species across the membrane should be simulated more realistically, SUSD-pot AST is expected to be the stress test most suitable for investigating SUSD induced degradation of OER based RTAs.

However, two challenging questions regarding the Ir crossover remain: Firstly, the performance impact of Ir crossover if the cathode catalyst layers were previously exposed to any further degradation (e.g., Pt dissolution by voltage cycling). Secondly, the possible protecting impact on the cathode of crossed-over Ir due to the reverse-current effect. There were already reverse-current mitigation strategies reported, introducing an OER catalyst to the CCL to reduce carbon corrosion during SUSD events on the cathode [188, 189].

7   Conclusion and Outlook

7.1   Conclusion

Reversal Tolerance

To mitigate reversal events caused by gross fuel starvation, the introduction of oxygen evolution reaction (OER) co-catalysts in reversal tolerant anodes (RTAs) has been established recently. The embedded OER co-catalyst promotes water splitting over carbon corrosion during a reversal event.

This work presents different AST approaches on single cell level to investigate the reversal tolerance of OER based RTAs. The developed cyclic reversal (CR) AST is alternating short-term normal and reversal operation at low temperatures. This AST simulates short-term reversal events which can occur during freeze start-ups in automotive polymer electrolyte fuel cell (PEFC) stacks and showed a drastic deviating degradation behavior as observed during state-of-the-art non-cyclic reversal (NCR) ASTs, which are mimicking a prolonged reversal event.

During more realistic short-term reversal events (CR AST) MEA failure during normal operation was observed, whereas the OER activity in reversal mode maintained almost constant. This is strongly indicative of an OER recovery effect for short-term reversal events. In contrast, during non-cyclic reversal ASTs an OER catalyst deactivation is observed in the presence of carbon. The recovery effect for cyclic reversal AST was shown to culminate in still possible OER activity after the MEA failed during normal operation. Consequently, the application of common non-cyclic reversal ASTs could lead to unrealistic reversal tolerance determination. During prolonged reversal events, OER catalyst deactivation occurs and solely monitoring the OER activity is insufficient evidence for a healthy anode catalyst layer (ACL). Therefore, the developed CR AST allows for more realistic and comprehensive investigation of reversal tolerance by considering both, hydrogen oxidation reaction (HOR) and OER catalyst degradation.

The developed in-situ characterization methods allow for fast and cost efficient in-situ investigation of MEA failure and can be easily implemented during reversal ASTs. For temporary, repetitive reversal events MEA failure occurred during normal operation and could be attributed mainly to an HOR mass transport overpotential increase, induced by carbon corrosion. The hydrogen pump experiments could not just quantify HOR overpotential distribution but were able to indicate a structural change in the ACL during

CR AST. The structural change culminates in a layer collapse, validated via SEM images.

A significant dependence between HOR catalyst and reversal tolerance was found. Increasing the graphitization degree of the HOR catalyst was leading to a higher reversal tolerance (factor ≈ 2.4). This result is indicating, ACL component interactions are crucial to achieve highly durable RTAs.

The presented characterization methods can now serve as a tool set for fuel cell manufacturers to evaluate and optimize varying anode designs regarding their reversal tolerance and occurring failure modes. In addition, scientific research can use these methods and results as valuable input on further investigating the comprehensive reversal tolerance (considering HOR and OER capability simultaneously) and its dependency on material interactions within experimental investigations and numerical simulations.

Durability of OER based RTAs under transient conditions

The second part of the thesis aims at gaining insights into degradation of RTAs containing OER catalysts (supported IrO_2) during transient conditions and developing in-situ characterization methods to further evaluate the observed fuel cell degradation.

Transient anode conditions were applied by developing two varying start-up/shut-down (SUSD) ASTs. Moderate cathode degradation by the so-called reverse-current effect was achieved, to emphasize anode degradation (HOR and OER catalyst) and its subsequent impact on PEFC performance and secondary degradation effects within other cell compartments.

For the first time, in-situ characterization methods were developed to investigate the so-called Ir crossover effect. Due to the transient anode conditions, the OER co-catalyst can dissolute, migrate across the membrane and redeposit within the membrane and cathode electrode. Moreover, a significant impact on the determination of the Pt based oxygen reduction reaction (ORR) catalyst's *ECSA* by CO stripping and H_{upd} was found after Ir crossover. To the best of the author's knowledge, no such behavior has been reported so far, and this effect should be considered when evaluating electrode degradation by *ECSA* if an OER catalyst is present within the MEA.

In addition to the secondary cathode degradation by Ir poisoning, substantial anode degradation could be provoked by the developed SUSD ASTs. Due to the applied SUSD events, significant degradation of the HOR and OER catalyst was observed. For the OER catalyst, substantial dissolution was revealed by a decrease in anode OER activity. For the HOR catalyst, a significant HOR mass transport overpotential was observed and magnified at low temperatures and low hydrogen concentrations during hydrogen pump experiments. Consequently, the anode degradation induced by SUSD

events strongly indicates a structural impact on the ACL, resulting in reduced catalyst layer porosity. These results were corroborated by SEM and EDX results, where a significant anode thinning and OER catalyst dissolution was obtained.

Both, the degradation in HOR and OER capability was shown to substantially reduce the RTA's capability to mitigate reversal events. A decrease in reversal tolerance by 51% was observed after 1200 SUSD events, highlighting the importance of this aspect on application level, where reversal tolerance over the entire lifetime is crucial for PEFC durability.

The presented characterization methods can be used to comprehensively investigate the RTA stability regrading OER and HOR capability. The characterization techniques can be used by PEFC manufactures to investigate varying RTA concepts (varying catalysts, loadings, processing) regarding SUSD induced degradation. In addition, the results and methods can help in estimating the degradation impact on application level. Furthermore, scientific researchers can use the methods and results provided as starting point to gain further understanding in OER co-catalyst stability under transient conditions for varying co-catalysts and RTA designs as well as operating strategies.

7.2 Outlook

Still questions remain concerning evaluating the degradation of OER based RTA at the end of this work.

Reversal Tolerance

One of the major remaining questions regarding reversal tolerance is the impact of ACL components and their respective interactions as well as the impact of the ACL structure. Within this work a significantly improved reversal tolerance for a varying HOR catalyst (factor ≈ 2.4) was obtained, despite introducing an identical, highly active OER catalyst. Consequently, further understanding in material interaction is crucial to achieve optimized OER based RTA concepts. The interactions could be investigated both, experimentally as well as theoretically through simulations. As higlighted in this work, the HOR and OER capability as well as the structural integrity of the ACL is crucial for evaluating application relevant reversal tolerance. Therefore, e.g. the recently reported aspect of OER catalyst deactivation due to carbon species could be an promising aspect to further improve the understanding in component interaction. The temporary and/or local deactivation of OER catalysts most likely promotes carbon corrosion during reversal events, resulting in a loss in structural integrity and HOR catalyst. Despite an OER recovery effect obtained after short-term reversal events, supressing this OER

deactivation could increase reversal tolerance significantly by further decreasing carbon corrosion rates during reversal events.

Another aspect is to further tailor the developed reversal AST to the specific conditions expected for different applications. As degradation behavior was shown to substantially deviate between short-term and prolonged reversal events, reversal tolerance could for example significantly depend on reversal duration. However, determination of the expected degradation during field operation is challenging and would require a large fleet of PEFC systems where reversal events can be reliable characterized and detected. The latter in turn is requiring a wide range of sensors within the PEFC system (e.g. cell voltage monitoring, temperature, *RH*). Therefore, numerical modelling might be able to support and accelerate considerations on varying reversal durations in field applications.

Last but not least, the limited resource of Ir should be comprehensively considered when it comes to OER based RTA development. Incorporating IrO$_2$ catalysts currently offers the best trade off between OER activtiy and stability on a commercial level. Ir demand will most likely become a critical bottleneck in near future due to the targeted large scale green hydrogen production via PEM water electrolyzers [190]. However, green hydrogen production is in turn crucial for further commercialization of PEFCs [11]. Consequently, these competing demands require a comprehensive consideration of material-based mitigation strategy by OER based RTAs versus other mitigation strategies. The OER loading of reversal tolerant PEFCs should be reduced as much as possible for the respective application and could therefore e.g. be coupled with active system based mitigation strategies (for example cell voltage monitoring).

Durability of OER based RTAs under transient conditions

The major questions regarding RTA stability are the mechanism of Ir dissolution, migration of soluble Ir species and subsequent redeposition within other fuel cell components. Further fundamental understanding is mandatory to derive mitigating strategies for PEFC performance loss or reversal retention. Consequently, increasing and decreasing factors for Ir dissolution, either by transient dissolution or in the presence of reducing hydrogen atmosphere, are of particular interest to reduce primary degradation. This could be achieved for example by adjusted operation strategies or material improvements. To mitigate secondary degradation by migration and redeposition of soluble Ir species, further insigths in the Ir redeposition mechanism are crucial. For example, controlled redeposition (e.g. introduction of nucleation points) within the membrane could prevent fuel cell performance decay. Besides, the possible mitigating impact of crossed-over Ir species on cathode carbon corrosion, commonly induced by SUSD events, should be further investigated. The introduction of OER catalyst to the cathode catalyst layer has been previously reported as SUSD mitigation strategy [188, 189]. The SUSD ASTs presented in this work cannot resolve this aspect

circumferentially, as they were aiming for low cathode degradation by reducing the residence time of the migrating gas front during the SUSD events. However, crossed-over Ir could decrease cathode degradation during SUSD events in field application e.g. at high temperatures or *RH* [78, 97].

Another challenging factor revealed by this thesis is the determination of the apparent *ECSA* of Pt based catalysts in the presence of Ir species. The *ECSA* is a major key value used to estimate the degradation state of a fuel cell and derive further properties, e.g. after a durability stress test. Since at least metallic Ir is partly acitive within H_{upd} and CO adsoprtion, in-situ *ECSA* determination on MEA level for the HOR or ORR catalyst can be interfered by OER co-catalysts. To better destinguish different degradation effects and improve the understanding in degradation mechanisms, the separate *ECSA* determination of Pt and Ir with in-situ characterization methods is desirable.

8 Bibliography

[1] Barack Obama on Twitter. [Online]. Available: https://twitter.com/barackobama/status/514461859542351872?lang=de (accessed: Feb. 23 2022).

[2] B. C. O'Neill *et al.,* "Achievements and needs for the climate change scenario framework," *Nature climate change*, pp. 1–11, 2020, doi: 10.1038/s41558-020-00952-0.

[3] J. Uppenbrink, "Arrhenius and Global Warming," *Science*, vol. 272, no. 5265, p. 1122, 1996, doi: 10.1126/science.272.5265.1122.

[4] Washington Post, *Scientist says greenhouse effect is setting in.* [Online]. Available: https://www.washingtonpost.com/archive/politics/1988/06/24/scientist-says-greenhouse-effect-is-setting-in/3844f00f-42f4-420f-8811-62de6c989d8f/ (accessed: Feb. 19 2022).

[5] Intergovernmental Panel on Climate Change, "Climate Change 2021: The Physical Science Basis. Contribution of Working Group I to the Sixth Assessment Report of the Intergovernmental Panel on Climate Change," Cambridge University Press, 2021.

[6] J. E. Oliver, "Kyoto Protocol," in *Encyclopedia of Earth Sciences Series, Encyclopedia of world climatology*, J. E. Oliver, Ed., Dordrecht, Berlin, Heidelberg: Springer, 2005, p. 443.

[7] United Nations, "Framework Convention on Climate Change - The Paris Agreement," Paris: United Nations, 2015. Accessed: Feb. 19 2022. [Online]. Available: https://unfccc.int/documents/184656

[8] A. R. Ravishankara, D. A. Randall, and J. W. Hurrell, "Complex and yet predictable: The message of the 2021 Nobel Prize in Physics," *Proceedings of the National Academy of Sciences of the United States of America*, vol. 119, no. 2, 2022, doi: 10.1073/pnas.2120669119.

[9] T. M. Lenton *et al.,* "Climate tipping points - too risky to bet against," *Nature*, vol. 575, no. 7784, pp. 592–595, 2019, doi: 10.1038/d41586-019-03595-0.

[10] W. Botzen, S. Duijndam, and P. van Beukering, "Lessons for climate policy from behavioral biases towards COVID-19 and climate change risks," *World development*, vol. 137, p. 105214, 2021, doi: 10.1016/j.worlddev.2020.105214.

[11] Rod Borup, Ted Krause, Jack Brouwer, "Hydrogen is Essential for Industry and Transportation Decarbonization," *The Electrochemical Society Interface*, vol. 30, no. 57, 2021.

[12] G. R. Timilsina, "Are renewable energy technologies cost competitive for electricity generation?," *Renewable Energy*, vol. 180, pp. 658–672, 2021, doi: 10.1016/j.renene.2021.08.088.

[13] Fraunhofer Institute for Solar Energy Systems ISE, *Levelized Cost of Electricity: Renewables Clearly Superior to Conventional Power Plants Due to Rising CO2 Prices - Fraunhofer ISE.* [Online]. Available: https://www.ise.fraunhofer.de/en/press-media/press-releases/2021/levelized-cost-of-electricity-renewables-clearly-superior-to-conventional-power-plants-due-to-rising-co2-prices.html (accessed: Feb. 23 2022).

[14] A. Saeedmanesh, M. A. Mac Kinnon, and J. Brouwer, "Hydrogen is essential for sustainability," *Current Opinion in Electrochemistry*, vol. 12, pp. 166–181, 2018, doi: 10.1016/j.coelec.2018.11.009.

[15] Bryan S. Pivovar, Mark F. Ruth, Deborah J. Myers, Huyen N. Dinh, "Hydrogen: Targeting $1/kg in 1 Decade," *The Electrochemical Society Interface*, vol. 30, no. 57, 2021.

[16] Plamen Atanassov, Vito Di Noto, and Stephen McPhail, "From Hydrogen Manifesto, through Green Deal and Just Transition, to Clean Energy Act," *The Electrochemical Society Interface*, vol. 30, no. 57, 2021.

[17] European Comission, *The ninth U.S.-EU Energy Council.* [Online]. Available: https://ec.europa.eu/info/news/ninth-us-eu-energy-council-2022-feb-07_en (accessed: Feb. 23 2022).

[18] X. Ren, L. Dong, Di Xu, and B. Hu, "Challenges towards hydrogen economy in China," *International Journal of Hydrogen Energy*, vol. 45, no. 59, pp. 34326–34345, 2020, doi: 10.1016/j.ijhydene.2020.01.163.

[19] Hydrogen Council, "Hydrogen Insights: A perspective on hydrogen investment, market development and cost competitiveness," 2021. Accessed: May 2 2022. [Online]. Available: https://hydrogencouncil.com/wp-content/uploads/2021/02/Hydrogen-Insights-2021-Report.pdf

[20] IEA - International Energy Agency, "Market Report Series: Renewables 2018," Accessed: Feb. 22 2022. [Online]. Available: https://iea.blob.core.windows.net/assets/79e1943b-9401-478f-9f60-5e8c2bff9342/Market_Report_Series_Renewables_2018.pdf

[21] T. E. Lipman and A. Z. Weber, Eds., *Fuel Cells and Hydrogen Production*. New York, NY: Springer New York, 2019.

[22] US Environmental Protection Agency, *Fast Facts on Transportation Greenhouse Gas Emissions.* [Online]. Available: https://www.epa.gov/greenvehicles/fast-facts-transportation-greenhouse-gas-emissions (accessed: Feb. 23 2022).

[23] Intergovernmental Panel on Climate Change, "Climate change 2014 Synthesis Report," Geneva, Switzerland, 2014.

[24] D. A. Cullen *et al.,* "New roads and challenges for fuel cells in heavy-duty transportation," *Nature Energy*, vol. 6, no. 5, pp. 462–474, 2021, doi: 10.1038/s41560-021-00775-z.

[25] G. Berckmans, M. Messagie, J. Smekens, N. Omar, and L. Vanhaverbeke, "Cost Projection of State of the Art Lithium-Ion Batteries for Electric Vehicles Up to

2030," The international council on clean transportation 9, 2019. Accessed: Feb. 22 2022. [Online]. Available: https://theicct.org/sites/default/files/publications/EV_cost_2020_2030_20190401.pdf

[26] Daimler Truck AG, *Daimler Trucks begins rigorous testing of its fuel-cell truck.* [Online]. Available: https://media.daimlertruck.com/marsMediaSite/en/instance/ko/Daimler-Trucks-begins-rigorous-testing-of-its-fuel-cell-truck.xhtml?oid=50000349&ls=L2VuL2luc3RhbmNlL2tvLnhodG1sP29pZD00NzQ2OTQ2MSZyZWxJZD02MDgyOSZmcm9tT2lkPTQ3NDY5NDYxJnJlc3VsdEluZm9UeXBlSWQ9NDA2MjYmdmlld1R5cGU9dGh1bWJzJnNvcnREZWZpbml0aW9uPVBVQkxJU0hFRF9BVC0yJnRodW1iU2NhbGVJbmRleD0xJnJvd0NvdW50c0luZGV4PTUmZnJvbUluZm9UeXBlSWQ9NDA2Mjg!&rs=3 (accessed: Nov. 16 2021).

[27] Mark Luth, "Fuel Cell Customers - Medium and Heavy-Duty Transportation," *Fuel Cell & Hydrogen Energy Association*, 02 Sep., 2019. https://www.fchea.org/in-transition/2019/9/2/fuel-cell-customers-medium-and-heavy-duty-transportation (accessed: Feb. 22 2022).

[28] A. K. Breed, D. Speth, and P. Plötz, "CO2 fleet regulation and the future market diffusion of zero-emission trucks in Europe," *Energy Policy*, vol. 159, p. 112640, 2021, doi: 10.1016/j.enpol.2021.112640.

[29] Chris Randall, *COP26: 30 nations & 11 carmakers want to exit combustion transit.* [Online]. Available: https://www.electrive.com/2021/11/10/cop26-24-nations-6-carmakers-want-to-exit-combustion-transit/ (accessed: Feb. 23 2022).

[30] P. Campbell, "European truckmakers to phase out diesel sales decade earlier than planned," *Financial Times*, 14 Dec., 2020. https://www.ft.com/content/7d49589b-ff50-444d-8eef-b8abe5691f91 (accessed: Feb. 23 2022).

[31] C. Cunanan, M.-K. Tran, Y. Lee, S. Kwok, V. Leung, and M. Fowler, "A Review of Heavy-Duty Vehicle Powertrain Technologies: Diesel Engine Vehicles, Battery Electric Vehicles, and Hydrogen Fuel Cell Electric Vehicles," *Clean Technol.*, vol. 3, no. 2, pp. 474–489, 2021, doi: 10.3390/cleantechnol3020028.

[32] Deloitte & Ballard, "Fueling the Future of Mobility. Hydrogen and fuel cell solutions for transportation," vol. 1, 2020.

[33] Ahmet Kusoglu, "Chalkboard 1 - The Many Colors of Hydrogen," *The Electrochemical Society Interface*, vol. 30, no. 44, 2021.

[34] R. L. Borup *et al.,* "Recent developments in catalyst-related PEM fuel cell durability," *Current Opinion in Electrochemistry*, vol. 21, pp. 192–200, 2020, doi: 10.1016/j.coelec.2020.02.007.

[35] J. N. Schwämmlein, P. J. Rheinländer, Y. Chen, K. T. Freyer, and H. A. Gasteiger, "Anode Aging during PEMFC Start-Up and Shut-Down: H 2 -Air Fronts vs Voltage Cycles," *J. Electrochem. Soc.*, vol. 165, no. 16, F1312-F1322, 2018, doi: 10.1149/2.0611816jes.

[36] B. M. Stühmeier, M. R. Pietsch, J. N. Schwämmlein, and H. A. Gasteiger, "Pressure and Temperature Dependence of the Hydrogen Oxidation and Evolution Reaction Kinetics on Pt Electrocatalysts via PEMFC-based Hydrogen-Pump Measurements," *J. Electrochem. Soc.*, vol. 168, no. 6, p. 64516, 2021, doi: 10.1149/1945-7111/ac099c.

[37] B. K. Hong, P. Mandal, J.-G. Oh, and S. Litster, "On the impact of water activity on reversal tolerant fuel cell anode performance and durability," *Journal of Power Sources*, vol. 328, pp. 280–288, 2016, doi: 10.1016/j.jpowsour.2016.07.002.

[38] S. Zhang, X.-Z. Yuan, J. N. C. Hin, H. Wang, K. A. Friedrich, and M. Schulze, "A review of platinum-based catalyst layer degradation in proton exchange membrane fuel cells," *Journal of Power Sources*, vol. 194, no. 2, pp. 588–600, 2009, doi: 10.1016/j.jpowsour.2009.06.073.

[39] T. R. Ralph, M. P. Hogarth, "Catalysis for Low Temperature Fuel Cells: Part II: THE ANODE CHALLENGES," *Platinum Metals Rev.*, vol. 46, no. 3, 2002.

[40] D. Bentele, K. Aylar, K. Olsen, E. Klemm, and S. H. Eberhardt, "PEMFC Anode Durability: Innovative Characterization Methods and Further Insights on OER Based Reversal Tolerance," *J. Electrochem. Soc.*, vol. 168, no. 2, p. 24515, 2021, doi: 10.1149/1945-7111/abe50b.

[41] A. Albarbar and M. Alrweq, *Proton Exchange Membrane Fuel Cells*. Cham: Springer International Publishing, 2018.

[42] P. Kurzweil, *Brennstoffzellentechnik*. Wiesbaden: Springer Fachmedien Wiesbaden, 2013.

[43] F. J. Rodríguez-Varela and T. W. Napporn, Eds., *Advanced Electrocatalysts for Low-Temperature Fuel Cells*. Cham: Springer International Publishing, 2018.

[44] S. Srinivasan, *Fuel cells: From fundamentals to applications*. New York: Springer, 2006.

[45] U.S. Department of Energy (DOE), Ed., *Fuel Cell Handbook (Seventh Edition),* 7th ed. Morgantown, West Virginia, 2004. Accessed: Nov. 16 2021. [Online]. Available: https://netl.doe.gov/sites/default/files/netl-file/FCHandbook7.pdf

[46] Wolf Vielstich, Arnold Lamm, Hubert A. Gasteiger, Ed., *Handbook of Fuel Cells: Fundamentals, Technology, Applications*. Chichester: Wiley, 2007.

[47] J. Zhang, Ed., *PEM Fuel Cell Electrocatalysts and Catalyst Layers*. London: Springer London, 2008.

[48] Steele, B., Heinzel, "Materials for fuel-cell technologies," *Nature*, vol. 414, 2001, doi: 10.1038/35104620.

[49] A. Z. Weber *et al.,* "A Critical Review of Modeling Transport Phenomena in Polymer-Electrolyte Fuel Cells," *J. Electrochem. Soc.*, vol. 161, no. 12, F1254-F1299, 2014, doi: 10.1149/2.0751412jes.

[50] C. Simon, F. Hasché, and H. A. Gasteiger, "Influence of the Gas Diffusion Layer Compression on the Oxygen Transport in PEM Fuel Cells at High Water Saturation

Levels," *J. Electrochem. Soc.*, vol. 164, no. 6, F591-F599, 2017, doi: 10.1149/2.0691706jes.

[51] Frano Barbir, "CHAPTER 3 - Fuel Cell Electrochemistry," in *PEM Fuel Cells*, Frano Barbir, Ed., Burlington: Academic Press, 2005, pp. 33–72. [Online]. Available: https://www.sciencedirect.com/science/article/pii/B9780120781423500045

[52] R. Borup *et al.,* "Scientific aspects of polymer electrolyte fuel cell durability and degradation," *Chemical reviews*, vol. 107, no. 10, pp. 3904–3951, 2007, doi: 10.1021/cr050182l.

[53] V. Mittal, H. Kunz, and J. Fenton, "Membrane Degradation Mechanisms in PEM-FCs," *Meet. Abstr.*, MA2006-02, no. 8, p. 448, 2006, doi: 10.1149/MA2006-02/8/448.

[54] A. Orfanidi, P. Madkikar, H. A. El-Sayed, G. S. Harzer, T. Kratky, and H. A. Gasteiger, "The Key to High Performance Low Pt Loaded Electrodes," *J. Electrochem. Soc.*, vol. 164, no. 4, F418-F426, 2017, doi: 10.1149/2.1621704jes.

[55] K. Shinozaki, H. Yamada, and Y. Morimoto, "Relative Humidity Dependence of Pt Utilization in Polymer Electrolyte Fuel Cell Electrodes: Effects of Electrode Thickness, Ionomer-to-Carbon Ratio, Ionomer Equivalent Weight, and Carbon Support," *J. Electrochem. Soc.*, vol. 158, no. 5, B467, 2011, doi: 10.1149/1.3556906.

[56] M. Dou *et al.,* "Sb-Doped SnO 2 Supported Platinum Catalyst with High Stability for Proton Exchange Membrane Fuel Cells," *J. Electrochem. Soc.*, vol. 161, no. 12, F1231-F1236, 2014, doi: 10.1149/2.0761412jes.

[57] S. Henning *et al.,* "Pt-Ni Aerogels as Unsupported Electrocatalysts for the Oxygen Reduction Reaction," *J. Electrochem. Soc.*, vol. 163, no. 9, F998-F1003, 2016, doi: 10.1149/2.0251609jes.

[58] D. J. S. Sandbeck *et al.,* "The Dissolution Dilemma for Low Pt Loading Polymer Electrolyte Membrane Fuel Cell Catalysts," *J. Electrochem. Soc.*, vol. 167, no. 16, p. 164501, 2020, doi: 10.1149/1945-7111/abc767.

[59] Reza B. Moghaddam and E. Bradley Easton, "The interplay between impedance parameters, structure, and performance of fuel cell catalyst layers," *Chemical Engineering Science*, vol. 224, p. 115792, 2020, doi: 10.1016/j.ces.2020.115792.

[60] C. Zhou, L. Guo, L. Chen, X. Tian, T. He, and Q. Yang, "Pore-Scale Modeling of Air–Water Two Phase Flow and Oxygen Transport in Gas Diffusion Layer of Proton Exchange Membrane Fuel Cell," *Energies*, vol. 14, no. 13, p. 3812, 2021, doi: 10.3390/en14133812.

[61] X. LI and I. SABIR, "Review of bipolar plates in PEM fuel cells: Flow-field designs," *International Journal of Hydrogen Energy*, vol. 30, no. 4, pp. 359–371, 2005, doi: 10.1016/j.ijhydene.2004.09.019.

[62] J. Zhang, F. Coms, and S. Kumaraguru, "Editors' Choice—Necessity to Avoid Titanium Oxide as Electrocatalyst Support in PEM Fuel Cells: A Membrane Dura-

bility Study," *J. Electrochem. Soc.*, vol. 168, no. 2, p. 24520, 2021, doi: 10.1149/1945-7111/abe5e9.

[63] H. Lohse-Busch, K. Stutenberg, M. Duoba, and S. Iliev, "Technology Assessment Of A Fuel Cell Vehicle: 2017 Toyota Mirai," U.S. Department of Energy (DOE) report, 2018. Accessed: Feb. 22 2022. [Online]. Available: https:// publications.anl.gov/anlpubs/2018/06/144774.pdf

[64] Jason Marcinkoski, Ram Vijayagopal, Jesse Adams, Brian James, John Kopasz,Rajesh Ahluwalia, "DOE Hydrogen and Fuel Cells Program Record 19006: Technical Targets for Hydrogen-Fueled Long-Haul Tractor-Trailer Trucks," 2019. Accessed: Feb. 22 2022. [Online]. Available: https://www.hydrogen.energy.gov/ pdfs/19006_hydrogen_class8_long_haul_truck_targets.pdf

[65] G. Hinds and E. Brightman, "Towards more representative test methods for corrosion resistance of PEMFC metallic bipolar plates," *International Journal of Hydrogen Energy*, vol. 40, no. 6, pp. 2785–2791, 2015, doi: 10.1016/j.ijhydene.2014.12.085.

[66] D. A. Dillard *et al.*, "Seals and Sealants in PEM Fuel Cell Environments: Material, Design, and Durability Challenges," in *2nd International Conference on Fuel Cell Science, Engineering and Technology*, Rochester, New York, USA, 06142004, pp. 553–560.

[67] R. Mukundan *et al.*, "Membrane Accelerated Stress Test Development for Polymer Electrolyte Fuel Cell Durability Validated Using Field and Drive Cycle Testing," *J. Electrochem. Soc.*, vol. 165, no. 6, F3085-F3093, 2018, doi: 10.1149/2.0101806jes.

[68] J. C. Meier *et al.*, "Design criteria for stable Pt/C fuel cell catalysts," *Beilstein journal of nanotechnology*, vol. 5, pp. 44–67, 2014, doi: 10.3762/bjnano.5.5.

[69] P. J. Ferreira *et al.*, "Instability of Pt/C Electrocatalysts in Proton Exchange Membrane Fuel Cells," *J. Electrochem. Soc.*, vol. 152, no. 11, A2256, 2005, doi: 10.1149/1.2050347.

[70] M. Fathi Tovini *et al.*, "Degradation Mechanism of an IrO2 Anode Co-Catalyst for Cell Voltage Reversal Mitigation under Transient Operation Conditions of a PEM Fuel Cell," *J. Electrochem. Soc.*, vol. 168, no. 6, p. 64521, 2021, doi: 10.1149/1945-7111/ac0d39.

[71] S. Cherevko, N. Kulyk, and K. J. Mayrhofer, "Durability of platinum-based fuel cell electrocatalysts: Dissolution of bulk and nanoscale platinum," *Nano Energy*, vol. 29, pp. 275–298, 2016, doi: 10.1016/j.nanoen.2016.03.005.

[72] K. J. Mayrhofer, S. J. Ashton, J. C. Meier, G. K. Wiberg, M. Hanzlik, and M. Arenz, "Non-destructive transmission electron microscopy study of catalyst degradation under electrochemical treatment," *Journal of Power Sources*, vol. 185, no. 2, pp. 734–739, 2008, doi: 10.1016/j.jpowsour.2008.08.003.

[73] K. J. Mayrhofer *et al.*, "Fuel cell catalyst degradation on the nanoscale," *Electrochemistry Communications*, vol. 10, no. 8, pp. 1144–1147, 2008, doi: 10.1016/j.elecom.2008.05.032.

[74] H. Wendt, "K. Kinoshita: Carbon, Electrochemical and Physical Properties John Wiley + Sons, Chichester, New York, Brisbane, Toronto 1988. 533 Seiten, Preis: £ 65.-," *Berichte der Bunsengesellschaft für physikalische Chemie*, vol. 92, no. 9, p. 1060, 1988, doi: 10.1002/bbpc.198800269.

[75] J. P. Meyers and R. M. Darling, "Model of Carbon Corrosion in PEM Fuel Cells," *J. Electrochem. Soc.*, vol. 153, no. 8, A1432, 2006, doi: 10.1149/1.2203811.

[76] A. P. Young, J. Stumper, and E. Gyenge, "Characterizing the Structural Degradation in a PEMFC Cathode Catalyst Layer: Carbon Corrosion," *J. Electrochem. Soc.*, vol. 156, no. 8, B913, 2009, doi: 10.1149/1.3139963.

[77] S. Maass, F. Finsterwalder, G. Frank, R. Hartmann, and C. Merten, "Carbon support oxidation in PEM fuel cell cathodes," *Journal of Power Sources*, vol. 176, no. 2, pp. 444–451, 2008, doi: 10.1016/j.jpowsour.2007.08.053.

[78] T. Mittermeier, A. Weiß, F. Hasché, and H. A. Gasteiger, "PEM Fuel Cell Start-Up/Shut-Down Losses vs Relative Humidity: The Impact of Water in the Electrode Layer on Carbon Corrosion," *J. Electrochem. Soc.*, vol. 165, no. 16, F1349-F1357, 2018, doi: 10.1149/2.0931816jes.

[79] J. Kwon, P. Choi, and K. Eom, "A Comparison Study on the Carbon Corrosion Reaction under Saturated and Low Relative Humidity Conditions via Transmission Line Model-Based Electrochemical Impedance Analysis," *J. Electrochem. Soc.*, vol. 168, no. 6, p. 64515, 2021, doi: 10.1149/1945-7111/ac0aaf.

[80] D. A. Stevens and J. R. Dahn, "Thermal degradation of the support in carbon-supported platinum electrocatalysts for PEM fuel cells," *Carbon*, vol. 43, no. 1, pp. 179–188, 2005, doi: 10.1016/j.carbon.2004.09.004.

[81] Y. Liu, C. Ji, W. Gu, J. Jorne, and H. A. Gasteiger, "Effects of Catalyst Carbon Support on Proton Conduction and Cathode Performance in PEM Fuel Cells," *J. Electrochem. Soc.*, vol. 158, no. 6, B614-B621, 2011, doi: 10.1149/1.3562945.

[82] N. Macauley *et al.,* "Carbon Corrosion in PEM Fuel Cells and the Development of Accelerated Stress Tests," *J. Electrochem. Soc.*, vol. 165, no. 6, F3148-F3160, 2018, doi: 10.1149/2.0061806jes.

[83] J. Wang, G. Yin, Y. Shao, S. Zhang, Z. Wang, and Y. Gao, "Effect of carbon black support corrosion on the durability of Pt/C catalyst," *Journal of Power Sources*, vol. 171, no. 2, pp. 331–339, 2007, doi: 10.1016/j.jpowsour.2007.06.084.

[84] R. T. White *et al.,* "Four-dimensional joint visualization of electrode degradation and liquid water distribution inside operating polymer electrolyte fuel cells," *Scientific reports*, vol. 9, no. 1, p. 1843, 2019, doi: 10.1038/s41598-018-38464-9.

[85] R. K. Ahluwalia *et al.,* "Achieving 5,000-h and 8,000-h Low-PGM Electrode Durability on Automotive Drive Cycles," *J. Electrochem. Soc.*, vol. 168, no. 4, p. 44518, 2021, doi: 10.1149/1945-7111/abf507.

[86] H. A. Gasteiger, S. S. Kocha, B. Sompalli, and F. T. Wagner, "Activity benchmarks and requirements for Pt, Pt-alloy, and non-Pt oxygen reduction catalysts for

PEMFCs," *Applied Catalysis B: Environmental*, vol. 56, 1-2, pp. 9–35, 2005, doi: 10.1016/j.apcatb.2004.06.021.

[87] S. Ye, M. Hall, H. Cao, and P. He, "Degradation Resistant Cathodes in Polymer Electrolyte Membrane Fuel Cells," *ECS Trans.*, vol. 3, no. 1, pp. 657–666, 2006, doi: 10.1149/1.2356186.

[88] P. Yu, M. Pemberton, and P. Plasse, "PtCo/C cathode catalyst for improved durability in PEMFCs," *Journal of Power Sources*, vol. 144, no. 1, pp. 11–20, 2005, doi: 10.1016/j.jpowsour.2004.11.067.

[89] Y. Shao, G. Yin, Y. Gao, and P. Shi, "Durability Study of Pt∕C and Pt∕CNTs Catalysts under Simulated PEM Fuel Cell Conditions," *J. Electrochem. Soc.*, vol. 153, no. 6, A1093, 2006, doi: 10.1149/1.2191147.

[90] S. V. Selvaganesh, P. Sridhar, S. Pitchumani, and A. K. Shukla, "A Durable Graphitic-Carbon Support for Pt and Pt 3 Co Cathode Catalysts in Polymer Electrolyte Fuel Cells," *J. Electrochem. Soc.*, vol. 160, no. 1, F49-F59, 2013, doi: 10.1149/2.051301jes.

[91] C. Wang, M. Ricketts, A. P. Soleymani, J. Jankovic, J. Waldecker, and J. Chen, "Effect of Carbon Support Characteristics on Fuel Cell Durability in Accelerated Stress Testing," *J. Electrochem. Soc.*, vol. 168, no. 4, p. 44507, 2021, doi: 10.1149/1945-7111/abf265.

[92] R. Bashyam, P. He, S. Wessel, and S. Knights, "Impacts of Cathode Loading on Ru Crossover Related PEFC Durability," *ECS Trans.*, vol. 41, no. 1, pp. 837–844, 2011, doi: 10.1149/1.3635617.

[93] P. He, T. Cheng, R. Bashyam, A. P. Young, and S. Knights, "Relative Humidity Effect on Anode Durability in PEMFC Startup/Shutdown Processes," *ECS Trans.*, vol. 33, no. 1, pp. 1273–1279, 2010, doi: 10.1149/1.3484620.

[94] T. T. H. Cheng, N. Jia, and P. He, "Characterization of the Degree of Ru Crossover and Its Performance Implications in Polymer Electrolyte Membrane Fuel Cells," *J. Electrochem. Soc.*, vol. 157, no. 5, B714, 2010, doi: 10.1149/1.3356939.

[95] K. C. Neyerlin, W. Gu, J. Jorne, and H. A. Gasteiger, "Study of the Exchange Current Density for the Hydrogen Oxidation and Evolution Reactions," *J. Electrochem. Soc.*, vol. 154, no. 7, B631, 2007, doi: 10.1149/1.2733987.

[96] T. Engl, L. Gubler, and T. J. Schmidt, "Fuel Electrode Carbon Corrosion in High Temperature Polymer Electrolyte Fuel Cells-Crucial or Irrelevant?," *Energy Technology*, vol. 4, no. 1, pp. 65–74, 2016, doi: 10.1002/ente.201500217.

[97] T. Mittermeier, A. Weiß, F. Hasché, G. Hübner, and H. A. Gasteiger, "PEM Fuel Cell Start-up/Shut-down Losses vs Temperature for Non-Graphitized and Graphitized Cathode Carbon Supports," *J. Electrochem. Soc.*, vol. 164, no. 2, F127-F137, 2017, doi: 10.1149/2.1061702jes.

[98] A. Taniguchi, T. Akita, K. Yasuda, and Y. Miyazaki, "Analysis of electrocatalyst degradation in PEMFC caused by cell reversal during fuel starvation," *Journal of*

Power Sources, vol. 130, 1-2, pp. 42–49, 2004, doi: 10.1016/j.jpowsour.2003.12.035.

[99] H. Chen, X. Zhao, T. Zhang, and P. Pei, "The reactant starvation of the proton exchange membrane fuel cells for vehicular applications: A review," *Energy Conversion and Management*, vol. 182, pp. 282–298, 2019, doi: 10.1016/j.enconman.2018.12.049.

[100] K. H. Lim, W. H. Lee, Y. Jeong, and H. Kim, "Analysis of Carbon Corrosion in Anode under Fuel Starvation Using On-Line Mass Spectrometry in Polymer Electrolyte Membrane Fuel Cells," *J. Electrochem. Soc.*, vol. 164, no. 14, F1580-F1586, 2017, doi: 10.1149/2.0731714jes.

[101] J. H. Ohs, U. Sauter, S. Maass, and D. Stolten, "Modeling hydrogen starvation conditions in proton-exchange membrane fuel cells," *Journal of Power Sources*, vol. 196, no. 1, pp. 255–263, 2011, doi: 10.1016/j.jpowsour.2010.06.038.

[102] N. Danilovic *et al.,* "Activity-Stability Trends for the Oxygen Evolution Reaction on Monometallic Oxides in Acidic Environments," *The journal of physical chemistry letters*, vol. 5, no. 14, pp. 2474–2478, 2014, doi: 10.1021/jz501061n.

[103] P. Mandal, B. K. Hong, J.-G. Oh, and S. Litster, "Understanding the voltage reversal behavior of automotive fuel cells," *Journal of Power Sources*, vol. 397, pp. 397–404, 2018, doi: 10.1016/j.jpowsour.2018.06.083.

[104] The Fuel Cell Store, *Carbon Black - Vulcan XC 72R.* [Online]. Available: https://www.fuelcellstore.com/vulcan-xc-72r (accessed: Nov. 24 2021).

[105] Y. Wang *et al.,* "Study of relative humidity on durability of the reversal tolerant proton exchange membrane fuel cell anode using a segmented cell," *Journal of Power Sources*, vol. 449, p. 227542, 2020, doi: 10.1016/j.jpowsour.2019.227542.

[106] Y. Wang *et al.,* "Study of failure mechanisms of the reversal tolerant fuel cell anode via novel in-situ measurements," *International Journal of Hydrogen Energy*, vol. 45, no. 1, pp. 996–1007, 2020, doi: 10.1016/j.ijhydene.2019.10.189.

[107] C. Qin, J. Wang, D. Yang, B. Li, and C. Zhang, "Proton Exchange Membrane Fuel Cell Reversal: A Review," *Catalysts*, vol. 6, no. 12, p. 197, 2016, doi: 10.3390/catal6120197.

[108] W. Daud, R. E. Rosli, E. H. Majlan, S. Hamid, R. Mohamed, and T. Husaini, "PEM fuel cell system control: A review," *Renewable Energy*, vol. 113, pp. 620–638, 2017, doi: 10.1016/j.renene.2017.06.027.

[109] S. D. Knights, K. M. Colbow, J. St-Pierre, and D. P. Wilkinson, "Aging mechanisms and lifetime of PEFC and DMFC," *Journal of Power Sources*, vol. 127, 1-2, pp. 127–134, 2004, doi: 10.1016/j.jpowsour.2003.09.033.

[110] J. Jung, B. Park, and J. Kim, "Durability test with fuel starvation using a Pt/CNF catalyst in PEMFC," *Nanoscale research letters*, vol. 7, no. 1, p. 34, 2012, doi: 10.1186/1556-276X-7-34.

[111] X. Wang, R. K. Ahluwalia, and A. J. Steinbach, "Kinetics of Hydrogen Oxidation and Hydrogen Evolution Reactions on Nanostructured Thin-Film Platinum Al-

loy Catalyst," *J. Electrochem. Soc.*, vol. 160, no. 3, F251-F261, 2013, doi: 10.1149/2.028303jes.

[112] R. Atanasoski, D. van der Vliet, D. Cullen, and L. Atanasoska, "Durable Catalysts for Fuel Cell Protection during Transient Conditions," DOE/3M Company Award DE-EE0000456. Accessed: Nov. 25 2021. [Online]. Available: https://www.hydrogen.energy.gov/pdfs/review14/fc006_atanasoski_2014_o.pdf

[113] A. Pătru, A. Rabis, S. E. Temmel, R. Kotz, and T. J. Schmidt, "Pt/IrO 2 –TiO 2 cathode catalyst for low temperature polymer electrolyte fuel cell – Application in MEAs, performance and stability issues," *Catalysis Today*, vol. 262, pp. 161–169, 2016, doi: 10.1016/j.cattod.2015.09.009.

[114] R. Marić, C. Gebauer, M. Nesselberger, F. Hasché, and P. Strasser, "Towards a Harmonized Accelerated Stress Test Protocol for Fuel Starvation Induced Cell Reversal Events in PEM Fuel Cells: The Effect of Pulse Duration," *J. Electrochem. Soc.*, vol. 167, no. 12, p. 124520, 2020, doi: 10.1149/1945-7111/abad68.

[115] S. W. Lee, B. Lee, C. Baik, T.-Y. Kim, and C. Pak, "Multifunctional Ir–Ru alloy catalysts for reversal-tolerant anodes of polymer electrolyte membrane fuel cells," *Journal of Materials Science & Technology*, vol. 60, pp. 105–112, 2021, doi: 10.1016/j.jmst.2020.05.020.

[116] E. You, M. Min, S.-A. Jin, T. Kim, and C. Pak, "Highly Durable, Cost-Effective, and Multifunctional Carbon-Supported IrRu-Based Catalyst for Automotive Polymer Electrolyte Fuel Cell Anodes," *J. Electrochem. Soc.*, vol. 165, no. 6, F3094-F3099, 2018, doi: 10.1149/2.0121806jes.

[117] T. Joo, L. Hu, B. K. Hong, J.-G. Oh, and S. Litster, "On the origin of deactivation of reversal-tolerant fuel cell anodes under voltage reversal conditions," *Journal of Power Sources*, vol. 472, p. 228439, 2020, doi: 10.1016/j.jpowsour.2020.228439.

[118] L. Hu, B. K. Hong, J.-G. Oh, and S. Litster, "Robust Operation of Fuel Cell Systems in Subfreezing Conditions: A Material-Based Solution to Achieve Better Anode Durability," *ACS Appl. Energy Mater.*, vol. 2, no. 10, pp. 7152–7161, 2019, doi: 10.1021/acsaem.9b01108.

[119] Z. Liu, L. Yang, Z. Mao, W. Zhuge, Y. Zhang, and L. Wang, "Behavior of PEMFC in starvation," *Journal of Power Sources*, vol. 157, no. 1, pp. 166–176, 2006, doi: 10.1016/j.jpowsour.2005.08.006.

[120] T. R. Ralph, S. Hudson, and D. P. Wilkinson, "Electrocatalyst Stability In PEMFCs And The Role Of Fuel Starvation And Cell Reversal Tolerant Anodes," *ECS Trans.*, vol. 1, no. 8, pp. 67–84, 2006, doi: 10.1149/1.2214545.

[121] D. Liang, Q. Shen, M. Hou, Z. Shao, and B. Yi, "Study of the cell reversal process of large area proton exchange membrane fuel cells under fuel starvation," *Journal of Power Sources*, vol. 194, no. 2, pp. 847–853, 2009, doi: 10.1016/j.jpowsour.2009.06.059.

[122] C. Cai *et al.,* "Water electrolysis plateau in voltage reversal process for proton exchange membrane fuel cells," *Journal of Power Sources*, vol. 455, p. 227952, 2020, doi: 10.1016/j.jpowsour.2020.227952.

[123] T.-Y. Kim, S. W. Lee, and C. Pak, "Optimization of carbon-supported Ir–Ru alloys for polymer electrolyte fuel cell anodes under cell reversal," *Journal of Industrial and Engineering Chemistry*, vol. 85, pp. 87–93, 2020, doi: 10.1016/j.jiec.2020.01.024.

[124] C. Cai *et al.,* "Carbon corrosion: A novel termination mechanism of the water electrolysis plateau during voltage reversal," *Journal of Power Sources*, vol. 473, p. 228542, 2020, doi: 10.1016/j.jpowsour.2020.228542.

[125] T. Labi, F. van Schalkwyk, S. M. Andersen, P. Morgen, S. C. Ray, and J. Chamier, "Increasing fuel cell durability during prolonged and intermittent fuel starvation using supported IrOx," *Journal of Power Sources*, vol. 490, p. 229568, 2021, doi: 10.1016/j.jpowsour.2021.229568.

[126] C.-W. Roh, H.-E. Kim, J. Choi, J. Lim, and H. Lee, "Monodisperse IrOx deposited on Pt/C for reversal tolerant anode in proton exchange membrane fuel cell," *Journal of Power Sources*, vol. 443, p. 227270, 2019, doi: 10.1016/j.jpowsour.2019.227270.

[127] J. Wang *et al.,* "Highly efficient, cell reversal resistant PEMFC based on PtNi/C octahedral and OER composite catalyst," *International Journal of Hydrogen Energy*, vol. 45, no. 15, pp. 8930–8940, 2020, doi: 10.1016/j.ijhydene.2020.01.054.

[128] C. E. Moore, J. Eastcott, M. Cimenti, N. Kremliakova, and E. L. Gyenge, "Novel methodology for ex situ characterization of iridium oxide catalysts in voltage reversal tolerant proton exchange membrane fuel cell anodes," *Journal of Power Sources*, vol. 417, pp. 53–60, 2019, doi: 10.1016/j.jpowsour.2019.02.006.

[129] S. Stucki, G. G. Scherer, S. Schlagowski, and E. Fischer, "PEM water electrolysers: evidence for membrane failure in 100kW demonstration plants," *J Appl Electrochem*, vol. 28, no. 10, pp. 1041–1049, 1998, doi: 10.1023/A:1003477305336.

[130] C. A. Reiser *et al.,* "A Reverse-Current Decay Mechanism for Fuel Cells," *Electrochem. Solid-State Lett.*, vol. 8, no. 6, A273, 2005, doi: 10.1149/1.1896466.

[131] A. Ohma, K. Shinohara, A. Iiyama, T. Yoshida, and A. Daimaru, "Membrane and Catalyst Performance Targets for Automotive Fuel Cells by FCCJ Membrane, Catalyst, MEA WG," *ECS Trans.*, vol. 41, no. 1, pp. 775–784, 2011, doi: 10.1149/1.3635611.

[132] E. Colombo, A. Bisello, A. Casalegno, and A. Baricci, "Mitigating PEMFC Degradation During Start-Up: Locally Resolved Experimental Analysis and Transient Physical Modelling," *J. Electrochem. Soc.*, vol. 168, no. 5, p. 54508, 2021, doi: 10.1149/1945-7111/abf4eb.

[133] C. Wang *et al.,* "Improved Carbon Corrosion and Platinum Dissolution Durability in Automotive Fuel Cell Startup and Shutdown Operation," *J. Electrochem. Soc.*, vol. 168, no. 3, p. 34503, 2021, doi: 10.1149/1945-7111/abe6ea.

[134] W. Gu, R. N. Carter, P. T. Yu, and H. A. Gasteiger, "Start/Stop and Local H2 Starvation Mechanisms of Carbon Corrosion: Model vs. Experiment," *ECS Trans.*, vol. 11, no. 1, pp. 963–973, 2007, doi: 10.1149/1.2781008.

[135] R. T. Atanasoski, D. A. Cullen, G. D. Vernstrom, G. M. Haugen, and L. L. Atanasoska, "A Materials-Based Mitigation Strategy for SU/SD in PEM Fuel Cells: Properties and Performance-Specific Testing of IrRu OER Catalysts," *ECS Electrochemistry Letters*, vol. 2, no. 3, F25-F28, 2013, doi: 10.1149/2.006303eel.

[136] E. Brightman, G. Hinds, and R. O'Malley, "In situ measurement of active catalyst surface area in fuel cell stacks," *Journal of Power Sources*, vol. 242, pp. 244–254, 2013, doi: 10.1016/j.jpowsour.2013.05.046.

[137] J. Wu, X. Z. Yuan, H. Wang, M. Blanco, J. J. Martin, and J. Zhang, "Diagnostic tools in PEM fuel cell research: Part IIPhysical/chemical methods," *International Journal of Hydrogen Energy*, vol. 33, no. 6, pp. 1747–1757, 2008, doi: 10.1016/j.ijhydene.2008.01.020.

[138] E. Barsoukov and J. R. Macdonald, Eds., *Impedance Spectroscopy: Theory, experiment, and applications*. Hoboken, NJ, USA: John Wiley & Sons, Inc, 2018. [Online]. Available: https://onlinelibrary.wiley.com/doi/book/10.1002/9781119381860

[139] S. Trasatti and O. A. Petrii, "Real surface area measurements in electrochemistry," *Pure and Applied Chemistry*, vol. 63, no. 5, pp. 711–734, 1991, doi: 10.1351/pac199163050711.

[140] R. W. Lindström, K. Kortsdottir, M. Wesselmark, A. Oyarce, C. Lagergren, and G. Lindbergh, "Active Area Determination of Porous Pt Electrodes Used in Polymer Electrolyte Fuel Cells: Temperature and Humidity Effects," *J. Electrochem. Soc.*, vol. 157, no. 12, B1795, 2010, doi: 10.1149/1.3494220.

[141] T. R. Garrick, T. E. Moylan, M. K. Carpenter, and A. Kongkanand, "Editors' Choice—Electrochemically Active Surface Area Measurement of Aged Pt Alloy Catalysts in PEM Fuel Cells by CO Stripping," *J. Electrochem. Soc.*, vol. 164, no. 2, F55-F59, 2017, doi: 10.1149/2.0381702jes.

[142] S. M. Alia, K. E. Hurst, S. S. Kocha, and B. S. Pivovar, "Mercury Underpotential Deposition to Determine Iridium and Iridium Oxide Electrochemical Surface Areas," *J. Electrochem. Soc.*, vol. 163, no. 11, F3051-F3056, 2016, doi: 10.1149/2.0071611jes.

[143] S. Watzele *et al.,* "Determination of Electroactive Surface Area of Ni-, Co-, Fe-, and Ir-Based Oxide Electrocatalysts," *ACS Catal.*, vol. 9, no. 10, pp. 9222–9230, 2019, doi: 10.1021/acscatal.9b02006.

[144] E. Martinez-Laserna, I. Gandiaga, E. Sarasketa-Zabala, J. Badeda, D.-I. Stroe, M. Swierczynski, A. Goikoetxea, "Battery second life: Hype, hope or reality? A

critical review of the state of the art," *Renewable and Sustainable Energy Reviews*, no. 93, pp. 701–718, 2018, doi: 10.1016/j.rser.2018.04.035.

[145]   S. Cherevko, A. R. Zeradjanin, A. A. Topalov, N. Kulyk, I. Katsounaros, and K. J. J. Mayrhofer, "Dissolution of Noble Metals during Oxygen Evolution in Acidic Media," *ChemCatChem*, vol. 6, no. 8, pp. 2219–2223, 2014, doi: 10.1002/cctc.201402194.

[146]   S. Cherevko *et al.,* "Oxygen and hydrogen evolution reactions on Ru, RuO 2 Ir, and IrO 2 thin film electrodes in acidic and alkaline electrolytes: A comparative study on activity and stability," *Catalysis Today*, vol. 262, pp. 170–180, 2016, doi: 10.1016/j.cattod.2015.08.014.

[147]   G. C. Da Silva, M. R. Fernandes, and E. A. Ticianelli, "Activity and Stability of Pt/IrO 2 Bifunctional Materials as Catalysts for the Oxygen Evolution/Reduction Reactions," *ACS Catal.*, vol. 8, no. 3, pp. 2081–2092, 2018, doi: 10.1021/acscatal.7b03429.

[148]   R. Makharia, M. F. Mathias, and D. R. Baker, "Measurement of Catalyst Layer Electrolyte Resistance in PEFCs Using Electrochemical Impedance Spectroscopy," *J. Electrochem. Soc.*, vol. 152, no. 5, A970, 2005, doi: 10.1149/1.1888367.

[149]   M. Murbach, B. Gerwe, N. Dawson-Elli, and L. Tsui, "impedance.py: A Python package for electrochemical impedance analysis," *Journal of Open Source Software*, vol. 5, no. 52, p. 2349, 2020, doi: 10.21105/joss.02349.

[150]   K. C. Neyerlin, W. Gu, J. Jorne, A. Clark, and H. A. Gasteiger, "Cathode Catalyst Utilization for the ORR in a PEMFC," *J. Electrochem. Soc.*, vol. 154, no. 2, B279, 2007, doi: 10.1149/1.2400626.

[151]   J. Durst, C. Simon, F. Hasché, and H. A. Gasteiger, "Hydrogen Oxidation and Evolution Reaction Kinetics on Carbon Supported Pt, Ir, Rh, and Pd Electrocatalysts in Acidic Media," *J. Electrochem. Soc.*, vol. 162, no. 1, F190-F203, 2015, doi: 10.1149/2.0981501jes.

[152]   S. Henning *et al.,* "Unsupported Pt 3 Ni Aerogels as Corrosion Resistant PEFC Anode Catalysts under Gross Fuel Starvation Conditions," *J. Electrochem. Soc.*, vol. 165, no. 6, F3001-F3006, 2018, doi: 10.1149/2.0531802jes.

[153]   K. C. Neyerlin, H. A. Gasteiger, C. K. Mittelsteadt, J. Jorne, and W. Gu, "Effect of Relative Humidity on Oxygen Reduction Kinetics in a PEMFC," *J. Electrochem. Soc.*, vol. 152, no. 6, A1073, 2005, doi: 10.1149/1.1897368.

[154]   J. I. Goldstein, D. E. Newbury, J. R. Michael, N. W. Ritchie, J. H. J. Scott, and D. C. Joy, *Scanning Electron Microscopy and X-Ray Microanalysis*. New York, NY: Springer New York, 2018.

[155]   N. Garland, T. Benjamin, and J. Kopasz, "DOE Fuel Cell Program: Durability Technical Targets and Testing Protocols," *ECS Trans.*, vol. 11, no. 1, pp. 923–931, 2007, doi: 10.1149/1.2781004.

[156]   U.S. Department of Energy (DOE), "Fuel Cell Technologies Office Multi-Year Research, Development, and Demonstration Plan - Section 3.4 Fuel Cells," 2016.

Accessed: Dec. 1 2021. [Online]. Available: https://www.energy.gov/sites/default/files/2017/05/f34/fcto_myrdd_fuel_cells.pdf

[157] F. Zhou, S. J. Andreasen, S. K. Kær, and D. Yu, "Analysis of accelerated degradation of a HT-PEM fuel cell caused by cell reversal in fuel starvation condition," *International Journal of Hydrogen Energy*, vol. 40, no. 6, pp. 2833–2839, 2015, doi: 10.1016/j.ijhydene.2014.12.082.

[158] H. A. Gasteiger *et al.,* "Catalyst Degradation Mechanisms in PEM and Direct Methanol Fuel Cells," in *Mini-Micro Fuel Cells*, Kakaç, S., Pramuanjaroenkij, A., Vasiliev, L. (eds), Ed., pp. 225–233.

[159] I. A. Schneider and S. von Dahlen, "Start-Stop Phenomena in Channel and Land Areas of a Polymer Electrolyte Fuel Cell," *Electrochem. Solid-State Lett.*, vol. 14, no. 2, B30, 2011, doi: 10.1149/1.3518520.

[160] I. Jang, I. Hwang, and Y. Tak, "Attenuated degradation of a PEMFC cathode during fuel starvation by using carbon-supported IrO2," *Electrochimica Acta*, vol. 90, pp. 148–156, 2013, doi: 10.1016/j.electacta.2012.12.034.

[161] L. Hu, B. K. Hong, J.-G. Oh, and S. Litster, "Investigation of Hydrogen Starvation of Polymer Electrolyte Fuel Cells in Freezing Condition Using Reference Electrode," *ECS Trans.*, vol. 80, no. 8, pp. 535–542, 2017, doi: 10.1149/08008.0535ecst.

[162] A. P. Young, V. Colbow, D. Harvey, E. Rogers, and S. Wessel, "A Semi-Empirical Two Step Carbon Corrosion Reaction Model in PEM Fuel Cells," *J. Electrochem. Soc.*, vol. 160, no. 4, F381-F388, 2013, doi: 10.1149/2.061304jes.

[163] K. H. Kangasniemi, D. A. Condit, and T. D. Jarvi, "Characterization of Vulcan Electrochemically Oxidized under Simulated PEM Fuel Cell Conditions," *J. Electrochem. Soc.*, vol. 151, no. 4, E125, 2004, doi: 10.1149/1.1649756.

[164] D. R. Baker, D. A. Caulk, K. C. Neyerlin, and M. W. Murphy, "Measurement of Oxygen Transport Resistance in PEM Fuel Cells by Limiting Current Methods," *J. Electrochem. Soc.*, vol. 156, no. 9, B991, 2009, doi: 10.1149/1.3152226.

[165] A. Z. Weber and A. Kusoglu, "Unexplained transport resistances for low-loaded fuel-cell catalyst layers," *J. Mater. Chem. A*, vol. 2, no. 41, pp. 17207–17211, 2014, doi: 10.1039/C4TA02952F.

[166] M. Pourbaix, *Atlas of Electrochemical Equilibria in Aqueous Solution,* 2nd ed. Houston, Texas 77084: National Association of Corrosion Engineers, 1974.

[167] Z. Wang, X. Guo, J. Montoya, and J. K. Nørskov, "Predicting aqueous stability of solid with computed Pourbaix diagram using SCAN functional," *npj Comput Mater*, vol. 6, no. 1, 2020, doi: 10.1038/s41524-020-00430-3.

[168] K. Christmann, K. A. Friedrich, and N. Zamel, "Activation mechanisms in the catalyst coated membrane of PEM fuel cells," *Progress in Energy and Combustion Science*, vol. 85, p. 100924, 2021, doi: 10.1016/j.pecs.2021.100924.

[169] S. Kabir *et al.,* "Elucidating the Dynamic Nature of Fuel Cell Electrodes as a Function of Conditioning: An ex Situ Material Characterization and in Situ Elec-

trochemical Diagnostic Study," *ACS applied materials & interfaces*, vol. 11, no. 48, pp. 45016–45030, 2019, doi: 10.1021/acsami.9b11365.

[170] X.-Z. Yuan, S. Zhang, J. C. Sun, and H. Wang, "A review of accelerated conditioning for a polymer electrolyte membrane fuel cell," *Journal of Power Sources*, vol. 196, no. 22, pp. 9097–9106, 2011, doi: 10.1016/j.jpowsour.2011.06.098.

[171] S. S. Kocha and B. G. Pollet, "Advances in rapid and effective break-in/conditioning/recovery of automotive PEMFC stacks," *Current Opinion in Electrochemistry*, vol. 31, p. 100843, 2022, doi: 10.1016/j.coelec.2021.100843.

[172] Tim Van Cleve *et al.,* "(Invited) Linking Ionomer/Electrocatalyst Interactions to Membrane Electrode Assembly Performance and Durability in Proton Exchange Membrane Fuel Cells," *ECS Meeting Abstracts*, MA2021-02, no. 36, p. 1047, 2021, doi: 10.1149/ma2021-02361047mtgabs.

[173] W. Bi, G. E. Gray, and T. F. Fuller, "PEM Fuel Cell Pt∕C Dissolution and Deposition in Nafion Electrolyte," *Electrochem. Solid-State Lett.*, vol. 10, no. 5, B101, 2007, doi: 10.1149/1.2712796.

[174] G. S. Harzer, J. N. Schwämmlein, A. M. Damjanović, S. Ghosh, and H. A. Gasteiger, "Cathode Loading Impact on Voltage Cycling Induced PEMFC Degradation: A Voltage Loss Analysis," *J. Electrochem. Soc.*, vol. 165, no. 6, F3118-F3131, 2018, doi: 10.1149/2.0161806jes.

[175] S. Cherevko, S. Geiger, O. Kasian, A. Mingers, and K. J. Mayrhofer, "Oxygen evolution activity and stability of iridium in acidic media. Part 2. – Electrochemically grown hydrous iridium oxide," *Journal of Electroanalytical Chemistry*, vol. 774, pp. 102–110, 2016, doi: 10.1016/j.jelechem.2016.05.015.

[176] S. Cherevko, S. Geiger, O. Kasian, A. Mingers, and K. J. Mayrhofer, "Oxygen evolution activity and stability of iridium in acidic media. Part 1. – Metallic iridium," *Journal of Electroanalytical Chemistry*, vol. 773, pp. 69–78, 2016, doi: 10.1016/j.jelechem.2016.04.033.

[177] T. Reier, M. Oezaslan, and P. Strasser, "Electrocatalytic Oxygen Evolution Reaction (OER) on Ru, Ir, and Pt Catalysts: A Comparative Study of Nanoparticles and Bulk Materials," *ACS Catal.*, vol. 2, no. 8, pp. 1765–1772, 2012, doi: 10.1021/cs3003098.

[178] V. Pfeifer *et al.,* "The electronic structure of iridium oxide electrodes active in water splitting," *Physical chemistry chemical physics : PCCP*, vol. 18, no. 4, pp. 2292–2296, 2016, doi: 10.1039/c5cp06997a.

[179] J. Stoll, F. P. Orfino, M. Dutta, and E. Kjeang, "Four-Dimensional Identical-Location X-ray Imaging of Fuel Cell Degradation during Start-Up/Shut-Down Cycling," *J. Electrochem. Soc.*, vol. 168, no. 2, p. 24516, 2021, doi: 10.1149/1945-7111/abe56b.

[180] M. Łukaszewski, "Electrochemical Methods of Real Surface Area Determination of Noble Metal Electrodes – an Overview," *Int. J. Electrochem. Sci.*, pp. 4442–4469, 2016, doi: 10.20964/2016.06.71.

[181] S. Rudi, C. Cui, L. Gan, and P. Strasser, "Comparative Study of the Electrocatalytically Active Surface Areas (ECSAs) of Pt Alloy Nanoparticles Evaluated by Hupd and CO-stripping voltammetry," *Electrocatalysis*, vol. 5, no. 4, pp. 408–418, 2014, doi: 10.1007/s12678-014-0205-2.

[182] E. Antolini, "The problem of Ru dissolution from Pt–Ru catalysts during fuel cell operation: analysis and solutions," *J Solid State Electrochem*, vol. 15, no. 3, pp. 455–472, 2011, doi: 10.1007/s10008-010-1124-7.

[183] P. Zelenay, Y. S. Kim, R. Bashyam, and J.-H. Choi, "Ruthenium Crossover in DMFCs Operating with Different Proton Conducting Membranes," *ECS Trans.*, vol. 1, no. 8, pp. 437–445, 2006, doi: 10.1149/1.2214574.

[184] K.-S. Lee *et al.,* "Surface structures and electrochemical activities of Pt overlayers on Ir nanoparticles," *Langmuir : the ACS journal of surfaces and colloids*, vol. 27, no. 6, pp. 3128–3137, 2011, doi: 10.1021/la103825s.

[185] T. Pauporté, F. Andolfatto, and R. Durand, "Some electrocatalytic properties of anodic iridium oxide nanoparticles in acidic solution," *Electrochimica Acta*, vol. 45, no. 3, pp. 431–439, 1999, doi: 10.1016/S0013-4686(99)00282-0.

[186] JEOL Ltd., *Energy table for EDS analysis.* [Online]. Available: https://www.unamur.be/services/microscopie/sme-documents/Energy-20table-20for-20EDS-20analysis-1.pdf (accessed: May 27 2022).

[187] US National Institute of Standards and Technology, *NIST DTSA-II Software.* [Online]. Available: https://www.cstl.nist.gov/div837/837.02/epq/dtsa2/index.html (accessed: May 27 2022).

[188] J.-G. Oh, W. H. Lee, and H. Kim, "The inhibition of electrochemical carbon corrosion in polymer electrolyte membrane fuel cells using iridium nanodendrites," *International Journal of Hydrogen Energy*, vol. 37, no. 3, pp. 2455–2461, 2012, doi: 10.1016/j.ijhydene.2011.10.072.

[189] S.-E. Jang and H. Kim, "Effect of water electrolysis catalysts on carbon corrosion in polymer electrolyte membrane fuel cells," *Journal of the American Chemical Society*, vol. 132, no. 42, pp. 14700–14701, 2010, doi: 10.1021/ja104672n.

[190] C. Minke, M. Suermann, B. Bensmann, and R. Hanke-Rauschenbach, "Is iridium demand a potential bottleneck in the realization of large-scale PEM water electrolysis?," *International Journal of Hydrogen Energy*, vol. 46, no. 46, pp. 23581–23590, 2021, doi: 10.1016/j.ijhydene.2021.04.174.
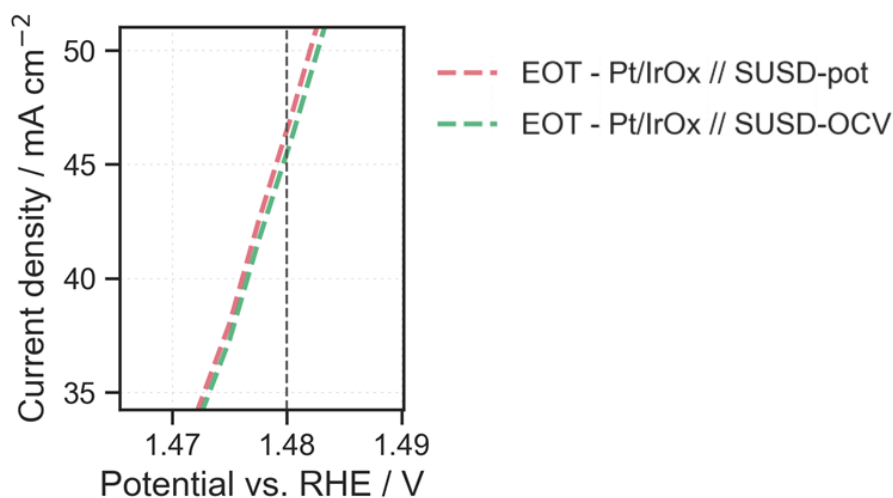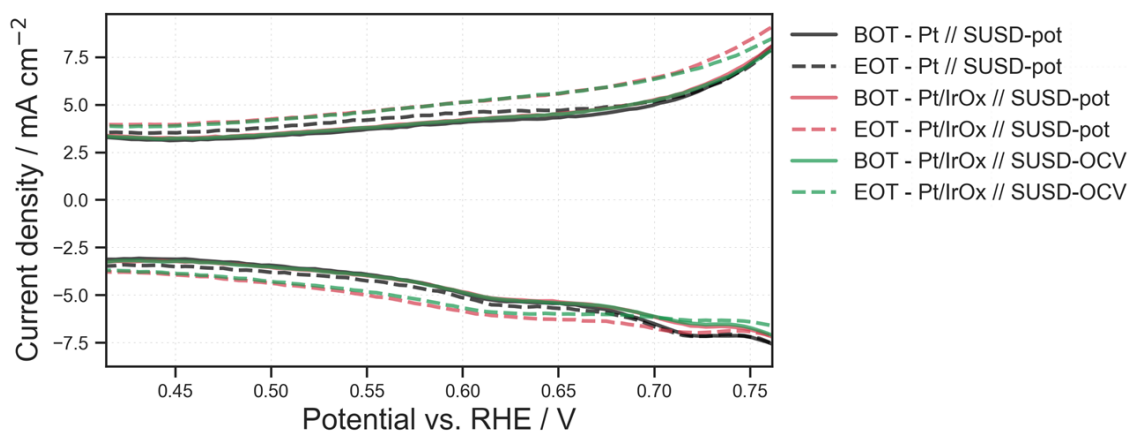
Appendix
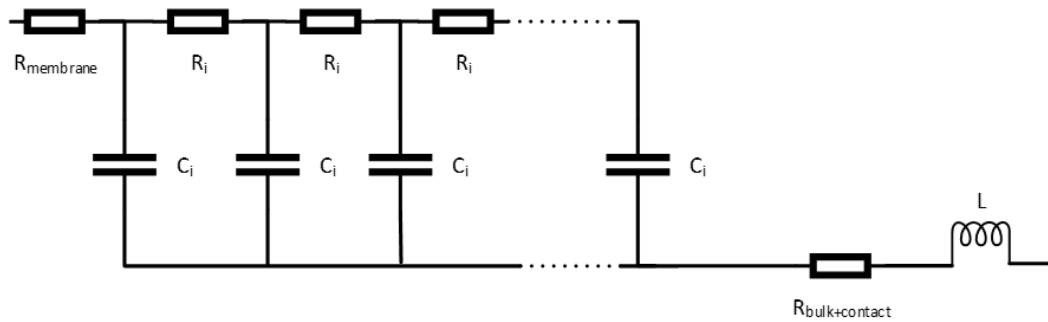
Appendix-Figure 1: Equivalent circuit model used for fitting electrochemical impedance spectroscopy data. Model according to Makharia et al. [148].
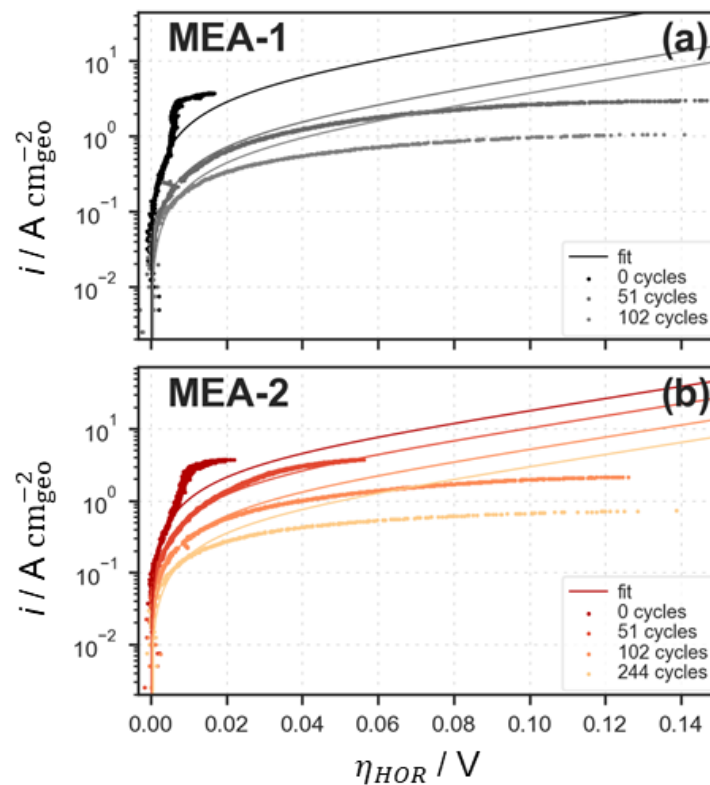

Appendix-Figure 2: H₂ pump polarization curves corrected by E_{rev} and iR_Ω (points) and their fit to the Butler-Volmer equation (solid lines) during CR AST for (a) MEA-1 and (b) for MEA-2. For fitting, a symmetry factor of 0.5 and current densities below the onset of mass transport limitation (< 1 A cm⁻² BOL and <0.2 A cm⁻² for all subsequent measurements) were considered.

Appendix-Figure 3: Intercept of cathode OER polarization curves corresponding to Figure 6.3, illustrating the overlap of the EOT data.


Appendix-Figure 4: Cathode H$_{upd}$ CV curves corresponding to Figure 6.5, illustrating the double layer decrease after SUSD events.
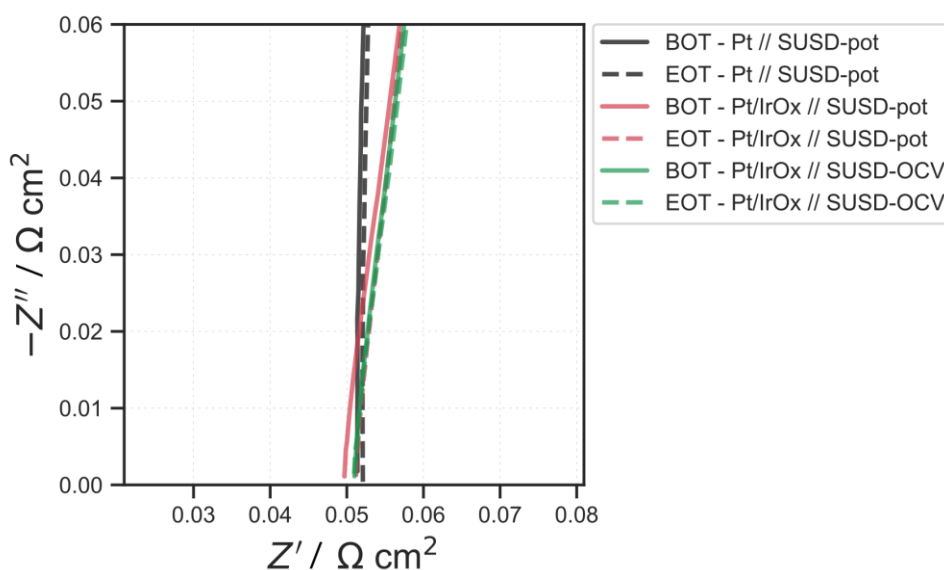
Appendix-Figure 5: Anode impedance spectra prior (BOT) and succeeding SUSD AST (EOT) for each MEA//AST combination (cf. legend). Measurements were performed at 68° C, 100% *RH* and 1 bar$_g$.
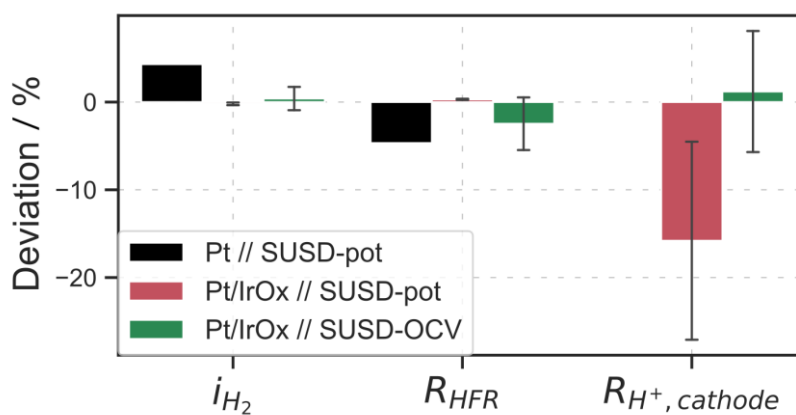
Appendix-Figure 6: Changes in hydrogen crossover current density i_{H_2}, MEA's high frequency resistance R_{HFR} and CCL proton resistance $R_{H+, cathode}$ after SUSD AST was performed. Values determined from the respective CV and EIS measurements at 68° C, 100% *RH* and 1 bar$_g$. For Pt-MEA no $R_{H+, cathode}$ could be derived via numerical fitting due to the absence of a characteristic 45° line in the Nyquist plot.
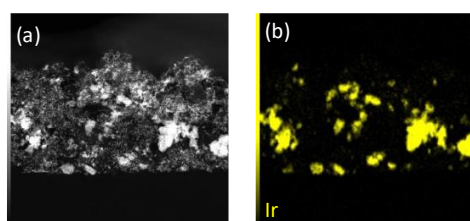
Appendix-Figure 7: EDX mapping analysis performed on the pristine anode catalyst layer of MEA-2. Images were recorded using a Jeol JEM-ARM200F scanning transmission electron microscope. (a) Selected area for EDX mapping. (b) Ir element mapping.
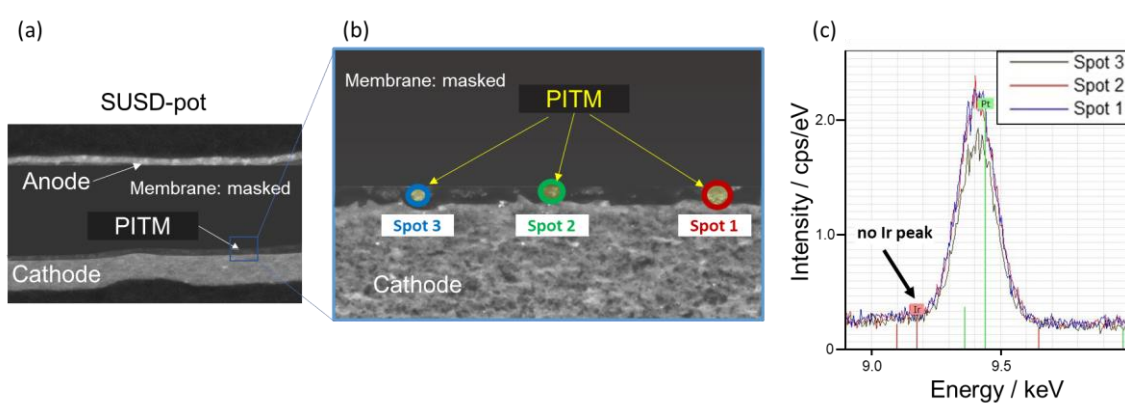
Appendix-Figure 8: (a) SEM image after SUSD-pot AST corresponding to Figure 6.18 (PITM: platinum in the membrane). (b) Detail from (a) with marked spots, at which EDX analysis was performed. (c) EDX spectra of the marked spots, identifying the precipitation as platinum.
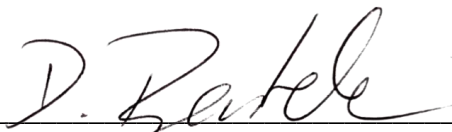
Declaration

I hereby declare that this dissertation is entirely my own work except where otherwise indicated. Passages and ideas from other sources have been clearly indicated.

Ich versichere, dass ich die vorliegende Arbeit selbständig verfasst und keine anderen als die angegebenen Quellen und Hilfsmittel benutzt habe. Aus fremden Quellen entnommene Passagen und Gedanken sind als solche kenntlich gemacht.

Waiblingen, 12.07.2023

Dominik Claudius Bentele